New Methods for Seismic Performance Evaluation and Retrofit of Nonductile Concentrically Braced Frames

Andrew D. Sen

A dissertation
submitted in partial fulfillment of the
requirements for the degree of

Doctor of Philosophy

University of Washington

2018

Reading Committee:

Charles W. Roeder, Chair

Jeffrey W. Berman, Chair

Dawn E. Lehman

Richard Wiebe

Program Authorized to Offer Degree:
Civil and Environmental Engineering

University of Washington

Abstract

New Methods for Seismic Performance Evaluation and Retrofit of Nonductile Concentrically Braced Frames

Andrew D. Sen

Co-Chairs of the Supervisory Committee:
Professor Charles W. Roeder
Civil and Environmental Engineering

Professor Jeffrey W. Berman
Civil and Environmental Engineering

Concentrically braced frames (CBFs) have been used in steel construction as seismic-force-resisting systems for many decades and constitute a substantial proportion of existing building infrastructure. Until about 1990, CBFs were designed without the codified capacity-based and other ductile design provisions that ensure safety in today's special CBFs (SCBFs) used in regions with high seismic risk. Thousands of these older and potentially nonductile CBFs (NCBFs) remain in service in the high-seismicity areas of the west coast of the US and other more moderately seismically vulnerable regions. These NCBFs utilize a wide variety of connections, components, and frame configurations with deficiencies expected to lead to significant damage and potential collapse in earthquakes. Seismic retrofit of NCBFs may be necessary to ensure occupant safety and building functionality, but current engineering guidance for determining retrofit need and type is limited.

The state of practice evaluates the seismic vulnerability of CBFs using simplistic models for braces, beams, and columns, and the nonlinear behavior of connections is typically not considered; it is clear that the vulnerability depends on more complex component behavior. To develop more comprehensive engineering methods that can accurately estimate the vulnerability of NCBFs and the improved performance of retrofitted NCBFs, integrated

experimental and computational research programs were conducted. First, two series of large-scale experiments of existing and retrofitted NCBF subassemblages were performed to investigate brace, connection, and beam deficiencies common to NCBFs. The experiments identified critical deficiencies but also beneficial yielding mechanisms (e.g., bolt-hole elongation, beam yielding in the chevron configuration, etc.) which could be retained in retrofit. Experimentally validated, nonlinear modeling approaches capable of simulating brace fracture, connection fracture, weak frame elements, and post-fracture response of components with secondary yielding mechanisms were then developed to advance numerical simulation capabilities. These models were used to enable system-level response-history analysis for seismic performance evaluation. Specifically, the seismic performance (including collapse) of three- and nine-story buildings were investigated at multiple (5) hazard levels. The models were also used to evaluate retrofit strategies; these results combined with the experimental work were used to develop a cost-effective seismic retrofit methodology based on balancing yielding mechanisms and suppressing severe failure modes.

TABLE OF CONTENTS

LIST OF FIGURES

LIST OF TABLES

ACKNOWLEDGMENTS

First, I must acknowledge my advisors, Profs. Charles Roeder, Jeffrey Berman, and Dawn Lehman for their substantial contributions to not only this work, but my academic career. Their guidance over the past six years at the University of Washington is sincerely appreciated, and they have shaped the researcher, educator, and learner that I am today. I would also like to thank Prof. Richard Wiebe, who served on my doctoral reading committee, and Prof. Ann Bostrom, who was supportive and engaged as a graduate school representative.

I owe a great deal more to many other faculty, students, and staff at this institution and others who have made a positive impact on my doctoral studies. Profs. Keh-Chyuan Tsai (National Taiwan University) and Masayoshi Nakashima (Kyoto University) provided eager international perspectives on structural steel design and earthquake engineering during my visits to their laboratories. These trips abroad would also not have been possible without the help of collaborating students, research fellows, and post-doctoral researchers; in particular, I thank Drs. Ching-Yi Tsai and Konstantinos Skalomenos for their help and friendship.

Closer to home in Seattle, there are almost too many of my fellow students to thank. Dan Sloat, Molly Johnson, Ryan Ballard, Marsha Swatosh, Clare Terpstra, and Sara Ibarra were all excellent colleagues and instrumental in the work presented in this document. My officemates over the years in More 236, particularly Nasser Marafi, Ramona Barber, Max Stephens, and Travis Thonstad, provided more technical and mental support than they know. It was also a pleasure to work with a number of visiting international students, including Tao Li, Ruyue Liu, Nader Naderpour, and Lingli Pan, who brought tireless work ethics to the research team.

Finally, I would be sincerely remiss without mentioning my family, who have supported

me from across the country during this difficult but rewarding period of my life.

The material in this disseration is based upon work supported by the National Science Foundation (NSF) Network for Earthquake Engineering Simulation under Grant No. CMMI-1208002, the NSF Gradaute Research Fellowship under Grant No. DGE-1256082, and the East Asia and Pacific Summer Institutes Fellowship under Grant No. OISE-1614277. The American Society of Civil Engineers Structural Engineering Institute also funded this work through the O. H. Ammann Research Fellowship. The American Institute of Steel Construction provided substantial support in the form of material donations for experimental research. The numerical research was facilitated by the use of Texas Advanced Computing Center through a DesignSafe-CI allocation, and the NSF Natural Hazards Engineering Research Infrastructure: Cyberinfrastructure awardees of NSF Grant No. CMMI-1520817 are gratefully acknowledged. Any opinion, findings, and conclusions or recommendations expressed in this material are those of the author and do not necessarily reflect the views of the sponsoring agencies.

DEDICATION

To my late grandparents, David and Peggy Cassady and John and Patricia Sen.

Chapter 1

INTRODUCTION

1.1 Background and Motivation

Steel concentrically braced frames (CBFs) are seismic-force-resisting systems with considerable strength and stiffness which are well suited for accommodating architectural requirements. CBFs are composed of braces, gusset plates, and beams and columns (i.e., framing elements). The braces are the primary source of lateral resistance and energy dissipation in CBFs. For buckling braces, opposing brace pairs are used to provide symmetric resistance, as in the common configurations shown in Fig. 1.1. The colors in Fig. 1.1 indicate braces which would be in either compression or tension at the same time under lateral loading of the structures in the same direction.

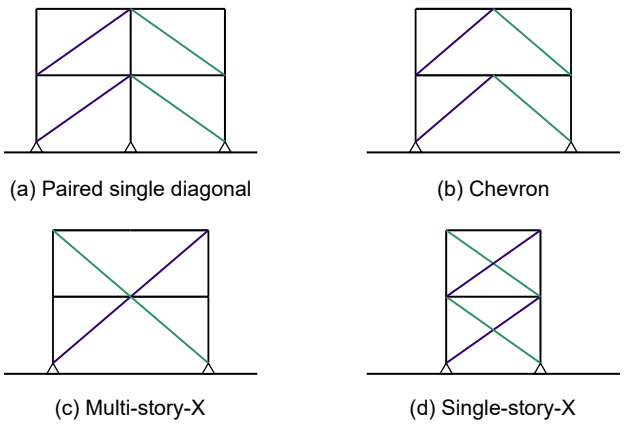

Figure 1.1: Common brace configurations

CBFs have been used for many years in regions with high seismic hazards, but capacity-based and other ductile design requirements were not codified before 1988. The 1988 Uniform

Building Code (UBC) (ICBO 1988) introduced the principle of capacity design to provide sufficient strength of the adjacent components to elastically sustain demands resulting from brace yielding in tension and buckling in compression. Today, Special CBFs (SCBFs) in the American Institute of Steel Construction (AISC) *Seismic Provisions for Structural Steel Buildings* (AISC 2017a) are expected to have sufficient ductility by:

- Limiting bracing configurations to avoid unacceptable inelastic deformations,
- Proportioning lateral resistance between the compressive and tensile braces,
- Limiting member (global) and cross-sectional width-to-thickness (local) slenderness ratios for braces and framing members to ensure ductile behavior,
- Requiring connections to develop the expected brace capacity and to accommodate end rotation of the brace, and
- Requiring demand critical welds with minimum Charpy V-Notch (CVN) toughness for connecting seismic-force-resisting components.

By satisfying these provisions, SCBFs are intended to maintain resistance at large inelastic deformations through a yielding and failure hierarchy which, at a minimum, includes brace buckling in compression and brace yielding in tension. SCBFs may also exhibit secondary yield mechanisms which are not explicitly considered in design, including beam yielding, column yielding, panel-zone yielding, and gusset-plate connection yielding. The occurrence and importance of these mechanisms are implied by the beam and column local slenderness and gusset-plate clearance geometric limits above. The expected and preferred failure mode is brace fracture after numerous, large cyclic deformation demands.

CBFs built prior to about 1990 do not satisfy most of the above requirements and consequently have unknown seismic performance. Here, these older CBFs are termed nonductile CBFs (NCBFs). While the vulnerability of NCBFs has been recognized by the engineering

community, relatively little previous research has been conducted on NCBFs to identify the scope of deficiencies, quantify their seismic performance, and develop validated rehabilitation schemes.

The building stock of NCBFs in existing infrastructure is substantial; thousands remain in service in regions with high seismic hazard in the US and are expected to remain in service for years to come. Based on the significant gap between vintage and modern building codes (including both design provisions and seismic demands), seismic retrofit of these buildings is expected to be required to ensure safety of the building occupants and maintain functionality following an earthquake. The American Society of Civil Engineers (ASCE) *Seismic Evaluation and Retrofit of Existing Buildings* (ASCE 2017b) is intended to provide guidance for modeling recommendations, performance acceptance criteria, and retrofit strategies for CBFs, but it does not address complex connection behaviors and system characteristics which are expected to affect response.

1.2 Research Objectives

The research presented in this document addresses these gaps in the understanding of the behavior of NCBFs in order to establish their vulnerability and evaluate effective retrofit schemes. The specific objectives of the research program are to:

1. Quantify and classify the behavior of different deficiencies on the subassemblage level through large-scale experimentation.

2. Develop nonlinear modeling approaches to simulate key characteristics of NCBFs, including brace fracture, gusset-plate connection yielding and fracture, beam yielding in the chevron configuration, and column buckling.

3. Evaluate the seismic performance of existing and retrofitted NCBF buildings using response-history analysis.

4. Provide a retrofit design methodology for NCBFs by prioritizing deficiencies and promoting balanced design principles.

1.3 Document Overview

This document describes a comprehensive, integrated experimental and computational research program which investigates NCBF behavior and develops new methods for evaluation and design. The chapters are organized as follows:

- Chapter 1 introduces NCBFs in the context of modern design, motivates the research program, and outlines the research program objectives.

- Chapter 2 reviews NCBF infrastructure based on drawing sets obtained from engineering firms, observed NCBF damage from post-earthquake reconnaissance, experimental research programs addressing NCBFs and related systems, and computational modeling of CBFs.

- Chapter 3 describes the setup, results, and findings from two large-scale experimental programs. This research was conducted at the University of Washington and National Center for Research on Earthquake Engineering in Taipei, Taiwan.

- Chapter 4 develops modeling approaches calibrated from experimental research to accurately simulate the complex yielding and failure sequence of NCBFs

- Chapter 5 discusses the seismic performance evaluation approach, including the design and modeling of the archetype buildings, selection and scaling of input ground motions, and interpretation of results using component damage states

- Chapter 6 characterizes the performance of four benchmark NCBFs in relation to four benchmark SCBF counterparts.

- Chapter 7 describes a seismic performance evaluation parametric study that investigates the effects of brace retrofit and severity of connection deficiencies.

- Chapter 8 provides a summary of the research program, major conclusions based on the combined experimental and computational research findings, and recommendations for future work.

Appendices provide a comprehensive notation list for the document, source code used to simulate fracture in nonlinear analysis, and lists of input ground motions used in response-history analysis.

Chapter 2
INFRASTRUCTURE AND LITERATURE REVIEW

This chapter reviews salient research which has advanced the understanding of CBF seismic performance using evaluative, experimental, and computational methods. A review of CBF deisgn expressions and existing NCBF infrastructure in the US conducted as part of this research project precedes the literature review to establish NCBF building characteristics. This work is described in greater detail in Sloat (2014) and Sen et al. (2016a). The subsequent literature review emphasizes past and concurrent research on NCBFs but introduces relevant SCBF research to provide a fundamental understanding of modern seismic design practice, nonlinear modeling approaches, and system performance expectations. Finally, a summary of the infrastructure and literature review is provided which helps motivate the experimental and computational research programs described in the following chapters.

2.1 CBF Design Expressions

The design expressions used in modern SCBF design are introduced here and will be used throughout this document to systematically evaluate NCBFs deficiencies. These expressions are based largely on the AISC *Specification for Structural Steel Buildings* (AISC 2017c), *Seismic Provisions for Structural Steel Buildings* (AISC 2017a), and *Steel Construction Manual* (AISC 2017d) and are used to compute demand-to-capacity ratios (DCRs) for limit states and analogous ratios for geometric limits (also referred to as DCRs herein).

2.1.1 Capacity-Based Design Demands

The expected brace forces in tension and compression are given by Eqs. 2.1 and 2.2 and used to determine the seismic demands on CBF components, including connections, beams, and

columns. These demands usually correspond to the maximum possible seismic demands in connection design, but idealized (or assumed) forces are used in several instances which will be noted below. Note that the expected brace forces are computed using the expected yield stress of the material, $R_y F_y$, since the actual yield stress of structural steel is usually larger than the nominal yield stress, F_y.

$$P_t = R_y F_y A_g \tag{2.1}$$

$$P_c = (1/0.877) F_{cre} A_g \tag{2.2}$$

The *Seismic Provisions* stipulate that SCBFs must be analyzed under two load scenarios: (1) a yielding and buckling load case in which all braces in tension develop P_t and all braces in compression develop P_c and (2) a post-buckling load case in which all braces in tension develop P_t and all braces in compression develop 30% of P_c. The second load scenario results in an "unbalanced" load where two or more braces intersect. The forces resulting from these load scenarios constitute the demands in the DCRs.

2.1.2 Brace-Gusset Assembly Evaluation

Braces and gusset-plate connections in CBFs are evaluated considering yielding mechanisms, failure modes, and geometric limits; Fig. 2.1 shows examples of each for a continuous, bolted shear-plate connection. Yielding mechanisms with DCRs approaching or greater than 1 are not permitted by code but are expected to enhance drift capacity, whereas failure modes with DCRs approaching or greater than 1 are expected to preclude brace fracture and therefore limit drift capacity. Geometric limits with DCRs exceeding 1 contribute to either premature fracture of the brace (local slenderness ratio, λ) or gusset-plate interface weld (clearance, Nt_p).

Table 2.1 provides the conventional AISC design expressions for braces and gusset plates. In the most recent *Seismic Provisions*, an additional check must be performed for the gusset-

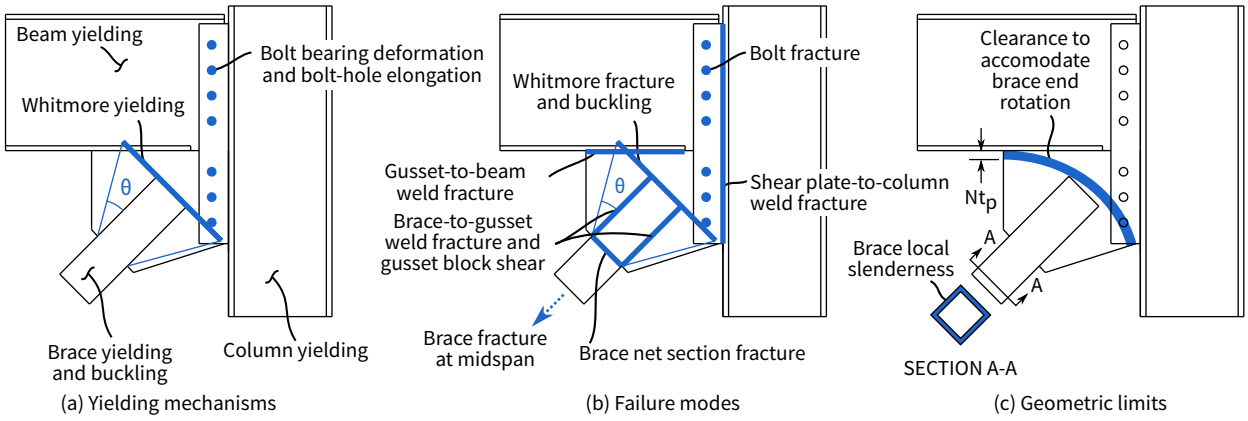

Figure 2.1: Common gusset-plate connection yielding mechanisms, failure modes, and geometric limits

plate interface welds based on the compressive demands of the brace and weak-axis bending of the plate (AISC 2017a); this change is not reflected in Table 2.1 but is discussed later in the document (see Chapter 4). Design expressions proposed for an enhanced, balanced design procedure (BDP) are also presented (Roeder et al. 2011b). The BDP provides an economical connection design and increases SCBF drift capacity by permitting controlled yielding in the gusset plate, utilizing an elliptical gusset-plate clearance (Lehman et al. 2008), and sizing the gusset-plate interface welds to develop the strength of the plate.

2.1.3 Beam Yielding Evaluation in Chevron Configuration

In the chevron configuration, the braces intersect at the midspan of the beam, which results in large unbalanced forces at this location. Therefore, the beam yielding DCR is calculated based on the large vertical and horizontal resultant forces in the idealized post-buckling load case defined above. These forces, given by Eqs. 2.4 and 2.6, are concentrated at the beam midspan as shown in Fig. 2.2a. The beam strength is evaluated with the AISC axial-flexural interaction equation (Eq. H1-1 in AISC (2017c)), which has been rewritten in Eq. 2.7 assuming (1) the horizontal resultant force, P_h, is distributed equally to each side of the beam

Table 2.1: Conventional and balanced design procedure limit-state and geometric-limit expressions (adapted from Roeder et al. (2011b))

	AISC conventional design (AISC 2010b, a)		Balanced design	
Criterion	Resistance (ϕR_{n}) or geometric limit	ϕ	Resistance (βR_{n}) or geometric limit	β
Yielding mechanisms				
Whitmore yielding	$\phi F_{\mathrm{y}} B_{\mathrm{w}} t_{\mathrm{p}}$	0.90	$\beta R_{\mathrm{y}} F_{\mathrm{y}} B_{\mathrm{w}} t_{\mathrm{p}}$	1.0
Failure modes				
Brace net-section fracture	$\phi U(R_{\mathrm{tb}} F_{\mathrm{ub}} A_{\mathrm{nb}} + F_{\mathrm{up}} A_{\mathrm{gp}})$	0.75	$\beta U(R_{\mathrm{tb}} F_{\mathrm{ub}} A_{\mathrm{nb}} + F_{\mathrm{up}} A_{\mathrm{gp}})$	0.95
Brace-to-gusset weld fracture (filler metal)	$\phi(0.6) F_{\mathrm{EXX}} N_{\mathrm{w}} L_{\mathrm{w}} (0.707) w_{br}$	0.75	Same as AISC	0.75
Brace-to-gusset weld fracture (base metal)	$\phi(0.6) F_{\mathrm{u}} N_{\mathrm{s}} L_{\mathrm{w}} t_{\mathrm{f}}$	0.75	Same as AISC	0.75
Gusset-plate block shear	$\phi\{(0.6 F_{\mathrm{u}} A_{\mathrm{nv}} + U_{\mathrm{bs}} F_{\mathrm{u}} A_{\mathrm{nt}}) \leq (0.6 F_{\mathrm{y}} A_{\mathrm{gv}} + U_{\mathrm{bs}} F_{\mathrm{u}} A_{\mathrm{nt}})\}$	0.75	$\beta\{(0.6 F_{\mathrm{u}} A_{\mathrm{nv}} + U_{\mathrm{bs}} F_{\mathrm{u}} A_{\mathrm{nt}})\}$	0.85
Whitmore fracture	$\phi F_{\mathrm{u}} B_{\mathrm{w}} t_{\mathrm{p}}$	0.75	$\beta F_{\mathrm{u}} B_{\mathrm{w}} t_{\mathrm{p}}$	0.85
Gusset-plate buckling	$\phi B_{\mathrm{w}} t_{\mathrm{p}} F_{\mathrm{cr}}$	0.90	$\beta B_{\mathrm{w}} t_{\mathrm{p}} F_{\mathrm{cr}}$	0.90
Gusset-plate interface weld fracture	$\phi(0.6) F_{\mathrm{EXX}} [1 + 0.5(\sin\gamma)^{1.5}] 2 L_{\mathrm{w}} (0.707) w_p \geq \mathrm{UFM}$	0.75	$2(1.5)\beta(0.6) F_{\mathrm{EXX}} (0.707) w_p \geq R_{\mathrm{y}} F_{\mathrm{y}} t_{\mathrm{p}}$	0.75
Geometric limits				
Brace local slenderness	$\lambda \leq \lambda_{hd}$		Same as AISC	
Gusset-plate clearance	$2t_p$ linear		$8t_p$ elliptical	

and (2) a slab restrains the beam from flexural and lateral-torsional buckling.

$$P_h = (P_t + 0.3P_c)\cos\theta \tag{2.3}$$

$$= (R_y F_y A_g + 0.3(1.14) F_{cre} A_g)\cos\theta \tag{2.4}$$

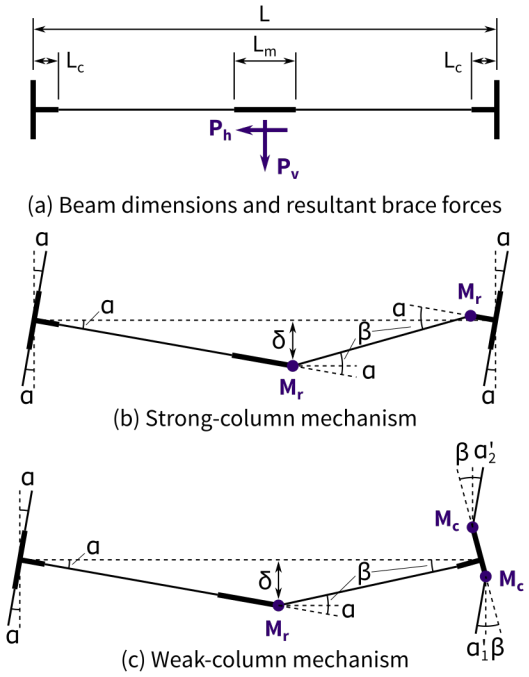

Figure 2.2: Combined beam-sway mechanisms for DCR calculation

$$P_h = (P_t - 0.3P_c)\sin\theta \tag{2.5}$$

$$= (R_y F_y A_g - 0.3(1.14)F_{cre}A_g)\sin\theta \tag{2.6}$$

$$DCR = \begin{cases} \dfrac{P_h/2}{P_y} + \dfrac{8}{9}\left(\dfrac{M_r}{M_p}\right) & \text{for } \dfrac{P_h/2}{P_y} \geq 0.2 \\ \dfrac{P_h/2}{2P_y} + \dfrac{M_r}{M_p} & \text{for } \dfrac{P_h/2}{P_y} < 0.2 \end{cases} \tag{2.7}$$

The required flexural strength, M_r, in Eq. 2.7 is determined from an assumed plastic mechanism for the beam. In practice, this beam is often treated as simply supported with no contribution from the gusset plates, and hence the required strength is calculated as in Eq. 2.8. This approach is considered conservative as it results in the largest possible flexural

demands on the beam; this necessitates the use of very deep, heavy beams which are not economical. When the DCR is computed using $(M_r)_{prac.}$, it is referred to as the $DCR_{prac.}$.

$$(M_r)_{prac.} = \frac{P_v L}{4} \tag{2.8}$$

A more realistic approach for computing M_r considers the rotational restraint between the beam and columns provided by the corner gusset plates and local strengthening of the beam at the corner and midspan gusset-plate locations. In this approach, M_r is computed using plastic analysis. The idealized brace unbalanced forces imply a large lateral deflection and hence the plastic mechanism considered here is a combined beam-sway mechanism. Depending on the strength of the beam and column, either a strong- or weak-column mechanism can form (Figs. 2.2b or c, respectively). Derivations of the required flexural strength using the virtual-work method for each case are provided below. The variables L, L_m, L_c, α, β, and δ are defined in Fig. 2.2a.

Since the beam DCRs are computed based on an idealized force distribution and incomplete plastic mechanism, it must be noted that these DCRs are viewed primarily as indices for beam strength.

Strong-Column Case Derivation

The angles α and β are related by the displacement δ at the right-hand side of the midspan gusset plate.

$$\left(\frac{L}{2} + \frac{L_m}{2}\right)\alpha = \left(\frac{L}{2} - \frac{L_m}{2} - L_c\right)\beta - L_c\alpha \tag{2.9}$$

$$\left(\frac{L}{2} + \frac{L_m}{2} + L_c\right)\alpha = \left(\frac{L}{2} - \frac{L_m}{2} - L_c\right)\beta \tag{2.10}$$

Rearrange to solve for β.

$$\beta = \left(\frac{\frac{L}{2} + \frac{L_m}{2} + L_c}{\frac{L}{2} - \frac{L_m}{2} - L_c} \right) \alpha \tag{2.11}$$

$$\beta = \left(\frac{L + L_m + 2L_c}{L - L_m - 2L_c} \right) \alpha \tag{2.12}$$

Equate external and internal virtual work.

$$W_{EXT} = W_{INT} \tag{2.13}$$

$$P_v \frac{L}{2} \alpha = 2M_r(\alpha + \beta) \tag{2.14}$$

Rearrange to solve for M_r.

$$M_r = \frac{P_v L}{4} \alpha (\alpha + \beta)^{-1} \tag{2.15}$$

$$M_r = \frac{P_v L}{4} \alpha \left[\alpha + \left(\frac{L + L_m + 2L_c}{L - L_m - 2L_c} \right) \alpha \right]^{-1} \tag{2.16}$$

$$M_r = \frac{P_v L}{4} \left(1 + \frac{L + L_m + 2L_c}{L - L_m - 2L_c} \right)^{-1} \tag{2.17}$$

Define L' as $L - L_m - 2L_c$ and substitute L for $L' + L_m + 2L_c$.

$$M_r = \frac{P_v L'}{8} \tag{2.18}$$

Weak-Column Case Derivation

The angles α and β are related by the displacement δ at the right-hand side of the midspan gusset plate.

$$\left(\frac{L}{2}+\frac{L_m}{2}\right)\alpha=\left(\frac{L}{2}-\frac{L_m}{2}\right)\beta \tag{2.19}$$

$$(L+L_m)\alpha=(L-L_m)\beta \tag{2.20}$$

Rearrange to solve for β.

$$\beta=\left(\frac{L+L_m}{L-L_m}\right)\alpha \tag{2.21}$$

Equating external and internal virtual work and taking $\alpha=\alpha_1'=\alpha_2'$, Here, M_c is the column plastic moment capacity reduced for the axial forces from gravity loading in the load combination of interest.

$$W_{EXT}=W_{INT} \tag{2.22}$$

$$P_v\frac{L}{2}\alpha=(M_r+2M_c)(\alpha+\beta) \tag{2.23}$$

Rearrange to solve for M_r.

$$M_r = \frac{P_v L}{2} \alpha \left(\alpha + \beta\right)^{-1} - 2M_c \tag{2.24}$$

$$M_r = \frac{P_v L}{2} \alpha \left[\alpha + \left(\frac{L + L_m}{L - L_m}\right) \alpha\right]^{-1} - 2M_c \tag{2.25}$$

$$M_r = \frac{P_v L}{2} \left(1 + \frac{L + L_m}{L - L_m}\right)^{-1} - 2M_c \tag{2.26}$$

Define L' as $L - L_m$ and substitute L for $L' + L_m$.

$$M_r = \frac{P_v L'}{4} - 2M_c \tag{2.27}$$

2.2 Review of Existing Infrastructure

A review of NCBF buildings was conducted to determine the frequency and severity of deficiencies with respect to current design procedures. These buildings had a variety of uses, including offices, schools, hospitals, and warehouses, and were primarily located on the West Coast of the US. Table 2.2 summarizes the age distribution of buildings surveyed and reports their governing building codes as available. As indicated in the table, the buildings were built between 1974 and 1992. The CBFs in these buildings utilized hollow structural section (HSS), pipe, wide-flange, angle, and built-up-angle braces. Typically, these braces were oriented in either paired single-diagonal or chevron configurations, though X- and multi-story-X configurations were also used. Figure 2.3 shows an example frame from the infrastructure review which uses both the single-diagonal and chevron configuration within the same bay, which may result in a vertical irregularity if the lateral-load path is not well detailed. A wide variety of gusset-plate connection configurations were also documented, eight of which are shown in Fig. 2.4.

From this set of buildings, 12 low- to mid-rise buildings with relatively complete drawing

Table 2.2: Infrastructure review building age and code use distribution

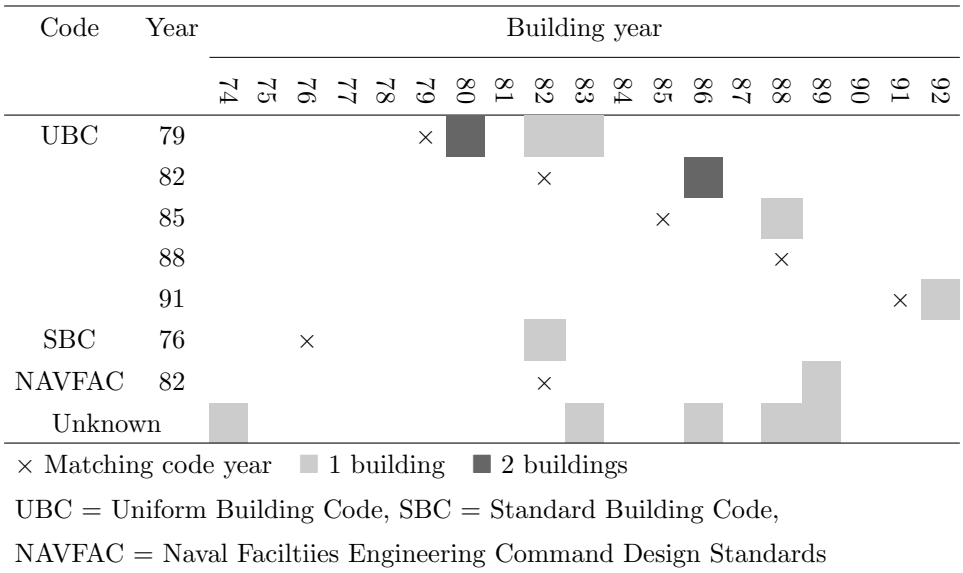

sets were selected for advanced study. Buildings with more than 9 stories were excluded, since their CBFs tended to have heavy connection configurations which were less common (e.g., the double integrated shear plate connection in Fig. 2.4g). DCRs were computed for connections and members in each building based upon the expected capacities of the braces as required for SCBFs in the *Seismic Provisions* (AISC 2017a). These values were computed without resistance factors and using expected material properties for all capacities in this document in order to evaluate the relative vulnerability of the limit states.

Table 2.3 reports the maximum DCRs for various limit states in each building. In this table, the buildings have been assigned identifying names which consist of the (1) last two digits of the building year, (2) state abbreviation in which the building is located, and (3) number of stories. For example, "74CA6" refers to a 6-story building in California designed in 1974. In addition to limit-state DCRs, Table 2.3 contains information on geometric limits and system irregularities.

The large quantity of DCRs above 1 in Table 2.3 indicate a wide variety of common NCBF deficiencies. While many of the buildings had gusset plates susceptible to Whitmore

Table 2.3: Infrastructure review building maximum limit-state DCRs, geometric-limit DCRs, and system irregularities

Criterion	Building ID											
	74CA6	80CA4	80WA8	82OR9	82TN4	83CA2	83CA3	86CA4	86WA3	88CA3	88UT1	92WA2
Framing member limit states												
Chevron beam yielding (DCR)	—	1.7	—	—	1.6	4.4	6.3	5.9	3.8	8.8	—	5.1
Column buckling	1.2	2.2	1.2	—	1.0	1.3	3.7	3.9	3.0	1.6	1.0	0.9
Brace-gusset connection yielding mechanisms												
Whitmore yielding (30°)	1.1	1.5	1.4	—	0.8	—	1.6	1.1	1.5	0.8	1.1	1.0
Whitmore yielding (37.5°)	0.8	1.3	1.2	—	0.8	—	1.6	0.9	1.5	0.7	0.8	0.8
Gusset-pl.-interface bolt bearing	—	—	0.7	—	0.9	—	—	0.8	—	—	—	—
Brace-gusset connection failure modes												
Brace net section fracture	0.9	1.2	1.2	—	0.8	—	1.1	1.1	1.1	1.3	1.4	1.3
Gusset-plate block shear	1.1	1.0	0.8	—	0.4	—	0.5	0.7	0.7	0.6	0.6	0.8
Brace-to-gusset weld fracture	—	1.0	—	—	1.1	—	1.0	0.9	1.3	1.6	—	1.4
Brace-to-gusset bolt fracture	0.6	—	1.1	—	—	—	—	—	—	—	1.8	—
Gusset-pl.-interface weld frac. (UFM)	—	—	1.1	—	0.7	—	—	0.7	2.2	—	1.0	0.6
Gusset-pl.-interface weld frac. (BDP)	—	—	2.0	—	2.1	—	—	0.8	1.3	—	1.3	1.1
Gusset-pl.-interface bolt frac.	—	—	1.4	—	1.3	—	—	0.7	—	—	—	—
Geometric limits												
Brace local slenderness (λ/λ_{hd})	0.8	2.3	0.9	0.9	1.4	0.8	2.7	2.7	1.7	1.2	0.9	1.9
Gusset-plate clearance[a] ($8t_p/L_{clear}$)	—	4.2	(5.0)	—	(33)	—	(3.9)	(3.2)	280	1.6	(9.9)	6.8
System irregularities												
Alternating brace configurations	—	—	✓	—	✓	—	✓	—	✓	—	—	✓
Vertical discontinuity	—	—	✓	✓	✓	—	—	—	✓	✓	—	—

[a]Values in parentheses indicate the elliptical clearance model does not fit and Nt_p describes the distance to zero clearance.

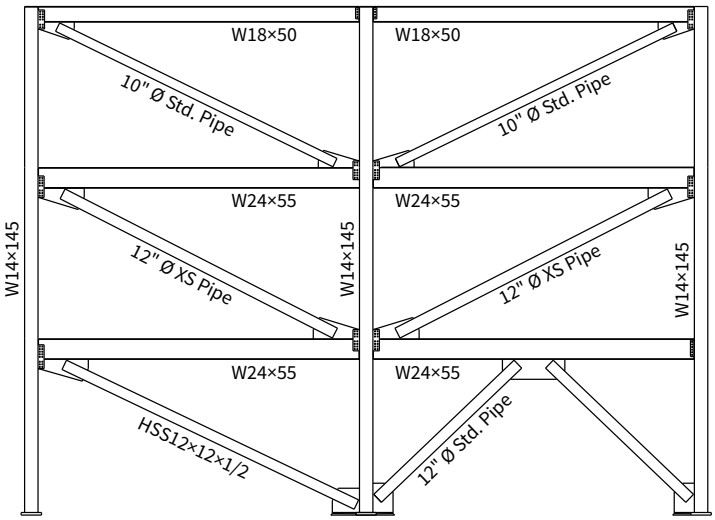

Figure 2.3: Example system configuration from infrastructure review

yielding, this is a yielding mechanism which potentially increases deformation capacity and limits demand on other connections elements and/or members. Still, the evaluation revealed numerous issues, which are summarized as follows:

- All buildings with chevron CBFs had beams which were too weak to develop the idealized brace unbalanced forces,
- 67% of buildings had columns with buckling DCRs of at least 1.2,
- 67% of buildings had net section fracture DCRs above 1.0 (no braces had net section reinforcement),
- 83% of buildings with gusset-plate-interface welds had DCRs greater than 1.0 using the BDP expressions,
- Only 1 building with HSS braces satisfied the current local slenderness requirements,

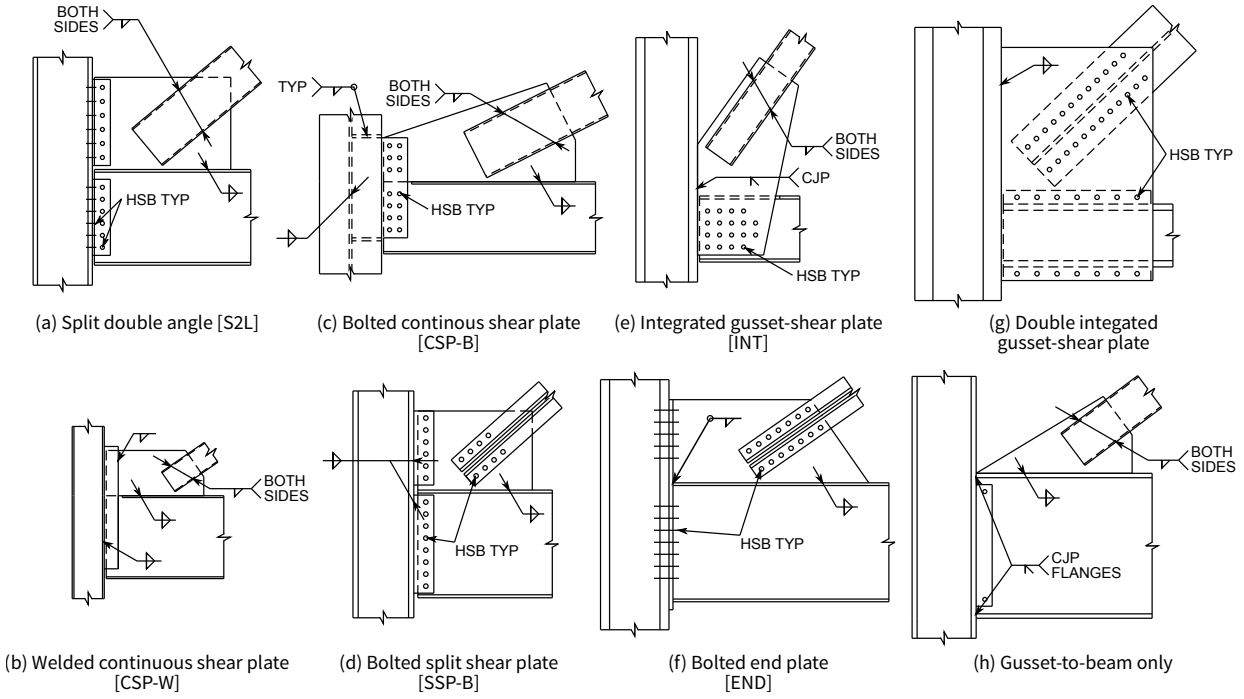

Figure 2.4: Examples of connection configurations from infrastructure review

- None of the buildings had adequate clearance to permit brace end rotation, and
- 58% of buildings had potential system irregularities.

Further, the weld strength deficiencies are likely compounded by the use of weld filler metal with relatively low toughness compared to modern demand-critical weld requirements (AISC 2017a).

2.3 Post-Earthquake Performance Evaluation

Past earthquakes provide a real but limited basis for identifying and understanding NCBF vulnerabilities. Relatively few collapses of CBF buildings due to earthquakes have been observed compared to other structural systems, but it is unclear whether this reflects a

system characteristic or random variability. Nonetheless, significant damage to CBFs has been documented in the aftermath of large earthquakes in Japan and the US. Important observations from these events are detailed below in chronological order.

2.3.1 1978 Miyagiken-oki Earthquake

The 1978 Miyagiken-oki Earthquake (M7.7) occurred on June 12, 1978 near the city of Sendai, Japan and was one of the first events to signficantly damage steel structures in Japan (Tanaka et al. 1980). Many of the nearly 1,300 steel buildings damaged were braced frames, which were commonly used in warehouses and factories in the area (Tanaka et al. 1980). Figure 2.5a shows an NCBF building which collapsed in the earthquake. The braces were angle sections oriented in the X-configuration, and tensile yielding of the braces was precluded by fracture of the bolted brace-to-gusset plate connection. Fracture of bracing connections was reported in 107 total buildings, including brace-to-gusset-plate connections (Fig. 2.5b) and gusset-plate-to-frame connections (Fig. 2.5c). Of these buildings, 6 were considered to have collapsed and 13 had residual interstory drift greater than 3.33%.

The widespread damage to CBFs around Sendai clearly illustrated deficiencies in connections which could not develop the strength of the brace. As a consequence, the Japanese building code was modified to increase the design forces for CBFs by 1.5 and require that bracing connections be designed to resist 1.2 times the brace tensile yield force (Tanaka et al. 1980).

2.3.2 1994 Northridge Earthquake

The 1994 Northridge Earthquake (M6.7) occurred near Los Angeles, CA on January 17, 1994 and remains the most damaging event for steel structures in the US. Although no steel buildings collapsed, damage was identified in over 150 buildings (Mahin 1998). Much of the post-earthquake response focused on the performance of steel moment-resisting frame buildings, as many sustained beam-column connection fractures. However, CBFs were damaged and, in some cases, required extensive repair.

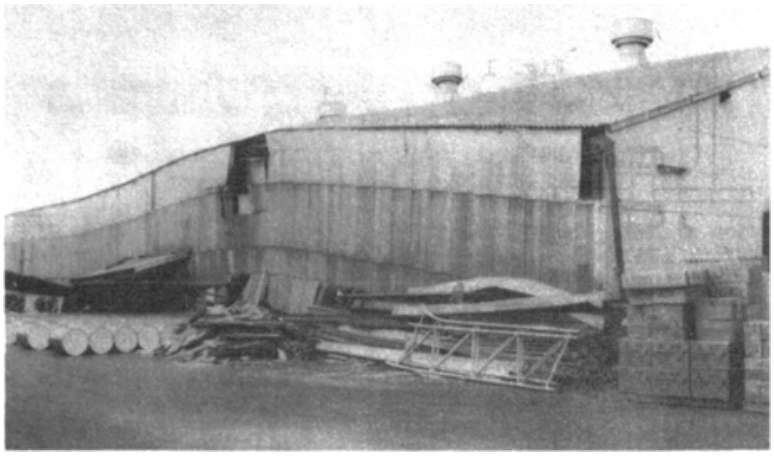

(a) Collapsed warehouse building

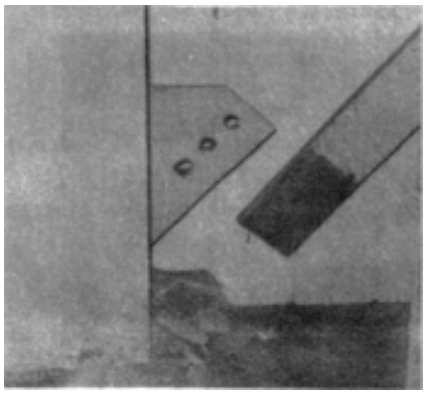

(b) Fractured bolts in brace-to-gusset-plate connection

(c) Fractured gusset-plate-to-column weld

Figure 2.5: CBF damage in 1978 Miyagiken-oki Earthquake (Tanaka et al. 1980)

Tremblay et al. (1995) reported the observations from 11 CBFs subjected to strong ground motion in the 1994 Northridge Earthquake, 9 of which had structural damage. Examples of CBF damage included brace buckling and fracture, brace connection fracture, and anchor-bolt yielding and failure. The most heavily damaged CBF was a 4-story office building located near North Hollywood and owned by Hewlett-Packard (referred to herein as the "HP Building"; see Fig. 2.6) (Kelly et al. 2000). The building was constructed in 1986 and conformed to the 1980 Los Angeles Building Code (similar to the 1982 UBC (ICBO 1982)). Braces were square HSS oriented in the chevron configuration and slotted and welded to

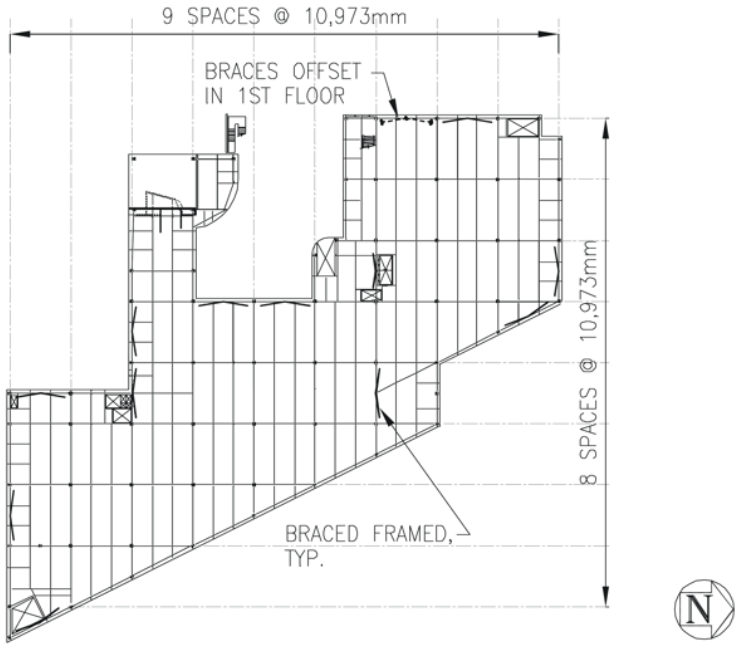

Figure 2.6: HP Building plan at 2nd story (Kelly et al. 2000)

gusset plates which had bolted double-angle connections. Nonstructural damage was limited and residual drift was negligible, but further investigation revealed that every 2nd-story brace in one direction had brace fracture in the plastic hinge region (Fig. 2.7a) or brace-to-gusset-plate weld fracture (Fig. 2.7b). The braces had a local slenderness ratio of 29, which is 2.1 times that allowed in current SCBFs (AISC 2017b); this resulted in premature local cupping in the braces after brace buckling, which precipitated fracture. Kelly et al. (2000) suggest that this severe brace damage was used to justify more stringent local slenderness requirements for HSS braces in subsequent *Seismic Provisions*.

The HP Building was repaired within 120 days of the earthquake to conform with the requirements of the 1992 Los Angeles Building Code and the 1994 UBC (ICBO 1994). Although nearly all structural damage was concentrated on the second floor, the entire building was upgraded. The main features of the repair included:

- Zipper columns connecting chevron beam midspans along the height of the building

(a) Fractured brace (Kelly et al. 2000)

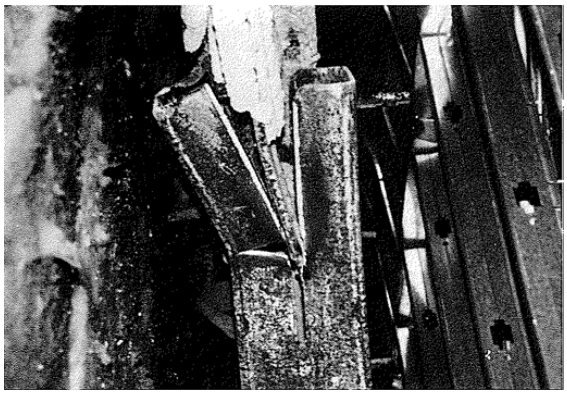

(b) Fractured brace-to-gusset-plate weld (Tremblay et al. 1995)

Figure 2.7: HP Building structural damage

to avoid soft-story behavior perceived to have been caused by the original chevron configuration,

- Wide flange braces which have greater deformation capacity than HSS braces,
- Connections designed to develop the full capacity of the braces, and
- Reinforced columns using steel side plates to avoid buckling.

2.3.3 1995 Hyogoken-Nanbu (Kobe) Earthquake

The 1995 Hyogoken-Nanbu Earthquake (M6.9) occurred near Kobe, Japan one year after the 1994 Northridge Earthquake. Similar to the 1978 Miyagiken-oki Earthquake, nearly 1300 steel structures were damaged in the event; however, significantly more steel buildings, 90, were considered collapsed or near collapse following the 1995 Hyogoken-Nanbu Earthquake (AIJ 1995a). One hundred thirty (130) buildings with CBFs in at least one direction had structural damage, including 10 which collapsed. Hence, as with the 1994 Northridge Earthquake, moment-resisting frames were more extensively damaged (AIJ 1995b). Collapses of

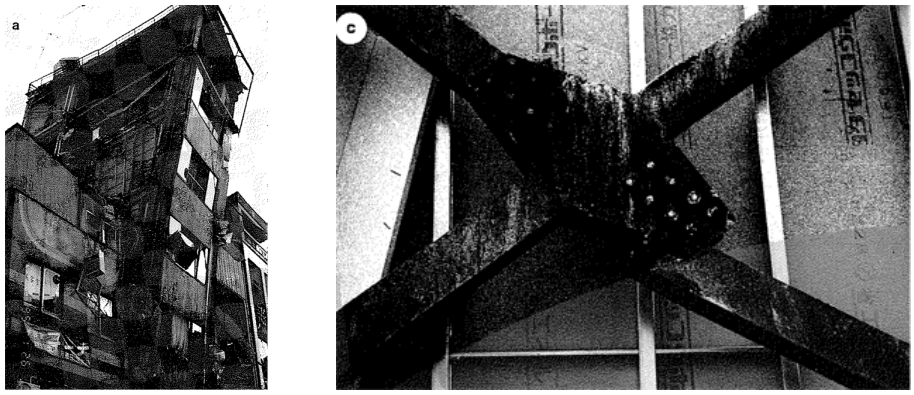

(a) Building with excessive residual drift

(b) Fractured brace at net section

Figure 2.8: CBF damage in 1995 Hyogoken-Nanbu Earthquake (Tremblay et al. 1996)

CBFs only occurred in buildings with light bracing members such as rods, angles, and flat bars, which were generally associated with older construction; modern design practice at the time usually necessitated larger cross sections, typically round tubular and wide-flange sections (Tremblay et al. 1996; Nakashima et al. 1998). Figure 2.8a shows an irreparable building which had fractured flat bar braces.

As in prior earthquakes, typical CBF damage consisted of brace buckling and fracture, connection fracture, and anchor rod pull-out or fracture. In some instances, beam-to-column connections were damaged. It is noted that typical practice in Japan uses fully restrained beam-to-column connections in conjunction with bracing, and this added strength, stiffness, and redundancy likely mitigated more severe damage to CBFs.

2.3.4 2011 Tohoku-oki Earthquake

The 2011 Tohoku-oki Earthquake (M9.1) occurred off the east coast of Honshu, Japan on March 11, 2011 and affected much of the same region as the 1978 Miyagiken-oki Earthquake (Okazaki et al. 2013). Due to the large tsunami generated from the earthquake, it is difficult to quantify the total extent of ground-shaking-related damage. CBF buildings in this region

(a) Fractured gusset plate in office building

(b) Fractured connecting plate in parking structure

Figure 2.9: CBF damage in 2011 Tohoku-oki Earthquake (Okazaki et al. 2013)

are predominantly warehouse, factory, or parking structures, though some older (pre-1981) non-industrial-use CBF buildings remain. In recent years, CBFs have become less popular in Japan in favor of buckling-restrained braced frames (BRBFs) and supplemental damping systems. Okazaki et al. (2013) describe two CBF structures damaged in the event: a three-story office building and a two-story parking structure. Both sustained connection fractures due to poor detailing, as depicted in Fig. 2.9.

The damage to the parking structure is notable because the braces were oriented in the chevron configuration. The connecting plate shown in Fig. 2.9b forms an eccentric connection between the brace and gusset plate, which led to concentrated bending and fracture of the connecting plate. The beams were simply supported and too weak to develop the unbalanced brace forces in the tension and compression braces, resulting in a yielding-beam plastic mechanism. Slight permanent deformation of the beam is visible in Fig. 2.9b. The damage sustained by the connecting plates was clearly more severe than that by the beams, and it is possible that the yielding-beam mechanism prevented more severe damage by limiting the forces which could be developed through the connecting plates in tension.

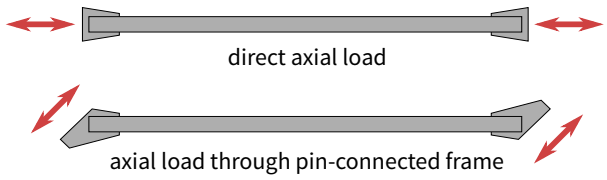

Figure 2.10: Brace-gusset assembly experiment loading methods

2.4 Experimental Research

Experimental research investigating the seismic behavior of CBFs has been active since the 1970s. This work can be broadly categorized as either brace-gusset or frame subassemblage tests.

2.4.1 Brace-Gusset Subassemblage Behavior

A large number of tests have been conducted which isolate the brace and gusset plates to investigate component cyclic behavior (Wakabayashi et al. 1977, 1980; Black et al. 1980; Astaneh-Asl et al. 1986; Liu and Goel 1987; Lee 1988; Shaback and Brown 2003; Tremblay et al. 2003; Yang and Mahin 2005; Han et al. 2007; Fell et al. 2009; Richard 2009). Typically, braces are tested as in Fig. 2.10 by directly applying axial load to the member or through lateral loading of a pin-connected frame. These experiments have established the hysteretic behavior and fracture life of braces with different cross-sectional shapes, local and global slenderness ratios, and material properties.

Rectangular HSS braces are common in US design practice and are a major focus of this work. After buckling, their cyclic behavior is driven by strain concentration in the plastic hinge region(s) of the member. At large compressive deformations, the brace wall on the compressive face of the plastic hinge cups inward due to the incompatibility of the cross-sectional shape and extreme curvature demand. At the same time, the corners of the section bulge outward. This phenomena is referred to as "local cupping" deformation and is depicted in Fig. 2.11. Tearing of the brace initiates at the corners of the cupped region

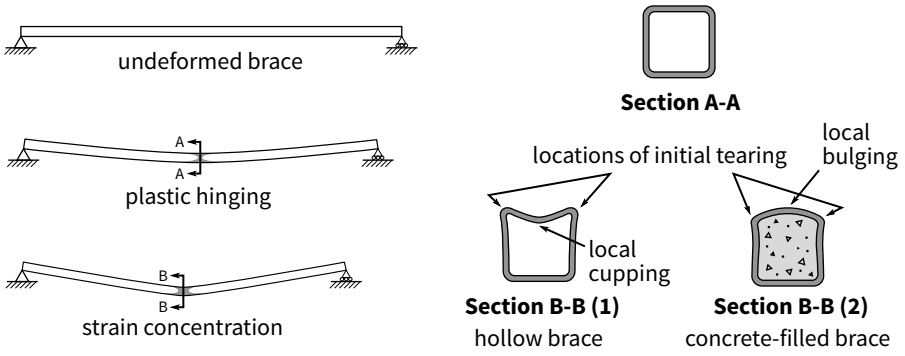

Figure 2.11: Global and local rectangular HSS brace compressive deformation

and propagates through to the cupped wall and eventually the entire cross section (brace fracture). Gugerli and Goel (1982) tested four rectangular HSS braces with local slenderness (cross-sectional width-to-thickness) ratios between 12 and 28. These tests showed that higher local slenderness ratios resulted in premature onset of local cupping, which in turn reduced fracture life. This finding has been supported by dozens of subsequent tests of rectangular HSS which are summarized in Chapter 4.

Gugerli and Goel (1982) also tested comparably sized wide flange braces and found that their fracture life was longer than the tubular braces. In view of the apparent deficiency of rectangular HSS braces with somewhat large local slenderness ratios, Liu and Goel (1988) and Lee (1988) investigated the use of concrete in-fill to mitigate local cupping and thereby extend fracture life. Test variables included local slenderness ratio, global slenderness ratio, concrete compressive strength, and the use of steel fibers in the concrete. The braces were designed as composite members and the concrete filled the entire brace, including the gusset plate region, resulting in a larger initial buckling load. However, the post-buckling strengths of the braces with and without concrete in-fill were similar. The concrete was effective in delaying strain concentration in the brace and resulted in local bulging rather than local cupping in the plastic hinge region (see Fig. 2.11). The effect was beneficial even with low-strength ($f'_c = 2$ ksi) concrete, as the primary function of the concrete was to restrain inward

deformation of the relatively weak brace wall. More compact (lower local slenderness ratio) cross sections benefited less from the concrete in-fill, as local cupping was already delayed in such cross sections.

Brace-gusset subassemblage testing has also been used to determine appropriate seismic design and detailing of brace connections. For example, Astaneh-Asl et al. (1986) performed a series of tests on double-angle braces with gusset plates to justify a $2t_p$ linear clearance between the brace end and line of restraint to accommodate end rotation of the brace through flexural yielding of the plate. This clearance model remains common in practice today. In addition, testing by Yang and Mahin (2005) of slotted-and-welded tubular brace connections was used to demonstrate the vulnerability of net section fracture in such connections and the use of reinforcement plates to suppress it.

2.4.2 Frame Subassemblage Behavior

Dozens of frame subassemblage experiments have been conducted in the past 20 years, including single-bay tests of 1-, 2-, and 3-story frames under quasi-static, pseudo-dynamic, or dynamic loading. These tests investigate more realistic behavior than their brace-gusset subassemblage counterparts, since the braces or gusset plates are attached to beams and columns. These tests have been invaluable toward advancing the understanding of bracing configuration effects, complex behavior at the brace-beam-column intersection, gusset plate design, and frame-action influence on system behavior. Most frame subassemblage tests focused on the behavior of SCBFs to validate and improve their design, whereas limited testing of other CBF systems (NCBF, OCBF, and "$R = 3$") have been performed.

SCBF Experiments

A substantial number of SCBFs were tested at the University of Washington as part of the NSF-funded research project entitled "International Hybrid Simulation of Tomorrow's Braced Frame Systems" (CMMI-0619161). Each test consisted of a one-bay, one-story frame with a single brace attached to the corners of the frame with gusset plates, as shown in

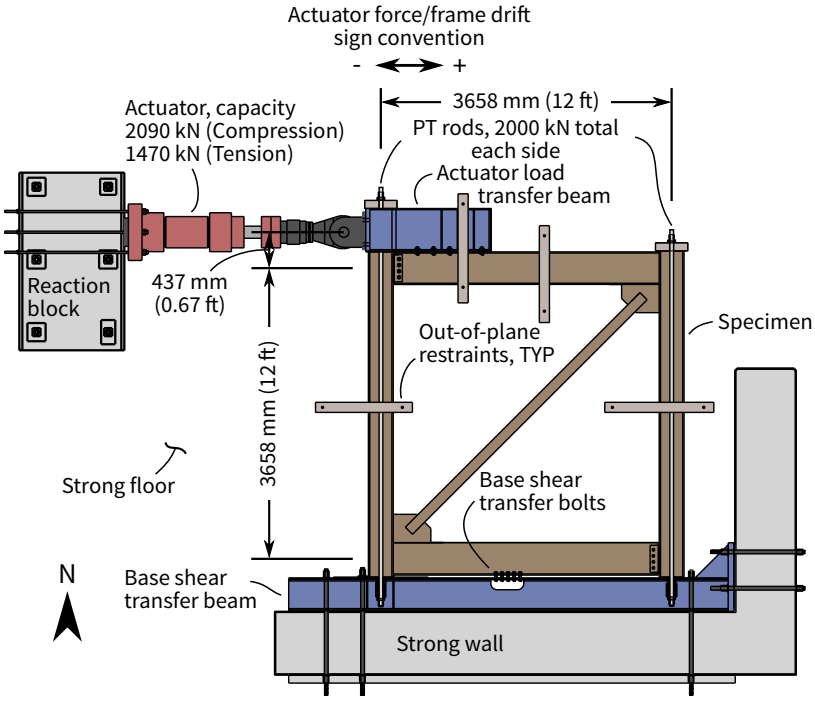

Figure 2.12: One-story, single-diagonal SCBF test setup

Fig. 2.12. The specimens were loaded quasi-statically with fully reversed cyclic, increasing-amplitude protocols. This test program is summarized in Table 2.4, which has been reproduced from Roeder et al. (2011b). All specimens had HSS5×5×3/8 braces except Specimen WF-23, which had a W6×25 brace with similar tensile yield strength. Full details of the specimens can be found in Johnson (2005), Herman (2007), Kotulka (2007), and Powell (2010).

The one-story, single-diagonal SCBF test program was used to develop the balanced design procedure (BDP), which promotes a yielding and failure hierarchy to increase system deformation capacity by nearly 50% compared to conventional designs (Roeder et al. 2011b). The BDP provides alternative limit-state expressions and balance factors (β) which are anlogous to resistance factors (ϕ) for design of SCBF connections, as detailed in Table 2.1. As

Table 2.4: Summary of one-story, single-diagonal SCBF tests (Roeder et al. 2011b)

Specimen	Description	Gusset thickness and clearance	Failure mode	Drift range (%)
HSS-1	AISC design – fillet welds by UFM	13 mm – $2t_p$ linear	Weld fracture	2.8
HSS-2	HSS-1 w/ fillet weld sized to cap. of plate	13 mm – $6t_p$ ellipse	Brace fracture	4.0
HSS-3	BDP – fillet weld sized to capacity of plate	13 mm – $6t_p$ ellipse	Brace fracture	5.0
HSS-4	BDP – fillet weld sized to capacity of plate	13 mm – $9.4t_p$ ellipse	Brace fracture	4.8
HSS-5	BDP – fillet weld sized to capacity of plate	10 mm – $8t_p$ ellipse	Brace fracture	5.5
HSS-6	BDP – HSS-5 except fillet welds reinforced	10 mm – $8t_p$ ellipse	Brace fracture	4.8
HSS-7	BDP – fillet weld sized to capacity of plate	22 mm – $6t_p$ ellipse	Brace fracture	4.0
HSS-8	BDP – fillet weld sized to capacity of plate	10 mm – $3t_p$ ellipse	Brace fracture	4.6
HSS-9	BDP – CJP weld	13 mm – $6t_p$ ellipse	Brace fracture	3.7
HSS-10	BDP – tapered gusset, fillet weld sized to cap. of plate	13 mm – $7t_p$ ellipse	Brace fracture	4.5
HSS-11	Heavy beam – fillet weld sized to cap. of plate	22 mm – $6t_p$ ellipse	Brace fracture	2.6
HSS-12	AISC design – CJP weld	13 mm – $2t_p$ linear	Brace fracture	3.5
HSS-13	BDP – CJP weld	13 mm – $7t_p$ ellipse	Brace fracture	4.1
HSS-14	No net section reinf. – fillet welds sized to cap. of plate	10 mm – $8t_p$ ellipse	Brace fracture	3.9
HSS-15	BDP – min. block shear, fillet welds sized to cap. of plate	10 mm – $6t_p$ ellipse	Brace fracture	4.1
HSS-17	BDP – tapered gusset, fillet welds sized to cap. of plate	10 mm – $9t_p$ ellipse	Brace fracture	4.9
HSS-18	BDP – bolted shear pl., fillet welds sized to cap. of plate	10 mm – $8t_p$ ellipse	Brace fracture	4.2
HSS-20	BDP – bolted end plate	10 mm – $7t_p$ ellipse	Brace fracture	4.0
HSS-21	BDP – bolted end plate	10 mm – $7t_p$ ellipse	Bolt fracture	4.2
HSS-22	BDP – tapered gusset, unwelded beam flanges	10 mm – $8t_p$ ellipse	Gusset tearing	4.0
WF-23	BDP – W6×25 brace	10 mm – $8t_p$ ellipse	Weld fracture	5.6
HSS-24	BDP	10 mm – $6t_p$ ellipse	Brace fracture	4.4
HSS-25	Heavy beam – no net section reinf., CJP weld	22 mm – $6t_p$ ellipse	Brace fracture	3.3
HSS-26	Heavy beam – no net section reinf., near-fault loading	22 mm – $6t_p$ ellipse	Net section	1.7
HSS-27	No net section reinf., near-fault loading	10 mm – $8t_p$ ellipse	Net section	2.5
HSS-28	BDP – tapered gusset	10 mm – $8t_p$ ellipse	Brace fracture	4.7

mentioned previously, the BDP allows controlled yielding of the gusset plate as a secondary yielding mechanism. The BDP also recommends the use of the $8t_p$ elliptical clearance model (Lehman et al. 2008) rather than the $2t_p$ linear clearance model (Astaneh-Asl et al. 1986). This clearance model used in conjunction with the BDP limit-state expressions results in thinner, more compact gusset plates which are less susceptible to interface weld tearing and fracture.

The tests by Roeder et al. (2011b) also clearly demonstrated the effects of brace, gusset-

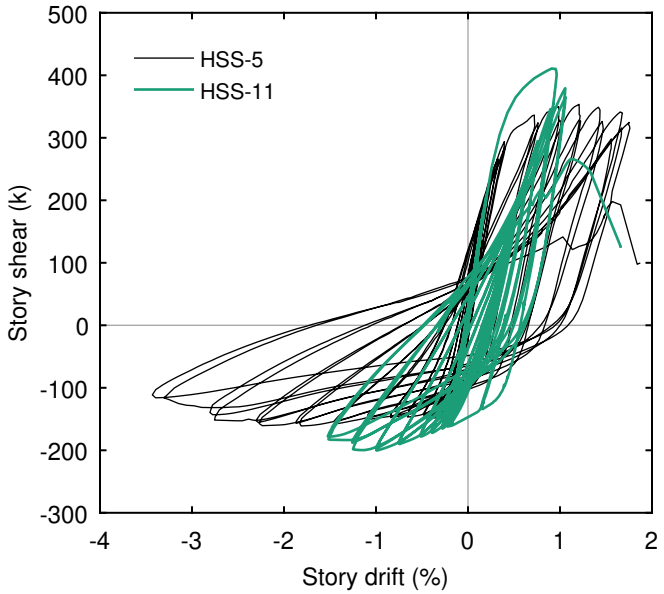

Figure 2.13: Hysteretic responses of Specimens HSS-5 and HSS-11

plate, beam, and column characteristics on SCBF behavior. Welded gusset plates provided significant restraint at the beam-column connection, resulting in large lateral resistance due to frame action. However, relatively strong and stiff framing members increase demand on the brace and thereby reduce its deformation capacity (Specimens HSS-11 and HSS-25 in Table 2.4). Figure 2.13 shows the behavior an SCBF designed with the BDP (Specimen HSS-5) compared to one with a heavy beam and thicker gusset plate than required by the BDP (Specimen HSS-11). Both specimens sustained brace fracture but at very different drift demands. Specimen HSS-5 had a larger drift capacity because the gusset plates yielded in tension and reduced deformation demand on the brace. In contrast, nearly all inelasticity was concentrated in the brace in Specimen HSS-11, and its drift capacity was reduced since the gusset plates and beams were relatively strong and stiff.

Several multi-story experiments were also performed as part of the NSF-funded research project, including two-story SCBF tests at the University of California, Berkeley (Uriz and Mahin 2008; Lai and Mahin 2013) and two- and three-story multi-story-X SCBF tests at

the National Center for Research on Earthquake Engineering (NCREE) in Taipei, Taiwan (Roeder et al. 2011a; Lumpkin et al. 2012).

Uriz and Mahin (2008) tested the two-story, chevron SCBF shown in Fig. 2.14, which was compliant with the 1997 *Seismic Provisions* (AISC 1997). The specimen was tested under quasi-static, fully reversed cyclic loading applied at the roof. Figure 2.15 shows base shear versus roof drift and first-story drift hystereses for the specimen. The first-story braces buckled as intended and fractured after a total story drift range of approximately 3.7% was achieved. Flexural resistance of the frame contributed significantly to the system resistance. The beam was sized to resist the unbalanced load at the brace intersection resulting from the difference in the compressive and tensile resistances of the braces and promoting a "yielding-brace" mechanism. However, the braces did not yield in tension due to elastic, downward deflection of the beam. After brace fracture, the columns sustained significant damage adjacent to the beam-column connections, where cracking initiated in the interior flanges and extended into the webs at a story-drift range of 5.7%. Subsequent damage localized in the weakened first story of the frame.

Multi-story-X SCBFs develop a yielding-brace mechanism through a continuous load path at the beam midspan brace intersection. In this configuration, the force unbalance at the beam midspan is small, permitting the use of lighter beams. This configuration was tested in two- (TCBF1) and three-story (TCBF2) configurations at NCREE, as documented in Roeder et al. (2011a) and Lumpkin et al. (2012), respectively, and illustrated in Fig. 2.16. In the three-story configuration, the third-story braces are oriented in the chevron configuration. Similar to the test by Uriz and Mahin (2008), the frames were loaded quasi-statically at the roof. However, slabs on metal decks were cast at each floor to provide partial composite action in the lower stories and full composite action on the upper story, providing more realistic boundary conditions.

Table 2.5 summarizes the test specimen designs and experiment results. All frames sustained delayed brace fracture at larger drift range capacities and less severe beam and column damage than reported in prior studies, due in part to the improved gusset-plate design

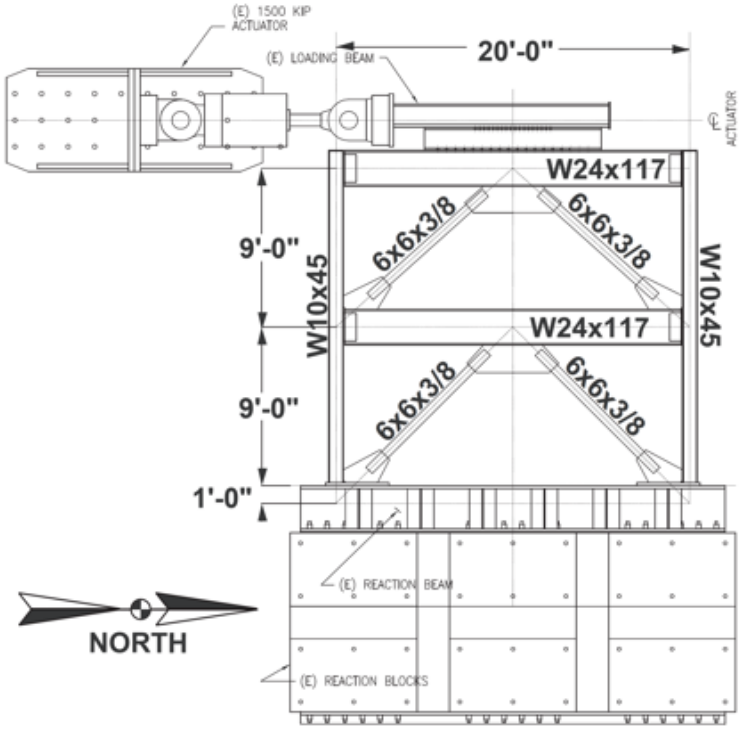

Figure 2.14: Two-story, chevron SCBF test setup at the University of California, Berkeley (Uriz and Mahin 2008)

using the BDP. In the TCBF2 series of tests, the midspan gusset plates were designed with a $6t_p$ vertical offset from the adjacent beam flange; this detail provided adequate clearance to permit brace-end rotation and mitigate severe tearing of the gusset-plate interface welds.

NCBF, OCBF, and "$R = 3$" Experiments

A smaller subset of frame subassemblage experiments have investigated the behavior of CBFs that lack special seismic detailing, including existing and retrofitted NCBFs and modern OCBFs and "$R = 3$" CBFs more common in regions with low and moderate seismic risk. Perhaps the earliest of such tests were conducted in the 1980s as part of a US-Japan cooperative research program (Foutch et al. 1987; Roeder 1989; Fukuta et al. 1989). These tests represented the state of the practice at the time, but are today considered tests of NCBFs.

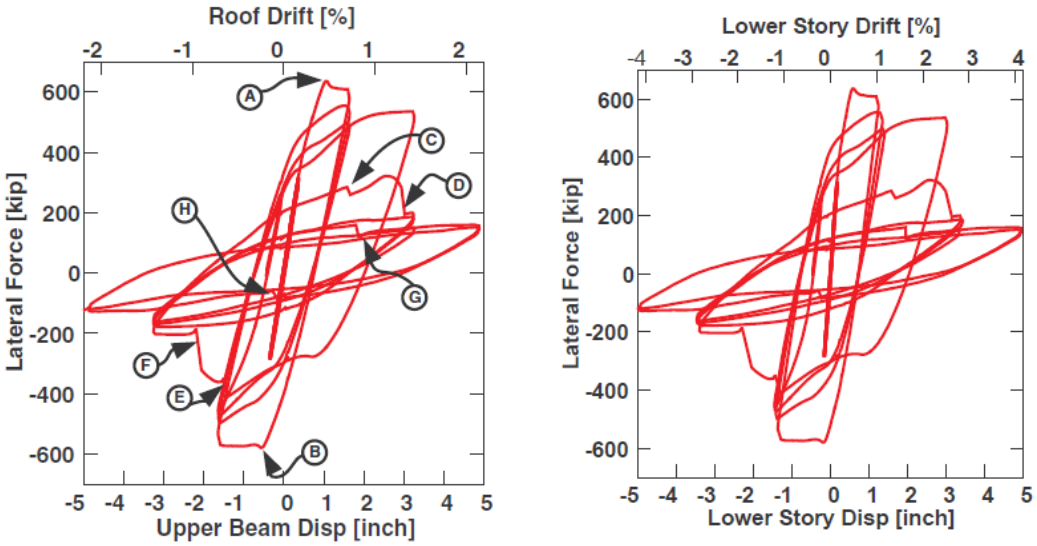

Figure 2.15: Hysteretic response of SCBF specimen tested by Uriz and Mahin (2008)

Table 2.5: Summary of multi-story-X SCBF tests (Roeder et al. 2011b)

Specimen	Description	Gusset thickness and clearance	Failure mode	Average drift range (%)
TCBF1-HSS	BDP – two story	10 mm – $8t_p$ linear	Brace fracture	4.3
TCBF1-WF	BDP – two story, wide-flange brace	10 mm – $8t_p$ ellipse	Brace fracture	6.2
TCBF1-T	BDP – two story, tapered gusset plate	20 mm – $2t_p$ linear	Brace fracture	5.6
TCBF2-HSS	BDP – three story	10 mm – varies	Brace fracture	3.8
TCBF2-WF	BDP – three story, wide-flange brace	10 mm – varies	Brace fracture	4.9
TCBF2-IP	BDP – three story, in-plane buckling	20 mm – $2t_p$ linear	Brace fracture	3.5

The specimens had rectangular, tubular braces (ST or built-up sections) oriented in the chevron configuration. The beams were not designed to resist the post-buckling unbalanced brace forces; during this era of construction, beams would only need to resist gravity loading (shear and bending moment) and seismic load delivered from the diaphragm and story above (axial). However, the beams were designed with fully restrained beam-to-column connections, which was (and remains) consistent with Japanese design.

Foutch et al. (1987) describes a full-scale, six-story CBF tested at the Large Size Structures Laboratory of the Building Research Institute in Tsukuba, Japan. Roeder (1989)

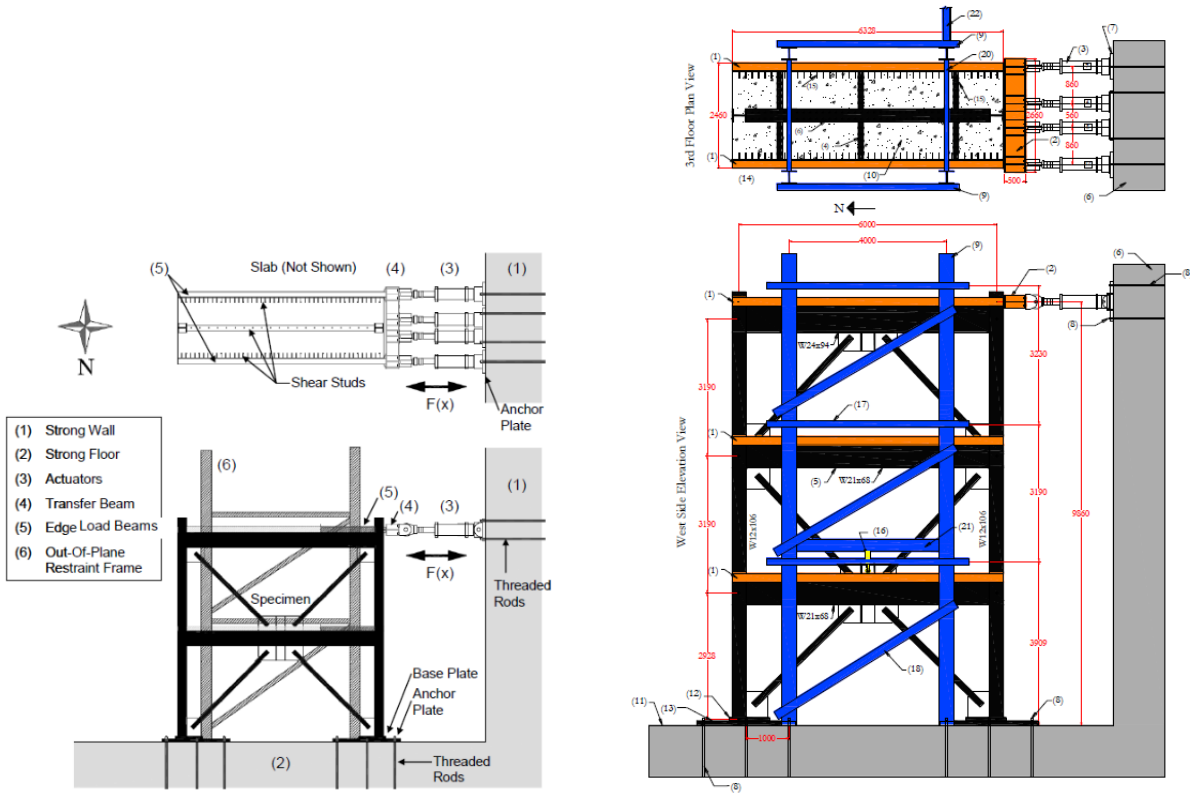

(a) TCBF1 test setup (Clark 2009)

(b) TCBF2 test setup (Lumpkin 2009)

Figure 2.16: Multi-story-X SCBF test setup at NCREE

provides additional details of this test. Figure 2.18 and Table 2.6 show the frame elevation and design information, respectively. The braces were welded directly to the beams and columns to provide full end restraint. All braces were locally slender except at the first story. The beam *DCR* values reported in Table 2.6 relate the beam strength to the current *Seismic Provisions* (AISC 2017a). Beam *DCR* decreased along the height of the building, as the beam size remained nearly the same but the brace sizes decreased.

The frame was tested under pseudo-dynamic loading using an acceleration record from the 1978 Miyagiken-oki Earthquake scaled to three different peak ground accelerations: 0.066 g, 0.25 g, and 0.51 g. As noted above, this earthquake damaged many steel buildings in the vicinity of Sendai, Japan. Figure 2.19 shows the hysteretic response of the first two stories

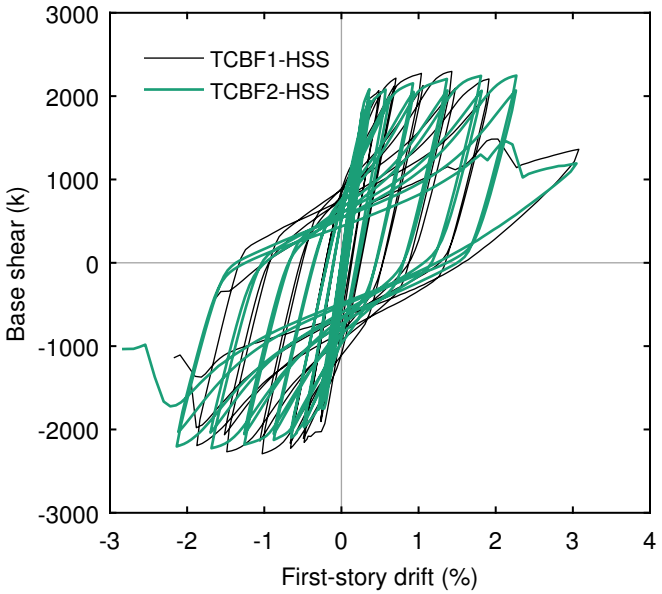

Figure 2.17: Hysteretic responses of Specimens TCBF1-HSS and TCBF2-HSS

under the final and most severe loading intensity. Despite the large beam DCR values at these stories, their lateral resistance did not degrade significantly, though the maximum story-drift range demand in the frame was relatively small at 2.2% (second story). As shown in Fig. 2.20, damage to the frame was widespread. Brace buckling and beam and/or column yielding occurred at each story except the sixth. The beams sustained large downward deflections at their midspans due to the post-buckling unbalanced brace forces. While this damage was a serious concern due to an unusual beam splice detail at this location, it did not compromise lateral resistance. Brace tearing or fracture occurred on the second and third stories, where the brace local slenderness ratio (b/t in Table 2.6) was largest. Notably, tearing did not occur on the first story where the beam DCR was nearly 4.0 but the brace local slenderness ratio was low.

A second series of tests was conducted at the Building Research Institute with half-scale specimens with varying brace and beam sizes (Fukuta et al. 1989). The specimens were three-story chevron CBFs with a stiff load beam at the top story as shown in Fig. 2.21.

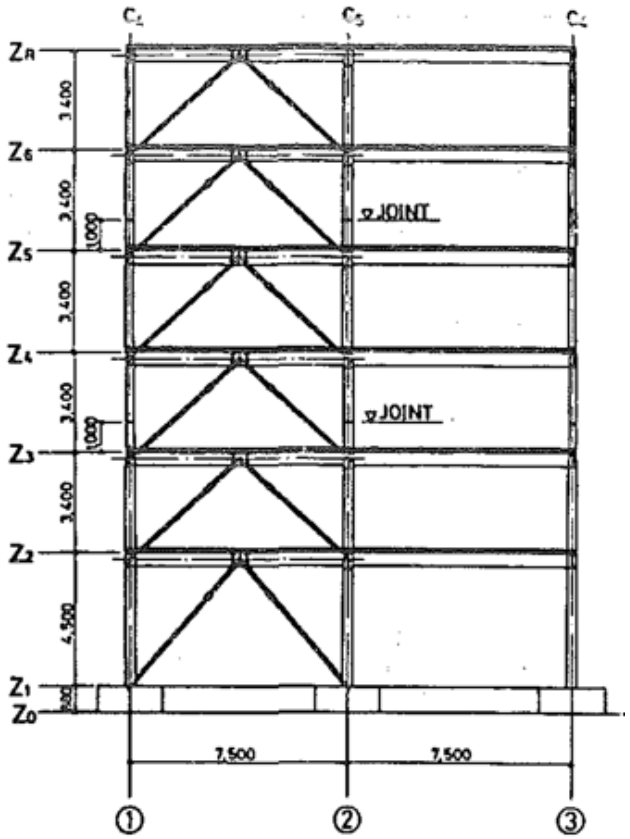

Figure 2.18: Six-story frame elevation in US-Japan cooperative research program (Foutch et al. 1987)

These tests investigated the effects of beam strength in the chevron configuration in greater detail. Table 2.7 provides details for the five CBF specimens tested. Note that Specimens 1 and 2 had partially composite slabs, whereas the other specimens had bare steel beams. The braces were connected to the frame with compact gusset plates without clearance to permit-brace end rotation.

Each of the specimens was loaded quasi-statically at the roof with reversed cyclic displacement histories; all but Specimen 2 used an increasing-amplitude protocol. The frames developed yielding-beam mechanisms on their lower stories, limiting tensile elongation of the braces and preventing fracture, though some tearing was observed. This effect resulted in

Table 2.6: Summary of six-story US-Japan specimen design (Foutch et al. 1987)

Story	Story height (mm)	Beam section	Brace section	Brace b/t	Beam DCR
6	3400	W16×31	ST4×4×3/16	18	1.8
5	3400	W18×35	ST4×4×3/16	18	1.5
4	3400	W18×35	ST5×5×1/4	17	2.0
3	3400	W18×40	ST6×6×1/4	21	2.1
2	3400	W18×40	ST6×6×1/4	21	2.1
1	4500	W18×40	ST6×6×1/2	9.0	3.9

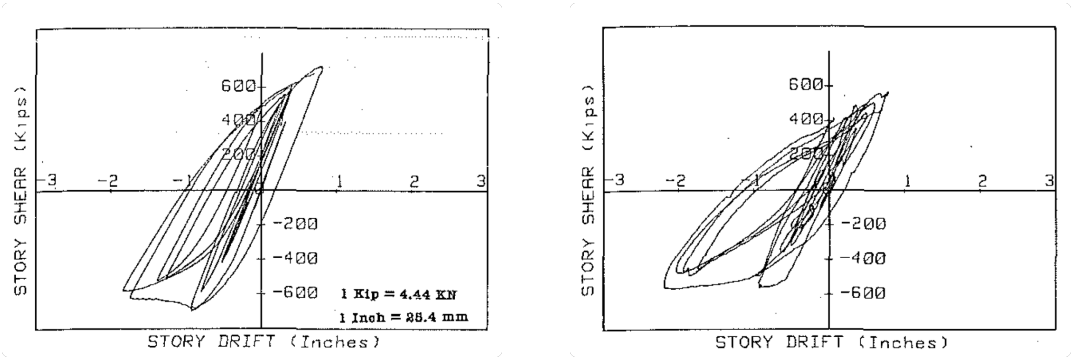

(a) First story ($DCR = 3.9$) (b) Second story ($DCR = 2.1$)

Figure 2.19: Six-story US-Japan specimen hysteresis in final test (Foutch et al. 1987)

relatively ductile behavior with full hysteresis similar to a moment-resisting frame for DCRs below 3. Examples of the first-story hysteretic responses are plotted in Fig. 2.22. The specimens shown had the same beam section but different brace sizes, resulting in different beam DCRs. Specimen 4 had significantly larger strength degradation after brace buckling compared to Specimen 1, which can be attributed to the larger beam DCR.

These collaborative US-Japan tests advanced the understanding of the interaction between the braces and beam in the chevron configuration and resulted in more stringent design requirements for CBFs–specifically to avoid the yielding-beam mechanism. However, the tests largely did not address bracing connection issues which have manifest in numerous

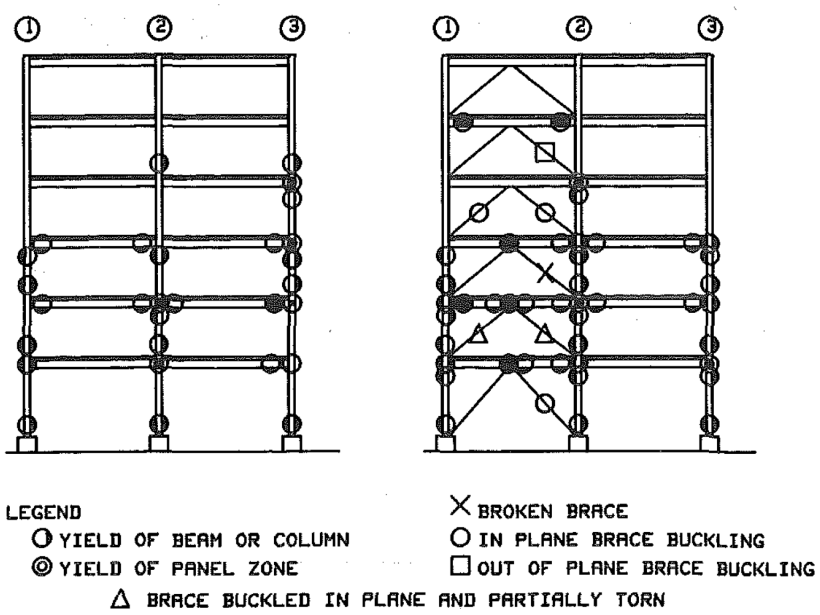

Figure 2.20: Six-story US-Japan specimen damage after final test (Foutch et al. 1987)

past earthquakes. A pilot experiment at the University of Washington was conducted to catalyze research investigating NCBF seismic performance, including the impact of brace and connection deficiencies Hsiao et al. (2014). The test setup previously used to study SCBFs (Fig. 2.12) was repurposed for this experiment. The specimen had an ASTM A500 HSS6×6×1/4 brace, which had a local slenderness ratio of 23. The brace was connected to gusset plates with welded-bolted double-angle connections as shown in Fig. 2.23a. The connection welds were generally undersized based on the capacity of the brace; most critically, the brace-to-gusset-plate weld had a DCR of 1.7. This weld fractured in the test after a drift range of only 1.3%, resulting in a significant loss of lateral resistance (Fig. 2.23b). This damage is consistent with that of welded brace connections observed in the HP Building following the 1994 Northridge Earthquake (Tremblay et al. 1995; Kelly et al. 2000). The specimen had significant residual strength due to frame action and contact between the brace and gusset plate in compression.

Testing of two-story existing and retrofitted NCBFs was performed at the University of

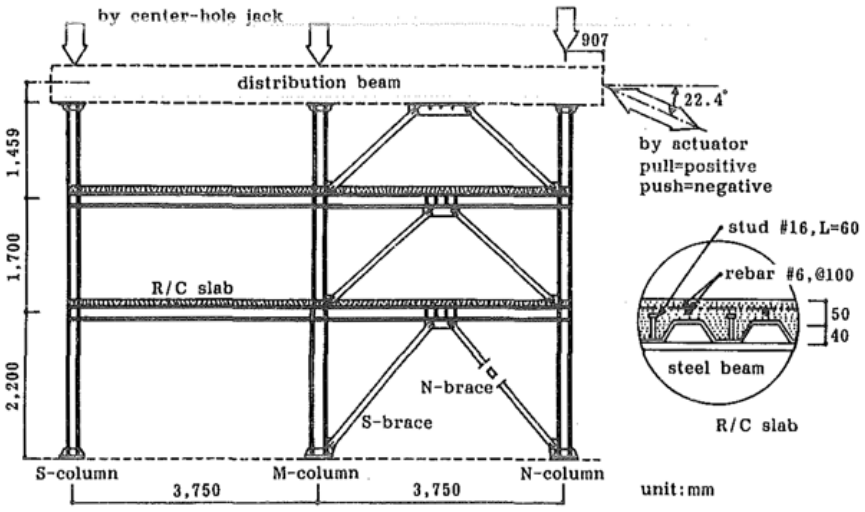

Figure 2.21: Three-story frame elevation in US-Japan cooperative research program (Fukuta et al. 1989)

California, Berkeley concurrently with the experimental research program described herein (Simpson and Mahin 2018). As with the work in this document, these experiments were conducted under the NSF-funded project entitled "Collaborative Developments for Seismic Rehabilitation of Vulnerable Braced Frames" (CMMI-1208002). The setup for these tests is illustrated in Fig. 2.24. Each specimen had W10×54 columns with one oriented for strong-axis bending and the other oriented for weak-axis bending in the plane of the frame. The beams were W14×53 sections. In Specimens NCBF-B-1 and NCBF-B-2, the braces were locally slender HSS7$\underline{7}$×1/4 and HSS6×6×3/16 sections on the first and second stories, respectively. However, in Specimen NCBF-B-2, the braces were filled with concrete to delay local cupping and fracture. Table 2.8 shows the beam DCRs for these two specimens; note that the first story has different DCRs depending on the direction of loading, since the weak-axis-oriented column had considerably lower flexural strength than the beam.

The specimens were loaded with quasi-static, fully reversed cyclic displacement histories with increasing amplitude using actuators at both stories. Their hysteretic responses are plotted in Fig. 2.25. Drift concentrated in the second story in Specimen NCBF-B-1,

Table 2.7: Summary of three-story US-Japan test program (Fukuta et al. 1989)

Specimen	Story	Story height (mm)	Beam section	Brace section (d×b×t)	Beam *DCR*
1–3	3	1459	–	105×45×4.5	–
	2	1700	W8×10	105×45×4.5	2.2
	1	2200	W8×13	110×55×4.5	2.0
4	3	1459	–	70×35×6.0	–
	2	1700	W8×10	70×35×6.0	2.9
	1	2200	W8×13	70×40×9.0	3.1
5	3	1459	–	105×45×4.5	–
	2	1700	W8×13	105×45×4.5	2.7
	1	2200	W10×17	110×55×4.5	1.5

Table 2.8: Two-story Berkeley NCBF specimen information

Specimen	Description	Story	Beam *DCR*	Failure mode	Drift range (%)
NCBF-B-1	Existing NCBF with locally slender braces	2	1.5	Brace fracture	3.3
		1	0.7–1.4	–	–
NCBF-B-2	Retrofitted NCBF with concrete-filled braces	2	1.5	–	–
		1	0.7–1.4	Brace fracture, column tearing	2.0, 8.1

resulting in premature fracture of both braces at a drift range of 3.3%. The yielding-beam mechanism formed after brace buckling, resulting in 24 mm of midspan deflection in the second-story beam. In Specimen NCBF-B-2, the braces were strengthened by the concrete in-fill, resulting in drift concentration in the first story rather than the second. One brace buckled on this story and fractured after a drift range of 2.0%, which was lower than in the hollow-brace specimen. It is hypothesized that the larger force demands due to the concrete in-fill exacerbated the local deformation demands to precipitate fracture. The second brace did not buckle or fracture, resulting in behavior like that of an eccentrically braced frame (EBF) with a long link. This behavior was sustained until a drift range of 8.1% was reached, at which point substantial tearing of the column bases occurred.

Another experimental study conducted concurrently with this research focused on the

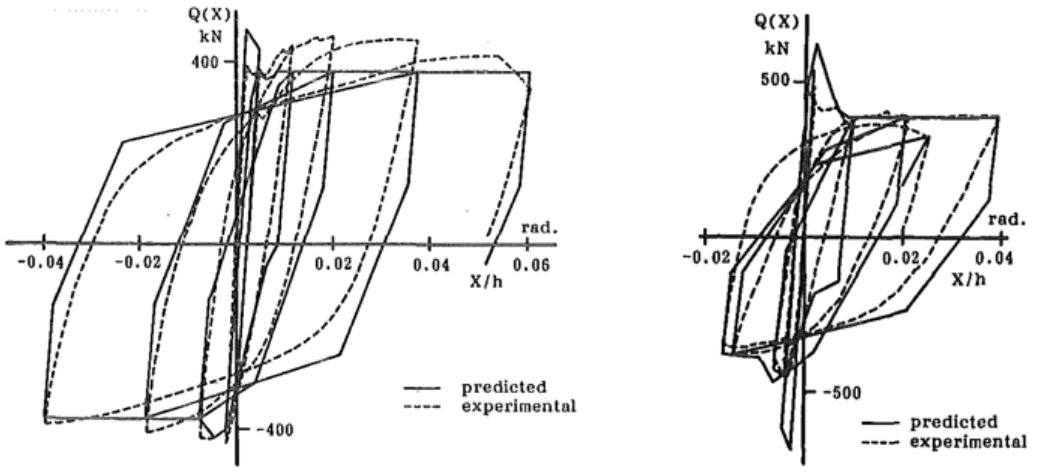

(a) Specimen 1 (weaker braces, $DCR = 2.0$)

(b) Specimen 4 (stronger braces, $DCR = 3.1$)

Figure 2.22: First-story hysteretic response from three-story US-Japan tests (Fukuta et al. 1989)

behavior of OCBFs and "$R = 3$" CBFs Bradley et al. (2017). These systems share design characteristics of NCBFs in that the braces have less stringent local slenderness requirements and the connections and framing members do not require capacity design. Two-story specimens of each type, shown in Fig. 2.26, were tested at Lehigh University's Advanced Technology for Large Structural Systems Engineering Research Center. The OCBF and "$R = 3$" specimens were oriented in the multi-story-X and chevron configurations, respectively. The specimens were loaded quasi-statically with actuators at both stories, and each sustained connection fractures which resulted in large reductions in resistance as indicated in the hystereses in Fig. 2.27. The OCBF specimen had limited reserve capacity after a drift range of 3.1% due to connection fracture on both stories. On the other hand, the "$R = 3$" specimen had substantial resistance after fracture of a brace-to-gusset-plate weld on the first story due to the formation of an EBF mechanism, similar to Specimen NCBF-B-2 from Simpson and Mahin (2018).

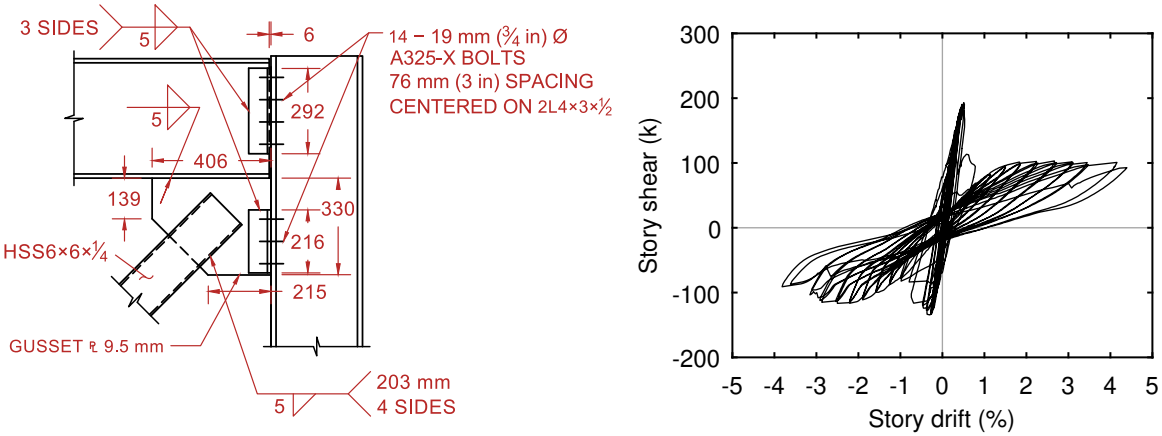

(a) Brace and connection details

(b) Hysteretic response

Figure 2.23: NCBF pilot experiment overview

2.5 Computational Research

Substantial research efforts have focused on modeling and seismic performance evaluation of SCBFs using nonlinear analysis. This research provides a foundation for modeling NCBFs, and hence the methods discussed here will be extended in Chapter 4. As with experimental research, fewer computational studies have addressed NCBFs, OCBFs, and "$R = 3$" CBFs; these previous efforts are also detailed below.

2.5.1 SCBF Modeling in OpenSees

Accurate nonlinear analysis modeling approaches have been well established for SCBFs for research applications (Uriz and Mahin 2004; Hsiao et al. 2012, 2013a; Karamanci and Lignos 2014). These approaches have been implemented in *OpenSees* (McKenna et al. 2010) and employ a combination of fiber-based beam-column elements and rotational springs as in Fig. 2.28 to simulate the intended SCBF yielding and failure hierarchy, including brace fracture. These models feature:

- Rigid offsets or stiff, elastic beam-column elements between the frame work point and

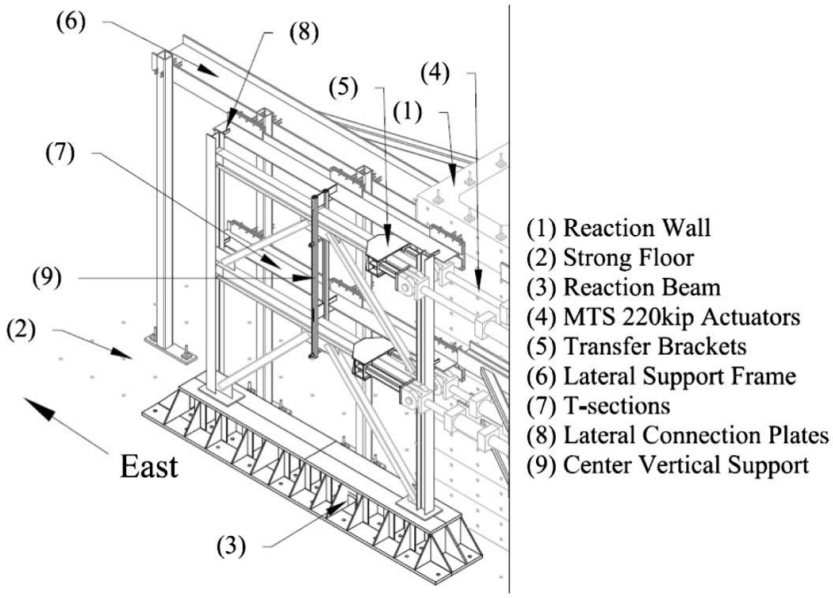

Figure 2.24: Two-story NCBF test setup at University of California, Berkeley (Simpson and Mahin 2018)

end of the brace,

- Nonlinear rotational spring elements at the brace ends to simulate flexural yielding of the gusset plate,
- Nonlinear beam-column elements discretized along the brace end-to-end length to numerically simulate P-δ effects with a series of P-Δ effects,
- Initial imperfection in the brace geometry in the direction of buckling to "seed" P-δ moment,
- Fiber-based cross sections at each element integration point, and
- Fibers with steel constitutive models capable of simulating yielding and kinematic hardening and wrapped with either a low-cycle fatigue (LCF) or maximum strain range (MSR) fracture material.

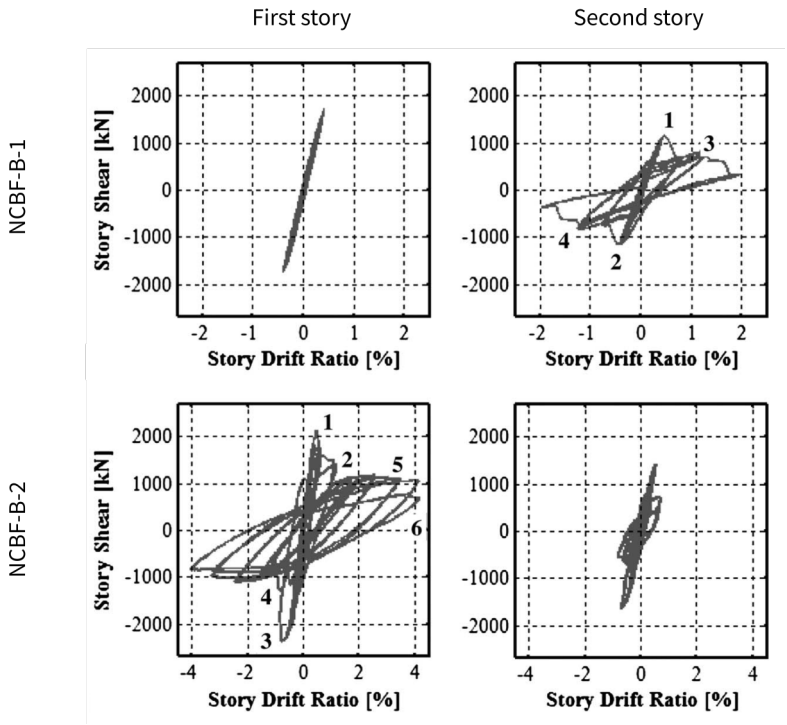

Figure 2.25: Hysteretic response of each story of NCBF-B specimens (Simpson and Mahin 2018)

Table 2.9 details the specific brace modeling approaches recommended in previous research. A major emphasis of this work was to simulate brace fracture in order to evaluate building damage and potential collapse in nonlinear response-history analysis, and each researcher proposed different criteria for predicting fracture at the fiber level. Fracture of an individual fiber is simulated using a material wrapper which monitors strain history in the underlying material and initiates fracture of the fiber.

Uriz and Mahin (2004) proposed an LCF model to trigger fracture, which is implemented in *OpenSees* as the *Fatigue* material. The Fatigue material uses the Coffin-Manson relationship (Eq. 2.28) and a modified rainflow-counting algorithm to compute an accumulated damage index based on Miner's rule, DI, which is the sum of damage indices for all full or half cycles, DI_i (Eq. 2.29). In Eq. 2.28, ε_0 is the strain amplitude at which one cycle would result in fracture, N_f is the number of constant-amplitude cycles to cause fracture, and m

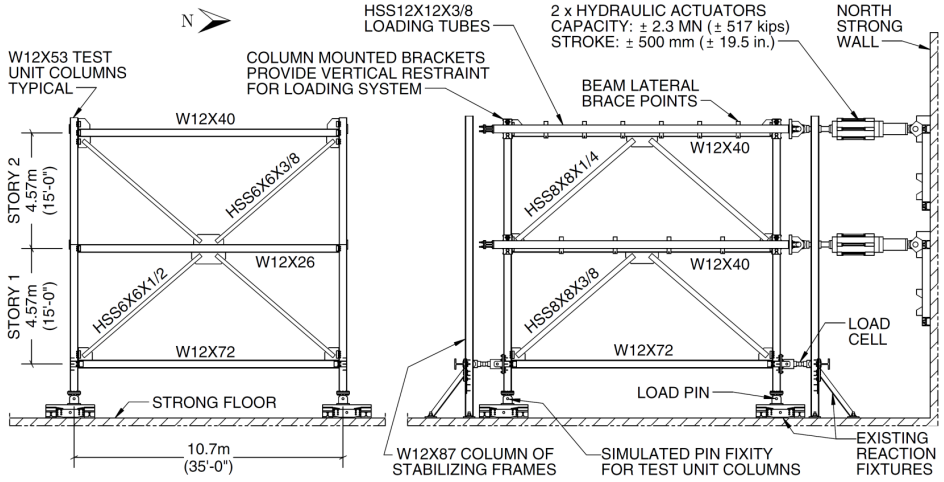

Figure 2.26: Two-story OCBF (left) and "$R = 3$" (right) test setups (Bradley et al. 2017)

is a parameter which controls the rate of damage accumulation at the strain amplitude ε_i. (Uriz and Mahin 2008) calibrated values of ε_0 and m using four tests of HSS6×6×3/8 braces with different load histories (Yang and Mahin 2005). Karamanci and Lignos (2014) recalibrated ε_0 and m using a substantially larger brace database. As in earlier work by Hsiao et al. (2013a), the fracture criterion was correlated with several non-dimensionalized brace parameters b/t, L_c/r (KL/r), and E/F_y. The resulting ε_0 prediction equation is given by Eq. 2.30 for rectangular HSS braces; similar equations were developed for round HSS and wide-flange braces.

$$\varepsilon_i = \varepsilon_0 \left(N_f\right)^m \tag{2.28}$$

$$DI_i = \begin{cases} \dfrac{1}{10^{m^{-1}\log\left(\frac{\varepsilon_i}{\varepsilon_0}\right)}} & \text{for full cycle} \\ \dfrac{1/2}{10^{m^{-1}\log\left(\frac{\varepsilon_i}{\varepsilon_0}\right)}} & \text{for half cycle} \end{cases} \tag{2.29}$$

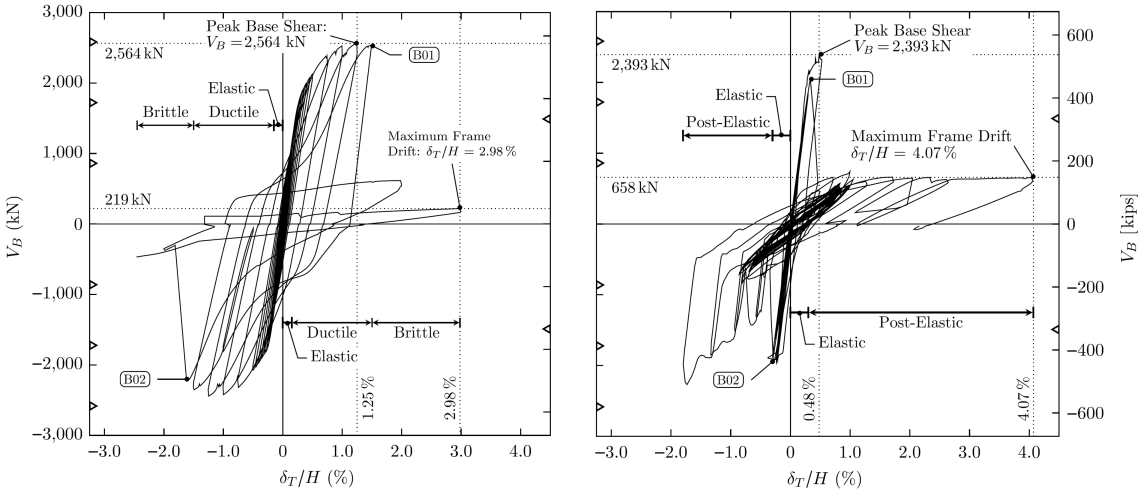

Figure 2.27: Two-story OCBF (left) and "$R = 3$" (right) frame hystereses (Bradley et al. 2017)

$$\varepsilon_0 = 0.291 \left(\frac{b}{t}\right)^{-0.613} \left(\frac{L_c}{r}\right)^{-0.484} \left(\frac{E}{F_y}\right)^{0.303} \tag{2.30}$$

Hsiao et al. (2013a) developed an alternative approach for predicting and simulating fracture using MSR, which is difference between the maximum and minimum strains in the total deformation history of the fiber. This approach is implemented in the *MaxStrainRange* material in *OpenSees*. Equation 2.31 was calibrated from dozens of tests of braces to predict the MSR at fracture (MSR_f) with non-dimensionalized parameters. The predicted MSR_f values resulted in less error between the predicted (numerically simulated) and experimental brace deformation ranges compared to the LCF model with the parameters from Uriz and Mahin (2008). Correlation between predicted and calibrated values of MSR_f and ε_0 is similar, with respective R^2 of 0.41 and 0.49.

$$MSR_f = 0.1435 \left(\frac{b}{t}\right)^{-0.4} \left(\frac{L_c}{r}\right)^{-0.3} \left(\frac{E}{F_y}\right)^{0.2} \tag{2.31}$$

The modeling recommendations proposed by Hsiao et al. (2012) also included methods to accurately account for the secondary resistance provided by gusset plates, beams, columns,

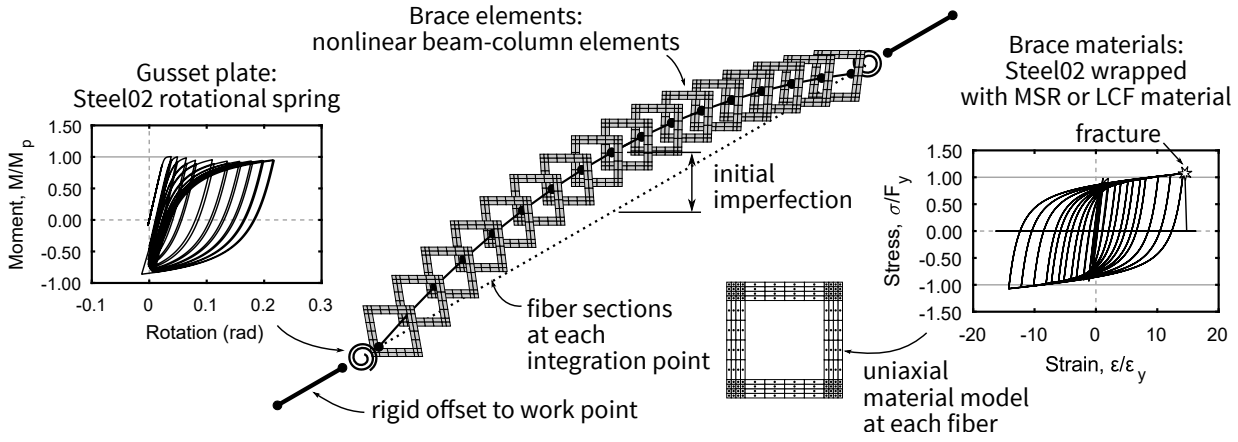

Figure 2.28: Typical *OpenSees* brace-gusset subassemblage model

and gravity connections. Figure 2.29 illustrates the basic modeling approach for a brace-beam-column intersection. The gusset-plate out-of-plane rotational spring properties are based on the physical characteristics of the plate: the yield stress, thickness, Whitmore width, and length. The gusset plate also provides significant in-plane restraint at this joint and, therefore, the beam is simulated as fully restrained to the column and the braces, beams, and columns are offset from the work point with rigid or stiff, elastic elements. Based on data from experimental testing of SCBFs (Roeder et al. 2011b), an offset of 75% of the gusset plate dimension was calibrated for the beam offset. The beams and columns are modeled with force-based beam-column elements with fiber sections to simulate yielding under combined axial force and bending moment. Beam-to-column joints which are not adjacent to gusset plates are often connected with bolted shear plates, and these connections provide significant reserve lateral resistance after brace fracture Hsiao et al. (2013b). Liu and Astaneh-Asl (2004) describe a moment-rotation backbone curve model which simulates bolt slip, bolt bearing, concrete crushing (for composite beams) and fracture due to binding of the beam and column flanges.

Table 2.9: Previously developed rectangular HSS brace model recommendations

Reference	Number of force-based elements	Number of integration points	Fiber discretization	Initial imperfection	Fracture model
Uriz and Mahin (2004, 2008)	20	3	10–15 layers along depth	$L/2000$–$L/1000$	LCF ($m = -0.5$, $\varepsilon_0 = 0.095$)
Hsiao et al. (2012, 2013a)	16	4	4×4[a]	$L/500$	MSR (Eq. 2.31)
Karamanci and Lignos (2014)	8	5	10×4[a]	$L/1000$	LCF ($m = -0.3$, $\varepsilon_0 \rightarrow$ Eq. 2.30)

[a] m×n = m fiber layers along the wall flat and n fiber layers through the wall thickness

2.5.2 NCBF, OCBF, and "R = 3" Modeling in OpenSees

In a continuation of the pilot NCBF study conducted at the University of Washington described above (see Fig. 2.23), Hsiao et al. (2014) conducted nonlinear response-history analysis of NCBF buildings with deficient brace-to-gusset welds similar to the experiment. The SCBF model in Fig. 2.29 was modified with an elastic translational spring at the brace end to represent the weld. A material wrapper was used with the elastic material to simulate fracture. The spring stiffness and fracture deformation was calibrated to match the hysteretic response of the experiment, which is plotted in Fig. 2.23b. This component model was implemented in a larger system model of a three-story NCBF building located in Seattle and designed to meet the 1988 UBC ICBO (1988). The building plan and elevation was based on the three-story SAC building (FEMA 2000).

The NCBF building and equivalent SCBF buildings designed using conventional design methods (AISC 2010a) and the BDP were subjected to the SAC ground-motion suites consistent with 2%/50-year and 10%/50-year probabilities of exceedance (Somerville et al. 1997). Figure 2.30 provides statistics for the seismic performance of the brace, connection, and frame for the three buildings and at each hazard level investigated. The results suggest

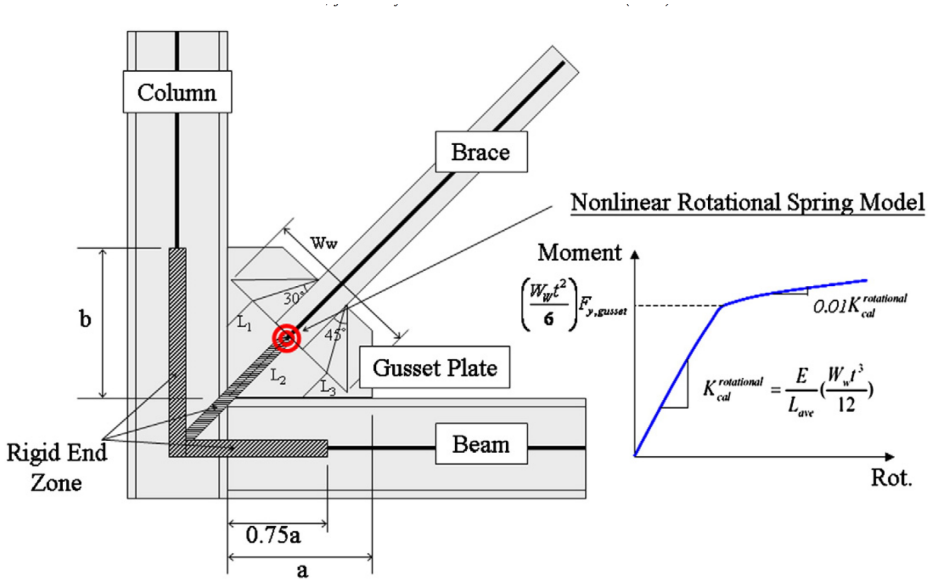

Figure 2.29: Brace-beam-column intersection model (Hsiao et al. 2012)

that the NCBF has a very high probability of damage and a small probability of collapse at the 10%/50-year hazard level. In contrast, the SCBF braces or connections would not be expected to fracture, and no instances of collapse of occurred in the SCBFs at this hazard level. Under ground shaking representative of the 2%/50-year hazard level, the percentage of ground motions causing collapse was 1.7 times higher in the NCBF compared to the SCBF designed to the BDP.

Sizemore et al. (2017) modeled OCBFs and "$R = 3$" CBFs in *OpenSees* based on the two-story tests documented by Bradley et al. (2017). These tests had similar premature failure modes to the NCBF pilot study, and a similar method for modeling brace-to-gusset-plate weld fracture using a translational spring was developed. Figure 2.31 details this model, which has similar rigid offsets from the frame work point as was recommended by Hsiao et al. (2012). In contrast, the nonlinear response of the beams and columns was modeled using rotational spring elements rather than distributed-plasticity (force-based beam-column) elements. Further, the beam-to-column connection was not fully restrained in this model; instead, the beam was attached to the column with a zero-length fiber section with individual

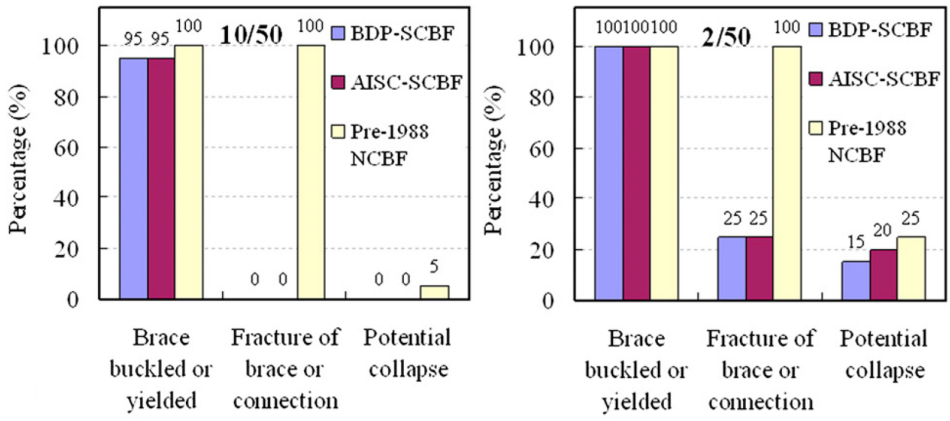

Figure 2.30: Seismic performance statistics for three-story NCBF with deficient brace-to-gusset-plate weld (Hsiao et al. 2014)

fibers at each bolt line. The fiber material simulated the hysteretic response of the bolted double-angle connection, including the effects of angle bearing, bolt slip, and beam-column flange binding.

The response of the test specimens was simulated well using the model in Fig. 2.31. These models were extended to conduct a parametric study which investigated cyclic response of three-story OCBFs and "$R = 3$" CBFs using static analysis. The study focused on the quantifying the effects of system type and brace configuration (chevron and multi-story-X) on the reserve capacity of three-story frames and found that a chevron configuration with a yielding-beam mechanism resulted in greater strength and deformation capacity after fracture of the connections.

2.6 Summary

- Extrapolating the infrastructure review results to represent existing NCBFs in the US and around the world, thousands of buildings are potentially vulnerable to sustaining serious damage or collapse when subjected to large ground motions.

- Evidence of CBF damage in past earthquakes, although largely located in Japan, sup-

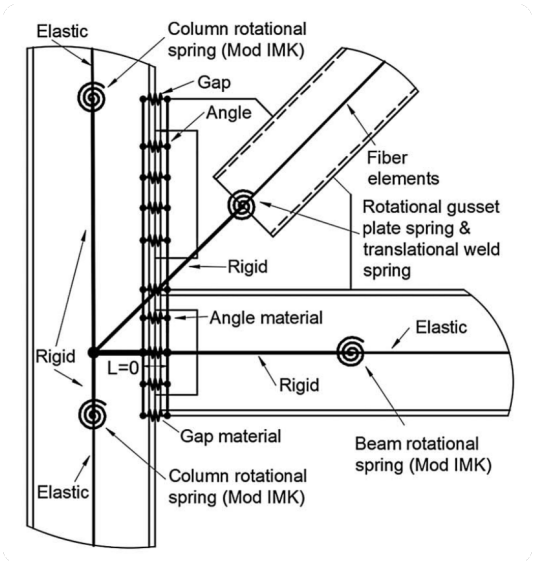

Figure 2.31: Two-story OCBF or "$R = 3$" brace-beam-column intersection model (Sizemore et al. 2017)

ports concerns of brace and connection vulnerabilities in particular. Few CBFs had detrimental beam or column damage which was not associated with base connections. Instances of collapse have also been sparse. However, these findings are anecdotal and do not necessarily suggest that these issues are less critical.

- Prior experimental and computational studies indicate potential benefits of a yielding-beam plastic mechanism which is expected to from in many chevron NCBFs, yet it has been discouraged in modern design practice and is perceived as a deficiency in older construction.

- Computational methods for simulating SCBFs are robust but not directly suitable for simulating NCBFs, which can develop many alternative yielding mechanisms and failure modes. Brace-to-gusset-plate weld deficiencies have been studied experimentally and computationally, but many others may impact system performance.

Chapter 3

EXPERIMENTAL BEHAVIOR OF EXISTING AND RETROFITTED BRACED FRAMES

Previous experimental research evaluating the seismic behavior of NCBFs in their existing and retrofitted conditions is sparse. The infrastructure review in Chapter 2 characterizes the severity and frequency of many deficiencies relative to current *Seismic Provisions* (AISC 2017a), but the effect of individual deficiencies (or combinations of deficiencies) on seismic response is uncertain. This chapter describes a substantial experimental research program undertaken to quantify these effects through large-scale testing of NCBF subassemblages. An overview of the testing program is provided, followed by detailed descriptions of specimen characteristics and observed response. The specimens are then generalized under one of four behavior types based on their yielding and failure sequence. These results are used to evaluate the success of different retrofit schemes and inform a retrofit priority for existing NCBFs. This information will be used in subsequent computational research to evaluate the seismic performance representative of existing and retrofitted NCBFs.

This chapter has been largely adapted from previously published journal articles by the author: Sen et al. (2016a), Sen et al. (2016b), and Sen et al. (2017).

3.1 Experimental Research Program Overview

Two series of tests were conducted to advance the understanding of NCBF behavior. The first series was conducted at the University of Washington Structural Research Laboratory to examine the impacts of common brace and connection deficiencies identified in the infrastructure review and evaluate the efficacy of relatively noninvasive retrofit schemes. This testing was performed using the same one-story, one-bay, single-diagonal-brace setup used

(a) Single-diagonal configuration

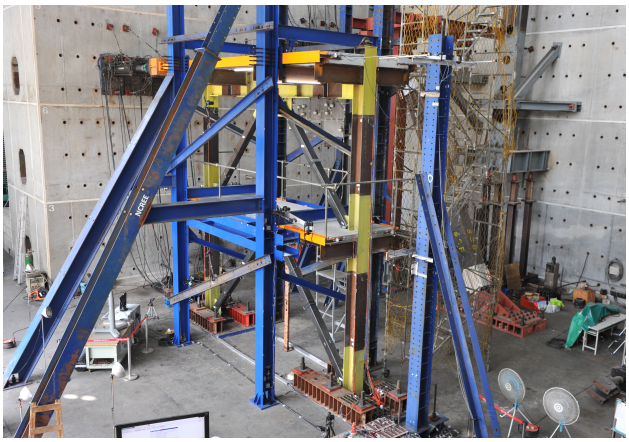

(b) Chevron configuration

Figure 3.1: Overview photographs of typical test specimens

in previous SCBF research (Roeder et al. 2011b) (shown in Figs. 2.12 and 3.1a), which permitted testing of a wide variety of connection details. The second series was conducted at the National Center for Research on Earthquake Engineering (NCREE) in Taipei, Taiwan. This facility enabled testing of two-story, one-bay, chevron NCBFs to examine the impact of a yielding-beam mechanism in the context of existing and retrofitted systems. This test setup was comparable to those used in prior tests of SCBFs (Roeder et al. 2011a; Lumpkin et al. 2012) at NCREE and is shown in Fig. 3.1b.

In total, twenty-two (22) experiments were conducted in the test program. These ex-

periments have been described in detail in previous master's theses or doctoral dissertation (Hsiao 2012; Sloat 2014; Johnson 2014; Sen 2014; Ballard 2015; Swatosh 2016). Table 3.1 summarizes the basic features of each specimen and maps them to their respective reference documents.

As Table 3.1 indicates, eight (8) different gusset-plate connection configurations identified in the infrastructure review were investigated, including:

- bolted-welded split double angles (S2L-BW),
- bolted-bolted split double angles (S2L-BB),
- welded continuous shear plates (CSP-W),
- bolted continuous shear plates (CSP-B),
- bolted split shear plates (SSP-B),
- bolted end plates with welded gusset plates (END),
- integrated gusset-shear plates (INT), and
- welded gusset plates (WLD).

Examples of these configurations in the infrastructure review are shown in Fig. 2.4. It is noted that welded gusset plates are often used in modern SCBF design and were extensively investigated in prior SCBF research (Roeder et al. 2011b). However, this configuration was less common in NCBFs, and hence the research focused on other connection configurations.

Retrofit measures tested included:

- concrete in-fill or replacement of braces with SCBF-compliant braces designed for out-of-plane (OOP) buckling,

- connection reinforcement with welds or bolts, and

- protection of gusset-plate interface welds from out-of-plane rotation demands with in-plane (IP) buckling or buckling-restrained braces (BRBs).

Most of the experiments used square HSS braces, which were common in existing infrastructure. Square HSS braces remain common in SCBF design and are therefore likely choices in retrofit. Rectangular HSS braces and BRBs were utilized in several retrofit specimens in the single-diagonal configuration, and one chevron test had wide-flange braces. The HSS and wide-flange braces were slotted and fillet-welded to the gusset plates.

The following sections describe the single-diagonal and chevron test programs, respectively, including test setup, specimen design, and observed response.

3.2 One-Story, Single-Diagonal Subassemblage Testing

3.2.1 Test Setup

The one-story, single-diagonal test program consisted of eighteen (18) specimens, as listed in Table 3.1. The experimental setup designed by Johnson (2005) was repurposed for this study. Each specimen had two W12×72 columns and W16×45 beams with an equal bay width and story height of 3,658 mm (12 ft), resulting in a 45° brace angle. These member sizes were not intended to simulate existing conditions but were selected to permit focus on the brace and connection behavior. Though the frame members and geometry were the same throughout, the brace and connection designs differed for each specimen. Important design information for these specimens, are provided in Table 3.2 and the drawings in Fig. 3.2.

Each specimen was loaded using a single actuator attached to a load beam, which was bolted to the north beam of the test frame to transfer load into the system. The south beam was bolted at its midspan to a transfer beam post-tensioned to the laboratory's strong wall to transfer the majority of the lateral load out of the system. The columns were post-tensioned with a 2,000 kN compressive force to restrain uplift and simulate gravity loading; it

Table 3.1: Summary of NCBF tests

Specimen	Description	Gusset-plate configuration	Reference document	Reference identifier
One-story, single-diagonal configuration				
1E	Deficient brace and connection (pilot study)	S2L-BW	Hsiao (2012)	NCBF32
2E	Deficient brace and connection	CSP-W	Sloat (2014)	NCBF1
3E	Deficient brace and connection	SSP-B	Johnson (2014)	NCBF3-1
2O	Deficient connection	CSP-W	Sloat (2014)	NCBF1-R2
4O	Deficient connection	S2L-BB	Swatosh (2016)	NCBF0-2
5O	Deficient connection	CSP-B	Johnson (2014)	NCBF2
6O	Deficient connection	CSP-B	Swatosh (2016)	NCBF2-2
7O	Deficient connection	SSP-B	Johnson (2014)	NCBF3-2
8O	Deficient connection	END	Ballard (2015)	NCBF4-R1
9O	Deficient connection	INT	Ballard (2015)	NCBF5
4O-W	4O with weld reinf. retrofit	S2L-BB	Swatosh (2016)	NCBF0-2R
8O-W	8O with weld reinf. retrofit	END	Swatosh (2016)	NCBF4-R1W
2C-B	2O with bolt reinf. and concrete-filled brace retrofit	CSP-W$^+$	Sloat (2014)	NCBF1-R5
2Ia	2O with in-plane buckling retrofit (square HSS brace)	CSP-W	Sloat (2014)	NCBF1-R3
2Ib	2O with in-plane buckling retrofit (rect. HSS brace)	CSP-W	Sloat (2014)	NCBF1-R4
8I	8O with in-plane buckling retrofit (rect. HSS brace)	END	Ballard (2015)	NCBF4-R2
5BR	5O with BRB retrofit	CSP-B	Ballard (2015)	NCBF2-R1
8BR	8O with BRB retrofit	END	Ballard (2015)	NCBF4-R3
Two-story, chevron configuration				
TNCBF1-N-HSS			Sen (2014)	–
(2F)	Strong beam, deficient braces and connections	CSP-W		
(1F)	Weak beam, deficient braces and connections	WLD		
TNCBF1-R-HSS			Sen (2014)	–
(2F)	Same as TNCBF1-N-HSS	CSP-W		
(1F)	Weak beam, in-plane buckling repair	WLD		
TNCBF1-R-WF			Sen (2014)	–
(2F)	Same as TNCBF1-N-HSS	CSP-W		
(1F)	Weak beam, wide-flange brace repair	WLD		
TNCBF2-D-HSS			Sen (2014)	–
(2F)	Strong beam, BDP connections	WLD		
(1F)	Weak beam, BDP connections	WLD		

S2L-BW = bolted-welded split double angle; S2L-BB = bolted-bolted split double angle; CSP-W = welded continuous shear plate; CSP-B = bolted continuous shear plate; SSP-B = bolted split shear plate; END = bolted end plate; INT = integrated gusset-shear plate; WLD = welded gusset plate

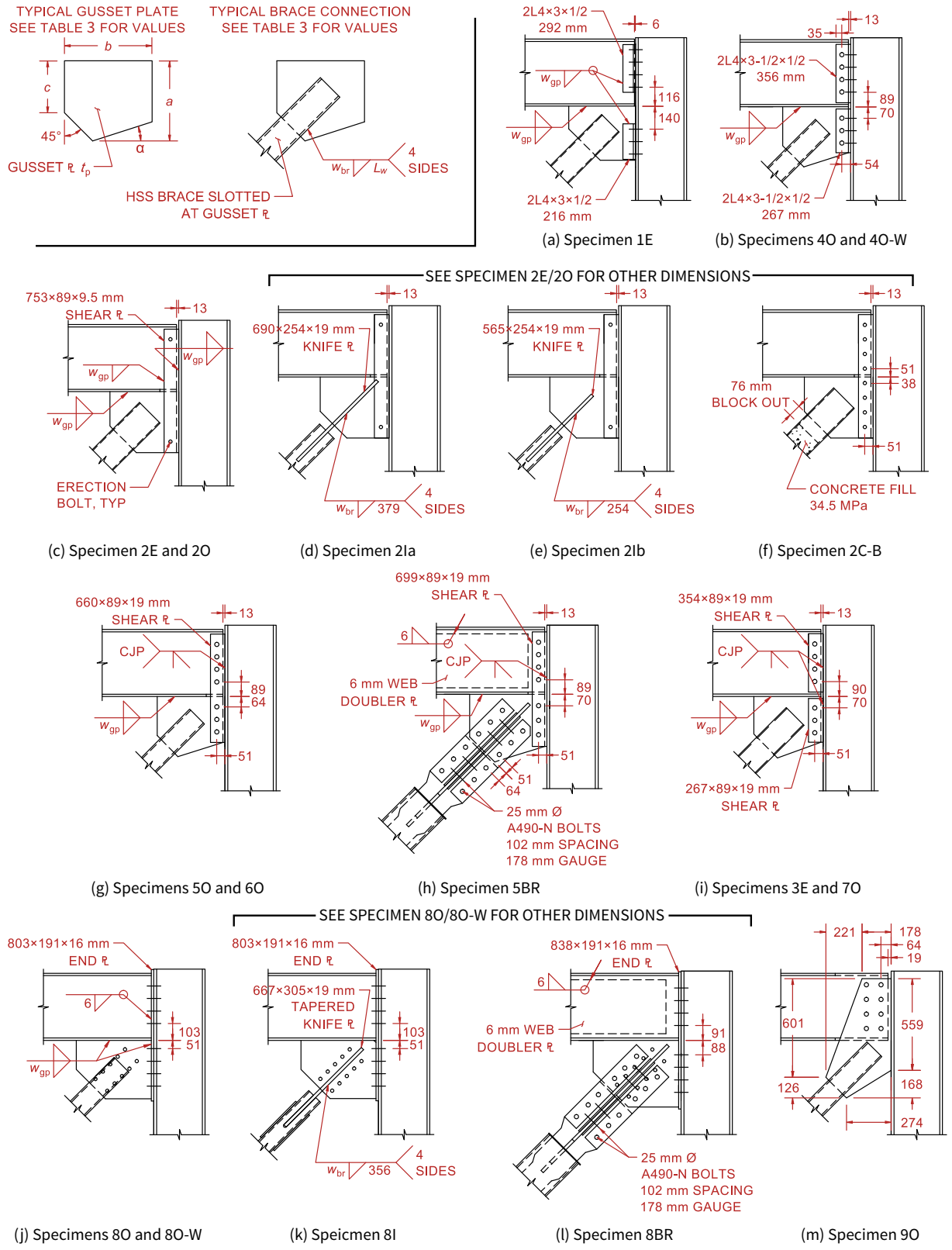

Figure 3.2: Specimen connection drawings from single-diagonal experimental program

Table 3.2: Single-Diagonal Specimen Connection Information

Specimen	Gusset plate						Vertical connection fasteners				Brace		
	t_p (mm)	a (mm)	b (mm)	c (mm)	α (deg)	w_{gp} (mm)	Bolt type	Bolt dia. (mm)	Spacing (mm)	Gauge (mm)	Section	L_w (mm)	w_{br}^a (mm)
1E	9.5	330	406	139	0.0	5[a]	A325-X	19	76	–	HSS6×6×1/4	203	5
2E	9.5	372	407	210	0.0	8[b]	–	–	–	–	HSS7×7×1/4	229	11
2O	9.5	372	407	210	0.0	8	–	–	–	–	HSS5×5×3/8	229	11
2Ia	9.5	372	407	210	0.0	8	–	–	–	–	HSS5×5×3/8	254	11
2Ib	9.5	372	407	210	0.0	8	–	–	–	–	HSS6×4×3/8	254	11
2C-B	9.5	372	407	210	0.0	8	A490-N	19	89	–	HSS7×7×1/4[d]	229	11
3E	19.1	375	410	229	19.7	8	A325-X	25	76	–	HSS6×6×1/4	254	11
4O	12.7	366	401	237	17.7	8	A325-X	25	76	127	HSS5×5×3/8	254	11
4O-W	12.7	366	401	237	17.7	(8) 11[c]	A325-X	25	76	127	HSS5×5×3/8	254	11
5O	19.1	366	401	238	17.5	11	A325-X	25	76	–	HSS5×5×3/8	254	11
5BR	19.1	412	457	260	17.2	11	A325-X	25	76	–	BRB - 163×19 mm	398	8
6O	12.7	367	401	237	17.7	8	A325-X	25	76	–	HSS5×5×3/8	254	11
7O	12.7	366	400	239	17.5	8	A325-X	25	76	–	HSS5×5×3/8	254	11
8O	15.9	356	457	178	0.0	6	A490-N	22	76	89	HSS5×5×3/8	216	13
8O-W	15.9	356	457	178	0.0	(6) 14[c]	A490-N	22	76	89	HSS5×5×3/8	216	13
8I	15.9	356	457	178	0.0	6	A490-N	22	76	89	HSS6×4×3/8	254	11
8BR	15.9	406	521	193	0.0	6	A490-N	22	76	89	BRB - 163×19 mm	436	7
9O	22.2	See Fig. 3.2m				–	A325-X	25	89	89	HSS5×5×3/8	330	8

Note: Welds do not meet demand critical requirements unless otherwise noted
[a]Demand critical weld electrode used
[b]Demand critical weld electrode used except for shear plate-to-gusset and -beam weld
[c](Underlying non-demand critical weld size) Total weld size including demand critical weld overlay
[d]Filled with concrete

is assumed that some of the story shear was transferred through the columns. The specimens were tested in the plane of the strong floor, and out-of-plane restraints were provided for the beams and columns to provide lateral stability.

The specimens were subjected to a fully reversed, cyclic loading protocol with increasing amplitude based upon *ATC-24* (ATC 1992). It is noted that some failure modes, such as net-section fracture of the brace, are only likely under large, tension-dominant deformation demands, as may occur in near-fault loading (Roeder et al. 2011b). Because this effect has

been previously studied, the brace net-section failure mode has been specifically neglected in this study.

3.2.2 Specimen Design

The test specimens were designed to evaluate specific yielding mechanism and failure modes in the context of existing conditions and several practical retrofit schemes. As a result, the specimens had characteristics meeting some SCBF design requirements while failing others. Deficiencies for the specimens are given in Table 3.3, where the DCRs were computed using the measured material properties of the steel (Table 3.4 in lieu of the expected material properties. Note that the DCRs do not include resistance factors and are thus larger than would be computed in practice. Based on material availability and the objectives of individual tests, the specimens utilized a mix of compliant and noncompliant weld metal relative to the minimum toughness requirements for demand critical welds in the *Seismic Provisions* (AISC 2017a) (indicated in Table 3.2).

Three NCBF specimens (1E, 2E, and 3E) are considered baseline specimens which establish key aspects of NCBF behavior and are shown in Fig. 3.2(a, c, and i), with dimensions given in Table 3.2. These specimens were designed with design DCRs consistent with those computed in the infrastructure review. Each had locally slender HSS braces ($\lambda/\lambda_{hd} \geq 1.9$), less rotational clearance than recommended to permit brace-end rotation ($8t_p/Nt_p \geq 2.7$), welds which did not satisfy the BDP size requirements, and other specific connection deficiencies reported in Table 3.3.

Simple and practical retrofit schemes to improve the deformation capacity of the system and minimize the vulnerability of the brace-to-gusset-plate connection (recall that this failure mode was observed in the pilot study) were devised and tested, as diagrammed in Fig. 3.3. The diagram shows that, for example, Specimen 2O is a retrofit of Specimen 2E, and Specimens 2Ia and 2Ib are more advanced retrofits designed to mitigate vulnerabilities observed in Specimen 2O. The retrofit procedure was not simulated; thus, the specimens were fabricated directly from the drawings in Fig. 3.2. Some connection deficiencies were

Table 3.3: Single-Diagonal Specimen DCRs and Results

Specimen	Yielding mechanisms			Failure modes						Geometric limits		Test results[c]	
	Whitmore yielding		SP or L bolt bearing[a]	Brace-to-GP weld	GP horizontal interface weld		GP vertical interface weld		SP or L bolt fracture[a]	Brace local slenderness (λ/λ_{hd})	Elliptical clearance[b] ($8t_p/Nt_p$)	Failure mode	Drift range (%)
	UFM	BDP	UFM		UFM	BDP	UFM	BDP	UFM				
1E	1.0	0.8	–	1.7	0.6	1.3	0.9	1.3	–	1.86	5.6	BRW	1.3
2E	1.2	1.0	–	1.0	0.6	0.7	1.2	1.4	–	2.31	2.7	BRF	1.5
3E	0.4	0.4	0.4/0.7	0.8	0.4	1.6	–	–	1.0/0.8	1.86	7.0	GPW	1.8
2O	1.3	1.1	–	0.8	0.5	0.7	1.2	1.4	–	0.95	2.1	SPW	3.3
4O	0.9	0.8	0.9/1.1	0.8	0.5	1.0	–	–	0.7/0.5	0.97	3.6	GPW	3.1
5O	0.5	0.5	0.6/0.9	0.7	0.6	1.2	–	–	1.4/1.0	0.95	5.3	BRF	4.8
6O	0.9	0.8	1.0/0.9	0.8	0.9	1.0	–	–	1.5/1.1	0.97	3.6	GPW	2.4
7O	0.7	0.7	0.8/0.9	0.7	0.6	1.2	–	–	1.4/1.0	0.95	3.5	GPW	2.7
8O	0.7	0.6	–	0.8	0.6	1.6	0.7	1.6	–	0.95	2.0	GPW	2.9
9O	0.9	0.7	–	0.8	–	–	–	–	–	0.95	(10)	BRF	5.0
4O-W	0.9	0.8	0.9/1.1	0.8	0.4	0.7	–	–	0.7/0.5	0.97	3.6	BRF	5.9
8O-W	0.7	0.6	–	0.8	0.3	0.7	0.4	0.7	–	0.97	2.0	BRF	4.9
2C-B	1.2	1.0	1.0/1.0	1.0	0.6	0.7	1.2	1.4	2.0/2.0	2.31[d]	2.7	GPW	3.2
2Ia	1.1	0.8	–	0.7	0.5	0.7	1.2	1.4	–	0.95	–	GPW	3.1
2Ib	1.5	1.2	–	0.7	0.5	0.7	1.1	1.4	–	1.15	–	SPW	2.3
8I	0.8	0.7	–	0.8	0.6	1.6	0.7	1.6	–	1.21	–	GPW	3.9
5BR	0.8	0.7	0.5/0.8	–	0.4	0.7	–	–	1.3/0.9	–	–	GPB	4.9
8BR	0.6	0.5	–	–	0.5	1.6	0.6	1.6	–	–	–	GPW	4.5

Note: SP = Shear Plate; L = Angle; GP = Gusset Plate; UFM = Uniform Force Method; BDP = Balanced Design Procedure; BRW = Brace-to-GP Weld Fracture; BRF = Brace Fracture; GPW = GP-to-Beam Weld Fracture; SPW = SP-to-Gusset/Beam Weld Fracture; GPB = GP-to-Shear Plate Bolt Fracture;
DCRs associated with failure modes are underlined (and bold if greater than 1)
[a]First DCR is for SP- or L-to-GP bolts, second DCR is for SP- or L-to-beam bolts
[b]Parentheses indicate the elliptical clearance model does not fit; Nt_p describes the distance to zero clearance
[c]Failure mode and drift range correspond to point of 20% lateral resistance degradation
[d]Brace filled with concrete

Table 3.4: Single-Diagonal Test Material Properties

Component	Shape or plate thickness	$F_{y,meas}$ (MPa)	$F_{u,meas}$ (MPa)
Column	W12×72	357	500
Beam	W16×45	397	515
Brace	HSS7×7×1/4	444	545
Brace	HSS6×6×1/4	405	501
Brace	HSS5×5×3/8	425	461
Brace[a]	HSS5$\frac{5}{8}$×3/8	427	483
Brace[b]	HSS6×4×3/8	397	458
Brace[c]	HSS6×4×3/8	436	485
Brace	BRB - core plate area 3088 mm^2	317	400
Plate	9.5 mm (3/8 in)	345	486
Plate	13 mm (1/2 in)	455	612
Plate	16 mm (5/8 in)	389	531
Plate[c]	16 mm (5/8 in)	394	578
Plate	19 mm (3/4 in)	415	586
Plate[d]	19 mm (3/4 in)	265	523
Plate	22 mm (7/8 in)	271	479

[a]Specimens 8O and 9O only
[b]Specimen 2Ib only
[c]Specimen 8I only
[d]Specimen 8BR only

retained in retrofit in order to evaluate their impacts on behavior, and hence many of the DCRs in Table 3.3 are above 1.0 for the retrofit specimens.

Four (4) brace retrofit schemes were tested where the original connections were largely retained and the brace was retrofitted with (1) a more compact OOP-buckling or (2) IP-buckling brace, (3) a BRB, or (4) in-fill with concrete to delay local deformation leading to brace fracture (Liu and Goel 1988). Other retrofits focused on mitigating horizontal and/or vertical gusset-plate interface weld vulnerability by (1) reinforcing existing, non-notch-tough gusset-plate welds with SCBF-compliant weld overlays, (2) reinforcing the connection with bolts, or (3) eliminating OOP deformation demand on the welds using an IP-buckling brace or a BRB.

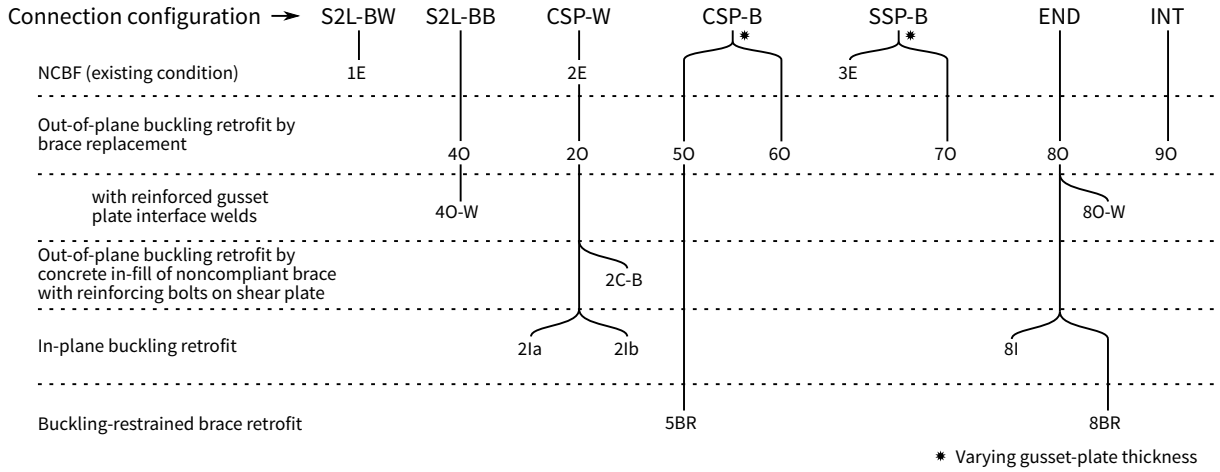

Figure 3.3: Diagram of single-diagonal experimental program

Brace-replacement retrofit in practice would require removal of the existing brace and would likely require removal of the concrete slab adjacent to the gusset plate because the gusset plate and brace end were commonly embedded in the slab in older construction. This procedure would be beneficial to accommodate end rotation of the brace during OOP buckling. If the brace is replaced, the new brace-to-gusset-plate connection can be designed to satisfy current design requirements and potentially shortened to maximize the elliptical clearance toward $8t_p$. However, if the brace is retained in the case of concrete in-fill, this connection may also require rehabilitation techniques not tested in this study. The gusset-plate connection retrofits described previously would almost certainly also require removal of the concrete slab around the connection.

3.2.3 Test Observations

Table 3.3 summarizes the test results. The failure mode is defined here as the mechanism which caused 20% lateral resistance degradation when the brace is in tension. This threshold describes in an initial-fracture damage state characterized by a significant shift in strength and stiffness because initial fracture may not be immediately evident among the gradual

degradation of the brace in compression and the connections in general. Although such degradation at drift range less than 4% is not preferred, some specimens maintained significant resistance beyond this initial loss, which can be important for collapse prevention (Hsiao et al. 2014). Therefore, understanding the true relevance of this damage state warrants study using nonlinear response-history analysis, which is addressed in subsequent chapters.

Normalized story shear versus drift response for each specimen are provided in this section (e.g., Fig. 3.4). In all hystereses in this section, the story shear (measured force applied by the actuator) is normalized by V_t, the lateral component of either the tensile yield capacity for buckling braces or design maximum compression forces for BRBs. The frame response beyond the loss of brace resistance (i.e., resistance only due to frame action) is not plotted but is indicated by the presence of an unfilled circle on the hysteresis. Full response histories that include this post-fracture loading can be found in the references in Table 3.1.

The term drift is defined here as the ratio between the story displacement and story height (i.e., equivalent to inter-story drift ratio), and it is expressed as a percentage. Although the imposed loading protocol was symmetric, the actual drift sustained by the frame was not necessarily symmetric because of losses between the actuator, frame, and reaction elements. To account for these effects, the reported drift was derived from the measured deformation between the southwest and northeast work points of the frame. The term "drift range" is defined as the sum of the absolute peak drifts in both loading directions and is used as the primary deformation measure since the response of the brace is dependent on both tensile and compressive deformations.

Existing NCBFs

Specimen 1E tested a locally slender square HSS brace (λ/λ_{hd} of 1.9) with the bolted-welded split double-angle connection shown in Fig. 3.2a. The brace-to-gusset-plate weld was significantly undersized (DCR of 1.7) but demand critical welds were used throughout. The deficient brace-to-gusset-plate weld dominated the response of the specimen, as this weld fractured at 1.3% drift range. Local cupping of the brace developed prior to weld fracture,

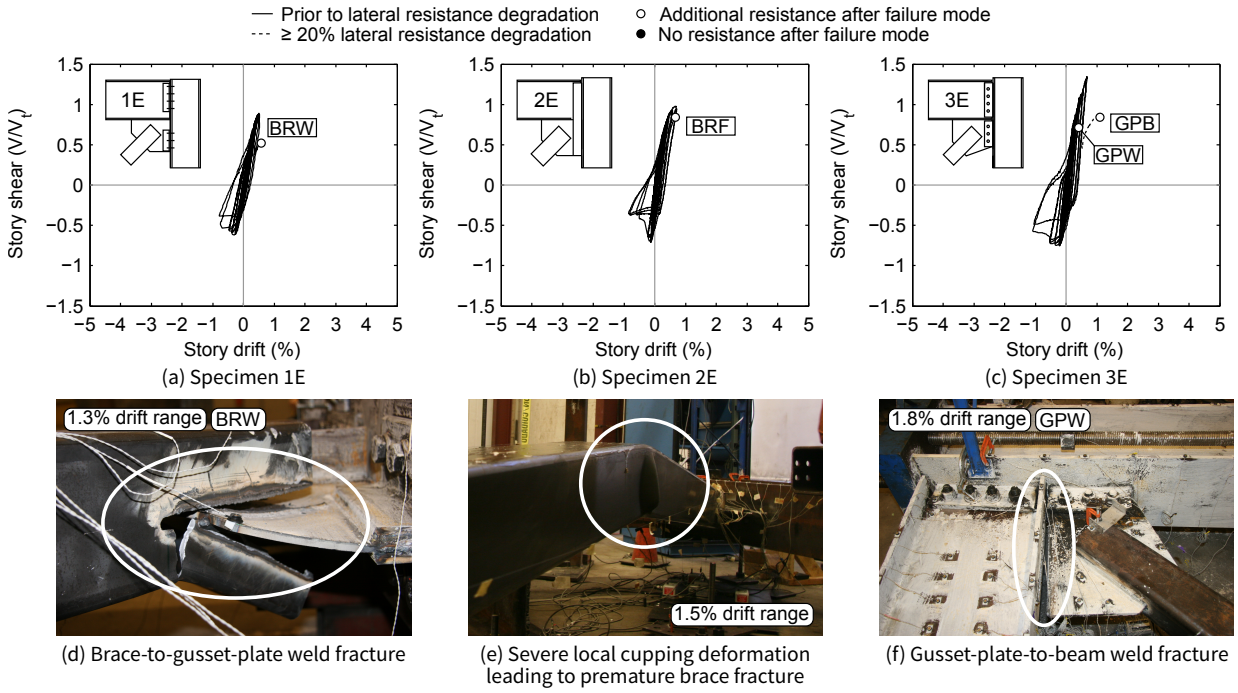

Figure 3.4: Hysteretic responses and failure modes for existing NCBF specimens

but tearing did not initiate. This suggests a higher retrofit priority for brace-to-gusset-plate welds with DCRs of at least 1.7 rather than for locally slender HSS braces with λ/λ_{hd} of 1.9. Despite fracture at a low drift range, the frame had stable post-fracture response due to frame action and re-engagement of the brace with the gusset plate in compression. The frame maintained between 40 and 60% of its peak resistance up to a drift range of 8.2%, at which point the resistance severely deteriorated due to fracture of one of the angles.

Specimen 2E had welded continuous shear plates with a brace-to-gusset-plate weld DCR of 1.0, a highly noncompliant brace (λ/λ_{hd} of 2.3), and a deficient shear-plate-to-gusset-plate and -beam weld by size (DCRs of 1.2 and 1.4 for the CDP and BDP, respectively) and toughness. The brace developed severe local cupping deformation at its midspan shortly after brace buckling, which was followed by brace fracture (BRF) at 1.5% drift range. Specimen 2E demonstrated that the well-documented low deformation capacity of locally slender HSS

braces (e.g., Goel (1992)) can dominate NCBF behavior.

Specimen 3E had a bolted split shear-plate connection with a deficient gusset-plate-to-beam (i.e., horizontal interface) weld by the BDP (DCR of 1.6) but not the CDP (DCR of 0.4), a brace λ/λ_{hd} of 1.9, and demand critical welds only for the brace-to-gusset-plate weld. Specimen 3E sustained severe local cupping deformation and brace tearing at relatively low drifts but failed because of gusset-plate-to-beam weld fracture (GPW) at a 1.8% drift range. This was a consequence of the high gusset-plate-to-beam weld DCR by the BDP, low filler-metal toughness, and low gusset-plate clearance. The results show the CDP can provide misleading connection demands because of the UFM-based DCRs for this weld were well below 1. Weld fracture resulted in a 20% reduction in lateral resistance and was followed quickly by gusset-plate-to-shear-plate bolt fracture at 2.2% drift range; this secondary failure mode was driven by the relatively thick gusset plate, which did not permit bolt-hole elongation.

Each of these NCBF specimens had drift-range capacities of 1.8% or less and all had brittle failure modes. SCBFs can achieve drift ranges on the order of 5.0% prior to brace fracture if the connections are designed according to the BDP (Roeder et al. 2011b), and this additional deformation capacity may be very beneficial in large earthquakes. Based on these results, brace-to-gusset-plate weld, brace local slenderness, and gusset-plate-to-beam weld deficiencies (including weld size, weld toughness, and gusset-plate clearance) are viewed as candidates for seismic retrofit.

Out-of-Plane Buckling Brace Retrofit

Brace Replacement without Connection Retrofit. Specimens 2O, 4O, 5O, 6O, 7O, 8O, and 9O were tests of OOP-buckling retrofits where the theoretical existing, noncompliant HSS brace was replaced with a compliant HSS5×5×3/8 brace which had a $\lambda/\lambda_{\text{hd}}$ of 0.95 using measured material properties (Table 5). The brace-to-gusset weld was addressed such that all DCRs were between 0.7 and 0.8, but other connection deficiencies were retained. Figure 3.5 shows the hysteretic responses of these specimens.

Figures 3.5c and 3.5g show that Specimens 5O and 9O achieved 4.8% and 5.0% drift range, respectively, which is comparable to SCBFs, and sustained brace fracture (BRF). Specimen 5O had a bolted continuous shear-plate connection (see Fig. 3.2g) with a bolt-fracture DCR of 1.4 by the UFM and a gusset plate-to-beam weld DCR of 1.2 by the BDP. Further, the gusset plates had deficient elliptical clearance by a factor of 5.3. Despite these deficiencies, the specimen did not have bolt or weld fracture and the connection's deformation capacity appeared to benefit from the continuity of the shear plate and elongation of the bolt holes (Fig. 3.6a). Specimen 9O had an integrated gusset-shear plate (see Fig. 3.2m) with no major deficiencies except gusset-plate clearance to permit brace end rotation. Yielding and local deformation in the beam web (Fig. 3.6b) coupled with bolt-hole elongation in the beam web contributed to its overall deformation capacity.

Specimens 2O, 4O, 6O, 7O, and 8O had OOP-buckling retrofit without connection reinforcement and sustained weld fracture in either the gusset-to-beam weld (GPW) or the shear plate-to-gusset and -beam weld (SPW). Specimen 2O (see Fig. 3.2c) was notable because it had abrupt shear plate-to-gusset and -beam weld fracture resulting in loss of all lateral resistance (indicated by the filled circle in Fig. 3.5a), since the beam-to-column connection was compromised. This failure mode was not surprising, because the shear plate-to-gusset and -beam weld DCR exceeded 1.0 based for both the UFM and BDP. Specimen 8O (see Fig. 3.2j) sustained gusset-to-beam weld fracture resulting in the subsequent fracture of the gusset-to-end plate weld, and loss of brace resistance. However, the beam-to-column connection remained intact, allowing significant resistance from frame action to develop (indicated by the unfilled circle in Fig. 3.5f).

Specimens 4O, 6O, and 7O had bolted angle or shear-plate connections (see Figs. 3.2b, 3.2g, and 3.2i) and sustained gusset-to-beam weld fracture (GPW) between 2.4 and 3.1% drift range. After weld fracture, these connections still developed the brace force via the gusset-to-shear plate bolts. This post-weld-fracture behavior is depicted by the dashed lines in Figs. 3.5b, 3.5d, and 3.5e. Reserve capacity was maintained at drift ranges between 6.2 and 7.1%, when either the brace fractured (BRF) (Specimen 4O), the gusset plate tore-out due

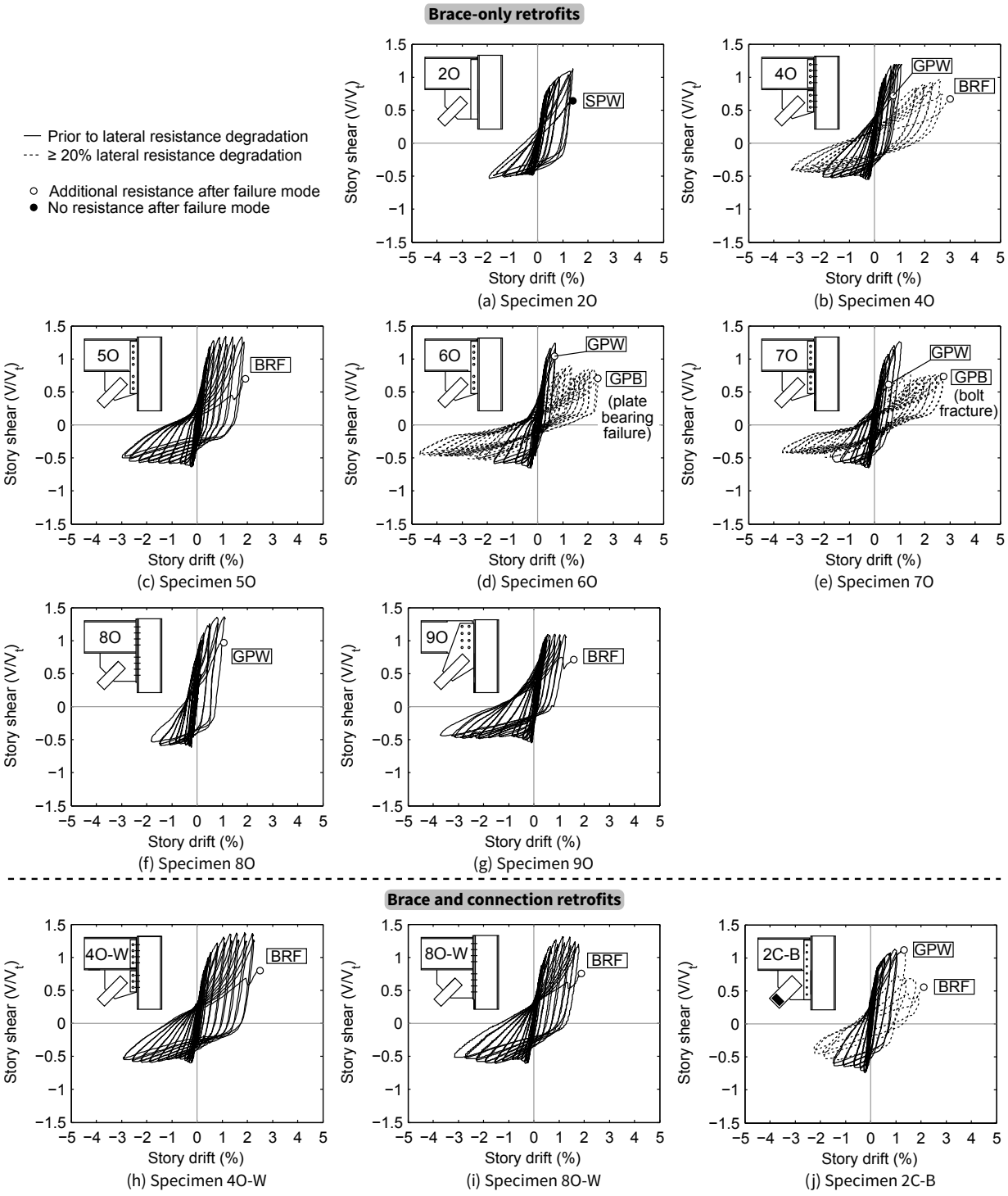

Figure 3.5: Hysteretic responses for retrofitted NCBF specimens using out-of-plane buckling braces

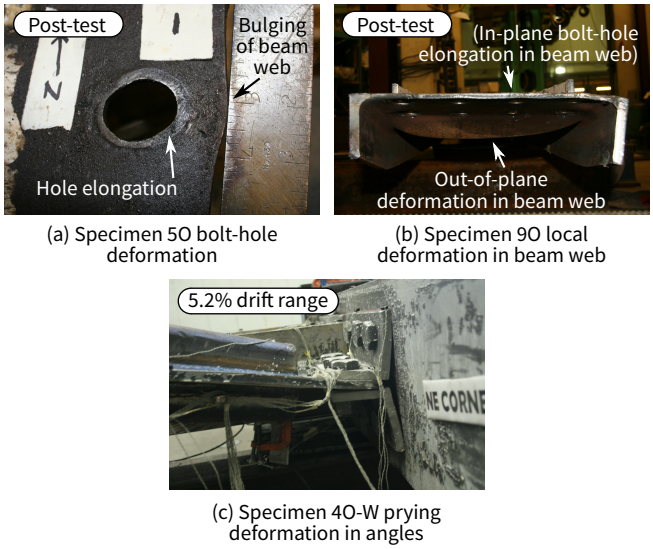

(a) Specimen 5O bolt-hole deformation

(b) Specimen 9O local deformation in beam web

(c) Specimen 4O-W prying deformation in angles

Figure 3.6: Yielding mechanisms in various out-of-plane buckling specimens

to bolt bearing (GPB) (Specimen 6O), or the gusset-plate bolts fractured (GPB) (Specimen 7O). These secondary failure modes were possible due to the bolt-hole elongation or angle-prying yielding mechanisms. Specimens 6O and 7O are discussed in Sen et al. (2016b) using a bolt bearing-to-fracture resistance ratio (BFRR) of 1.5 and 1.7, respectively. Nominal bolt strengths (AISC 2017c) were used in these calculations, but if measured properties were considered these ratios would likely be closer to 1, indicating relative balance between the plate-bearing and bolt-fracture limit states. In contrast, Specimen 3E had a BFRR of 2.4 and had gusset-to-shear plate bolt fracture at a drift range of only 2.2%.

Specimen 6O had continuous shear plates like Specimen 5O but had gusset-to-beam weld fracture (GPW) at 2.4% drift range rather than brace fracture at 4.8% drift range and relatively high bolt-bearing DCRs. This resulted in enough bolt-hole deformation in the gusset plate and beam web so that the bolt group was not engaged in a continuous manner, resulting in a less beneficial force distribution along the interface. Hence, the continuous shear plate in Specimen 6O resulted in a post-weld-fracture hysteretic behavior similar to the split shear plate in Specimen 7O.

Brace Replacement with Weld Reinforcement. Many of the above OOP-buckling-retrofit specimens, as well as Specimen 3E, clearly demonstrated the vulnerability of gusset-plate welds with OOP brace buckling. Except for Specimen 2O, these welds were not deficient by the UFM but highly deficient based on the BDP (see Table 2). The contrast in UFM and BDP DCRs was noted for most connections evaluated in the infrastructure review (see Table 1). Specimens 4O-W and 8O-W were devised to mitigate this vulnerability by reinforcing the welds with overlays of demand critical electrode to satisfy the BDP strength criteria including a resistance factor of 0.75 (Roeder et al. 2011b).

Specimen 4O-W (see Fig. 3.2b) had a bolted split double-angle connection that was nominally identical to that of Specimen 4O except the gusset-to-beam weld was reinforced such that the combined new and existing weld metal developed the yield capacity of the gusset plate. Table 2 shows the reduced weld DCRs and shows the angle-to-gusset and -beam bolt-group resistances of Specimen 4O-W were controlled by bolt bearing, so bolt fracture was not expected. The angles were about one-third the thickness needed to prevent prying if the full bolt tensile capacity is developed (DCR of 3.1) [Eq. 9-30b of the *Manual* (AISC 2017d)]. Significant prying deformation occurred without bolt fracture as shown in Fig. 3.6c, and brace fracture (BRF) occurred at 5.9% drift range (see Fig. 3.5h).

Specimen 8O-W (see Fig. 3.2j) had bolted end-plate connections nominally identical to Specimen 8O but with weld overlay reinforcement designed to develop the yield capacity of the gusset plate in combination with the existing welds; this significantly reduced weld DCRs (see Table 2). The end plate was not thick enough to prevent prying deformations with a DCR of 1.4 based on Eq. 9-30b of the *Manual* (AISC 2017d) considering the full bolt tensile capacity. The hysteretic response of Specimen 8O-W is shown in Fig. 3.5i. The horizontal and vertical gusset-plate welds were not damaged beyond the initiation of hairline cracks at the end of the gusset-to-beam weld, and brace fracture (BRF) occurred at 4.9% drift range.

The difference in drift range at brace fracture in Specimens 4O-W and 8O-W illustrates the influence of yielding mechanisms (in this case, the effect of having higher Whitmore yielding and prying DCRs).

Concrete-Filled HSS Brace with Bolt Reinforcement Specimen 2C-B (Fig. 3.2f) used a multifaceted retrofit scheme to improve the performance of Specimen 2E, which suffered weld fracture at a drift range of 1.5%. First, the existing locally slender brace (λ/λ_{hd} of 2.3) was filled with concrete to delay the development of local deformation and fracture of the brace. Second, eight 19 mm bolts were added to reinforce the welded shear plate. This retrofit strategy is advantageous because the brace and connection are not replaced. The concrete fill was blocked out 76 mm from the gusset-plate edge to avoid increasing the axial resistance of the brace.

Specimen 2C-B had improved performance over Specimen 2E as can be seen by comparing Figs. 3.5j and 3.5b. The concrete fill distributed initial local buckling deformation in several locations along the brace length (Fig. 3.7b) and delayed concentration of local deformation. Cupping deformation was prevented by the concrete and, instead, the brace walls bulged outward at large compressive deformations. The gusset-to-beam weld fractured (GPW) at the 3.2% drift range (Fig. 3.7c). The reinforcing bolts did not appear to affect the deformation capacity of the frame prior to weld fracture, but the bolts maintained a load path to the brace. At 4.4% drift range, the concrete-filled brace fractured in tension (Fig. 3.7e) due to the concentration of local deformation in compression (Fig. 3.7d). The reinforcing bolts retained the beam-to-column connection after gusset plate-to-beam weld and brace fracture until a drift range of 7.6%, when the shear plate tore along the bolt line in the gusset plate and the shear plate-to-beam weld fractured (SPW in Fig. 3.7f).

In-Plane Buckling Brace Retrofit

The high demands on the gusset-plate welds in OOP-buckling CBFs are clearly caused by the combined axial loads and bending of the gusset plate caused by brace end rotation. Elimination of the OOP deformation demands that drive weld fracture presents an alternative approach for protecting inadequate welds. An in-plane (IP) buckling retrofit strategy was studied as a method of achieving this. This strategy uses a knife plate, which is orthogonal to the gusset plate, to connect the brace and gusset plate as shown in Figs. 3.2d, 3.2e, and 3.2k.

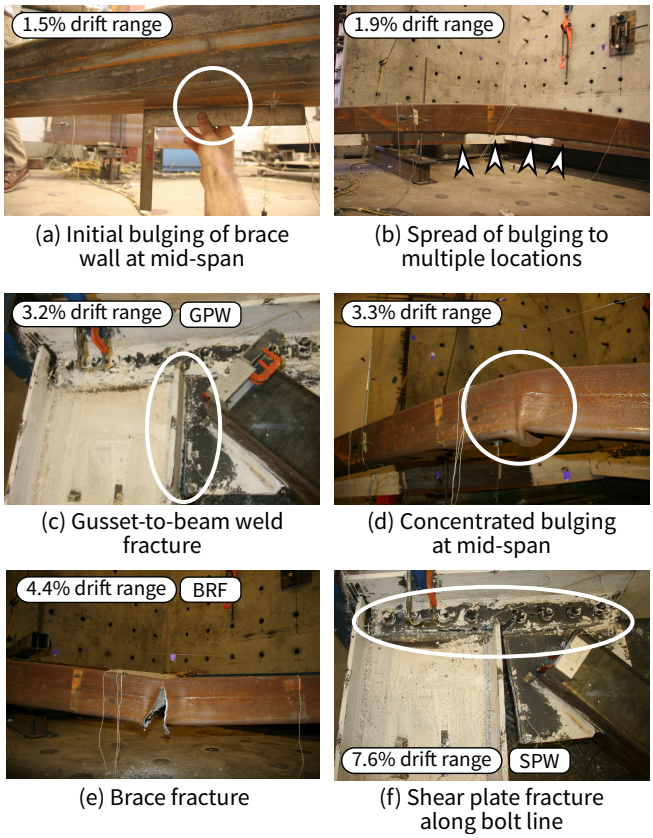

Figure 3.7: Local deformation progression in concrete-filled brace and connection fracture in Specimen 2C-B

This should encourage in-plane buckling of the brace and plastic hinging and tensile yielding of the knife plate. This would potentially increase the drift capacity of the frame and reduce the demands on the gusset-plate welds. Recent experiments with IP buckling have developed a basic understanding of the designing for this behavior (Lumpkin 2009; Tsai et al. 2013), but specific design requirements have not been codified. These prior works recommend a $3t_{\mathrm{kp}}$ offset between the brace end and gusset plate in the knife plate to provide boundary conditions that promote IP buckling, where t_{kp} is the knife-plate thickness. Specimens 2Ia, 2Ib, and 8I examined IP buckling retrofits of NCBFs using this recommendation with square and rectangular HSS braces.

Specimen 2Ia (Fig. 3.2d) had a welded continuous shear-plate connection with a seis-

mically compliant HSS5×5×3/8 brace and an IP-buckling brace-replacement retrofit. The 19-mm knife plate extended through the 9.5-mm gusset plate and into the shear plate to provide OOP stiffness to the connection, since the thickness of the gusset and shear plates was approximately half the thickness of the knife plate. Reducing OOP flexibility was critical because the buckling direction of the square brace depended on the relative stiffness of the connections. The width of the knife plate was limited by the column flange width for practical concerns, and the 19-mm knife plate was designed to develop the expected yield capacity of the brace. The DCRs of 1.2 and 1.4 using the UFM and BDP, respectively, for Specimen 2Ia indicate vulnerability of the vertical gusset-plate weld. The BDP for gusset-plate welds is intended to provide adequate resistance against OOP brace-buckling demands, but it is used here for IP-buckling cases since the gusset plate may yield due to tension on the Whitmore section and to accommodate joint rotations due to drift.

The force-displacement response of Specimen 2Ia is shown in Fig. 3.8a. The brace initially deflected OOP elastically due to the relative flexibility of the gusset plate. Since IP-buckling response was desired, the test was paused and a one-sided bearing restraint was installed at the brace midspan to prevent further OOP deflection. The brace buckled IP at 0.5% drift range. This event was dramatic and the frame?s lateral resistance immediately decreased to 68% of its resistance at buckling. As the frame was cycled to larger deformations, the knife plates developed plastic hinges and the gusset and shear plates yielded substantially (Fig. 3.8d). At 1.9% drift range, the brace began to deflect OOP in the direction opposite the bearing restraint, placing additional deformation demands on the gusset-to-beam and -shear plate welds. Cracking initiated in the gusset-to-beam weld at 2.2% drift range, in the shear plate-to-beam weld at 2.9% drift range (Fig. 3.8d), and in the shear plate-to-gusset weld at 3.1% drift range. These cracks propagated rapidly, aggravated by the low CVN toughness of the weld filler metal, and the gusset-to-beam weld fractured completely (GPW) at a drift range of 3.1%. This triggered fracture of the shear plate-to-gusset and -beam weld, and resulted in complete loss of lateral resistance (see filled circle in Fig. 3.8a). This test showed limited benefit of IP buckling in controlling damage to NCBF connections.

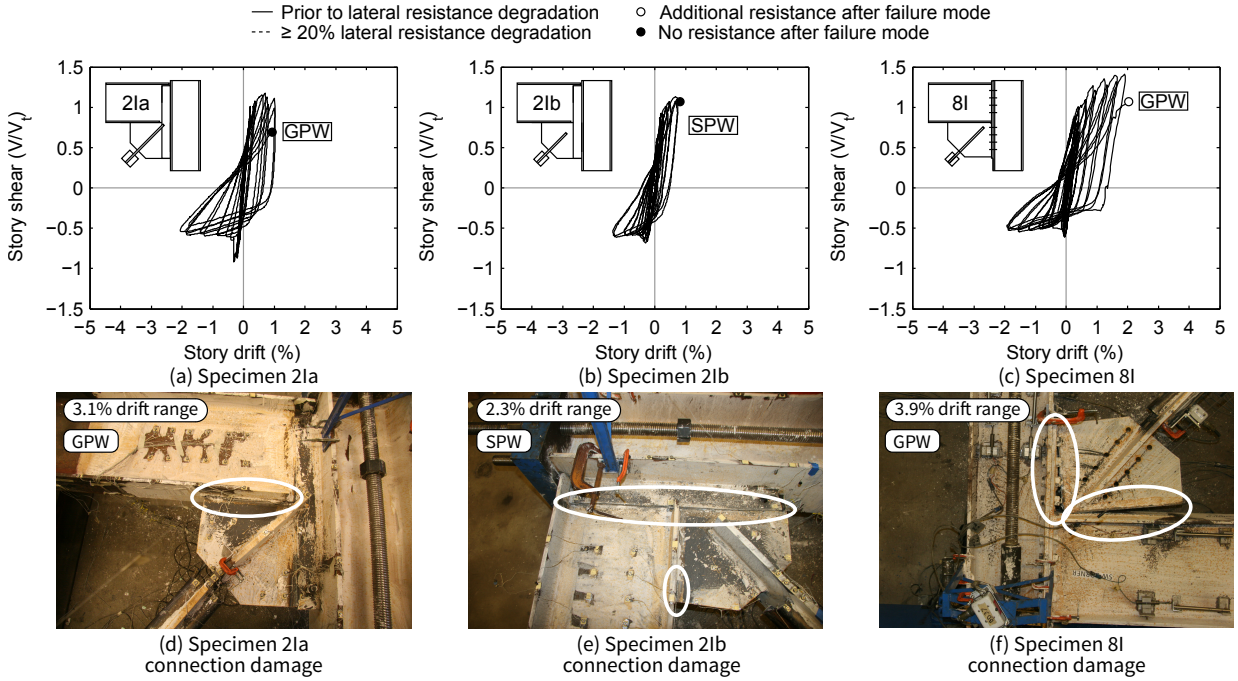

Figure 3.8: Hysteretic responses and failure modes for retrofitted NCBF specimens using in-plane buckling braces

Specimen 2Ia showed that the IP-buckling mode is not clearly isolated OOP buckling with square HSS brace due to connection flexibility. Though OOP deformation was initially artificially restrained, it developed again later in the test and contributed to the gusset plate-to-beam weld fracture. The specimen?s deformation capacity was larger than its unretrofitted counterpart (Specimen 2E) and had similar deformation capacity to OOP-buckling-retrofit counterpart (Specimen 2O).

Specimen 2Ib (Fig. 3.2e) was very similar to Specimen 2Ia but it had an HSS6×4×3/8 brace with its weak axis oriented to develop IP buckling. In addition, the knife plate was positioned further from the gusset-to-beam and -shear plate welds to avoid stress concentration in those regions. Since the knife plate-to-gusset connection was shorter than in Specimen 2Ia, the gusset plate's Whitmore section was smaller and the Whitmore yielding DCR was larger (1.5 as opposed to 1.1 in Specimen 2Ia). The shear plate-to-gusset and -beam weld

fracture DCRs were slightly larger than in Specimen 2Ia (1.1 and 1.4 computed using the UFM and BDP, respectively). The hysteresis for Specimen 2Ib is shown in Fig. 3.8b. The brace buckled IP at a drift range of 0.6% with essentially no OOP deformation. Yielding in the gusset plate was more extensive (see Fig. 3.8e) due to the higher Whitmore yielding DCR, and yielding in the shear plate was similarly widespread, as in Specimen 2Ia. The brace sustained an OOP deflection amounting to approximately 1.4% of its end-to-end length at 1.5% drift range. The gusset-to-beam weld cracked at 1.8% drift range, but cracking did not propagate substantially (lower circle in Fig. 3.8e). At 2.3% drift range, the shear plate-to-gusset and -beam weld fractured suddenly (SPW) with no prior indication of damage (upper circle in Fig. 3.8e). As indicated by the filled circle in Fig. 3.8b, there was no post-fracture resistance because the beam-to-column connection was compromised. The OOP deformation demands were minimal in Specimen 2Ib, but the deformation capacity was low due to the low-CVN-toughness weld material and high UFM DCRs.

Specimen 8I had an HSS6×4×3/8 brace oriented as with Specimen 2Ib and bolted end-plate connections (Fig. 3.2j) similar to Specimen 8O, which tested an OOP-buckling-retrofit and achieved a drift range of 2.9%. The "pre-existing" bolt holes in the gusset plate shown in Fig. 3.2j simulated a theoretically replaced bolted brace-to-gusset plate connection. The BDP indicated weld fracture vulnerability for the gusset-to-beam and -end plate welds, with DCRs of 1.6 each, but neither deficiency was indicated by the UFM. Figure 3.8c shows the hysteretic response of Specimen 8I. The brace buckled IP at a drift range of 0.5%. Yielding was noted around the remnant bolt holes, but had no appreciable effect on the overall behavior. The overall yielding in the gusset plate was substantially less than in Specimens 2Ia and 2Ib (see whitewash flaking in Figs. 3.8d, 3.8e, and 3.8f). Cracks developed on the knife plate-to-gusset welds at 0.6% drift range, but this filler metal was part of the retrofit and therefore satisfied demand critical toughness requirements, and so the cracks did not propagate. The gusset-to-beam weld initiated cracking at a drift range of 2.8% and the frame achieved a drift range of 3.9% before this weld fractured (GPW). Although gusset-to-beam weld fracture was the initial failure mode of the specimen, the gusset-to-end plate

weld fractured and tearing initiated at midspan of the brace during the next cycle at the same displacement level. The end-plate connection remained intact, allowing for significant post-fracture resistance. The specimen had 3.9% drift range, which was an improvement over the OOP-buckling-brace retrofit of the same connection (Specimen 8O). Initiation of tearing at the brace midspan indicated that the brace was also near fracture at this 3.9% drift range, because the brace had a λ/λ_{hd} of 1.2. The performance of Specimen 8I indicates that IP-buckling brace replacement is a feasible retrofit. However, the weld fracture observed in Specimen 8I suggests that the UFM may not identify gusset-plate weld vulnerabilities with IP buckling bracing.

Buckling-Restrained Brace Retrofit

Brace replacement with a BRB is another alternative considered for use with deficient gusset-plate welds, since they have no OOP deformation demands. BRB retrofit may be attractive because BRBs can span long distances without global and local slenderness issues and may have greater fracture life and energy dissipation capacity than a seismically compliant HSS brace; however, BRBs place large, concentric force demands on the connections, beams, and columns which can trigger unintended failure modes (Palmer et al. 2014).

The feasibility of using a BRB for brace replacement while retaining existing gusset-plate connections was examined in Specimens 5BR and 8BR. The BRBs had a yield force of 979 kN and a design maximum brace force of 1566 kN. The BRBs were bolted to the gusset plates as shown in Figs. 3.2h and 3.2l. Following the recommendation of Palmer et al. (2016), doubler plates were welded to the beam web in each specimen to reduce local damage. However, the recommendation for column web doubler plates was not heeded since the beam web was thinner than the column web and therefore a more serious concern.

Specimen 5BR (see Fig. 3.2h) retrofitted a bolted, continuous shear-plate connection, but the gusset plate in Specimen 5BR was larger than in Specimen 5O to accommodate the length of the BRB, which was a constraint on the test. In addition, the yield stress of the gusset plate of Specimen 5BR was lower than Specimen 5O, and the gusset-to-beam weld

DCR was lower for the BDP demands. Other DCRs were also lower because the design maximum capacity of the BRB (1566 kN) was lower than the yield capacity of the square HSS brace in Specimen 5O (1697 kN). The shear-plate bolt fracture DCRs were 1.3 and 0.9 for the gusset-plate and beam bolts, respectively. The shear-plate bolt bearing DCRs were lower in the gusset plate than in the beam web, and therefore gusset-plate bolt fracture was considered a likely vulnerability.

The hysteretic response of Specimen 5BR is shown in Fig. 3.9a, and as expected the response was relatively symmetric with full hysteretic loops and the force continued to increase significantly after yielding. The column flange adjacent to the shear plate sustained local damage at the 2.4% drift range. Cracking initiated in the gusset-to-beam weld at 3.4% drift range, and the local deformation in the column flange became more severe. Rotational demand from frame action was primarily accommodated through localized yielding in the column, bearing deformation in the bolts, and bolt-hole elongation in the plates and beam web. At 4.9% drift range, the shear plate-to-gusset bolts fractured (GPB) (circled in Fig. 3.9c). The frame lost significant resistance because the gusset-plate connection became more flexible without the bolts, leading to hinging of the brace outside the casing. This also caused local deformation in the beam flange adjacent to the gusset plate. Specimen 5BR had nearly the same deformation capacity as Specimen 5O but sustained significant beam and column damage (see Fig. 3.9c). Shear plate-to-gusset bolt fracture was predicted by the DCRs in Table 2.

Specimen 8BR (Fig. 3.2l) was a BRB retrofit of an NCBF with a bolted end-plate connection, which was also used in Specimens 8O, 8O-W, and 8I. Specimens 8O and 8I sustained gusset-to-beam weld fracture at 2.9% and 3.9% drift range, respectively; Specimen 8O-W had reinforced gusset-to-beam and -end-plate welds which mitigated this deficiency, leading to brace fracture at 4.9% drift range. The gusset plate in Specimen 8BR had larger dimensions than those in the aforementioned retrofit specimens to accommodate the length of the BRB. The horizontal and vertical gusset-plate welds had DCRs of 1.6 by the BDP as with Specimens 8O and 8I. However, Specimen 8BR had longer welds due to the larger

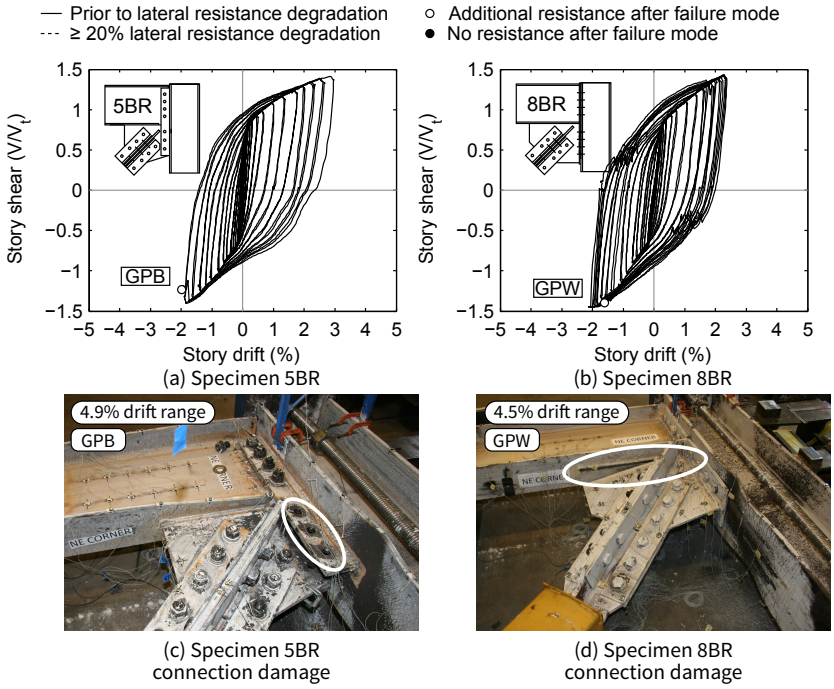

Figure 3.9: Hysteretic responses and connection/brace damage for BRB-retrofit specimens

gusset plate and therefore had lower weld DCRs (0.5 and 0.6 for the horizontal and vertical interfaces using the UFM).

As shown in Fig. 3.9b, the BRB yielded at the 0.7% drift range, and yielding in the gusset plate, column web, and column flanges just outside the gusset-plate region was observed at the 1.5% drift range. Cracking in the gusset-to-beam weld initiated at a drift range of 2.5%. At the 3.0% drift range, local deformation developed in the column flange just beyond the end plate, and this deformation increased at larger drifts when the BRB was in tension (maximum compression in the column). Extensive yielding in the columns caused axial shortening and loss of post-tensioning of the boundary frame to the strong wall, which led to uplift at the column base. At 4.5% drift range, the frame was unloaded and the post-tension rods were restressed. When reloading back to a drift range of 4.5%, the gusset plate-to-beam weld fractured (GPW) (circled in Fig. 3.9d), reducing the OOP restraint provided by the gusset plate; this caused the exposed portion of the BRB to hinge OOP. Weld fracture and

BRB hinging outside the casing resulted in a nearly 50% loss in lateral load at 4.8% drift range, and the test was ended here.

Gusset-to-beam weld fracture occurred at a higher drift range than in Specimens 8O and 8I, which also did not have reinforced gusset-plate welds. However, Specimen 8O had large OOP deformation demands and Specimen 8BR had a lower brace yield force than Specimen 8I. Hence, Specimen 8BR had enhanced deformation because the BRB eliminated OOP deformation demands and the reduced yield force of the BRB resulted in smaller demands on the welds until larger drifts.

3.3 Two-Story Chevron Subassemblage Testing

3.3.1 Test Setup

The two-story chevron specimens tested at NCREE in Taiwan are summarized in Table 3.5 and illustrated in Fig. 3.10. Figure 3.11 shows the experimental setup for these four tests. Each specimen consisted of two W12×72 columns, a W16×45 first-story beam, and a W24×94 second-story beam. Both beams had concrete slabs on metal decks with varying amounts of composite action. The W24×94 second-story beam was required to transfer the lateral load from the actuators to the specimen and thus designed as fully composite with welded web-welded flange beam-to-column connections; however, the test program objective was to evaluate the seismic response of chevron NCBFs with yielding beams and therefore the first story was the primary study region. Damage was expected to concentrate in the first story, while the second story provided reasonable boundary conditions for the lower level of the structure. Nearly elastic behavior of the second-story beam also permitted its reuse for all four tests. The W12×72 columns were reused despite yielding at the base during testing; it was judged that this did not have a large effect on the lateral strength, stiffness, or ductility of the system for subsequent testing.

The specimens were loaded quasi-statically using a fully reversed cyclic loading protocol at the roof using three 980-kN actuators in tandem. The actuator force was applied to

Table 3.5: Chevron Test Specimen Matrix

	Description	1F-beam composite action[a]	1F beam-column connections	1F-beam lateral bracing	Brace net-section reinforcement	1F-brace local slenderness	1F-gusset-plate OOP clearance	Demand-critical welds[b]
TNCBF1-N-HSS	Reference NCBF specimen	0%	WCSP	1/3 points	Adjacent to 2F beam only	Does not satisfy λ_{md}	None at corners, $2t_p$ vertical at midspan	None
TNCBF1-R-HSS	Repair with HSS braces (knife plate)	0%	WCSP (repaired)	1/3 points	All	Satisfies λ_{hd}	$0.5t_p$ elliptical at corners, $3.3t_p$ vertical at midspan	1F braces, connections, and repaired welds
TNCBF1-R-WF	Repair with wide flange braces	0%	WCSP (repaired)	1/3 points	All	Satisfies λ_{md} only	$8t_p$ elliptical at corners, $6t_p$ vertical at midspan	1F braces, connections, and repaired welds
TNCBF2-D-HSS	SCBF-compliant except 1F beam	30%	WWWF	1/3 points and mid-span	All	Satisfies λ_{hd}	$8t_p$ elliptical at corners, $6t_p$ vertical at midspan	All

Note: 1F = First story; 2F = Second story; WCSP = Welded continuous shear plate; WWWF = Welded web-welded flange; OOP = Out-of-plane
[a]Percentage based on axial yield capacity of the bare steel beam
[b]Column base and second story beam welds demand critical in all specimens

a transfer beam that delivered the loads to edge beams spanning the full length of the second-story floor slab. The slab was connected to the W24×94 beam by a double row of 19-mm-diameter shear studs spaced at 150 mm. Edge beams were also provided to the first-story slab to develop lateral restraint to the frame, but these edge beams were discontinuous to avoid stiffening or restraining the chevron beam which was expected to yield.

Column bases were attached to 75-mm base plates complete joint penetration (CJP) welds. The base plates were attached to 100-mm-thick anchor plates by thirty-five (35) 30-mm-diameter threaded rods, and each anchor plate was post-tensioned to the strong floor with six rods providing 10,800 kN of total force. This resulted in a relatively high degree of base fixity to ensure safety during this test, but this restraint may be larger than seen in many NCBFs.

The electrodes used to form welded connections varied based on the test objectives and

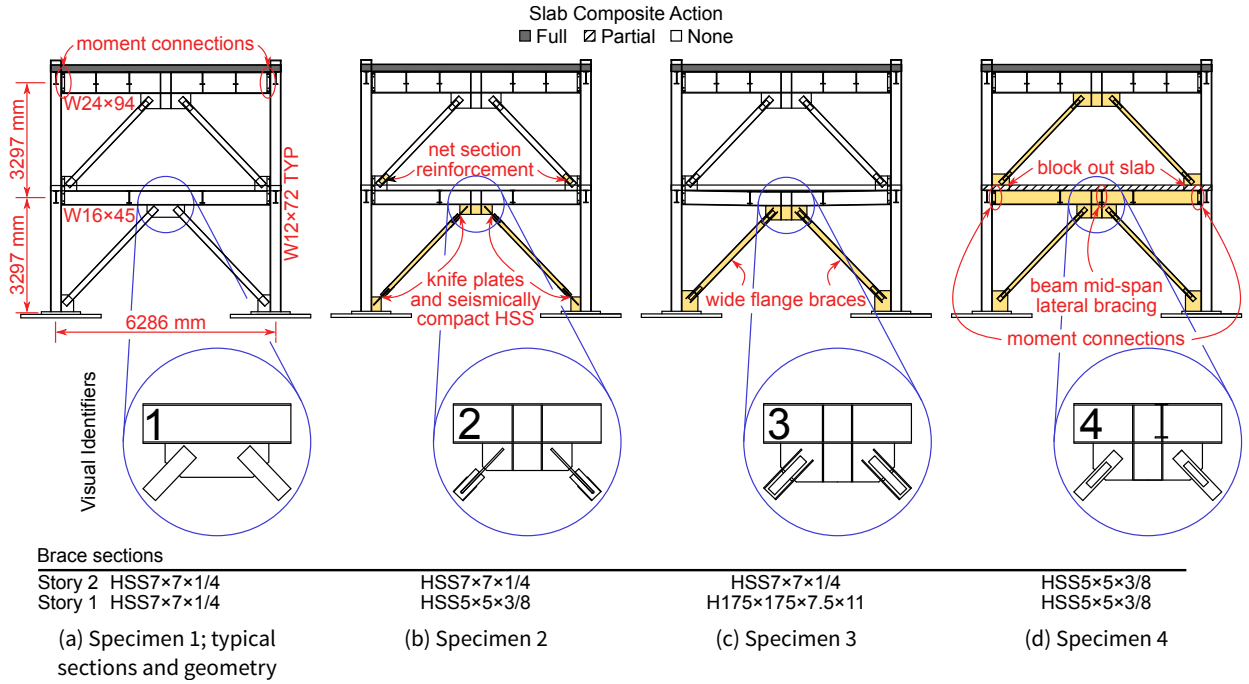

Figure 3.10: Chevron specimen elevations and visual identifiers

requirements of the test setup. For example, the welded web-welded flange connections between the second-story beam and columns used AWS E71T-1 electrodes because the beam and slab delivered the imposed lateral load to the frame. The column base CJP welds also used AWS E71T-1 electodes. On the other hand, welded connections representing NCBFs were formed with AWS E71T-7 electrodes.

The test specimens were surrounded by an OOP reaction frame as shown in Fig. 3.11. The OOP reaction frame simulated transverse framing, resisted OOP movement of the specimen, and provided lateral support to the beams. The chevron beams were laterally braced with stub floor beams attached to the slab and edge beams. At the second story, contact between the edge beams and the OOP reaction frame restrained lateral displacement, and rollers above the slab prevented torsional rotation of the beam. Lateral bracing was not provided to the midspans of the first- and second-story beams, except on the first story of Specimen TNCBF2-D-HSS, because this deficiency was noted in most NCBFs (Sloat 2014).

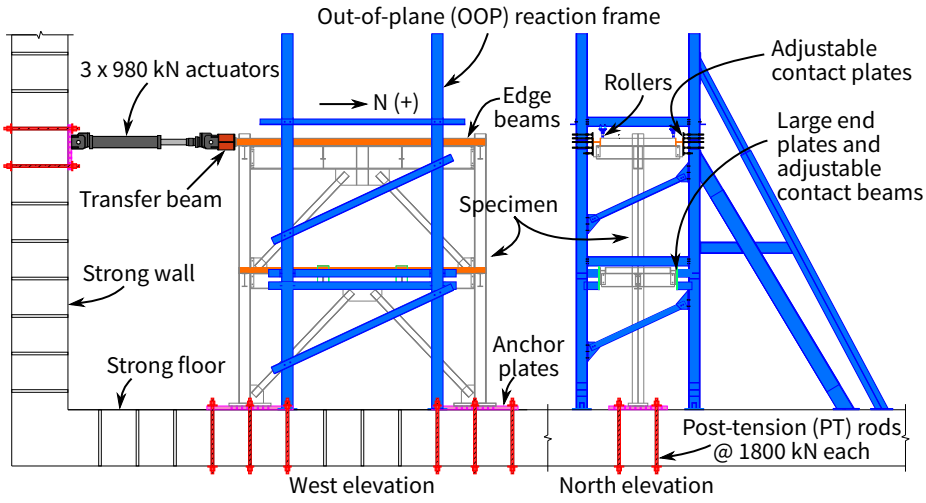

Figure 3.11: Chevron experimental setup

3.3.2 Specimen Design

Table 3.5 provides an overview of each specimen design. The drawings in Fig. 3.12 provide complete information on the geometry and details of each gusset-plate connection tested. DCRs for the braces, beams, and connections are reported in Table 3.7. These DCRs were computed without resistance factors and using the measured material properties in Table 3.6.

The specimens were tested sequentially as follows: TNCBF1-N-HSS, TNCBF1-R-HSS, TNCBF1-R-WF, and TNCBF2-D-HSS. This order is important because the columns and second-story beam were reused for all tests and the same first-story beam was used in the first three tests. Specimen TNCBF1-N-HSS tested an existing NCBF, and hence Specimens TNCBF1-R-HSS and TNCBF1-R-WF represented repairs of the damaged system. Specimen TNCBF2-D-HSS is not considered a repair, because most of the damaged components were replaced to resemble a new system, which would not be a realistic repair in practice. The following paragraphs summarize key aspects of each specimen.

Specimen TNCBF1-N-HSS had locally slender HSS7×7×1/4 braces with connections as illustrated in Figs. 3.12a, 3.12e, and 3.12g, and had numerous deficiencies. Table 3.7 indicates that the primary deficiencies were (1) beam yielding prior to brace yielding, (2) vulnerable

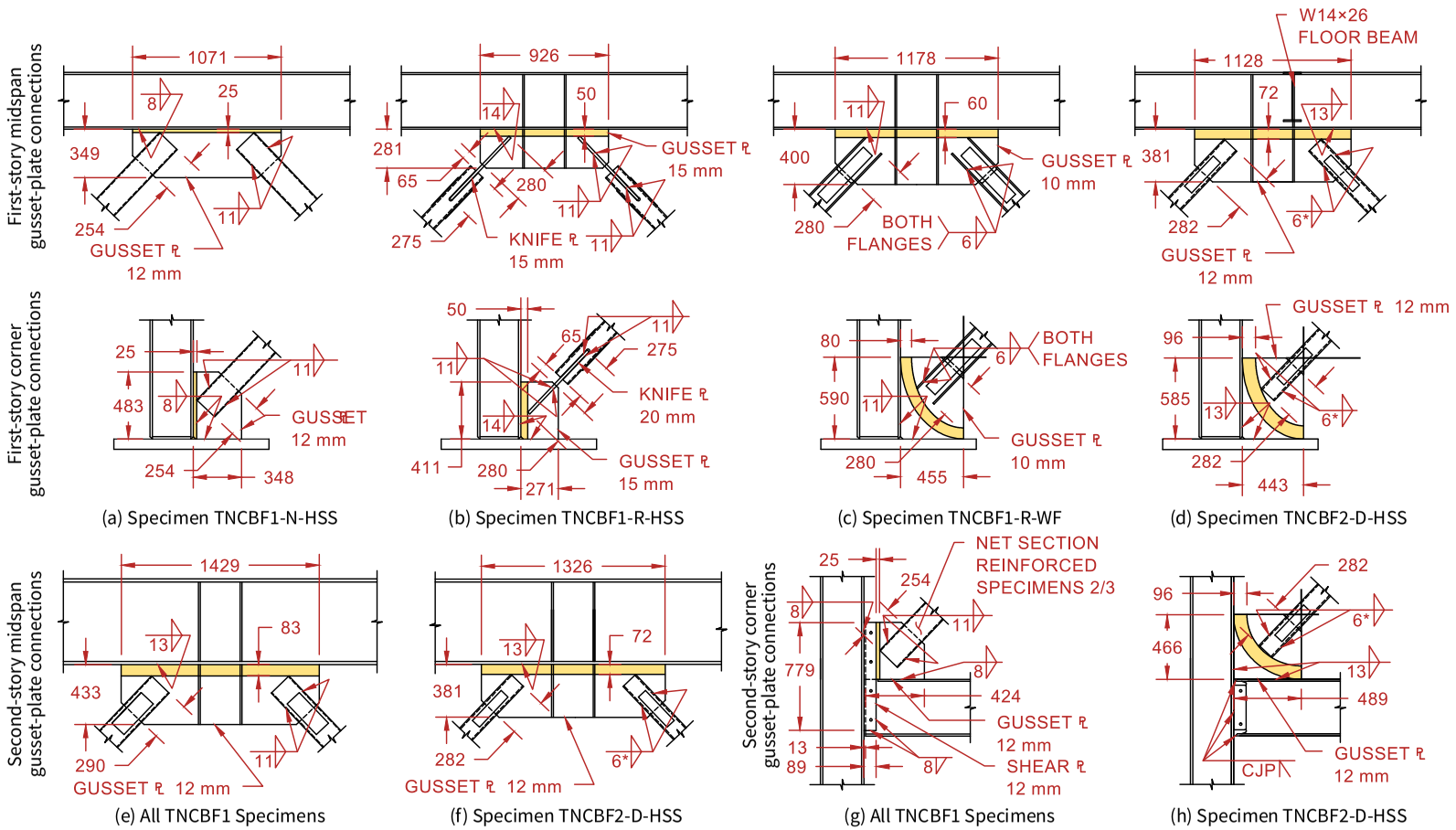

Figure 3.12: Chevron test specimen connection details

Table 3.6: Chevron Test Material Properties

Component	Shape or plate thickness	Yield stress, $F_{y,meas}$ (MPa)	Tensile strength, $F_{u,meas}$ (MPa)
Column	W12×72	395	506
Beam	W24×94	460	535
Beam	W16×45	414	521
Brace	HSS7×7×1/4	443	508
Brace	HSS5×5×3/8	438	504
Brace	H175×175×7.5×11	333	459
GP/SP	12 mm	337	504
GP/SP[a]	12 mm	445	548
GP	10 mm	395	513
GP	15 mm	424	541
KP	20 mm	416	536

Note: GP = Gusset plate; SP = Shear plate; KP = Knife plate
[a]Specimen 4 only

weld connecting the gusset plate to the beam, (3) vulnerable weld connecting the shear plate to the beam, and (4) brace local slenderness ratio, λ, exceeding the limit for SCBFs, λ_{hd}. The first-story beam-to-column connections were welded shear plates that were continuous from the bottom of the beam flange to the top of the gusset plate (i.e., CSP-W connections). The first-story beam had a 150-mm concrete floor slab on metal deck attached to the beam with puddle welds. The second-story braces were embedded in the concrete slab at the continuous shear plate connection. Welds were formed with American Welding Society (AWS) E71T-7 electrode, which does not meet demand critical toughness requirements and were undersized relative to the braces and gusset plates. The second-story beam had a 200-mm composite slab with numerous shear connectors and a welded web-welded flange (WWWF) connection, because lateral load was applied to the frame through this beam. This beam was used for all test specimens.

After testing, Specimen TNCBF1-N-HSS was repaired to construct Specimen TNCBF1-R-HSS. New HSS5×5×3/8 braces compliant with SCBF local slenderness requirements were attached to new 15-mm gusset plates using knife-plate connections that were designed for IP

Table 3.7: Chevron Specimen Component DCRs

Criterion	Specimen 1		Specimen 2	Specimen 3	Specimen 4	
	1F	2F[a]	1F	1F	1F	2F
Yielding mechanisms						
Whitmore yielding (30°)	0.95	0.94	0.88	0.88	0.75	0.72
Beam axial-flexural interaction	2.09	0.35	2.29	2.11	1.24	0.41
Failure modes						
Brace-to-GP weld	0.96	0.96	0.71	0.62	0.58	0.58
Brace net section rupture	1.25	1.25	0.92	0.74	0.87	0.87
GP horizontal interface weld (UFM)	0.76	0.66	0.50	0.45	0.40	0.32
GP horizontal interface weld (BDP)	0.82	0.82	0.74	0.58	0.67	0.67
GP vertical interface weld (UFM)	0.74	0.80	0.51	0.41	0.36	0.27
GP vertical interface weld (BDP)	0.82	1.64	0.74	0.58	0.67	0.67
SP-to-beam weld[b] (UFM)	1.78	–	1.78	1.78	–	–
SP-to-beam weld[b] (BDP)	1.64	–	1.64	1.64	–	–
SP-to-column weld[b] (UFM)	0.54	–	0.54	0.54	–	–
SP-to-column weld[b] (BDP)	0.82	–	0.82	0.82	–	–
Geometric limits						
Brace local slenderness (λ/λ_{hd})	2.27	2.27	0.94	1.08	0.94	0.94

Note: All ratios are DCRs except brace section compactness. A ratio greater than ϕ or β indicates the criterion is deficient with respect to current provisions (AISC 2017a) or the BDP (Roeder et al. 2011b), respectively. Measured material properties are considered. GP = Gusset plate; SP = Shear plate

[a]DCRs equivalent for the second stories of Specimens 2 and 3 except the brace net section rupture DCR, which was reduced to 0.92

[b]Connection includes the first-story beam-to-column connection and the second-story gusset plate connections

buckling, as illustrated in Fig. 3.12b. IP buckling is viewed as desirable since it may reduce the deformation demands on the gusset and permit the reuse of the existing gusset plates, therefore decreasing the complexity of a repair or retrofit. However, the gusset plates were replaced using demand-critical welds due to damage that occurred in the first test. The knife plates were 20-mm thick and had $3.25t_{kp}$, clearance between the brace and gusset plate to accommodate brace end rotation, where t_{kp} is the knife plate thickness (Lumpkin 2009; Tsai et al. 2013). The plate was sized such that its yield capacity just exceeded the tensile capacity of the brace [see Lumpkin (2009) for more information about the design method]. The second-story braces from Specimen TNCBF1-N-HSS were retained for Specimen TNCBF1-

R-HSS because they did not buckle during the first test, but net section reinforcement was added. Welds joining the continuous shear plate to the beam web and gusset were damaged during the first test, and approximately 180 mm of this weld was repaired with AWS E71T-1 electrode that meets demand-critical toughness requirements.

Specimen TNCBF1-R-HSS was then repaired to create Specimen TNCBF1-R-WF by using H175×175×7.5×11 wide-flange braces at the first story along with new gusset plate connections designed using the BDP (Roeder et al. 2011b); the new gusset plates are shown in Fig. 3.12c. The wide-flange braces met the moderately ductile local slenderness criteria in the AISC *Seismic Provisions* (AISC 2017a), but previous frame tests using this brace section developed greater deformation capacity than HSS5×5×3/8 braces (Lumpkin et al. 2012). Hence, these wide-flange braces were expected to place greater inelastic deformation demands on the yielding chevron beam. Specimen TNCBF1-R-HSS had 38 mm of residual midspan downward deflection of the first-story beam; the braces and gussets of Specimen TNCBF1-R-WF were designed to accommodate this geometry. The second-story braces were not repaired because they did not buckle in prior tests. The continuous shear plate welds were damaged during the second test and were repaired at both ends with E71T-1 electrode. In addition, 30-mm square sections were cut from the bottom of the first-story beam ends to prevent contact of the beam and column flanges during the expected downward deflection of the beam.

Specimen TNCBF2-D-HSS evaluated the performance of a yielding-beam chevron braced frame with ductile braces and connections, as shown in Figs. 3.12d, 3.12f and 3.12h. The columns and second-story beam were retained from the previous tests, but the lower beam and all braces and gusset plate connections were replaced. HSS5×5×3/8 braces were installed in both stories and were connected with 12-mm gusset plates. The new first-story beam was a W16×45 section (matching the previous specimens), but a single row of 19-mm-diameter shear studs spaced at 115 mm were installed to provide composite action, which is often present in modern gravity systems. Unlike the other specimens, the first-story beam was laterally braced at its midspan and had fully restrained WWWF beam-to-column

connections. At the second story, slab block outs 650 mm in length were provided around the corner gusset plates to permit brace-end rotation. The first-story beam strength was the only significant deficiency in this specimen (DCR of 1.24), but its DCR was smaller than the TNCBF1 specimens because Specimen TNCBF2-D-HSS used fully restrained beam-to-column connections.

3.3.3 Test Observations

The specimens were loaded with identical displacement-controlled, fully reversed, increasing-amplitude cyclic loading protocols using roof displacement based upon the ATC-24 protocol (ATC 1992). Displacement toward the north (actuators in compression) is positive as marked in Fig. 3.11. As in the prior discussion on single-diagonal tests, story drift range is the primary variable used in much of the data evaluation presented. Roof drift range is not discussed because the tests focused on the first-story response. Hystereses of the base shear and roof and story responses for each specimen are plotted in Fig. 3.13. The shear force is normalized to the predicted story shear at initial brace buckling, $V_{bb,n}$, given by Eq. 3.1

$$V_{bb,n} = 2P_{cr,n}\cos\theta_n + V_{fr,n} \tag{3.1}$$

where $P_{cr,n}$, θ_n, and $V_{fr,n}$ are, respectively, the critical buckling load of the brace (assuming K is 1 and L is the end-to-end length of the brace), the brace angle with respect to the horizontal, and the lateral resistance of the moment frame alone computed by linear elastic analysis at the lateral displacement corresponding to $P_{cr,n}$ in the braces. The subscript n is 1 or 2 for the first or second story, respectively. Table 3.8 presents key data from each test where base shear in normalized by $V_{bb,1}$ and beam deflection is normalized by the clear span beam length, L_b. The key test results are described here, but additional observations and figures, including the complete loading protocol, can be found in Sen (2014).

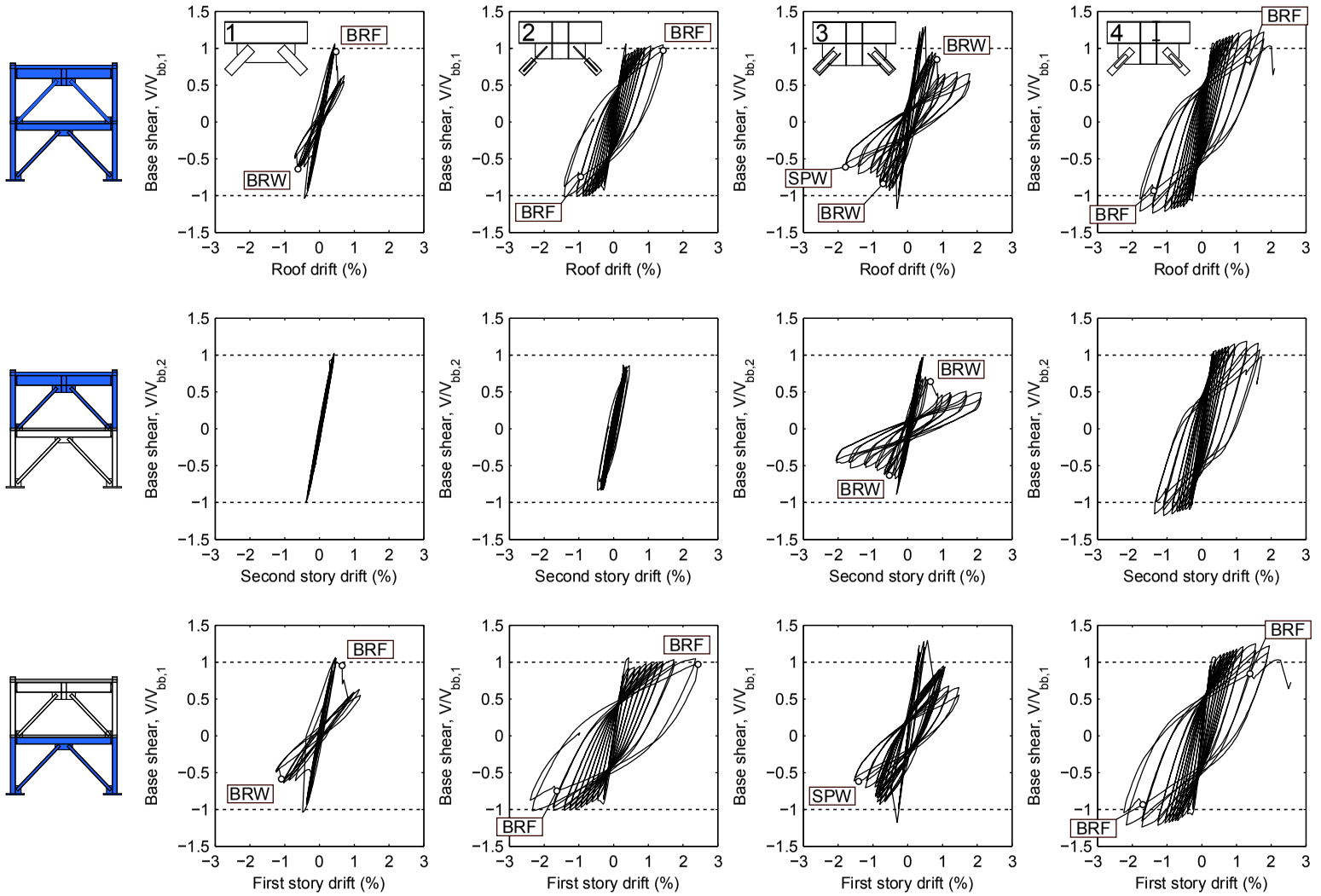

Figure 3.13: Chevron specimen roof- and story-drift hystereses

Table 3.8: Chevron Test Specimen Response

		Specimen TNCBF1-N-HSS	Specimen TNCBF1-R-HSS	Specimen TNCBF1-R-WF	Specimen TNCBF2-D-HSS
Description		NCBF reference	Knife-plate repair with HSS braces	Gusset-plate repair with wide-flange braces	SCBF except first-story beam strength
Failure mode		First-story brace fracture	First-story brace fracture	Second-story brace connection fracture	First-story brace fracture
Predicted base shear at brace buckling, $V_{bb,1}$ (kN)	Second story	2143	2143	2143	1653
	First story	2066	1756	1615	1571
Maximum base shear, $V/V_{bb,1}$		-1.04 / +1.06	-1.02 / +1.06	-1.18 / +1.29	-1.24 / +1.25
Maximum drift range[a], Δ/H (%)	Roof	1.42 (0.88)	2.85 (2.85)	3.57 (0.82)	3.57 (3.57)
	Second story	0.79 (0.79)	0.91 (0.91)	4.17 (0.78)	2.98 (2.98)
	First story	2.03 (0.96)	4.83 (4.70)	3.02 (0.86)	4.81 (4.15)
Maximum beam mid-span deflection, δ/L_b (%)	Second story	-0.01 / +0.11	-0.05 / +0.05	-0.06 / +0.12	-0.16 / +0.02
	First story	-0.28 / +0.51	-1.05 / +0.01	-0.54 / +0.08	-0.83 / +0.003
Residual beam mid-span deflection[b], δ/L_b (%)	Second story	+0.01	-0.01	+0.002	-0.02
	First story	-0.05	-0.58	-0.20	-0.39

Note: Positive base shear is associated with positive drift and positive beam deflection is upward
[a]Value in parentheses is maximum drift range in cycle prior to loss of 20% of maximum base shear in one direction
[b]Measured relative to initial deflection prior to testing

Specimen TNCBF1-N-HSS: Existing NCBF

The first column of Fig. 3.13 shows the response of Specimen 1; Fig. 3.14 highlights important damage states. Comparing the three plots of Fig. 3.13a shows that the inelastic deformation of Specimen TNCBF1-N-HSS was concentrated at the first story, while the second story remained essentially elastic. The frame was essentially elastic up to a 0.74% first-story drift range, and the south first-story brace buckled at a first-story drift range of 0.96%. Severe local cupping deformation developed at the middle of the brace after initial bucking (Fig. 3.14a), and tearing initiated at this damaged region when the brace was in tension. The south brace did not yield in tension but fractured at its midspan at the 1.18% drift range (see Fig. 3.14b) without buckling of the north brace. The north brace-to-gusset connection fractured at a first-story drift range of 2.24% (see Fig. 3.14c). After fracture, the frame lost

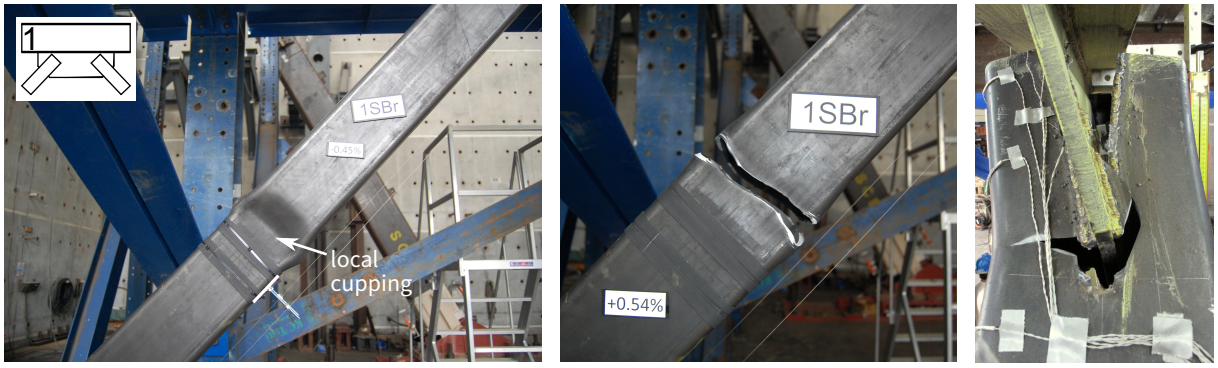

(a) South first-story brace local cupping after global buckling

(b) South first-story brace fracture

(c) North first-story brace-to-gusset plate connection fracture

Figure 3.14: Specimen TNCBF1-N-HSS test photographs

more than 40% of its maximum lateral resistance. Brace fracture occurred at much smaller deformations than expected with SCBFs, as is commonly noted with locally slender braces (Goel 1992).

After fracture of the south brace, the chevron beam yielded in flexure, limiting the axial deformation of the north brace such that its critical buckling and tensile yield force could not develop. Beam yielding was visible at the south beam-to-column connection and tearing of the shear plate-to-beam weld initiated. The first story effectively became an eccentrically braced frame with the south half of the beam acting as a very long link. Table 6 shows that the first-story beam had larger upward deflections than downward deflections, which suggests the beam developed limited composite action despite lacking shear connectors.

Transverse cracks in the north first-story brace net section initiated at a first-story drift range of 0.96%, where the brace reached its maximum tensile force (72% of tensile yield). This was not unexpected, since Table 3.7 indicates a DCR of 1.25 for net section fracture. The first-story north brace developed less than 50% of its tensile yield force after the south brace buckled and fractured, but also sustained net section cracking which propagated toward the brace end at a first-story drift range of 2.02% and resulted in fracture at a drift range 2.24%, as shown in Fig. 3.14c. This further reduced the lateral resistance to less than 50%

of the maximum value. While the second-story response was primarily elastic, small cracks initiated at the net section at the lower ends of the braces. The frame retained significant lateral resistance, but the test was stopped to allow use of the frame for other tests.

Specimen TNCBF1-R-HSS: In-Plane Buckling Repair

Specimen TNCBF1-R-HSS investigated using SCBF-compliant HSS braces with knife plates to achieve in-plane buckling as a retrofit or repair to an NCBF. Fig. 3.13b shows the force-deformation response; Fig. 3.15 shows salient damage states. During testing, in-plane buckling was not achieved, and instead the first-story braces buckled OOP at a first-story drift range of 0.73%. The hysteretic behavior (Fig. 3.13b) shows that inelastic deformation was concentrated in the first story and the second story remained primarily elastic. The total first-story drift range prior to brace fracture was 4.70%, which is similar to that expected for modern SCBFs (Roeder et al. 2011b). A yielding-beam mechanism developed, and the south and north first-story braces reached a maximum of 72% and 89% of their tensile yield force, respectively. The chevron beam had a maximum midspan deflection of 69 mm (1.05% of beam length), and the residual deflection at the end of the test was 38 mm (0.58% of beam length).

Fig. 3.16 shows the axial deformation of the south first-story brace, depicted by triangular markers and indicated by the connection sketch with the "2." The results show that the plastic deflection of the beam inhibited tensile elongation but permitted brace shortening in compression. Tensile elongation of these braces exceeded the theoretical yield elongation only after the first-story drift range reached 3.47%, but the actual tensile brace force was well below yielding at this deformation. The local deformation in the middle of the brace at 4.70% first-story drift range is shown in Fig. 3.15b. The braces fractured at this damaged location during the second cycle at this drift range as shown in Fig. 3.15c.

Specimen TNCBF1-R-HSS exhibited the yielding-beam mechanism; the response was stable and the specimen achieved a large drift range prior to significant reduction in peak cyclic capacity, as shown in Fig. 3.13b. Figure 3.17 shows that the story shear contributed

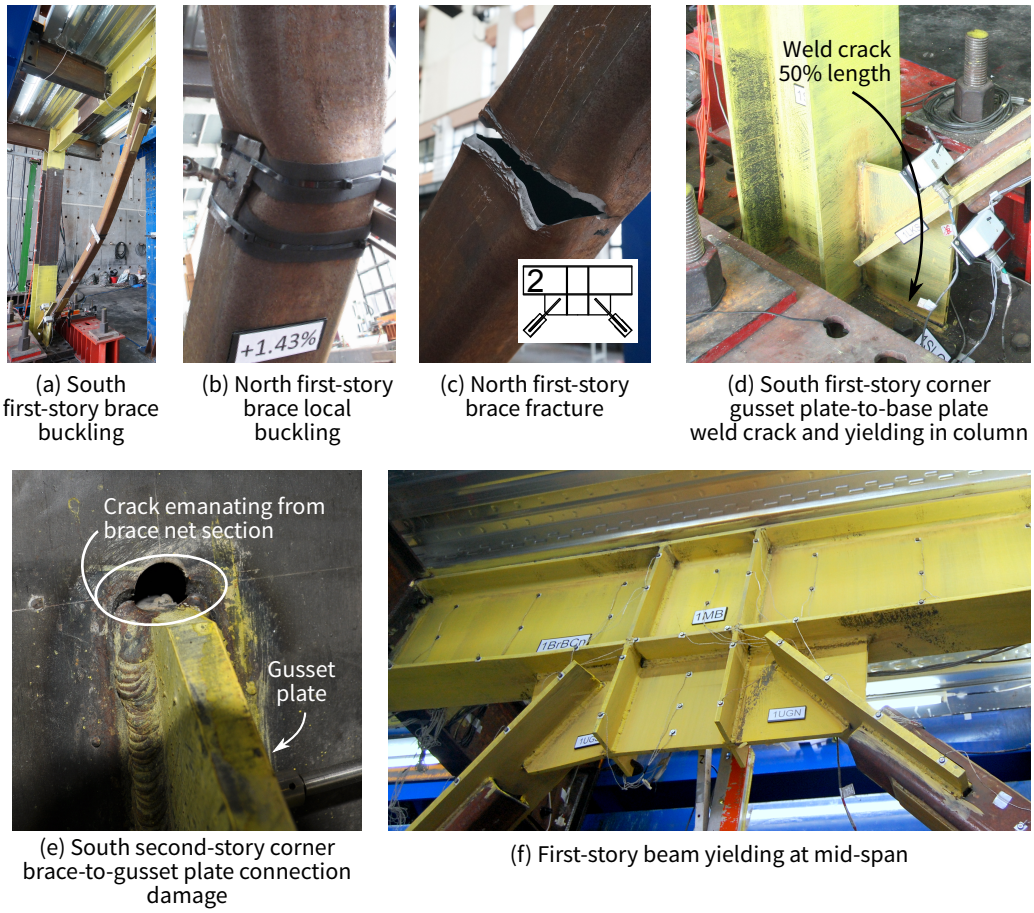

(a) South first-story brace buckling

(b) North first-story brace local buckling

(c) North first-story brace fracture

(d) South first-story corner gusset plate-to-base plate weld crack and yielding in column

(e) South second-story corner brace-to-gusset plate connection damage

(f) First-story beam yielding at mid-span

Figure 3.15: Specimen TNCBF1-R-HSS test photographs

by moment frame behavior increased after brace buckling, offsetting the limited force in the tension brace. Yielding was concentrated at the ends and midspan (see Fig. 3.15f) of the first-story beam, but no local buckling was observed. The columns yielded at their bases (see Fig. 3.15d) and below the lower first-story beam flange.

Although in-plane buckling was not achieved, the response was ductile and a yield hierarchy of brace buckling followed by gusset plate yielding developed; the latter was evidenced by the elliptical yield patterns in the gusset plates. The new welds joining the new gusset plate to the frame and base plates were demand critical welds sized according to the BDP (Roeder et al. 2011b). The south gusset plate-to-base plate weld developed a crack at a

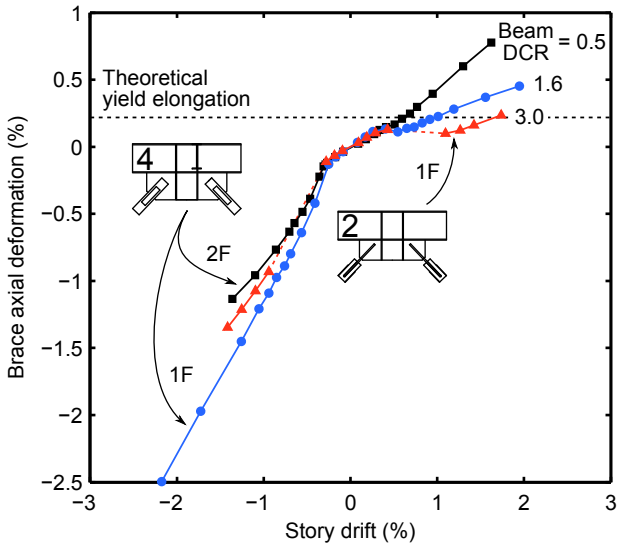

Figure 3.16: Axial deformation backbone curves of the south braces (negative deformation indicates compressive shortening and positive deformation indicates tensile elongation)

first-story drift range of 1.88% and grew to approximately 50% of the weld length by the end of the test (see Fig. 3.15d); smaller weld cracks developed in the other corner plate. However, no complete weld fractures occurred. The chevron beam had no lateral support at midspan, and twist deformations of the beam (up to 0.038 rad at midspan) were observed. The twisting deformations may have contributed to the OOP buckling rather than in-plane buckling, and it may also have decreased the demands on gusset plate welds.

The shear plate-to-beam welds were repaired after the first test, and both of these welds again developed cracks over approximately 30% of the weld length at the 4.83% first-story drift range. Beam-to-column connections in chevron CBFs with the beam-yielding mechanism are subjected to large rotational demands. The end of the beam adjacent to the compression brace undergoes the largest rotation because joint closing from drift and beam deflection must be accommodated.

The second story again remained elastic during this test. The brace net section cracks at the second-story corner gusset plates noted from the first test grew slightly in this test (see

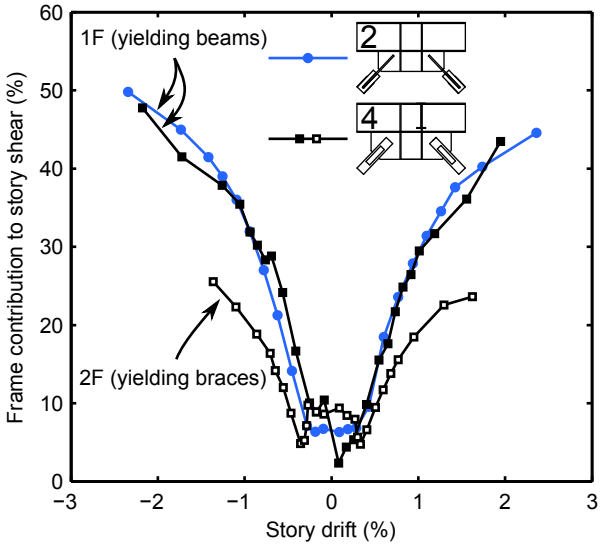

Figure 3.17: Frame contribution to lateral resistance

Fig. 3.15e).

Specimen 2 performed well and provided behavior comparable to an SCBF. The first-story beam had an DCR of about 2.3 considering the post-buckling brace demands specified in the current *Seismic Provisions* (AISC 2017a). The first-story gusset plate connections were not designed for OOP buckling, but they accommodated a drift range typical of that expected from SCBF designs (Roeder et al. 2011b). The continuous shear plate beam-to-column connections had undersized welds and were not made with demand critical electrodes, and these welds developed the large drift range although they were clearly distressed by the additional rotational demands. Additional retrofit of this connection might further improve seismic performance.

Specimen TNCBF1-R-WF: Wide-Flange Brace Repair

Specimen TNCBF1-R-WF investigated the use of wide-flange braces designed for OOP buckling and yield hierarchy using the BDP (Roeder et al. 2011b). Figure 3.13c shows that inelastic deformation occurred in both stories. The lower set of second-story brace-to-gusset

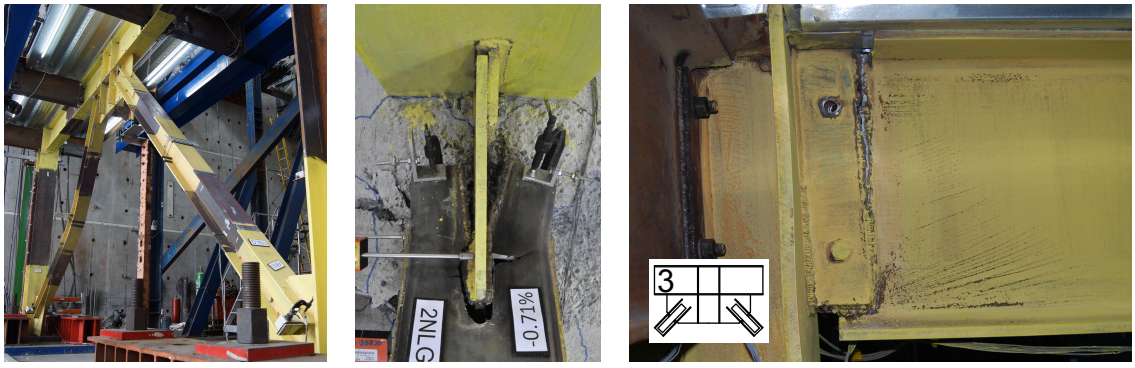

(a) South first-story brace buckling

(b) North second-story corner brace-to-gusset plate connection fracture

(c) South first-story beam-to-column connection fracture

Figure 3.18: Specimen 3 test photos

plate connections fractured at 1.18% story drift range (Fig. 3.18b). This was followed by fracture of the first-story beam-to-column connections (Fig. 3.18c) at a story drift range of 2.88%. It is noteworthy that the second-story components and connections were largely those from Specimen 1 and therefore, although not predicted, it is not unexpected that connection failure might occur due to the large number of high demand cycles from the three tests. However, because wide-flange braces are expected to sustain larger story drift demands than HSS braces, this test did not achieve its objective. Instead, the early connection failures limited the drift capacity of this specimen.

The first-story braces buckled OOP at first-story drift ranges of 0.63 and 1.23%. Initial buckling of the south brace is shown in Fig. 3.18a. Brace buckling resulted in a loss of between 40 and 50% of the maximum resistance in both loading directions. However, additional cycling resulted in hardening of the brace in compression. Higher tensile forces were not developed in the braces because beam yielding limited the brace tensile force and elongation. Nevertheless, the specimen recovered to approximately 75% of its maximum lateral resistance by 1.79% first-story drift range due to hardening in the braces and increased resistance from frame action.

Yielding of the first-story beam and the columns was limited at a 1.79% drift range, but

the weld between the shear plates and first-story beam web developed cracks. At 2.40% first-story drift range, the L-shaped fillet weld developed increased cracking, and at 2.88% drift range, the erection bolts in the shear plate fractured as weld cracks grew to approximately 50 to 60% of their length on both beam ends as shown in Fig. 3.18c. Fracture of the beam-to-column connections is attributed to the large connection rotations due to the yielding-beam mechanism, substandard initial condition of the welds (DCR of 1.78 using the UFM), residual effects of prior testing, and repairs made after prior tests.

The second story of Specimen TNCBF1-R-WF experienced more inelastic deformation than prior tests. The braces, which were also used in Specimens TNCBF1-N-HSS and TNCBF1-R-HSS, did not buckle in compression or yield in tension, but the second story was designed to develop the yielding-brace mechanism in Fig 1a. The brace-to-gusset plate welds fractured at a second-story drift range of 1.18% due to the propagation of cracks that initiated at the brace net section in prior tests (see Fig. 3.18b). These welds were simulating NCBF construction and were not demand critical welds. The failure mechanism was similar to the brace-to-gusset plate connection fracture that occurred during the test of Specimen TNCBF1-N-HSS (Fig. 3.14c). After fracture, the stiffness of the second story was dramatically reduced, as shown in Fig. 3.13c.

Specimen TNCBF1-R-WF performed poorly due to the brace-to-gusset plate connection and the continuous shear plate beam-to-column connection deficiencies noted in Table 3.8. Neither issue is a direct impact of the use of wide-flange braces.

Specimen TNCBF2-D-HSS: SCBF with Yielding Beam

Specimen TNCBF2-D-HSS was a chevron CBF which met all AISC SCBF (AISC 2017a) requirements except that the first-story beam was weaker than permitted (DCR of 1.24). All four braces buckled, resulting in inelastic deformation on both stories, as shown in Fig. 3.13d. The first and second stories achieved drift ranges of 4.12% and 2.98% prior to first-story brace fracture (no second-story components failed).

The specimen remained essentially elastic up to first and second story drift ranges of

0.59% and 0.63%, respectively, when brace buckling occurred. The yielding-beam mechanism developed in the first story shortly after brace buckling, but the second story had a beam with an DCR of 0.41, resulting in the yielding-brace mechanism. Hence, braces yielded in tension in the second story but the first-story braces only developed between 80 and 90% of their yield force. The gusset plates on both stories showed evidence of yielding because of the gusset plate deformation due to brace buckling. The first-story corner gusset-plate-to-column welds developed cracks, but these did not grow longer than 10% of the weld length.

The yielding-beam mechanism limited the tensile force in the brace but did not result in degradation of the lateral resistance of the frame, because flexural resistance of the frame supplemented the loss in resistance via frame action. Figure 3.17 shows that the contribution of frame action to story shear at the first story was about the same as in Specimen TNCBF1-R-HSS, even though the beam had composite action and an DCR approximately half that of Specimen TNCBF1-R-HSS. The midspan of the first-story beam deflected to a maximum of 0.83% of its total length. At the end of the test, beam yielding was minor at midspan and more substantial at the connection. Figure 3.17 shows that moment frame action contributed to less of the total story shear on the second story because the braces yielded in tension.

Local cupping deformation occurred at the midspan of both first-story braces at a first-story drift range of 2.44%. The north brace initiated tearing in this damaged region at a drift range of 4.12%, but there was virtually no loss of lateral resistance until 4.50% drift range, when the opposing (south) brace fractured. The test was ended at this point, although the frame retained significant lateral resistance due to moment frame behavior. The second-story braces did not fracture, but one brace developed local cupping deformation during the final lateral displacement excursion, where the story reached a maximum drift range of 3.09%.

Although the DCR for the first-story beam was just over 1.2 times that allowed by the current AISC *Seismic Provisions* (AISC 2017a), the frame clearly performed well and the beam had relatively little damage. The first-story beam-to-column and gusset connections of Specimen TNCBF2-D-HSS were designed to current SCBF requirements, and they accumulated little damage during the test. In addition, Specimen 4 (and all other previous

specimens) did not have column-to-base plate weld cracking or fracture, which has occurred in CJP welds in tests of CBFs with tapered gusset plates (Uriz and Mahin 2008) or no gusset plates (Lai and Mahin 2013) adjacent to the column bases. The rectangular gusset plates used in this test program extended at least 1.3 times the column depth up from the base plate, and this likely induced column plastic hinge formation further from these critical welds.

3.4 Yielding and Failure Hierarchy Trends

The existing NCBFs and many of the retrofitted NCBFs tested resulted in abrupt brace or connection fractures at small drift ranges. However, some retrofit specimens exhibited behavior comparable to SCBFs despite their apparent deficiencies due to the presence of secondary yielding mechanisms, such as bolt-hole elongation, connecting-element deformation associated with prying, and gusset-plate yielding. This observation illustrates the importance of using a BDP evaluation method that separates yielding mechanisms from failure modes for NCBF retrofit strategies.

The hysteretic responses of the NCBF and retrofitted-NCBF specimens are categorized into one of four behavior types in Fig. 3.19 based on the representative backbone curves in Fig. 3.20. The dashed lines in Fig. 3.20 indicate extrapolation beyond the measured solid lines. In Fig. 3.19, specimens marked with X-caps were tested to their ultimate deformation capacity (i.e., the specimen had no very little lateral resistance or the vertical-load-resisting system was compromised), whereas the largest measured drift range for other specimens is shown (after which they still had additional drift capacity that could not be measured because of test setup limitations). BRBs represent a fifth behavior type not shown in Fig. 3.20; the post-connection-fracture responses for these specimens were not tested.

The behavior types observed in these tests are distinguished by the severity and sequence of failure modes as illustrated in Fig. 3.21, which links (a) backbone curve behavior with (b) failure mode sequence and (c) example damage observations from the experimental program. Three types of failure modes (L1, L2, and L3) which represent different severity levels of

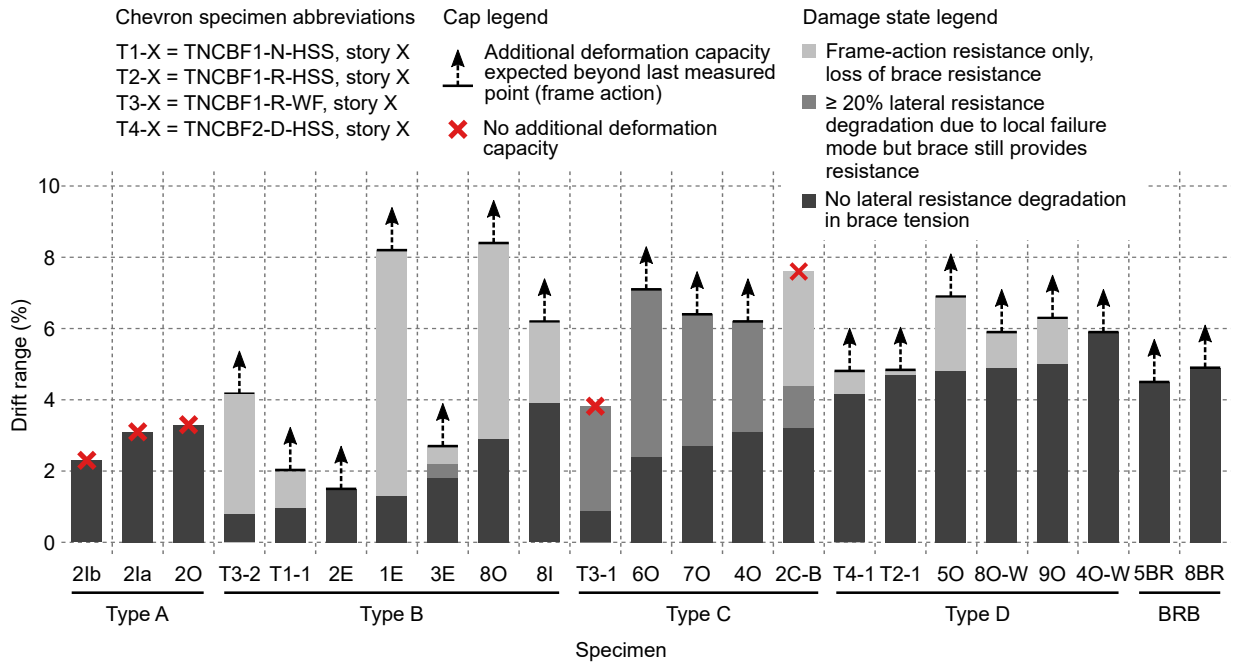

Figure 3.19: Specimen response grouped by behavior type

lateral resistance reduction are defined in Table 3.9. This table also provides examples of each failure mode type which are possible in brace-gusset subassemblages. The failure mode sequences in Fig. 3.21b describe the progression of system behavior from an initial state ("0") to a potential collapse due to an L3 failure mode. L3 failure modes were rarely observed in the experimental study (note that these correspond to the X-caps in Fig. 3.19), even at relatively large drifts following an L2 failure mode. Stepping alphabetically from Type A to Type D, the behavior types transition from highly ductile to ductile, with Type D representing behavior of an SCBF.

Type-A is clearly the most severe behavior where all lateral resistance is lost at less than 4% drift range (Specimens 2O, 2Ia, and 2Ib). The experiments suggest (1) welded continuous shear plate connections are most vulnerable to this behavior among the tested configurations, (2) OOP brace buckling demands on gusset plates and their welds are a major cause of this behavior, and (3) low-toughness weld crack propagation from other mechanisms (Specimen

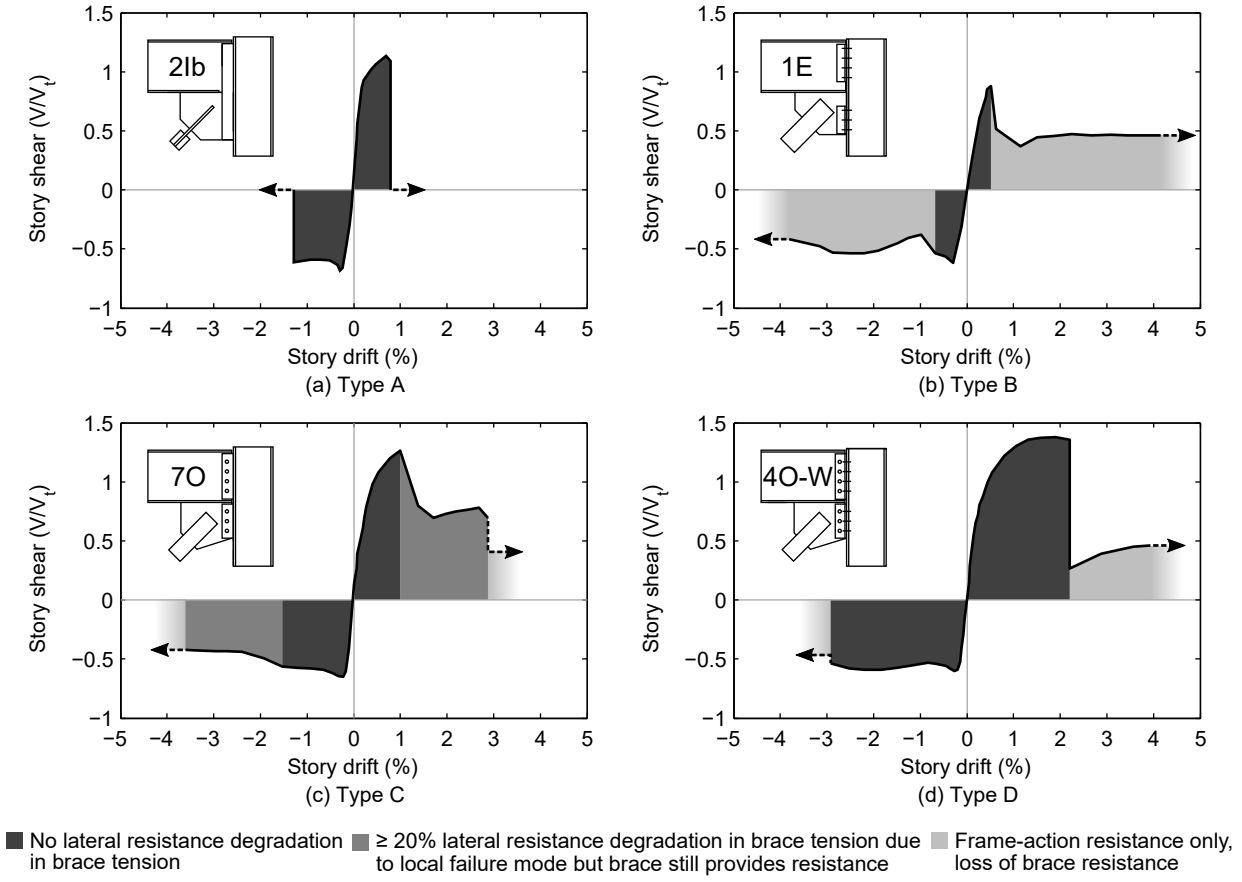

Figure 3.20: Representative backbone curves for CBF response types

2Ia) may also result in Type-A behavior. IP-buckling or BRB retrofit using lower-capacity braces are possible retrofits for Type-A behavior.

Type-B behavior is characterized by sudden loss of brace resistance at less than 4% drift range becuase of brace-to-gusset weld fracture (Specimens 1E and TNCBF1-R-WF), premature fracture of locally slender braces (Specimens 2E and TNCBF1-N-HSS), or fracture of both gusset-plate interface connections (Specimens 3E, 8O, and 8I), followed by measurable lateral resistance from frame action. Type-B behavior is severe and may require retrofit; however, the additional resistance from frame action may be important for collapse prevention (Hsiao et al. 2014).

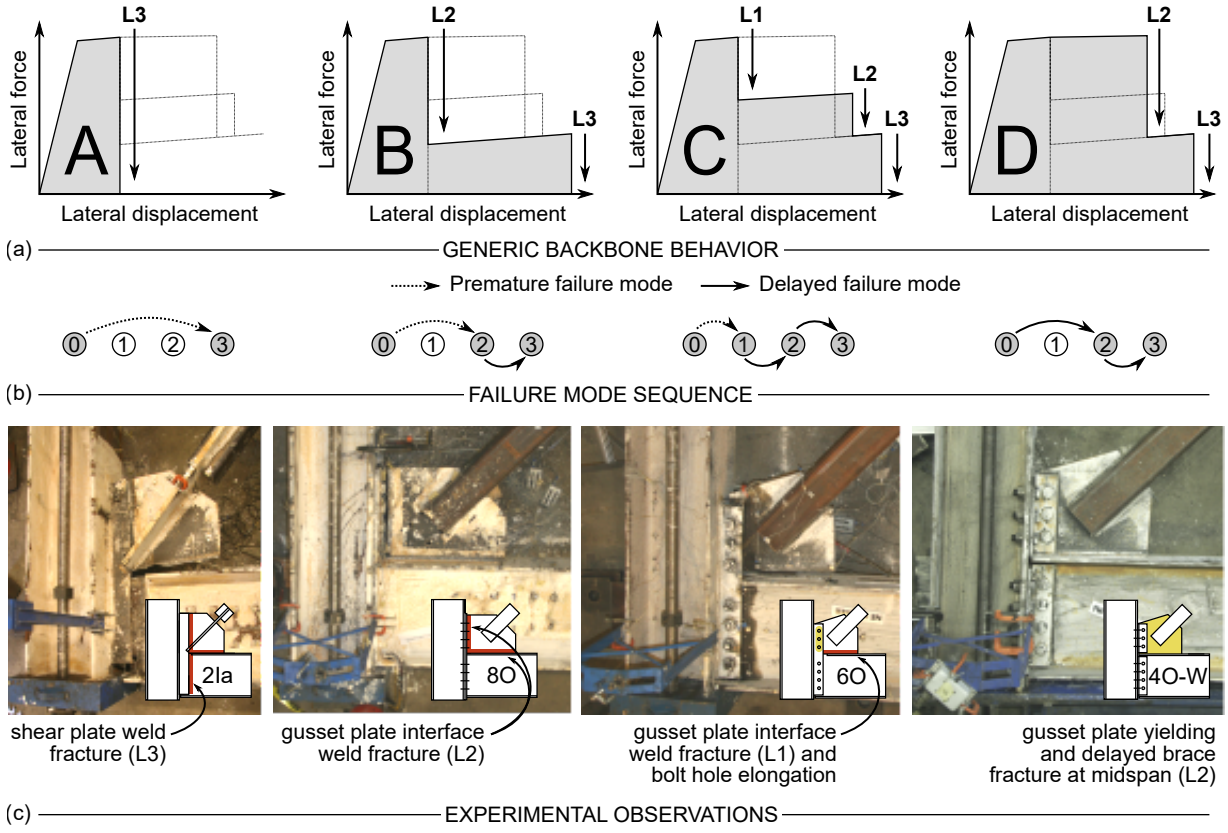

Figure 3.21: Overview of behavior types for brace-gusset subassemblages of existing and retrofitted NCBFs

Type-C behavior is characterized by loss of more than 20% of peak lateral resistance because of a connection failure at less than 4% drift range, but significant lateral resistance is retained because the brace load path is maintained to at least a 4% drift range. Specimens 2C-B, 4O, 6O, and 7O had Type-C behavior because their gusset-plate-to-beam welds fractured between 2.4 and 3.2% drift range but brace resistance was maintained via bolted shear-plate or double-angle connections. Specimens 2C-B, 6O, and 7O had sufficient balance between the bolt fracture and bearing limit states to prevent or delay bolt fracture [bearing-to-fracture resistance ratios (BFFRs) of 2.0, 1.5, and 1.7, respectively, using nominal bolt strengths]. Specimen 4O had relatively thin angles connecting the gusset plate to the col-

Table 3.9: Failure Mode Types

Type	Description	Examples
L1	Brace partially disconnected from the frame such that it continues to develop axial forces below its full tensile strength	• Fracture of a single gusset-plate interface connection
L2	Total loss of brace axial resistance with residual resistance provided by frame action	• Brace fracture • Brace-to-gusset-plate connection fracture (fracture of welds, bolts, net section, etc.) • Gusset-plate fracture (Whitmore section or block shear fracture) • Fracture of both gusset-plate interface connections
L3	Severe or total loss of lateral load resistance in the system, likely leading to collapse	• Beam-to-column connection fracture

umn, and local deformation of the angles provided significant rotational capacity. Type-C behavior has the potential for high residual deformation capacity.

Type-D behavior is characterized by brace fracture at greater than 4% drift range with frame resistance maintained after brace fracture. This is enabled by having secondary yielding mechanisms, such as Whitmore yielding, bolt-hole elongation, local deformation of connections susceptible to prying action, and beam yielding in the chevron configuration. Specimens 4O-W, 5O, 8O-W, 9O, TNCBF1-R-HSS, and TNCBF2-D-HSS exhibited Type-D behavior with brace fracture between drift ranges of 4.2 and 5.9%. Specimens 4O-W and 8O-W had reinforced horizontal and vertical gusset-plate interface welds designed to develop the yield capacity of the plate. Specimens 5O and 9O had gusset-plate-to-beam weld and gusset-plate clearance deficiencies, respectively, and both appeared to benefit from having continuous bolted connections.

3.5 Retrofit and Repair Evaluation

The tests of retrofitted and repaired NCBFs showed that the cyclic behavior of the frames was heavily influenced by brace type (OOP buckling, IP buckling, or buckling restrained), connection configuration, and severity of local deficiencies. Retrofits studied focused on improving the low deformation capacities of Specimens 1E, 2E, 3E, and TNCBF1-N-HSS

through either replacement or concrete in-fill of the existing brace and, in three cases, connection retrofit through bolt or weld reinforcement.

Brace-to-gusset-plate weld and brace local-slenderness deficiencies can be addressed by replacing the brace. All of the retrofitted buckling-brace specimens used demand critical brace-to-gusset welds sized for the brace yield force to preclude weld fracture. Specimen 8I demonstrated that an HSS brace which was not compliant with local slenderness requirements (λ/λ_{hd} of 1.21) developed a 3.9% drift range when weld fracture occurred. Specimens with Type-D behavior (see Fig. 3.21d) had HSS braces with λ/λ_{hd} of 0.95 and achieved between 4.2 and 5.9% drift range capacity. These were substantial improvements over Specimens 2E and TNCBF1-N-HSS which had a locally slender brace (λ/λ_{hd} of 2.31) that fractured at 1.5 and 1.2% drift range, respectively. Concrete fill of the HSS7×7×1/4 brace in Specimen 2C-B with block outs to prevent concrete-gusset plate contact provided a 4.4% drift range prior to brace fracture despite an earlier gusset-to-beam weld fracture.

Frame deformation capacity is influenced by both the brace and the connection, as noted in SCBF research (Roeder et al. 2011b). Brace replacement and concrete in-fill directly address the deformation capacity of the brace and new braces may be sized to reduce the vulnerability of some connection limit states, as partially examined with the BRB retrofits where connection fracture was delayed until BRB strain-hardening developed. Gusset-plate yielding was not detrimental to retrofit performance, though based on Table 4, many of the specimens would have been considered deficient using a 30° Whitmore angle (CDP). The 37° Whitmore angle (BDP) is less conservative and may provide important deformation capacity through yielding of the gusset plate. More critically, the experiments showed that the most common cause of strength degradation, gusset-plate horizontal and vertical interface weld fracture, is primarily driven by gusset-plate strength and deformation. This typically occurred at the gusset-plate-to-beam weld, which did not meet demand critical minimum toughness requirements. The BDP method was consistently reliable in evaluating these welds, while the CDP method typically provided unreliable predictions as shown by comparing failure modes to the DCRs in the single-diagonal test program in Table 3.3. Ex-

cluding Specimens 1E, 2E, and 9O and based on a DCR greater than 0.75 (the connections resistance factor) for positive identification of weld fracture, the BDP DCR predicted weld fracture with 80% accuracy (1 false positive and 2 false negatives), while the CDP DCR had 47% accuracy (0 false positives and 8 false negatives). In other words, the CDP DCRs indicated that 8 specimens had adequate welds which still fractured. Considering the 1.25 factor for nonuniform stress distributions with the UFM (AISC 2017d) only marginally improves these statistics for the CDP: 2 additional specimens would have welds that would barely be undersized. This discrepancy is attributable to the presence of deformation demands not accounted for in the UFM-derived demands, whereas the BDP methodology ensures that the welds develop the yield capacity of the gusset plate. Specimens with IP buckling or BRB retrofits tended to have gusset-to-frame weld fracture at higher drift ranges than their OOP-buckling retrofit counterparts since OOP deformation demands were mitigated.

Connections with inadequate gusset-plate clearance by the $8t_p$ elliptical clearance model tended to have gusset-to-beam or shear plate-to-gusset and -beam weld fracture at lower drift ranges. Specimen 9O, which had integrated gusset-shear plate connections with no elliptical clearance, was a notable exception, because significant rotation developed in other parts of the connection that may not be possible with most building connections. However, retrofits should seek to develop end rotation clearance approaching the $8t_p$ elliptical clearance model (Lehman et al. 2008), and this is especially important for fillet-welded gusset-plate connections.

In gusset-plate connections with bolted vertical-interface and welded horizontal-interface connections, bolt fracture was not common even when the DCRs exceeded 1, because bolt-hole elongation or local deformation associated with prying action contributed to significant inelastic deformation. Connections that are conservatively designed with respect to bolt bearing and prying may result in different end results. Bolt fracture was noted in Specimen 5BR (drift range of 4.9%) due to the high gusset-plate BFRR (2.4), which prevented bolt-hole elongation. Welded connections are stiff and cannot support deformation other than through yielding of the gusset plates. With low filler-metal toughness, weld cracking can

lead to fracture at small deformations.

IP-buckling and BRB retrofit schemes have design and construction challenges that OOP-buckling retrofits do not have. Retrofit or repair with IP-buckling braces requires careful consideration of the OOP end-rotational restraint, especially with square HSS braces and in the chevron configuration with relatively weak beams. Brace cross sections with a smaller radius of gyration for IP buckling may be necessary due to the uncertainty in quantifying connection stiffness. In Specimens 2Ib and 8I, HSS6×4×3/8 braces were designed such that the IP critical buckling load (using brace end-to-end length and K of 1) was less than the OOP critical buckling load (using knife plate end-to-end length and K of 1), and IP buckling was achieved.

BRBs develop significant strain-hardening that causes local beam and column damage. Web doubler plates to beams and columns mitigate this local damage, which can adversely affect the deformation capacity of the system as seen in Specimens 5BR and 8BR. Even with this damage, the drift range capacity of BRBs may exceed that of a comparable retrofit with OOP-buckling braces when connections have excessive DCRs by the BDP for the gusset-plate-interface welds because OOP bending demands are reduced. Specimens 8O and 8BR had DCRs of 1.6 for the BDP and reached drift ranges of 2.9 and 4.5%, respectively, prior to gusset-to-beam weld fracture.

3.6 Retrofit Priority

The observed failure hierarchies provide the basis for a retrofit priority for NCBFs. Table 3.10 summarizes retrofit priorities for different yielding mechanisms, failure modes, and geometric limits evaluated in the experimental research program. These priorities are based on DCRs which have been computed using measured material properties and are therefore comparable to those which could be computed in practice using expected material properties. Consistent with earlier calculations in this chapter, the DCRs do not include resistance factors. Three levels of retrofit priority are defined as follows:

Table 3.10: Retrofit Priority Summary

Criterion	Low	Moderate	High
Yielding mechanisms			
Whitmore yielding (30°)	DCR $\leq$ 1.3	(DCR $>$ 1.3)	
Chevron beam yielding	DCR $\leq$ 2.3	(DCR $>$ 2.3)	
Failure modes			
Brace-to-gusset-plate weld fracture	DCR $\leq$ 0.8	0.8 $<$ DCR $\leq$ 1.0	DCR $>$ 1.0
Gusset-plate interface weld fracture (BDP)	DCR $\leq$ 0.9	0.9 $<$ DCR $\leq$ 1.5	DCR $>$ 1.5
Shear-plate bolt fracture with BFRR $>$ 1.2 (UFM)	DCR $\leq$ 1.0	DCR $>$ 1.0	–
Shear-plate bolt fracture with BFRR $\leq$ 1.2 (UFM)	DCR $\leq$ 1.4	DCR $>$ 1.4	–
Geometric limits			
Rectangular HSS brace local slenderness	$\lambda/\lambda_{hd} \leq 1.2$	$1.2 < \lambda/\lambda_{hd} \leq 1.6$	$\lambda/\lambda_{hd} > 1.6$
Gusset-plate elliptical clearance	$Nt_p \geq 4t_p$	$4t_p > Nt_p \geq 2t_p$	$Nt_p < 2t_p$

Note: Expressions in parentheses indicate uncertainty in threshold between moderate and high priority since these values were not tested.

1. High priority deficiencies severely limit deformation capacity (typically to less than 2.0% drift range) and are recommended to be addressed in a minimum retrofit.

2. Moderate priority deficiencies can lead to failure modes that preclude fracture of ductile braces, but deformation capacity between 2.0 and 4.0% drift range is possible. Such deficiencies may be addressed in a retrofit seeking to provide a higher level of performance.

3. Low priority deficiencies do not significantly inhibit performance and greater than 4.0% drift range can likely be sustained without direct retrofit.

Chapter 4

DEVELOPMENT OF COMPONENT MODELING APPROACHES FOR NONLINEAR ANALYSIS

Experimental research on NCBFs has confirmed that their braces and connections are susceptible to a variety of premature failure modes which can limit ductility and potentially compromise stability. These failure modes can be mitigated in retrofit to provide improved behavior that is similar to SCBFs in some cases. Yet, the impacts of these deficiencies and retrofits remain unclear due to the limited modeling tools available to researchers and practicing engineers. In this chapter, modeling approaches for nonlinear analysis of CBFs are developed which can simulate the complex sequence of yielding and failure observed in experimental studies. These approaches enable seismic performance evaluation of existing and retrofitted NCBFs presented in subsequent chapters. The specific phenomena simulated by the proposed models include (1) fracture of rectangular of HSS braces with a wide range of local slenderness ratios and alternative load histories, (2) connection yielding and fracture models for different limit states, (3) beam yielding in the chevron configuration, and (4) column buckling. Model development and recommendations are discussed for each and then validated using two, two-story chevron NCBF experiments to demonstrate their adequacy.

This chapter is adapted from a journal article in preparation by the author: Sen et al. (2018).

4.1 Previously Developed Modeling Approaches for Nonlinear Analysis

Modeling approaches for nonlinear analysis of CBFs are provided in *ASCE/SEI 41-17* but focus almost entirely on the brace, which is modeled as an axial spring, as shown in Fig. 4.1a, with simplified behavior like that of the Type B backbone curve introduced in Figs. 3.19a

and 3.21a. In typical practice, the brace and beam ends would be modeled as pins and flexural yielding of the columns would be simulated using nonlinear rotational springs (again, with simplified behavior like that of Type B). This approach is depicted in Fig. 4.1a and significantly underestimates the strength and stiffness of the system (Hsiao et al. 2012). Further, *ASCE/SEI 41-17* requires brace connection limit states, which are known to be commonly deficient in NCBFs, to be analyzed as force-controlled actions unless explicit modeling approaches are implemented and the inelastic behavior is stable and ductile. Force-controlled actions have unacceptable performance if the demand computed from analysis exceeds the lower-bound strength of the component. However, deficiencies which are yielding mechanisms are not usually detrimental to system behavior and the development of a localized failure mode in the brace or connection does not constitute failure of the entire system. Thus, NCBF performance may be judged too severely without explicit nonlinear modeling.

More accurate nonlinear analysis modeling approaches have been well established for SCBFs for research applications (Hsiao et al. 2012; Uriz and Mahin 2004; Hsiao et al. 2013a; Karamanci and Lignos 2014; Tirca and Chen 2014). These approaches are have been implemented in *OpenSees* (McKenna et al. 2010) and employ a combination of fiber-based beam-column elements and rotational springs to simulate the intended SCBF yielding and failure hierarchy. The specific approach by Hsiao et al. (2012, 2013a), which is extended to NCBFs and other lower-ductility CBFs in this chapter, has the following characteristics:

- Beams and columns are modeled with a single force-based nonlinear beam-column element between work points with five (5) integration points per element,

- Braces are discretized with 16 elements between work points with four (4) integration points per element and given an initial sinusoidal imperfection with an apex of $L/500$,

- Braces, beams, and columns, have rigid offsets to account for connection geometry, including 75% of the gusset-beam connection length and the full gusset-column connection length, and

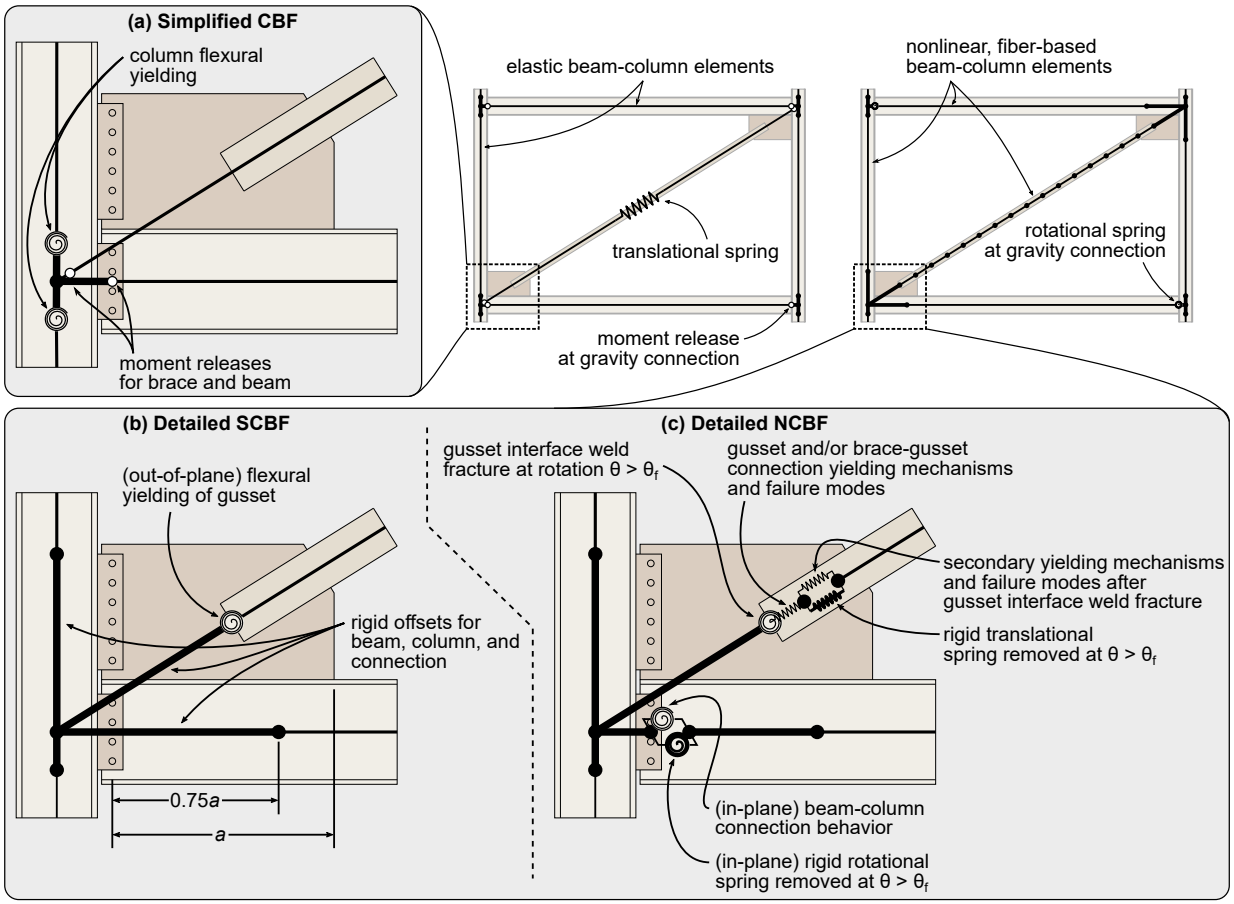

Figure 4.1: Nonlinear analysis approaches for CBFs

- Gusset plates are modeled with nonlinear springs in the rotational degree of freedom normal (out-of-plane) to the direction of buckling with rotational stiffness and moment capacity calculated using the yield strength, plates thickness, Whitmore width, and length.

The response of each line element (braces, beams, and columns) is obtained using fiber sections representing the initial cross-sectional shape of the member. Individual steel fibers are modeled with the Steel02 (Giuffré-Menegotto-Pinto) material (Menegotto and Pinto 1973; Filippou et al. 1983) The Type D behavior depicted in Fig. 3.21 can be simulated well for SCBFs, where the L2 failure mode is delayed brace fracture (following the intended yield-

ing and failure hierarchy). This is accomplished computationally with material "wrappers" which monitor strain history in the underlying material and initiate fracture of individual brace fibers based on either the maximum strain range (MSR) between tension and compression (Hsiao et al. 2013a) or a low-cycle fatigue (LCF) model (Uriz and Mahin 2004). When the fracture criterion is reached, the strength and stiffness of the fiber is reduced by the wrapper to nearly zero; conceptually, the fiber is removed from the section at that location, and the progressive fracture of the fibers leads to complete brace fracture.

To illustrate the effectiveness of the approach by Hsiao et al. (2012), two experiments of retrofitted NCBFs, Specimens 4O-W and 8O-W, were numerically simulated (these specimens are described in Sen et al. (2017)). Each consisted of a single diagonal braced bay, as shown in Fig. 4.2c. The corresponding OpenSees model for these systems are shown in Fig. 4.2d. The frames were theoretically retrofitted using a two-part scheme where (1) the brace was replaced with one that meets highly ductile local slenderness requirements and (2) the gusset-plate interface welds were reinforced with demand critical weld materials to produce sufficient combined thickenss to develop the tensile capacity of the gusset plate. The failure mode in each was delayed brace fracture, an L2 failure mode which is simulated using the MSR approach by Hsiao et al. (2013a) using experimentally calibrated MSR values at fracture (MSR_f). Figure 4.3 shows that the models approximate the global behavior of the specimens well both before and after brace fracture occurs.

While SCBFs and NCBFs with Type D behavior can be simulated using existing modeling approaches, research on advanced computational modeling of NCBFs with other behavior types has been comparatively sparse. Following *ASCE/SEI 41-17*, practicing engineers are permitted to consider the effects of NCBF deficiencies in post-analysis evaluation rather than through explicit modeling; researchers have employed this approach to evaluate fracture of HSS braces with and without concrete infill (Simpson and Mahin 2018) and brace connections Balazadeh-Minouei et al. (2017); **?**. Others have modeled NCBF deficiencies and retrofit strategies to better understand their implications on system behavior. For example, Rai and Goel (2003) analyzed a four-story NCBF damaged in the 1994 Northridge Earthquake using

SNAP-2DX (Rai et al. 1996) and simulated fracture of existing HSS braces with and without concrete infill. The improved fracture life resulting from the concrete fill was modeled using an equivalent (reduced) local slenderness ratio (Lee 1988) as an input parameter in a low-cycle fatigue model calibrated for hollow HSS braces (Tang and Goel 1987). More recently, Hsiao et al. (2014) and Sizemore et al. (2017) modeled CBFs in *OpenSees* with brace-to-gusset weld fracture using a nonlinear axial spring that fractures when the weld strength is exceeded. These explicit modeling approaches provide a basis for simulating NCBFs, but given the variety in both possible deficiencies and behavior types, there is a clear need for new modeling approaches which can be used to evaluate seismic performance beyond initial failure modes.

4.2 Brace Fracture Simulation

Brace fracture is an L2 failure type and the anticipated failure mode for SCBFs and NCBFs which do not have severe connection and system deficiencies. Under reversed cyclic loading characteristic of far-field earthqaukes, brace fracture is driven by (1) local deformation of the cross section (local cupping in HSS braces) associated with incompatibility between the undeformed cross-sectional shape and the large curvature demands at the plastic hinge location in compression and (2) subsequent axial deformation demand in tension. Slender cross sections (high b/t in HSS) develop this local post-buckling deformation at smaller deformations resulting in reduced fracture life. SCBFs delay this behavior by employing stockier cross sections which meet highly ductile member requirements of the *Seismic Provisions* (AISC 2017a). Fiber-based beam-column elements do not simulate this behavior, and hence calibration of the fracture criterion is required. Previously proposed brace-fracture models (e.g., Hsiao et al. (2013a), Karamanci and Lignos (2014), Tirca and Chen (2014)) are calibrated from non-dimensionalized geometric and material parameters: local slenderness ratio (b/t), global slenderness ratio ($L_c/r = KL/r$), and elastic-modulus-to-yield-stress ratio (E/F_y). This work focuses on fracture of rectangular HSS braces due to their popularity in construction and availability of test data; for research on round HSS and wide-flange sections, the

reader is referred to Karamanci and Lignos (2014), which uses the LCF approach proposed by Uriz and Mahin (2004).

As discussed in the literature review in Chapter 2, Hsiao et al. (2013a) proposed the following MSR_f prediction equation for rectangular HSS:

$$MSR_{f,force} = 0.1435 \left(\frac{b}{t}\right)^{-0.4} \left(\frac{L_c}{r}\right)^{-0.3} \left(\frac{E}{F_y}\right)^{0.2} \tag{4.1}$$

The value predicted by Eq. 4.1 is denoted $MSR_{f,force}$ herein because it was calibrated using force-based beam-column elements (FBEs). While Eq. 4.1 works well, particularly for SCBFs, several factors necessitated improvement of the MSR-based fracture criteria to simulate all CBFs:

- Displacement-based beam-column elements (DBEs) may be preferred for brace modeling since large, sudden changes in strength and stiffness due to buckling and fracture can be solved at the global level; in *OpenSees*, this allows for the use of more robust solution algorithms in comparison to FBEs., which were used in prior work by Hsiao et al. (2013a).

- Recent experimental research on chevron CBFs shows that brace fracture life is longer under reversed cyclic loading when the brace axial deformation demand in tension is limited, even if axial deformation in compression is large (Terpstra 2017). In chevron CBFs, this asymmetry in demand is attributed to beam deflection resulting from the unbalanced brace loads in tension versus compression, but similar effects exist in other bracing configurations when drift demand is asymmetric. This load-direction is not accounted for by existing modeling approaches and is incorporated into the MSR_f expression with a brace axial deformation ratio term.

- Additional experimental data is available for calibration that was not used in prior work, including data collected from tests with high-b/t rectangular HSS braces common to NCBFs and concrete-filled rectangular HSS braces which may be used in retrofit.

These issues are addressed through new brace fracture models based on the MSR approach by Hsiao et al. (2013a). Note that the brace fracture model in Eq. 4.1 and others proposed in this paper are sensitive to element type (displacement- or force-based), fiber discretization, element discretization, and steel constitutive model parameters and hysteretic rules. These properties are held constant in this study, where the element type is specified for each prediction equation, the brace section is discretized with four (4) fiber layers through the wall thickness and four (4) fiber layers along the wall flats and corners (128 total fibers), the brace length is discretized with 16 elements with four (4) integration points per element, and the *Steel02* material model in *OpenSees* is used with 1% kinematic strain hardening (R_0 of 15, cR_1 of 0.925, and cR_2 of 0.15). Using these models with different element types, discretization schemes, or material properties will not result in the same simulated brace fracture life and requires recalibration of the MSR_f. Table 4.1 provides the data used to calibrate the brace fracture models presented here.

4.2.1 Maximum Strain Range and Load History Effects

Equation 4.2 was developed to provide a new MSR_f prediction equation for rectangular HSS braces modeled with the approach described above, termed $MSR_{f,disp}$. In contrast to the previous MSR_f prediction equation proposed by Hsiao et al. (2013a) for FBEs (Eq. 2.31), this equation includes a term for brace axial deformation ratio and is calibrated from an expanded data set which includes 17 additional tests (59 total tests as documented in Table 4.1) of rectangular HSS braces from Lee (1988), Liu and Goel (1988), Sen et al. (2017, 2016a), and Richard (2009). The constant and variable coefficients (exponents in Eq. 4.2) were determined through linear regression of the data in logarithmic space ($R^2 = 0.72$). This data set includes a higher proportion of test data from braces with b/t ratios which exceed the highly ductile local slenderness ratio limit, λ_{hd}, than included in Hsiao et al. (2013a)

(37% versus 26%).

$$MSR_{f,disp} = 0.554 \left(\frac{b}{t}\right)^{-0.75} \left(\frac{L_c}{r}\right)^{-0.47} \left(\frac{E}{F_y}\right)^{0.21} \left(\frac{\delta_{c,max}}{\delta_{t,max}}\right)^{0.068} \tag{4.2}$$

Equation 4.2 also contains an additional term, $\delta_{c,max}/\delta_{t,max}$, which quantifies the brace load-direction bias as a ratio of the maximum global brace deformations recorded in compression and tension ($\delta_{c,max}$ and $\delta_{t,max}$, respectively). To compute the prediction equation, $\delta_{c,max}/\delta_{t,max}$ is calculated for each experiment simulation in *OpenSees* (as opposed to the measured value) when fracture occurs. Strain (and hence MSR_f) is a local measure, but axial brace deformation is considered here to avoid increasing the importance of the computed strain from fiber-based line-element models, where important local effects such as cupping are not simulated.

In Eq. 4.2, a larger $\delta_{c,max}/\delta_{t,max}$ ratio results in a larger $MSR_{f,disp}$ value. Figure 4.4 illustrates this load-history effect using Specimens Lee-6 and Lee-7 from (Lee 1988), which were brace-only tests as shown in Figs. Xa and Xb. These specimens were nominally identical with HSS4×4×1/4 braces with a 3.3-m end-to-end brace length loaded with different displacement histories characteristic of chevron CBFs with yielding beams. Deflection of the beam in this configuration limits tensile elongation and increases compressive shortening of the brace, which results in $\delta_{c,max}/\delta_{t,max}$ greater than unity, even if drift demand is symmetric. Specimens Lee-6 and Lee-7 had $\delta_{c,max}/\delta_{t,max}$ ratios of 12.4 and 4.92, respectively (see Fig. 4.4c). Specimen Lee-6 achieved a larger axial deformation range prior to fracture, corresponding to a larger MSR_f value (0.0550 versus 0.0479).

Unlike other parameters of $MSR_{f,disp}$, $\delta_{c,max}/\delta_{t,max}$ is not known *a priori*; instead, $\delta_{c,max}/\delta_{t,max}$ varies with time under reversed cyclic loading, as shown in Fig. 4.4c for Specimens Lee-6 and Lee-7. Consequently, $MSR_{f,disp}$ also varies with time and thus requires a specific computational implementation. In *OpenSees*, this is accomplished with the *MaxStrainRange* material wrapper. The source code for this material is provided in Appendix B. Tags of the brace end nodes can be passed to the *MaxStrainRange* material, allowing the

material to compute global deformation from the nodal coordinates and update $\delta_{c,max}/\delta_{t,max}$ and MSR_f at each step of the analysis.

4.2.2 Concrete-Filled Braces

In-filling locally slender HSS braces with concrete is an effective method for improving brace fracture life and presents an attractive seismic retrofit scheme for NCBFs (Liu and Goel 1988; Sen et al. 2017). To be effective, the concrete should delay strain concentration in the plastic hinge region of the brace in compression by preventing inward cupping of the brace wall, leading to a less severe outward deformation mode. This beneficial phenomenon has been observed in experiments of HSS braces designed to act either as composite or non-composite members. In composite HSS braces, the concrete fills the full length of the brace and increases its critical buckling load. If the concrete is blocked out just before the gusset plate region, the member is non-composite, as the concrete does not stiffen or strengthen the brace; this is advantageous in seismic retrofit since the brace demands on the connections, which are often vulnerable, would not be increased.

Steel-concrete composite action can be numerically simulated by including concrete fibers in the interior of the steel tube. In this work, a 4-by-4 grid of concrete fibers is used as in Fig. 4.5, matching the mesh length for the steel tube fibers. Using this formulation, the concrete is perfectly composite (perfect bond with no relative movement) with the steel. The concrete is modeled using *Concrete02* with very small tensile strength and stiffness to aid convergence. Unlike recommendations for modeling concrete-filled tubes subjected to lateral loads (e.g., Stephens et al. (2018)), the concrete strength deteriorates in compression after the peak compressive stress as shown in Fig. 4.5. Total strength degradation occurs at $10\varepsilon_{c0}$, where ε_{c0} is the strain at peak compressive stress defined as $(f'_c)^{1/4}/1150$ for f'_c in MPa (Chang and Mander 1994). This strength degradation is necessary to increase the tensile reloading stiffness of the brace after buckling; without degradation, the concrete will retain significant compressive stress until the brace has fully straightened. Using the concrete model in Fig. 4.5, the concrete fill primarily contributes to the initial buckling load of the

brace but does not signioficantly increase the post-buckling strength, which is consistent with experimental results.

Non-composite braces require no alteration to the fiber section. In both composite and non-composite cases, the improved fracture life attained with the concrete fill is accounted for with the MSR_f prediction equation given by Eq. 4.3, which is intended for use with displacement-based elements and denoted $MSR_{f,conc}$. This constant-$MSR_{f,conc}$ model was calibrated using numerical simulations of ten experiments with concrete-filled braces (specimens marked with superscript "a" in Table 4.1), and the constant value is the geometric mean of the calibrated $MSR_{f,conc}$ values. Linear models were considered using combinations of the same nondimensionalized parameters as in Eqs. 2.31 and 4.2, but correlation between the parameters and calibrated $MSR_{f,conc}$ values was not statistically significant. Note that the constant $MSR_{f,conc}$ value in Eq. 4.3 must be larger than the corresponding $MSR_{f,disp}$ for the bare steel tube, since a decrease in MSR_f due to concrete in-fill is not logical.

$$MSR_{f,conc} = 0.0505 \geq MSR_{f,disp} \tag{4.3}$$

Figures 4.5a and 4.5 show the effects of concrete in-fill using Specimens Liu-T633H and Liu-T633C6 from Liu and Goel (1988), which were brace-only experiments, as depicted in Fig. 4.2a. The specimens were nominally identical with HSS6×3×3/16 braces and the same load histories prior to fracture of the hollow brace specimen. The concrete-filled brace (Specimen Liu-T633C6) was designed to be composite using concrete with a specified compressive strength of 41.4 MPa (6 ksi). Comparing both Figs. 4.5a and 4.5b, the compressive strength, deformation range, and calibrated $MSR_{f,conc}$ of the composite brace are larger than those of the hollow brace. The additional compressive strength due to composite action is also simulated using the fiber model approach described above.

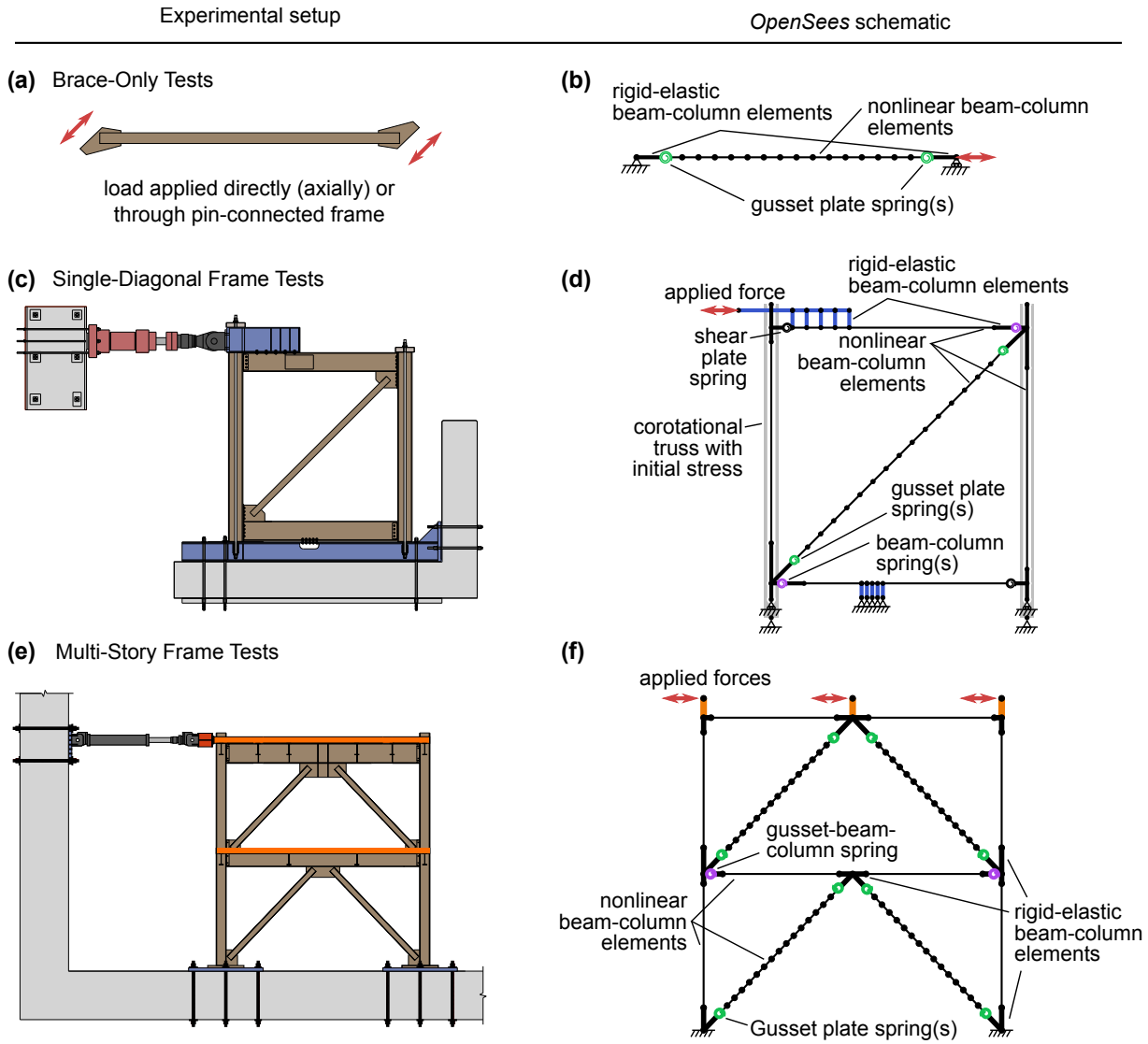

Figure 4.2: Experimental setup and corresponding *OpenSees* modeling approach for various experimental research programs

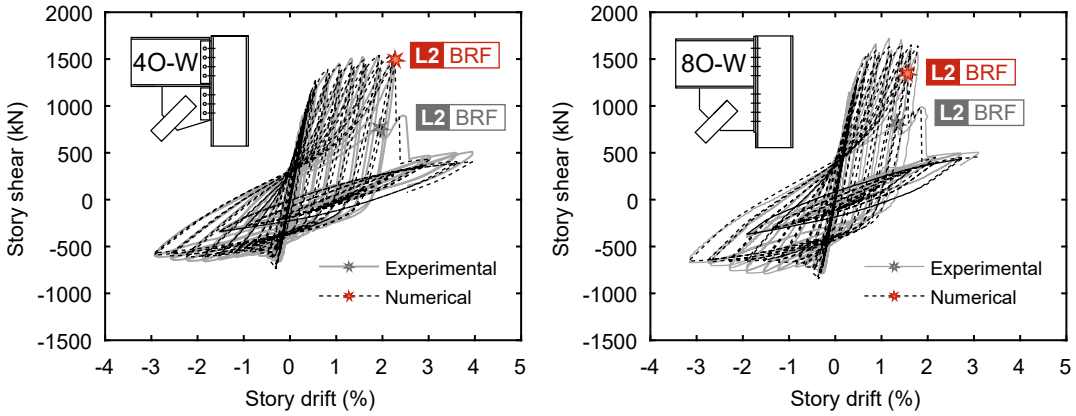

Figure 4.3: Comparison of experimental and numerical global behavior

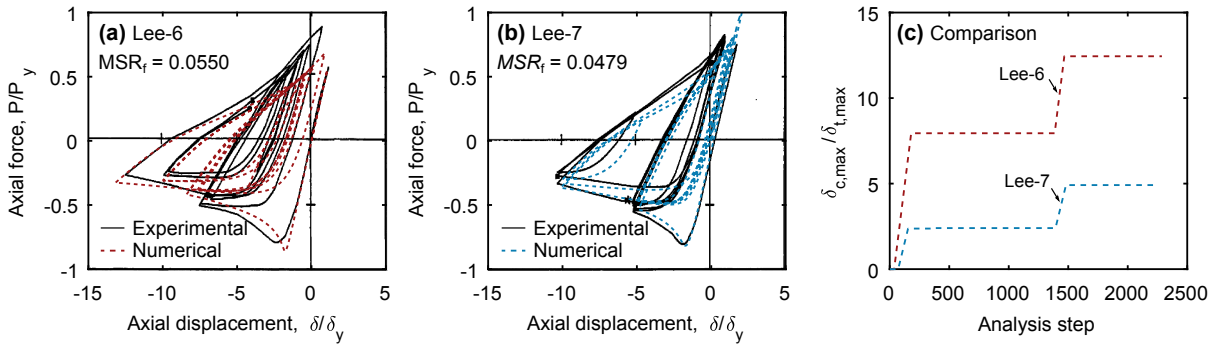

Figure 4.4: Experimental and numerical brace hysteretic response of specimens with (a) high $\delta_{c,max}/\delta_{t,max}$ ratio loading and (b) moderate $\delta_{c,max}/\delta_{t,max}$; (c) evolution of $\delta_{c,max}/\delta_{t,max}$ for each specimen

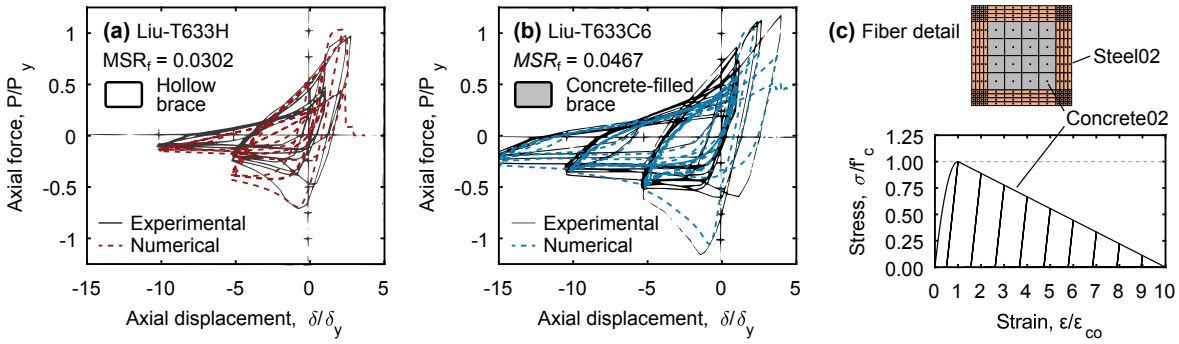

Figure 4.5: Experimental and numerical brace hysteretic response of specimens with (a) hollow and (b) concrete-filled braces; (c) modeling of composite fiber section and concrete material (not to scale)

Table 4.1: Rectangular HSS Brace Test Data

Reference	Specimen	Brace	Grade	b/t	L_c/r	E/F_y	$\delta_{c,max}/\delta_{t,max}$	δ_{range} (%)	$MSR_{f,disp}$
Johnson (2005)	HSS2	HSS5×5×3/8	A500	11.3	79	414	1.26	3.18	0.0387
	HSS3	HSS5×5×3/8	A500	11.3	82	414	1.84	3.91	0.0412
	HSS4	HSS5×5×3/8	A500	11.3	81	396	1.58	3.88	0.0425
	HSS5	HSS5×5×3/8	A500	11.3	82	396	1.80	4.41	0.0442
Herman (2007)	HSS6	HSS5×5×3/8	A500	11.3	81	448	1.65	4.04	0.0421
	HSS7	HSS5×5×3/8	A500	11.3	72	448	1.99	3.50	0.0438
	HSS8	HSS5×5×3/8	A500	11.3	83	448	1.06	4.10	0.0422
	HSS9	HSS5×5×3/8	A500	11.3	79	448	1.79	3.28	0.0350
	HSS10	HSS5×5×3/8	A500	11.3	79	441	1.25	3.84	0.0399
	HSS11	HSS5×5×3/8	A500	11.3	69	441	1.32	2.51	0.0324
Kotulka (2007)	HSS12	HSS5×5×3/8	A500	11.3	71	441	2.15	3.27	0.0421
	HSS13	HSS5×5×3/8	A500	11.3	79	441	1.03	3.42	0.0387
	HSS14	HSS5×5×3/8	A500	11.3	82	441	0.88	3.66	0.0410
	HSS15	HSS5×5×3/8	A500	11.3	84	441	1.08	3.52	0.0380
Powell (2010)	HSS17	HSS5×5×3/8	A500	11.3	82	441	1.20	4.24	0.0414
	HSS24	HSS5×5×3/8	A500	11.3	82	448	1.18	3.69	0.0377
	HSS25	HSS5×5×3/8	A500	11.3	69	448	2.72	3.15	0.0401
Clark (2009)	TCBF1-1	HSS125×125×9	A500	10.9	55	451	0.88	3.00	0.0683
	TCBF1-3	HSS125×125×9	A500	10.9	70	451	0.88	3.76	0.0556
Lumpkin (2009)	TCBF2-1	HSS5×5×3/8	A500	11.3	66	435	1.66	2.83	0.0553
Fell et al. (2009)	Kanvinde-1	HSS4×4×1/4	A500	14.2	62	433	0.98	2.76	0.0509
	Kanvinde-2	HSS4×4×1/4	A500	14.2	62	433	3.01	4.03	0.0555
	Kanvinde-4	HSS4×4×3/8	A500	8.5	64	403	1.00	5.09	0.0694
Yang and Mahin (2005)	Yang-4	HSS6×6×3/8	A500	14.2	39	479	0.34	2.20	0.0527
	Yang-5	HSS6×6×3/8	A500	14.2	39	479	0.96	2.55	0.0560

[a]Concrete-filled brace

Continued on next page

Reference	Specimen	Brace	Grade	b/t	L_c/r	E/F_y	$\delta_{c,max}/\delta_{t,max}$	δ_{range} (%)	$MSR_{f,disp}$
Uriz and Mahin (2008)	Uriz-SCBF-1	HSS6×6×3/8	A500	14.2	46	479	1.34	2.98	0.0590
Shaback and Brown (2003)	Shaback-1B	RHS127×127×8.0	G40.21-350W	12.9	52	475	1.94	3.08	0.0552
	Shaback-2A	RHS152×152×8.0	G40.21-350W	16.0	52	452	1.56	2.15	0.0458
	Shaback-2B	RHS152×152×9.5	G40.21-350W	13.0	51	452	1.94	2.51	0.0491
	Shaback-3A	RHS127×127×6.4	G40.21-350W	16.8	63	434	2.89	2.29	0.0437
	Shaback-3B	RHS127×127×8.0	G40.21-350W	12.9	63	475	1.73	2.29	0.0410
	Shaback-3C	RHS127×127×9.5	G40.21-350W	10.4	60	434	2.79	3.00	0.0492
	Shaback-4A	RHS152×152×8.0	G40.21-350W	16.0	62	452	2.57	2.15	0.0407
	Shaback-4B	RHS152×152×9.5	G40.21-350W	13.0	58	452	3.02	2.48	0.0463
Han et al. (2007)	Han-S77-28	HSS100×100×3.2	SPSR400	28.3	71	507	0.98	0.80	0.0213
Lee (1988)	Lee-1	RHS5×5×0.188	A500	25.7	64	469	2.43	0.89	0.0283
	Lee-2	RHS5×5×0.188	A500	25.7	32	465	2.53	0.95	0.0304
	Lee-4	RHS4×4×0.125	A500	31.5	78	500	5.44	1.18	0.0330
	Lee-5	RHS4×4×0.250	A500	14.2	80	392	11.73	2.71	0.0477
	Lee-6	RHS4×4×0.250	A500	14.2	43	392	12.44	1.86	0.0550
	Lee-7	RHS4×4×0.250	A500	14.2	43	392	4.92	1.59	0.0479
	Lee-8[a]	RHS5×5×0.188	A500	25.7	32	465	5.34	1.61	0.0440
	Lee-9[a]	RHS4×4×0.125	A500	31.5	41	500	7.67	1.20	0.0505
	Lee-10[a]	RHS4×4×0.125	A500	31.5	41	500	2.85	1.75	0.0500
	Lee-11[a]	RHS4×4×0.125	A500	31.5	41	509	13.93	1.84	0.0445
	Lee-12[a]	RHS4×4×0.250	A500	14.2	43	392	7.94	2.20	0.0680
	Lee-13[a]	RHS4×4×0.250	A500	14.2	43	509	7.67	2.20	0.0535
Liu and Goel (1987)	Liu-T633H	HSS6×3×3/16	A500	31.5	48	537	1.70	2.02	0.0302
	Liu-T633C6[a]	HSS6×3×3/16	A500	31.5	48	537	4.11	2.66	0.0536
	Liu-T633C4[a]	HSS6×3×3/16	A500	31.5	48	483	2.79	1.98	0.0525
	Liu-T424H	HSS4×2×1/4	A500	14.2	80	537	3.11	2.72	0.0464
	Liu-T424C6[a]	HSS4×2×1/4	A500	14.2	80	537	3.04	2.73	0.0485
	Liu-T422H	HSS4×2×1/8	A500	31.5	75	537	3.50	1.62	0.0240
Tremblay et al. (2003)	Tremblay-S3A	RHS76×76×4.8	G40.21-350W	12.8	147	514	1.00	2.73	0.0333

[a]Concrete-filled brace

Continued on next page

Reference	Specimen	Brace	Grade	b/t	L_c/r	E/F_y	$\delta_{c,max}/\delta_{t,max}$	δ_{range} (%)	$MSR_{f,disp}$
Sloat (2014)	NCBF-2E	HSS7×7×1/4	A500	27.0	59	450	2.16	0.63	0.0208
	NCBF-2C-B[a]	HSS7×7×1/4	A500	27.0	59	450	1.86	1.73	0.0436
Johnson (2014)	NCBF-3E	HSS6×6×1/4	A500	22.8	56	494	1.25	1.60	0.0237
	NCBF-5O	HSS5×5×3/8	A500	11.3	71	469	1.51	4.01	0.0423
Ballard (2015)	NCBF-8I	HSS6×4×3/8	A500	14.2	73	459	1.27	3.68	0.0388
Swatosh (2016)	NCBF-4O-W	HSS5×5×3/8	A500	11.3	81	503	1.19	4.31	0.0406
	NCBF-8O-W	HSS5×5×3/8	A500	11.3	80	430	1.63	4.13	0.0410
Sen (2014)	TNCBF1-N-HSS	HSS7×7×1/4	A500	27.0	52	451	1.46	1.20	0.0325
	TNCBF1-R-HSS	HSS5×5×3/8	A500	11.3	73	456	8.51	2.72	0.0485
	TNCBF2-D-HSS	HSS5×5×3/8	A500	11.3	73	456	5.48	2.67	0.0484
Ibarra (2018)	Chevron-5	HSS4×4×5/16	A500	10.7	84	453	11.99	3.67	0.0462
Richard (2009)	RHS4	HSS10×10×1/2	A500	18.5	43	504	0.99	2.09	0.0389
	RHS10	HSS10×10×3/8	A500	25.7	60	476	1.66	2.39	0.0234
	RHS12	HSS10×10×3/8	A500	25.7	43	466	1.00	1.30	0.0265
	RHS13	HSS10×10×5/16	A500	31.4	43	585	1.00	1.30	0.0245

[a]Concrete-filled brace

4.3 Gusset Plate Connection Simulation

Most of the observed variation in the behavior of NCBF and retrofitted NCBF specimens is attributed to yielding mechanisms and failure modes associated with the gusset plate connection. NCBFs are known to have a wide range of gusset plate connection configurations, particularly at the brace-beam-column intersection (i.e., corner gusset plates) (Sen et al. 2016b). For example, Fig. 3.21c shows four (4) corner gusset-plate connections, each eliciting different behavior types (Types A through D each with various sequences of limit-state types). The connection configuration itself does not determine the behavior type but it affects which limit states are present and hence which behavior types are possible. For instance, a connection without a yielding mechanism on the vertical interface would not be able to develop Type C behavior if the horizontal gusset-plate interface connection fractured (see Specimen 8O in Fig. 3.21c). On the other hand, if the vertical interface was a bolted connection with the potential for bolt-hole elongation (e.g., $BFRR \leq 1.2$), a secondary yielding mechanism could develop after gusset-to-beam weld fracture to result in Type C behavior (see Specimen 6O in Fig. 3.21c). The modeling approach is therefore dependent upon an intact load path and the yielding mechanisms and failure modes that control connection behavior.

This section provides a framework for modeling gusset plate connections with the capability of producing any of the behavior types shown in Fig. 3.21. These behavior types are simulated here through specific consideration of the gusset plate axial yielding, brace-to-gusset weld fracture, and gusset plate interface weld fracture limit states, but it is possible to extend the framework to model other limit states if their component response can be rationally predicted.

4.3.1 Gusset-Plate Yielding

Gusset-plate axial yielding in tension is generally a beneficial yielding mechanism which can increase the drift capacity of CBFs. If a gusset plate yields in tension, inelastic deformation

demand is shared between the brace and plate, reducing demands on the brace and delaying brace fracture. Encouraging this mechanism just after brace tensile yielding in SCBFs is one of the central components of the BDP, which recommends the use of the expected yield stress of the plate and a balance factor (analogous to a resistance factor) of one for evaluating yielding of the Whitmore section (Roeder et al. 2011b). As indicated previously, tensile yielding of the gusset plate is simulated using an axial spring in the direction of the brace (Fig. 3c). This section describes how to determine the strength, stiffness and fracture of this axial spring model.

Using the BDP, the demand-to-capacity ratio (DCR) for gusset-plate yielding would be equal to one (1) using Eq. 4.4. In NCBFs, gusset-plate yielding may also occur since connections were not required to be designed for the expected strength of the brace in tension, the numerator in Eq. 4.4. If this DCR is greater than one, gusset-plate yielding controls the strength and the capacity of brace in tension cannot be developed, reducing the overall strength of the system.

$$DCR_{gpy} = \frac{(R_y F_y)_{br} A_g}{(R_y F_y)_p B_w t_p} \tag{4.4}$$

The axial behavior of the gusset plate can be approximated using the Whitmore section and length, where the strength and stiffness is approximated using Equations 4.5 and 4.6. Note that this geometry, shown in Fig. 4.6b, is used by Hsiao et al. (2012) to model the flexural strength and stiffness of the plate. The Whitmore length, L_{avg}, is the average of L_1, L_2, and L_3, where any of the individual lengths are negative if the Whitmore width extends beyond the gusset plate (e.g., the magnitude of L_3 would be negative in Fig. 4.6b).

$$P_y = (R_y F_y)_p B_w t_p \tag{4.5}$$

$$K = \frac{E B_w t_p}{L_{avg}} \tag{4.6}$$

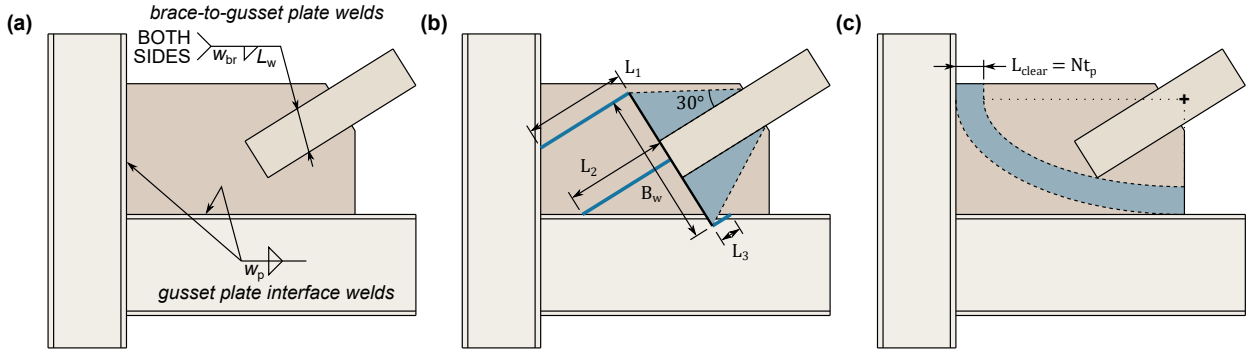

Figure 4.6: Gusset plate (a) weld details, (b) Whitmore width and length geometry, and (c) elliptical clearance geometry

This model for gusset-plate axial yielding was implemented in *OpenSees* using an axial spring in line with the brace (see Fig. 3c) with force-displacement behavior defined by the *Steel02* uniaxial material model. A kinematic strain-hardening ratio of 0.2% is recommended because it gave the most accurate computational simulation of the available experimental specimens. This axial spring can be used within the same zero-length element as the gusset plate's flexural spring.

Figure 4.7 shows an implementation of this model using Specimen 2O from Sen et al. (2017), where the gusset plate had a Whitmore yielding DCR of 1.3. Specimen 2O was a one-story, one-bay NCBF witha single diagonal brace as shown in Fig. 4.2c and modeled in Fig. 4.2d. In Fig. 4.7a, the gusset-plate yielding model is not implemented in the numerical simulation, and the lateral resistance of the system is overestimated. Results from the numerical simulation with the proposed model are shown in Fig. 4.7b, and Fig. 4.7c indicates that the spring yielded and elongated to approximately 7 mm, a large but reasonable deformation for the gusset plate. The failure mode of Specimen 2O was gusset-plate interface weld fracture, and simulation of this failure mode is described below.

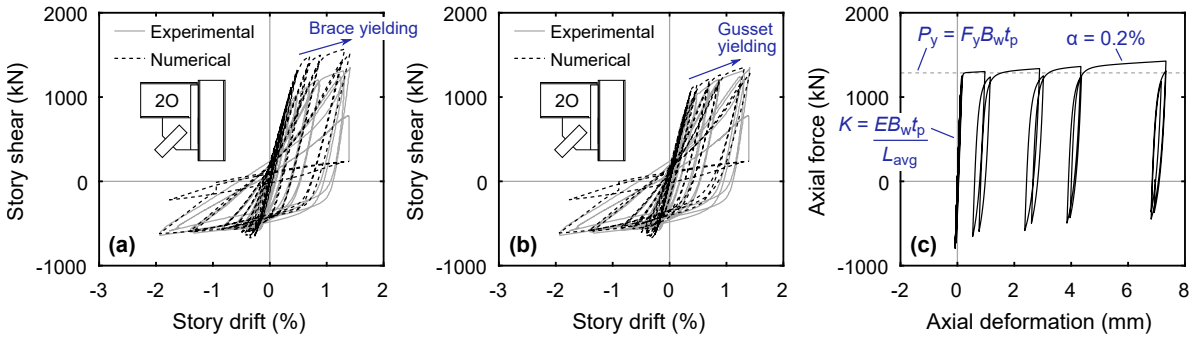

Figure 4.7: Experimental and numerical frame response of Specimen 2O (a) without and (b) with the gusset-plate yielding model; (c) response of corresponding gusset-plate axial spring

4.3.2 Brace-to-Gusset-Plate Weld Fracture

Fracture of the brace-to-gusset-plate welded joint is considered an L2 failure type since the brace load path is lost. Using HSS braces, the brace is most often slotted and connected to the gusset plate four longitudinal fillet welds of leg size w_{br} and length L_w (see Fig. 4.6). Consequently, the DCR for brace-to-gusset weld fracture is given by Eq. 4.7. A DCR less than or equal to the AISC resistance factor, $\phi = 0.75$, would be acceptable for modern design.

$$DCR_{brw} = \frac{(R_y F_y)_{br} A_g}{1.2\sqrt{2} F_{EXX} w_{br} L_w} \tag{4.7}$$

Several researchers have previously simulated the behavior of HSS brace-to-gusset plate welds, including fracture. Hsiao et al. (2014) implemented an axial spring at the brace end (similar to the spring for gusset plate yielding discussed above). The spring had a linear-elastic force-displacement behavior and a fracture displacement calibrated from the experimental response of a single NCBF specimen (Specimen 1E as described by Sen et al. (2017)). Sizemore et al. (2017) followed a similar approach for modeling brace-to-gusset weld fracture observed in experiments of "$R = 3$" CBFs and OCBFs. In this alternative model,

fracture was initiated based upon a force limit and post-fracture contact between the brace and gusset plate was simulated with a gap-contact element in parallel with the brace-to-gusset weld spring. This contact behavior has been observed in experiments of NCBFs (Sen et al. 2016a, 2017) but is difficult to predict, as the brace potentially bears on the gusset plate and/or adjacent concrete slab, which can in turn deform. Therefore, this behavior is not considered in the modeling approach.

A similar approach for modeling brace-to-gusset weld behavior without post-fracture contact is proposed here using existing understanding of weld nonlinear behavior. The AISC *Steel Construction Manual* (AISC 2017d) defines the normalized stress-deformation behavior of welds as Eq. 4.8 for use with the instantaneous center of rotation method when determining the weld-group strength. In Eq. 4.8, p is defined as the ratio of the weld deformation, Δ, to the deformation at ultimate load, Δ_m. This relationship, based upon work by Lesik and Kennedy (1990), is proposed for use in modeling brace-to-gusset weld fracture using a translational spring in the direction of the brace. Equation 4.9 utilizes Eq. 4.8 to develop a force-deformation relationship for a group of four concentrically loaded longitudinal fillet welds ($\theta_i = 0°$), as would be common for an HSS brace-to-gusset weld. Equation 9 uses Δ_m of $0.167w_{br}$, also based upon findings from Lesik and Kennedy (1990).

$$F_{nw}(p) = 0.60F_{EXX}\left(1.0 + 0.50\sin^{1.5}\theta_i\right)\left[p(1.9 - 0.9p)\right]^{0.3} \tag{4.8}$$

$$P_{brw}(\Delta) = 4.80F_{EXX}w_{br}L_w\left[\frac{\Delta}{w_{br}}\left(0.35 - \frac{\Delta}{w_{br}}\right)\right]^{0.3} \tag{4.9}$$

The force-deformation behavior of the brace-to-gusset weld can be modeled in *OpenSees* using an axial spring at the brace end, identical to the approach for the simulation of gusset-plate axial yielding. The generic *MultiLinear* uniaxial material can be used to model the force-deformation relationship given by Eq. 4.9; note that this material has a fully hysteretic response. Fracture can be modeled using the *MaxStrainRange* material wrapper with a

unidirectional deformation limit of Δ_u ($0.339w_{br}$ for longitudinally loaded welds). Note that if both gusset-plate axial yielding and brace-to-gusset weld fracture need to be modeled, these materials can be placed in series in *OpenSees* using the *Series* uniaxial material.

Figure 10 shows the dual implementation of gusset-plate axial yielding and brace-to-gusset weld fracture for Specimen 1E in Sen et al. (2017), where the Whitmore-yielding DCR was 1.0, the brace-to-gusset weld fracture DCR was 1.7, and the failure mode was brace-to-gusset weld fracture. In Fig. 4.8a, a base model is shown in which only the gusset-plate axial yielding model is implemented. Equation 4.2 was used to predict the $MSR_{f,disp}$ value for the locally slender HSS6×6×1/4 brace. Since the Whitmore-yielding DCR was not excessive, the brace yielded and fractured in tension (BRF) in the numerical simulation. Both the strength and deformation capacity prior to fracture are overpredicted compared to the experimental results. Figure 4.8b shows the response with a similar model which includes the proposed brace-to-gusset weld fracture (BRW) model (depicted in Fig. 4.8c) in series with the gusset-plate yielding spring. The lateral resistance when the brace is in tension (positive drift) and the fracture behavior are predicted well using a w_{br} of 1.25 times the specified weld leg size, which may be attributed to oversizing during fabrication or overstrength of the filler metal. In both the base model and proposed model results shown in Figs. 4.8a and 4.8b, the post-fracture resistance when the brace is in compression (negative drift) is underpredicted by the numerical simulation since post-fracture contact was not considered.

4.3.3 Gusset-Plate Interface Weld Fracture

One of the most common deficiencies reported in NCBFs is the inadequacy of the welds which connect the gusset plate to adjacent beams, columns, and other connecting elements (e.g., shear plates) (Sen et al. 2016b). These welds are termed gusset plate interface welds here, as indicated in Fig. 4.6a for a gusset plate welded directly to the beam and column. Such connections are common in CBFs, since one interface of the gusset plate can be shop-welded to the beam or column to facilitate erection. The remaining gusset plate interface is either welded or bolted in the field.

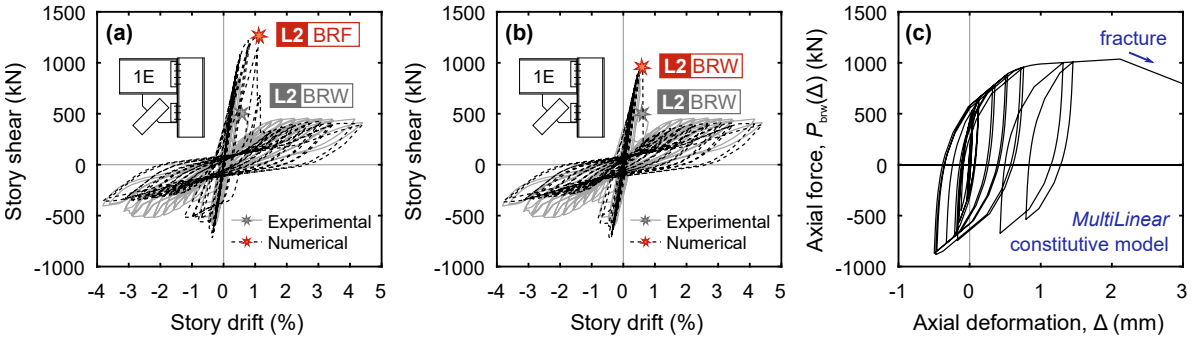

Figure 4.8: Experimental and numerical frame response of Specimen 1E (a) without and (b) with the brace-to-gusset weld fracture model; (c) response of corresponding gusset plate translational spring

Gusset-plate interface welds are vulnerable components of the connection since they are subjected to considerable in- and out-of-plane deformation demands due to opening and closing rotations of the beam-column joint and bending of the gusset plate in out-of-plane buckling configurations. Interface-weld tearing generally initiates after buckling when the brace is in compression, the beam-to-column connection is opening, and the plate is bent out of plane. When the brace is loaded subsequently in tension, weld fracture is possible under the larger shear demands. This failure mode is avoided in SCBFs by:

- Sizing the weld to develop the plastic capacity of the gusset plate;
- Providing adequate clearance to accommodate gusset-plate rotation when the brace buckles, usually with either the $2t_p$ linear (Astaneh-Asl et al. 1986) or $8t_p$ elliptical (Lehman et al. 2008) clearance model (see Fig. 4.6c); and
- Using filler metal which satisfies demand critical weld toughness requirements (AISC 2017a) to allow ductile tearing of the welds without complete fracture.

In the *Seismic Provisions* (AISC 2017a), the weld strength criterion is met by designing the weld to resist either $0.6R_yF_yt_p$ per unit length of shear (simplified approach) or the

assumed edge forces in combination with the reduced weak-axis flexural strength of the plate (Carter et al. 2016). The BDP provides a more stringent but well validated alternative approach based on the tensile capacity of the plate and weld (Roeder et al. 2011b). The BDP expression for the interface weld DCR is given by Eq. 4.10. For design purposes, DCR_{gpw} must be less than the corresponding resistance factor, $\phi = 0.75$. Note that for ASTM A572 Grade 50 plate and E70 electrodes, the required leg size in design is $0.82t_p$ for the BDP and $0.74t_p$ for the simplified AISC approach.

$$DCR_{gpw} = \frac{(R_y F_y)_p t_p}{0.9\sqrt{2} F_{EXX} w_p} \tag{4.10}$$

NCBFs are not expected to meet any of the above criteria to ensure ductile tearing of the gusset-plate interface welds, and recent experimental research suggests that these welds are prone to premature, brittle fracture after brace buckling has occurred (Sen et al. 2016b). Table 4.2 summarizes relevant data for seven tests of NCBFs in which gusset-plate interface weld fracture was the first failure mode. Equation 4.11 was calibrated from numerical simulation of these experiments, where the analytical fracture rotation, θ_f, is the gusset-plate spring rotation corresponding to gusset-plate interface weld fracture in the test. For practical purposes, gusset-plate rotation can be converted to brace compressive deformation using the expression $L\theta^2/2$, which is based upon small-angle approximations and an idealized triangular brace deflected shape. An upper-bound fracture rotation of 0.257 rad (or 3.3% brace compressive deformation) is recommended, which corresponds to the fracture rotation prediction for $8t_p$ elliptical clearance and DCR_{gpw} of 0.75. Note that this equation is calibrated from and intended for use with gusset-plate interface welds which do not meet demand critical weld toughness requirements. Higher fracture rotations would be expected in SCBFs with adequate clearance and weld strength.

$$\theta_f = 0.11 \left(\frac{L_{clear}}{t_p} \right)^{0.33} DCR_{gpw}^{-0.57} \leq 0.257 \text{ rad} \tag{4.11}$$

Table 4.2: Gusset-Plate Interface Weld Fracture Data from Sen et al. (2017)

Specimen	Connection configuration	DCR_{gpw}	L_{clear}/t_p	Analysis fracture rotation, θ_f (rad)	Failure mode and behavior type	Post-weld fracture description
2O	CSP-W	1.4	3.8	0.153	L3 / Type A	Near total loss of lateral resistance
2C-B	CSP-W$^+$	1.4	3.8	0.143	L1 / Type C	Bolt-hole elongation → Brace fracture (L2)
3E	SSP-B	1.6	3.8	0.0915	L2 / Type B	Simultaneous fracture of shear-plate bolts
4O	S2L-BB	1.0	1.2	0.155	L1 / Type C	Angle yielding → Brace fracture (L2)
6O	CSP-B	1.0	2.2	0.142	L1 / Type C	Bolt-hole elongation → Bolt-hole tearout (L2)
7O	SSP-B	1.2	2.3	0.140	L1 / Type C	Bolt-hole elongation → Bolt fracture (L2)
8O	END	1.6	4.1	0.141	L2 / Type B	Weld fracture on both gusset interface

CSP-W = Welded continuous shear plate, CSP-B = Bolted continuous shear plate, SSP-B = Bolted split shear plate, S2L-BB = Bolted-bolted split double angle, END = End plate
$^+$Connection reinforced with bolts along shear plate and brace filled with concrete as a retrofit

The behavior type for CBFs with gusset-plate interface weld fracture as the initial failure mode depends upon the presence of yielding mechanisms in the remaining connection components. The post-weld-fracture behavior of specimens with gusset-plate interface weld fracture is described in Table 4.2. With the exception of Specimen 2O, the gusset-to-beam weld fractured first in the specimens and thus the characteristics of the gusset-to-column connection determined the ultimate behavior. The welded gusset-to-end-plate connection tested (Specimen 8O) did not have yielding mechanisms in the adjoining end plates, and this weld fractured essentially simultaneously with the gusset-to-beam weld (Type B). Connections with bolted shear plates (Specimens 2C-B, 3E, 6O, and 7O) either had premature bolt fracture nearly simultaneously with the gusset-to-beam weld (Type B) or ductile bolt-hole elongation that led to a delayed failure mode (Type C), depending on the relative strength of the bolt bearing versus bolt shear limit sates. A similar phenomenon is possible with bolted double angle connections (Specimen 4O), where yielding of the angles can also provide significant deformation capacity if they are thin enough to induce prying action in the bolts and preclude bolt fracture (Type C).

Gusset-plate interface weld fracture results in reduced or total loss of load in the brace

(L1 or L2 failure-mode type, respectively). Both conditions can be simulated in *OpenSees* using the full combination of springs in Fig. 3c. Weld fracture can be triggered using the *MaxStrainRange* material wrapper on the rotational spring used to simulate flexural yielding of the gusset plate; similar to the brace, fracture is not triggered until the load direction reverses. Note that the rotation range is approximately equal to the rotation in one direction since rotation under brace tension is near zero. Using a rotation range criterion here is advantageous since the rotation direction does not need to be specified. A pair of translational springs is used to control post-fracture response. Upon weld fracture, the rigid axial spring element is removed by the *MaxStrainRange* material. The severity of weld fracture is a modeling decision determined by the presence of secondary yielding mechanisms possible in the connection. If weld fracture is an L2 failure mode (Type B behavior), the remaining spring is elastic and flexible, allowing essentially free translation of the brace end and no force development. If weld fracture is an L1 failure mode (Type C behavior), the remaining axial spring is nonlinear with force-deformation behavior representative of the remaining connection components. An analogous pair of rotational springs are used at the beam-column connection to simulate the fixity lost if the gusset-plate disconnects from the beam. This rigid spring is also removed by the *MaxStrainRange* material, and an appropriate moment-rotation behavior can be defined for the remaining spring.

Figure 4.9 shows how the model can be implemented to simulate gusset-plate interface weld fracture exhibiting Type B behavior (L2 failure mode), which was observed in Specimen 8O, as described in Sen et al. (2017) and in Table 4.2. In the experiment, both gusset-plate interface welds fractured simultaneously, completely disconnecting the gusset plate from the frame. The base model in Fig. 4.9a does not implement a fracture criterion based upon gusset-plate rotation, and the deformation capacity is overpredicted since the failure mode is delayed brace fracture. When the proposed model is implemented with a θ_f of 0.141 radians and no secondary yielding mechanism, the behavior of the frame both before and after gusset plate interface weld fracture (GPW) is well predicted (see Fig. 4.9b). Figure 4.9c shows the moment-rotation behavior of the gusset plate, which confirms that the gusset plate rotation

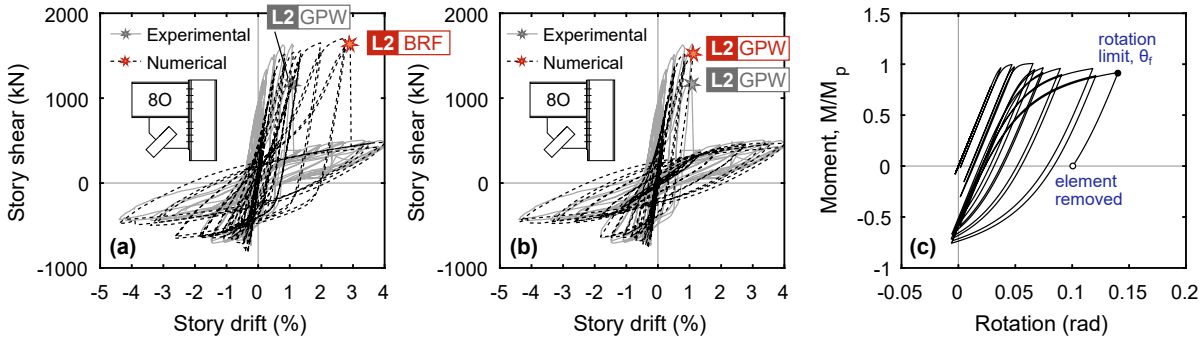

Figure 4.9: Experimental and numerical frame response of Specimen 8O (a) without and (b) with the gusset plate interface weld fracture model; (c) response of corresponding gusset plate rotational spring

is near zero in one direction and therefore the *MaxStrainRange* model can be used.

Use of a post-fracture axial spring to simulate the force-deformation behavior of a bolted-bolted double-angle connection on the vertical gusset plate interface is shown in Fig. 4.10 using Specimen 4O from Sen et al. (2017). The gusset-to-beam interface weld fractured in this experiment but local yielding of the gusset-to-column angles provided a secondary load path, resulting in significantly increased strength and deformation capacity. The secondary yielding translational spring was calibrated with the *Steel02* material model, and its force-deformation behavior is shown in Fig. 4.10c. A base model which includes gusset-plate interface weld fracture but no secondary yielding mechanism is shown in Fig. 4.10a. Here, weld fracture is incorrectly modeled as an L2 failure mode, and the post-fracture resistance is significantly lower than in the experiment. When the nonlinear spring behavior in Fig. 4.10c is introduced, the response in Fig. 4.10b is obtained, where the larger post-fracture resistance matches the experiment well and the L2 failure mode is delayed brace fracture.

4.4 Framing Member Simulation

At large lateral deformations, the beams, columns, and/or beam-column connections in CBFs are expected to yield, and consideration of the strength and stiffness provided by

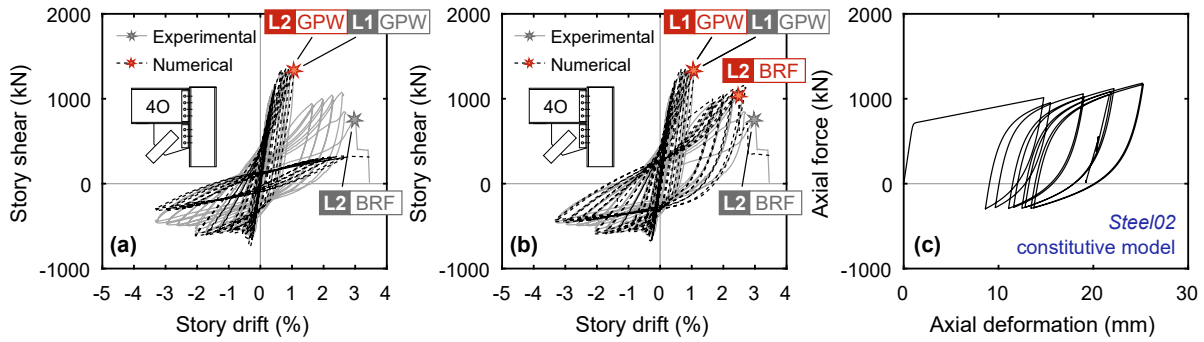

Figure 4.10: Experimental and numerical frame response of Specimen 4O (a) without and (b) with the gusset plate post-fracture model; (c) response of corresponding gusset plate post-fracture axial spring

these components can have a large effect on seismic response (Hsiao et al. 2013b). In US construction, beams and columns are most often wide-flange sections and beam-to-column connections that are not adjacent to gusset plates are often bolted shear plates. In SCBFs, ductility of the beams and columns is ensured by limiting cross-sectional width-to-thickness ratios ($b/2t_f$ and h/t_w) to meet the highly ductile criteria in the Seismic Provisions (AISC 2017a). Stability of these members is ensured through capacity design based on the expected brace forces and lateral bracing requirements for beams in chevron-configuration frames. NCBFs, in comparison, may have beams and columns which are more susceptible to local buckling and columns which may buckle globally prior to brace yielding. The following recommendations address modeling to simulate yielding and buckling of these components.

4.4.1 Beam-to-Column Connections

Beam-to-column connection stiffness and strength is often neglected when modeling CBFs in design practice, but it plays an important role in developing lateral resistance through frame action. Hsiao et al. (2012) investigated different modeling approaches for frames, including models with pinned, fully restrained, and realistic connections at the brace-beam-column intersection. The latter model is shown in Fig. 3b, where the gusset plate is modeled using

a nonlinear rotational spring and the brace, beam, and column are offset from the work point to account for the stiffening resulting from the gusset plate. The beam-to-column connection is fully restrained in this scenario because the gusset plate acts like a haunch to restrain relative rotation of the beam and column.

This modeling approach was developed for SCBFs and remains applicable for NCBFs unless gusset-plate interface weld fracture occurs (either L1 or L2). For example, in Specimen 8O in Fig. 4.9b, the gusset-plate interface weld fractures completely, disconnecting the plate from the frame. The gusset-plate therefore no longer restrains rotation of the beam-to-column connection, though the end plate still provides reduced rotational restraint. A similar effect occurs in Specimen 4O shown in Fig. 4.10b, but the retained beam-to-column connection is a bolted-bolted double angle, which provides considerably less restraint. The modeling approach in Fig. 3c can be employed to model these post-fracture scenarios using rigid and nonrigid elements in parallel. Upon gusset plate interface weld fracture, the rigid elements are removed from the analysis but the nonrigid elements, which simulate the post-fracture condition of the frame, are retained. This element removal procedure was accomplished using the *MaxStrainRange* material by inputting the tags of elements which are marked for removal when the fracture criterion is met.

The behavior of beam-to-column connections that are not adjacent to gusset plates, including connections part of the gravity framing in buildings, also greatly contributes to the lateral resistance and can help prevent collapse once the braces or brace connections have fractured (L2 failure mode type) (Hsiao et al. 2013b). The flexural and rotational capacity of these connections can be considered with nonlinear rotational springs. Liu and Astaneh-Asl (2004) provide guidance for such a modeling approach for bolted shear plates which are applicable for both new and NCBF-era construction.

4.4.2 Yielding-Beam Mechanism in Chevron-Configured CBFs

Recent experimental research on SCBFs (Terpstra 2017), existing and retrofitted NCBFs (Sen et al. 2016a; Simpson and Mahin 2018) and "$R = 3$" CBFs used in regions with low

seismic hazard (Bradley et al. 2017) has demonstrated the potential benefits of a plastic mechanism in which beam yielding precludes brace yielding in the chevron configuration. These tests show that beam yielding does not compromise and may even enhance CBF ductility. Further, after the first brace or brace connection fractures, the yielding beam mechanism can provide significant reserve capacity as the beam acts as long link in an eccentrically braced frame (EBF). This beam-yielding mechanism is not currently permitted in SCBF design but could be leveraged in retrofit of NCBFs. The proposed recommendations from Hsiao et al. (2012) for modeling beams in SCBFs (Fig. 3b) were employed to simulate this behavior, where the beam is modeled with one FBE (five integration points per element) between work points as in Fig. 4.2f. Since the beam is modeled as a fiber section, yielding can occur under the combined flexural and axial load induced by the braces.

4.4.3 Column Buckling

Columns in CBFs significantly contribute to system seismic response through frame action. In SCBFs, the columns are anticipated to yield under combined axial-flexural demands to accommodate drift demands and are designed to prevent buckling induced by the accumulated brace demands along the building height. SCBF columns are not designed for drift-induced flexural demands but are required to satisfy highly ductile local slenderness requirements to ensure ductility. Since buckling is not a concern with SCBF columns, they can be simulated using a single FBE at each story with at least five integration points along the height. Fiber-based approaches are recommended in favor of spring-based lumped plasticity formulations to account for axial-flexural interaction. While spring-based approaches can be used to simulate cyclic deterioration effects (Karamanci and Lignos 2014; Lignos and Krawinkler 2011), SCBF columns meet highly ductile requirements and thus are expected to have limited deterioration.

When the SCBF column design criteria are not met, as with NCBF columns, alternative modeling approaches must be considered. NCBF column design was based upon axial loads induced from the vertical gravity and lateral seismic forces. NCBF columns were not designed

to resist expected brace strengths and are potentially susceptible to column buckling if the brace axial force exceeds its design force. A modeling approach similar to that used for brace buckling is recommended for columns as shown in Fig. 4.11a. Here, the column is discretized with 12, equally spaced nonlinear beam-column elements (either DBEs or FBEs can be used since fracture is not modeled) with an initial imperfection of $L/1000$, which is consistent with the maximum out-of-straightness allowed by the AISC *Code of Standard Practice for Steel Buildings and Bridges* (AISC 2016). Each beam-column element has a fiber-based cross section at each of their 5 integration points. As with other steel components considered in this paper, the *Steel02* material model is used.

The recommended number of elements was determined from a study using Test 2 from Lamarche and Tremblay (2011), which investigated the compressive response of a W12×87 column under cyclic axial loading. The numerical response of the column using 12 FBEs is shown in Figs. 4.11b and 4.11c. An initial imperfection of $L/2000$ was used to match these test results (rather than $L/1000$), but such small imperfection should not necessarily be assumed in practice. Figure 4.12 shows the error in axial force and midheight deflection of this column using different element types and discretizations. The error plotted in Fig. 4.12 is the sum of the errors at each load reversal point in Figs. 4.11b and 4.11c. It can be seen that using more than 12 elements for either the displacement-based or force-based formulations provides only a marginal increase in accuracy based upon the measured response. If fewer than 12 elements are desired to reduce computational cost, FBEs are recommended for use in *OpenSees*.

4.5 Model Validation

The proposed computational modeling recommendations are validated using two experiments of two-story chevron CBFs tested at the National Center for Research on Earthquake Engineering in Taiwan as part of a research program investigating existing and retrofitted NCBF behavior (Sen et al. 2016a). These specimens, TNCBF1-N-HSS and TNCBF1-R-HSS, were introduced in Figs. 1b and 1c and have been selected since they demonstrated complex

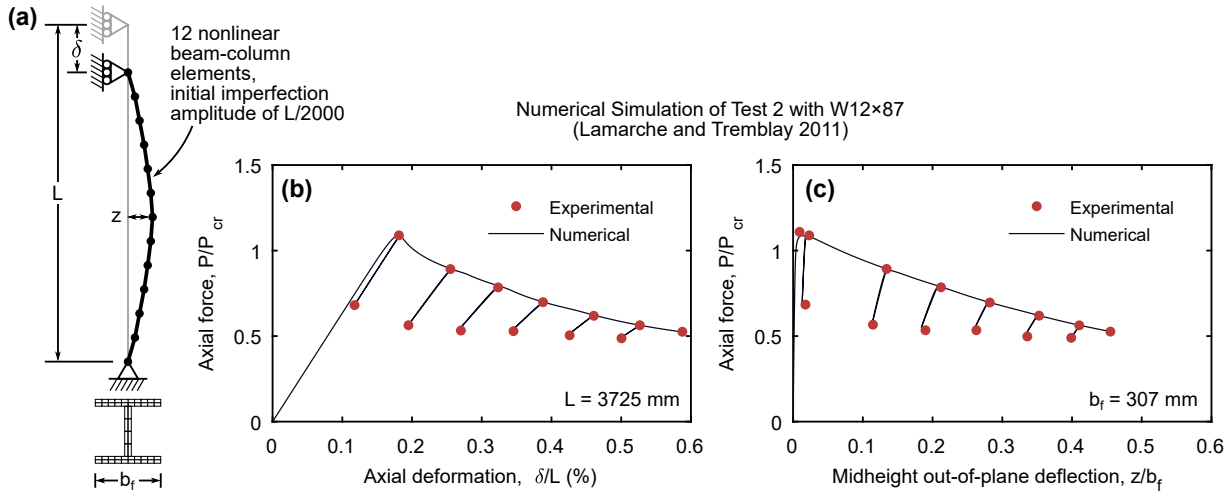

Figure 4.11: (a) Schematic of *OpenSees* column model and validation of numerically simulated (b) axial force-axial deformation and (c) axial force-midheight deflection responses

nonlinear behavior that would be atypical for SCBFs. Their experimental setup is shown in Fig. 4.2e. Further details of the specimens are reported in (Sen et al. 2016a).

Specimen TNCBF1-N-HSS had HSS7×7×1/4 braces on both stories, which had a local slenderness ratio about twice that which is allowed for SCBFs in the Seismic Provisions (AISC 2017a). Thus, premature brace fracture was an expected failure mode. The brace ends were slotted and welded to the gusset plates and had gusset-plate yielding and brace-to-gusset weld fracture, and brace net-section fracture DCRs of 0.95, 0.96, and 1.3, respectively, for the first-story components. The beam was a W16×45 section with welded shear plate beam-to-column connections. Based on the development of P_t and $0.3P_c$ in the first-story braces (the post-buckling expected brace forces in tension and compression, respectively) and assuming simply supported beam ends, the beam had an axial-flexural interaction value of 2.1. The repaired specimen, TNCBF1-R-HSS, had SCBF-compliant HSS5×5×3/8 braces on the first story, a gusset-plate yielding DCR of 0.88, and a beam axial-flexural interaction value of 2.3. The brace-to-gusset weld and net-section fracture vulnerabilities were eliminated in the

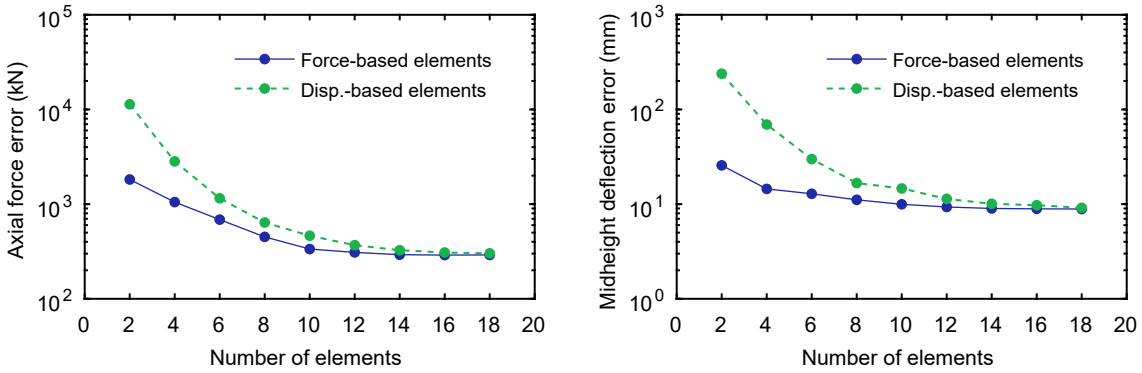

Figure 4.12: Convergence of (a) axial force error and (b) midheight deflection error in numerical simulation of Test 2 from Lamarche and Tremblay (2011)

repair, since these connections were replaced. Both specimens had concrete slabs on metal decks but did not have shear connectors to promote composite action. The second story of each specimen was designed to be intentionally strong in order to deliver the actuator load into the frame; consequently, the braces did not buckle on the second story of these tests.

The specimens were computationally simulated following the proposed modeling approaches, with the exception that the second-story braces were not given initial imperfection in order to prevent buckling and facilitate comparison of the results. In the test frames, the upper slab and beams were stiffer and stronger in the second story to permit load transfer from the actuators to the frame without yielding or damage. Figure 4.2f shows *OpenSees* models for the frames. The gusset-plate axial yielding and brace-to-gusset weld fracture mechanisms were simulated with axial springs in series at the brace ends. Brace fracture was simulated using the MSR method with the $MSR_{f,disp}$ prediction model given in Eq. 4.2 which accounts for load-history effects known to be important for braces in the chevron configuration. The first-story beam ends were connected to the columns with welded shear plates, which were modeled as nonlinear rotational springs with the Steel02 material behavior. The yield moment and elastic stiffness of the springs were based on the beam web properties. The frames were loaded to larger deformations in the simulations than in the

tests to attempt to observe the experimental specimens' failure modes.

Figures 4.13a through 4.13c plot the second- and first-story hysteretic responses and the first-story beam deflection for the specimen. Figure 4.14a compares the experimental and numerical sequence of yielding and failure for Specimen TNCBF1-N-HSS based upon first-story drift range. The dashed lines connect common events which occurred in both the experiment and numerical simulation. The proposed modeling recommendations result in good agreement between the experimental and numerical responses, but a single discrepancy remains. The story drift ranges at buckling and fracture of the first brace are very well predicted and result in the long-link EBF mechanism observed in the experiment. However, the rapid degradation of the brace resistance in compression does not occur in *OpenSees* since the fiber section does not simulate local deformation. This phenomenon is especially apparent in braces with high local slenderness ratios, like the HSS7×7×1/4 in the specimen. However, it is important to note that local cupping of braces with high-b/t leads to brace fracture very quickly, which is achieved with the proposed $MSR_{f,disp}$ fracture model. Thus, not simulating the immediate deterioration following buckling due to local cupping is unlikely to significantly change the predicted NCBF performance using the proposed modeling framework. Comparing the beam displacement-story drift plot in Fig. 4.13c, the downward beam deflection is overestimated in the numerical model, which indicates that some amount of composite action was developed in the beam in the experiment. Finally, the brace-to-gusset connection failure mode (BRW in Fig. 4.13c) did not occur in the numerical model, as the beam was too weak to develop demand in the brace-to-gusset weld translational spring necessary to induce fracture.

The experimental and numerical comparisons are similar for Specimen TNCBF1-R-HSS, as shown in Figs. 4.13d through 4.13f and Fig. 4.14b. The story drift ranges at buckling and tearing of the braces are well predicted using the modeling recommendations, as in Specimen TNCBF1-N-HSS. Tearing of the second brace occurs at a larger story drift range in the numerical analysis, and this may be related to the overpredicted beam deflection (see Fig. 4.13f) since the beam likely developed a some amount of composite action in the

experiment. The larger beam deflections in the analysis limit the tensile demand in the brace and hence increase its fracture life. The story drift ranges when brace local cupping deformation developed in the test are shown in Fig. 4.14b, however the absence of these effects in the numerical model is less consequential for the HSS5×5×3/8 braces since they have a low local slenderness ratio that meets the highly ductile criterion.

Despite minor discrepancies, the above indicates that the proposed modeling is appropriate for NCBFs and retrofitted NCBFs and is capable of reproducing the key behavior modes observed in large-scale experiments.

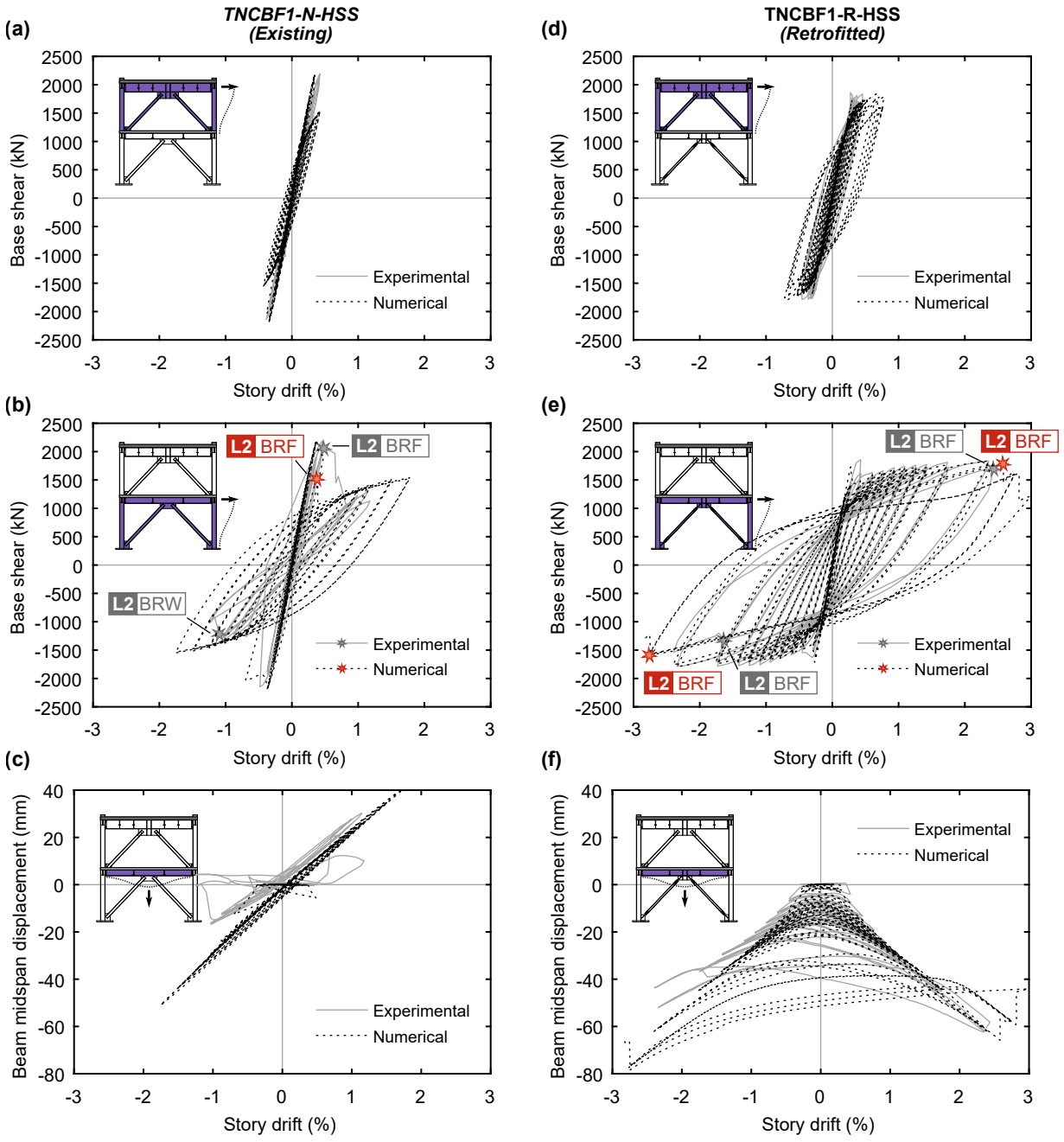

Figure 4.13: Comparison of experimental and numerical responses of existing and retrofitted NCBF specimens

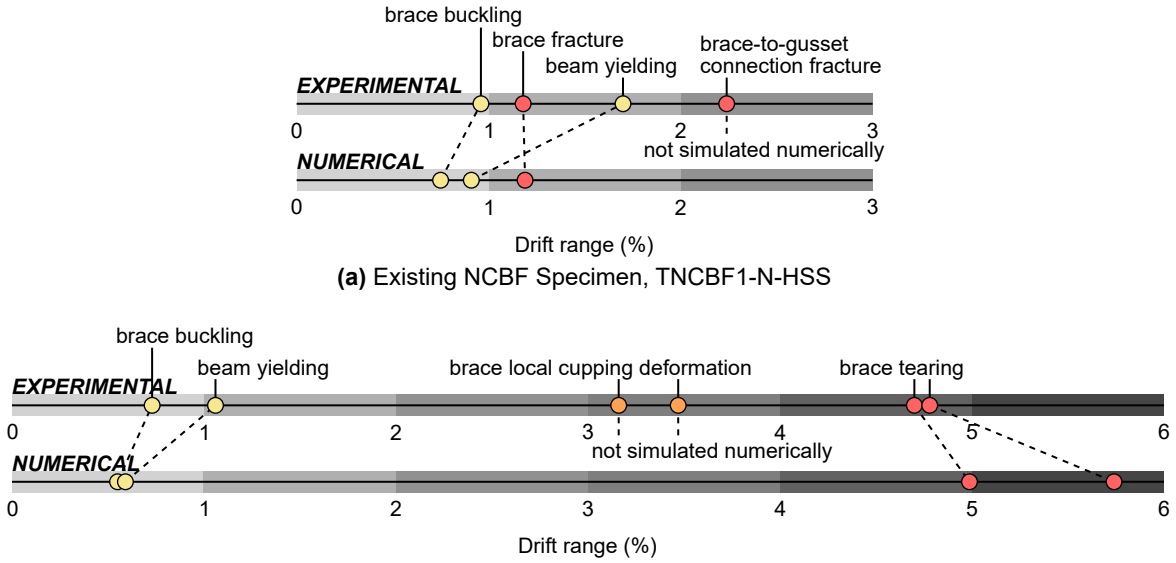

(a) Existing NCBF Specimen, TNCBF1-N-HSS

(b) Retrofitted NCBF Specimen, TNCBF1-R-HSS

Figure 4.14: Sequence of yielding and failure observed in experiments and numerical simulations for first-story of (a) existing and (b) retrofitted NCBF specimens

Chapter 5

METHODOLOGY FOR BUILDING SEISMIC PERFORMANCE EVALUATION

Seismic performance evaluation of existing and retrofitted NCBF buildings is critical for determining the need for and type of retrofit for NCBFs. Previous seismic performance evaluations of NCBFs have been limited in scope and sophistication due to lack of experimental data, which provide an understanding of potential yielding mechanisms and failure modes, and nonlinear modeling tools, which are calibrated from experiments to enable system analysis. Chapters 3 and 4 have addressed these two topics, respectively, and their findings are leveraged in this work to investigate the seismic performance of existing and retrofitted NCBF buildings. First, a brief review of previous research on system-level seismic performance evaluation of NCBFs provides context for this new contribution to the field. Then, NCBF and SCBF archetype buildings are developed which will be used to systematically evaluate performance. The input ground motions selected and scaled for the study are introduced. Finally, a series of engineering expressions are established from experiments to quantify structural damage.

5.1 Previous Research Evaluating NCBF Building Seismic Performance

Several prior research studies have investigated the seismic performance of NCBFs using nonlinear response-history analysis to understand the vulnerability of existing NCBFs and evaluate the effectiveness of various retrofit schemes. These are described below to establish the current understanding of building seismic performance and note limitations which will be addressed by the work in this document.

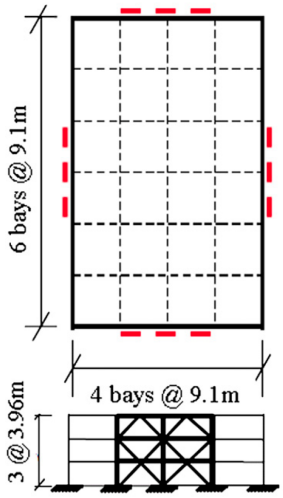

Figure 5.1: Elevation and plan of three-story building analyzed by Hsiao et al. (2014)

5.1.1 Existing NCBF with Brace-to-Gusset Weld Deficiency

Hsiao et al. (2014) evaluated the seismic performance of a three-story, multi-story-X NCBF designed to the *1988 UBC* (ICBO 1988) and compared its performance to SCBFs designed to *ASCE 7-10* (ASCE 2010) and using conventional (AISC 2010a) and balanced design procedures (Roeder et al. 2011b). The same building plans and elevations (Fig. 5.1) were used for each of the three buildings and were based on the three-story SAC building (FEMA 2000). The buildings were modeled using the approach established by Hsiao et al. (2012, 2013a) to accurately simulate brace buckling and yielding, gusset-plate flexural yielding, and beam and column yielding. The NCBF was modeled with a brace-to-gusset weld deficiency using axial springs at the brace ends. This axial spring was elastic and a material wrapper was used to simulate fracture. The spring stiffness and fracture deformation were calibrated to match the response of the connection in the pilot NCBF experiment (Specimen 1E in this document) (Hsiao et al. 2014). The resulting behavior is categorized as Type B, since the brace load path is compromised upon connection fracture. As noted in Table 3.3, the DCR for brace-to-gusset weld fracture was 1.7 and thus was considered a severe deficiency and a high priority for retrofit (Table 3.10).

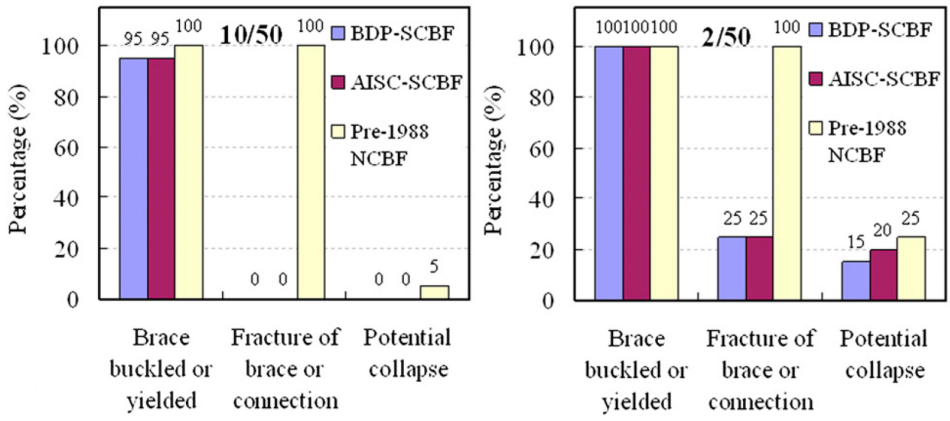

Figure 5.2: Seismic performance statistics for three-story NCBF with deficient brace-to-gusset-plate weld analyzed by Hsiao et al. (2014)

The NCBF and equivalent SCBF buildings were subjected to the SAC ground-motion suites consistent with 2%/50-year and 10%/50-year probabilities of exceedance (Somerville et al. 1997). Figure 5.2 provides statistics for the seismic performance of the brace, connection, and frame for the three buildings and at each hazard level investigated. The results suggest that the NCBF has a very high probability of damage and a small probability of collapse at the 10%/50-year hazard level. In contrast, the SCBF braces or connections would not be expected to fracture, and no instances of collapse of occurred in the SCBFs at this hazard level. Under ground shaking representative of the 2%/50-year hazard level, the percentage of ground motions causing collapse was 1.7 times higher in the NCBF compared to the SCBF designed to the BDP.

While the results show that the NCBF was more vulnerable to damage including collapse in comparison to the SCBFs, it is difficult to draw broad conclusions from this work, since only one existing building, brace configuration, behavior type (Type B), and deficiency severity was evaluated.

5.1.2 Existing and Retrofitted Chevron NCBFs

Balazadeh-Minouei et al. (2018a, b) conducted a series of analyses of existing and retrofitted

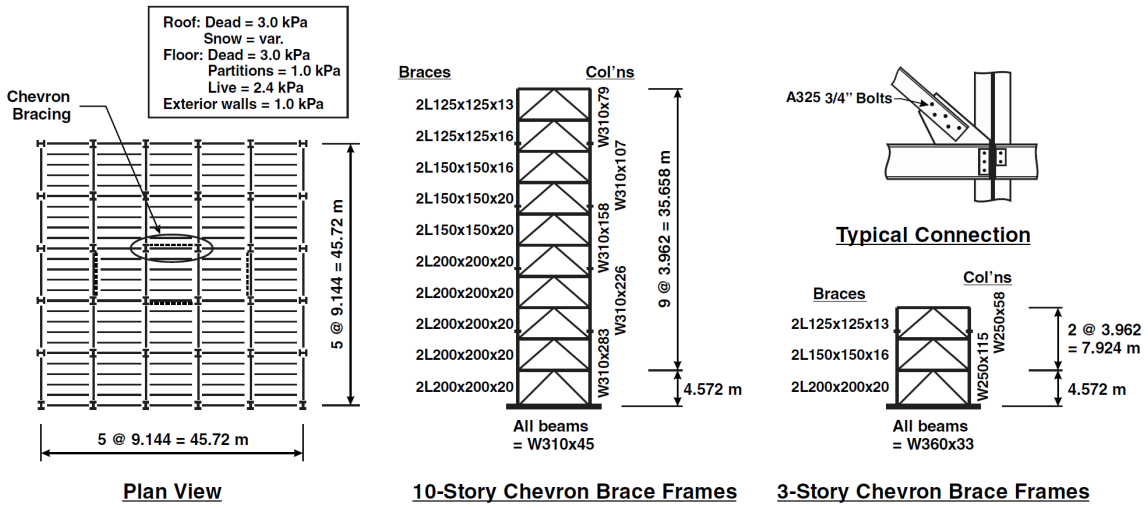

Figure 5.3: Elevation and plan of three- and ten-story NCBFs analyzed by Balazadeh-Minouei et al. (2018a)

chevron NCBFs which develop a yielding-beam plastic mechanism. Existing three- and ten-story NCBFs designed for a site in Vancouver, BC using the 1980 National Building Code of Canada (NBCC) (NRCC 1980) were evaluated along with various retrofit schemes for the ten-story NCBF. The building plan and elevations are shown in Fig. 5.3. The beams, columns, and connections in the existing buildings were relatively weak compared to the expected brace forces, but the connection deficiencies were not explicitly modeled. Instead, connection deficiencies were evaluated as force-controlled actions using the Tier-3 *ASCE 41-13* procedure. The beams and columns were modeled using force-based nonlinear beam-column elements to simulate buckling and yielding (additional analyses were performed with elastic beams and columns, but these are omitted here). The beams were pinned to the columns; they were restrained against out-of-plane buckling and lateral-torsional buckling, but were able to buckle in plane about their strong axis. The columns were oriented for weak-axis bending and were thus also susceptible to in-plane buckling.

The buildings were subjected to ten ground motions selected and scaled to the 2%/50-year probability of exceedance design spectrum in *NBCC 2010* (NRCC 2010). The three-story

building collapsed in 50% of the ground motions while the ten-story building collapsed in 100% of the ground motions. Collapse was preceded by either (1) a soft-story mechanism, (2) column buckling, or (3) beam in-plane buckling.

Since the ten-story frame was more vulnerable based on the analyses, several retrofit schemes were investigated. Four retrofits involved replacement of the braces to strengthen the system to resist linear, dynamic analysis demands and replacement of the beams to resist the unbalanced brace forces. These retrofits had performance which was considered unacceptable by the researchers, as at least 30% of the ground motions caused collapse in each building. An additional set of retrofits evaluated the impact of brace and beam replacement with the addition external framing (either moment frames or vertical trusses). These latter retrofits had performance which was considered acceptable because they effectively mitigated collapse and soft-story behavior.

The results from Balazadeh-Minouei et al. (2018a, b) reinforce the vulnerability of NCBFs, but under a somewhat extreme scenario where the beams are pinned to columns oriented for weak-axis bending and are weak enough to buckle. While some NCBFs may have these characteristics, the infrastructure review revealed a wide variety of beam and column DCRs in the existing building stock (Table 2.3). The retrofit schemes investigated were relatively expensive, since large portions of the existing frame required replacement or reinforcement. Further, the effects of brace and gusset-plate connection deficiencies were not modeled.

5.2 Archetype Building Development

5.2.1 Building Design

Three- and nine-story archetype buildings were designed to investigate low- and mid-rise system seismic performance. Past research on NCBFs and SCBFs has indicated that seismic performance depends on building height (Balazadeh-Minouei et al. 2018a; Hsiao et al. 2013b), hence this is an important parameter to study. For comparison and context, both NCBF and SCBF variants were designed for a site in Seattle (47.619°N, 122.333°W) with the same

building geometries and bracing configurations, shown in Fig. 5.4. These designs were based on buildings evaluated in the NCBF infrastructure review. High-rise building performance was not investigated, since CBFs in this height range are more likely employ different brace sections (e.g., wide flange) and connection details for which there is limited experimental data.

Each building has CBFs in both principal directions and uses the paired single diagonal and chevron configurations. In the three-story building, the paired single diagonal CBFs span the exterior bays in the longitudinal direction and the chevron CBFs are evenly spaced in the transverse direction within the interior columns. In the nine-story building, both the paired single diagonal and chevron CBFs are located on the building exterior. Note that, in all cases, the CBF columns do not coincide with CBFs in both directions (no biaxial bending or compounding axial loads from two independent CBFs) and are oriented for strong-axis bending in the plane of the CBF, which is consistent with the majority of the experimental research conducted on CBF subassemblages, including the specimens used to develop the connection models in Chapter 4. Columns oriented for weak-axis bending and adjacent connections have different potential yielding mechanisms and failure modes not considered here (Simpson and Mahin 2018).

The NCBF and SCBF buildings were designed using different design codes, design methods, and material specifications. Each building was designed to resist the same nominal gravity loads, including floor dead and live loads of 4.79 kPa (100 psf) and 2.63 kPa (55 psf) and roof dead and live loads of 3.83 kPa (80 psf) and 0.96 kPa (20 psf).

The NCBF buildings were designed following the *1979 Uniform Building Code* (ICBO 1979), referred to herein as *UBC-79*. The seismic base shear was computed using Eqs. 5.1 through 5.3 below, where Z is 3/4 for Zone 3, I is 1.0, and K is 1.00. The values C (Eq. 5.2) and S (conservatively assumed to be 1.5 here, following the *UBC-79* recommendations) account for the structure and site periods, respectively, but their product is capped at 0.14. The fundamental period of the structure, T, was estimated by Eq. 5.3 (Eq. 12-3A in *UBC-79*) where L_D is the length of the structure in the direction of the seismic force and h_n is

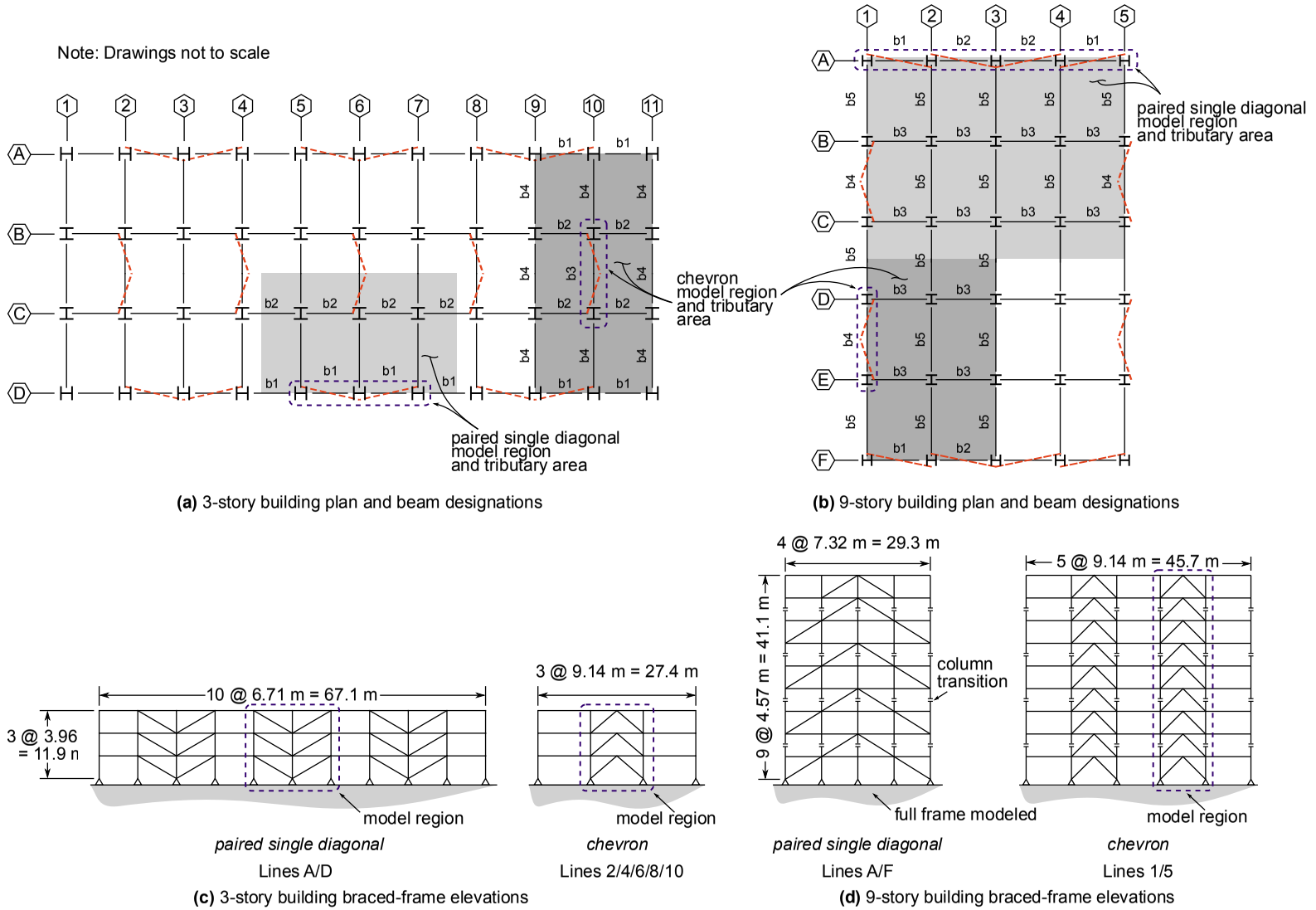

Figure 5.4: Archetype building geometry

Table 5.1: Archetype Building Design Characteristics

Category	Parameter	NCBF	SCBF
Design	Design code	*1979 Uniform Building Code*	*ASCE/SEI 7-16*
	Design method	Allowable Stress Design	Load and Resistance Factor Design
Braces	ASTM specification	A500 Gr. B	A500 Gr. B
	Nominal yield stress, F_y	317 MPa (46.0 ksi)	317 MPa (46.0 ksi)
	Expected yield stress, $F_{y,exp}$	412 MPa (59.8 ksi)	444 MPa (64.4 ksi)
	Ratio of expected-to-nominal yield stress	1.30	1.40
Beams and columns	ASTM specification	A36	A992
	Nominal yield stress, F_y	248 MPa (36.0 ksi)	345 MPa (50.0 ksi)
	Expected yield stress, $F_{y,exp}$	261 MPa (37.8 ksi)	379 MPa (55.0 ksi)
	Ratio of expected-to-nominal yield stress	1.05	1.10

the building height.

$$V_{1979} = ZIKCSW \tag{5.1}$$

$$C = \frac{1}{15\sqrt{T}} \leq 0.12 \tag{5.2}$$

$$T = \frac{0.05 h_n}{\sqrt{L_D}} \tag{5.3}$$

The design base shear for each building was distributed along the structure's height using the Equivalent Lateral Force (ELF) procedure, which is similar in both *UBC-79* and *ASCE 7-16*. The force applied at each story was determined from Eq. 5.4. Following *UBC-79*, a concentrated force, F_t, was applied at the top of the NCBF buildings using Eq. 5.5. This concentrated force has not been retained in modern practice (ASCE 2017a), and hence F_t

Table 5.2: Archetype Building Seismic-Force-Resisting System Characteristics

Parameter	NCBF		SCBF	
	3-story	9-story	3-story	9-story
Effective seismic weight, W (MN)	24.7	56.4	24.7	56.4
Paired single diagonal configuration				
Design base shear, V/W	0.10	0.076	0.18	0.072
Design period[a], T_{des} (s)	0.13	0.69	0.40	1.11
Analysis period, T_1 (s)	0.50	1.30	0.43	1.47
Chevron configuration				
Design base shear, V/W	0.10	0.076	0.18	0.072
Design period[a], T_{des} (s)	0.13	0.55	0.40	1.11
Analysis period, T_1 (s)	0.53	1.46	0.45	1.42

[a]Approximate period, T_a for NCBFs or minimum of $C_u T_a$ or the computed period for SCBFs

was zero for the SCBF design.

$$F_x = \frac{(V - F_t) w_x h_x}{\sum_{i=1}^{n} w_i h_i} \tag{5.4}$$

$$F_t = 0.07TV \leq 0.25V \tag{5.5}$$

The NCBFs were designed using Allowable Stress Design (ASD), including the 1/3 allowable stress increase permitted in *UBC-79* for braces, beams, and columns (this increase was not permitted for connections). However, CBFs were required to be designed with a 5/4 increase in seismic base shear, and hence the effective design base shear is 15/16 of the value computed by Eq. 5.1. This factor is accounted for in the design base shear shown for the NCBFs in Table 5.2.

The SCBF buildings were designed using ASCE/SEI 7-16 (ASCE 2017a) utilizing Load and Resistance Factor Design (LRFD) and assuming Site Class C soil with a V_{s30} of 537 m/s. All members satisfied the capacity-based and ductile design requirements of the *Seismic*

Provisions (AISC 2017a) with respect to strength and local slenderness. The braces were sized for seismic loads distributed using the ELF procedure in *ASCE/SEI 7-16*, where the design base shear, V_{2016}, was computed as C_sW. To determine C_s, the fundamental period of the structure, T, was taken as the calculated period capped by C_uT_a. A response modification factor, R, of 6 was used and the importance factor, I_e, was 1.0, consistent with the previous NCBF design.

Brace, beam, and column sections for the archetypes are shown in Tables 5.3, 5.4, 5.5, and 5.6, respectively. All braces were designed as ASTM A500 Gr. B members. The beams and columns were designed as ASTM A36 members in the NCBF and ASTM A992 members in the SCBF. The computational models simulating these buildings utilize the expected yield stress values shown as $F_{y,exp}$ in Table 5.1. The expected yield stresses for the NCBFs were based on historical mean values reported in the literature. For A36 steel used for hot-rolled shapes (i.e., beams and columnsin the NCBF buildings), Galambos and Ravindra (1978) reported an expected yield stress of $1.05F_y$ for this era of construction; this expected yield stress was much lower than the expected yield stress for modern A36 steel ($1.50F_y$) (AISC 2017a). It is noted that the expected strength of A36 steel has generally increased over time, and hence larger expected yield stresses may be appropriate in reality, especially for buildings constructed in the 1980s and beyond. The historic expected yield stress for A500 Gr. B braces was $1.30F_y$ based on data from Lee (1988) and Liu and Goel (1987). As with the A36 steel, this is lower than the expected yield stress for modern A500 Gr. B steel ($1.40F_y$). Expected yield stresses for the SCBFs are those reported in *AISC 341-16* (R_yF_y) (AISC 2017a).

Local and global slenderness ratios are provided for the brace sections listed in Table 5.3. These quantities are important for establishing brace fracture life and are inputs in Eq. 4.2 and other brace fracture models. The local slenderness ratio ($\lambda = b/t$) is presented here as a ratio to λ_{hd}, the maximum local slenderness ratio allowed for SCBF braces. For the NCBFs, the brace local slenderness ratios were between 1.6 and 2.2 times higher than would be allowed by current SCBF design. As required, the local slenderness ratios in the SCBF buildings

Table 5.3: Archetype NCBF and SCBF Building Brace Sizes

Story	NCBF			SCBF		
	Brace	λ/λ_{hd}	L_c/r	Brace	λ/λ_{hd}	L_c/r
3-story paired single diagonal						
3	HSS5-1/2×5-1/2×3/16	2.00	117	HSS5×5×3/8	0.82	128
2	HSS6×6×1/4	1.59	109	HSS5-1/2×5-1/2×3/8	0.93	116
1	HSS7×7×1/4	1.89	96	HSS5-1/2×5-1/2×3/8	0.93	120
3-story chevron						
3	HSS5×5×3/16	1.80	94	HSS4-1/2×4-1/2×5/16	0.91	102
2	HSS6×6×1/4	1.59	80	HSS5×5×3/8	0.82	94
1	HSS6×6×1/4	1.59	80	HSS5-1/2×5-1/2×3/8	0.93	90
9-story paired single diagonal						
9	HSS8×8×1/4	2.19	90	HSS6×6×1/2	0.72	123
8	HSS9×9×5/16	1.95	79	HSS6×6×1/2	0.72	123
7	HSS10×10×3/8	1.79	69	HSS6×6×1/2	0.72	123
6	HSS10×10×3/8	1.79	69	HSS7×7×1/2	0.87	103
5	HSS12×12×3/8	2.20	56	HSS7×7×1/2	0.87	103
4	HSS12×12×3/8	2.20	56	HSS7×7×5/8	0.66	102
3	HSS12×12×3/8	2.20	55	HSS7×7×5/8	0.66	102
2	HSS12×12×1/2	1.58	55	HSS7×7×5/8	0.66	102
1	HSS12×12×1/2	1.59	59	HSS8×8×5/8	0.78	91
9-story chevron						
9	HSS6×6×3/16	2.20	89	HSS4-1/2×4-1/2×5/16	0.91	115
8	HSS7×7×1/4	1.89	75	HSS4-1/2×4-1/2×5/16	0.91	115
7	HSS8×8×1/4	2.19	65	HSS5×5×3/8	0.82	104
6	HSS8×8×5/16	1.71	63	HSS5×5×3/8	0.82	104
5	HSS8×8×5/16	1.71	62	HSS5-1/2×5-1/2×3/8	0.93	92
4	HSS9×9×5/16	1.95	58	HSS5-1/2×5-1/2×3/8	0.93	92
3	HSS9×9×5/16	1.95	58	HSS6×6×1/2	0.72	85
2	HSS9×9×5/16	1.95	58	HSS6×6×1/2	0.72	85
1	HSS9×9×5/16	1.95	55	HSS6×6×1/2	0.72	88

Table 5.4: Archetype NCBF and SCBF Building Beam Sizes

Story	Section (DCR[a])				
	b1	b2	b3	b4	b5
3-story NCBF					
3	W16×45	W16×25	W21×55 (2.5)	W21×55	–
2	W16×67	W16×31	W21×73 (2.2)	W21×73	–
1	W16×67	W16×31	W21×73 (2.4)	W21×73	–
3-story SCBF					
3	W16×26	W16×57	W24×146 (0.7)	W21×55	–
2	W16×26	W16×57	W24×162 (0.5)	W21×55	–
1	W16×26	W16×57	W24×162 (0.6)	W21×55	–
9-story NCBF					
9	W18×65	W18×65	W18×35	W21×55 (2.7)	W21×83
8	W18×86	W18×86	W18×35	W21×83 (2.1)	W21×83
7	W18×65	W18×65	W18×35	W21×83 (1.9)	W21×83
6	W18×86	W18×86	W18×35	W21×83 (2.5)	W21×83
5	W18×65	W18×65	W18×35	W21×83 (1.5)	W21×83
4	W18×86	W18×86	W18×35	W21×83 (2.3)	W21×83
3	W18×65	W18×65	W18×35	W21×83 (1.6)	W21×83
2	W18×86	W18×86	W18×35	W21×83 (1.6)	W21×83
1	W18×65	W18×65	W18×35	W21×83 (1.6)	W21×83
9-story SCBF					
9	W16×57	W16×57	W16×26	W24×146 (0.8)	W21×55
8	W16×57	W16×57	W16×26	W24×131 (0.5)	W21×55
7	W16×57	W16×57	W16×26	W24×146 (0.3)	W21×55
6	W16×57	W16×57	W16×26	W24×146 (0.4)	W21×55
5	W16×57	W16×57	W16×26	W24×131 (0.1)	W21×55
4	W16×57	W16×57	W16×26	W24×131 (0.1)	W21×55
3	W16×57	W16×57	W16×26	W24×146 (0.6)	W21×55
2	W16×57	W16×57	W16×26	W24×146 (0.7)	W21×55
1	W16×57	W16×57	W16×26	W24×131 (0.6)	W21×55

[a]DCR shown in parentheses if beam is part of chevron CBF

Table 5.5: 3-Story NCBF and SCBF Building Column Sizes

Story	Section (DCR[a])				
	D-5, D-7	D-6	B-10	B-9, B-11	A-11
3-story NCBF					
3	W10×39 (0.5)	W10×33	W10×49 (0.3)	W10×49	W10×33
2	W10×39 (1.2)	W10×33	W10×49 (0.8)	W10×49	W10×33
1	W10×39 (2.0)	W10×33	W10×49 (1.3)	W10×49	W10×33
3-story SCBF					
3	W10×88 (0.2)	W10×68	W10×68 (0.2)	W10×39	W10×39
2	W10×88 (0.4)	W10×68	W10×68 (0.5)	W10×39	W10×39
1	W10×88 (0.7)	W10×68	W10×68 (0.8)	W10×39	W10×39

Note: Example column locations shown; same sections for typical column locations.
[a]DCR shown in parentheses if column is part of CBF and develops excessive compressive forces under expected brace forces

were less than or equal to λ_{hd} ($\lambda/\lambda_{hd} \leq 1.0$). The global slenderness ratios ($L_c/r = KL/r$) of the NCBF braces tended to be lower than those of the SCBF braces. Lower global slenderness ratios are associated with decreased brace fracture life Goel (1992), and the larger SCBF global slenderness ratios correspond to the lower local slenderness ratio requirements, which steer the engineer toward smaller but stockier cross sections. Note that the maximum permitted global slenderness ratio in both *UBC-79* and the current *Seismic Provisions* is 200 (ICBO 1979; AISC 2017a); this corresponds to a general limit for steel compression members in the former document and a specific limit for SCBF braces in the latter document. All braces in this study had global slenderness ratios less than 200.

Tables 5.4, 5.5 and 5.6 include DCRs in parentheses for members which would be subjected to large demands from the braces under the idealized load cases in the *Seismic Provisions* (AISC 2017a). The post-brace-buckling load case induces the largest demands in beams in chevron CBFs due to the large resultant vertical and horizontal forces. NCBFs were not designed for these forces and the beams considered here had DCRs between 1.5 and 2.7. These DCRs correspond to DCR_{prac} values between 2.3 and 3.7, which assume simply supported beam end conditions and neglect the stiffening effect of gusset plates welded to

the beam.

The column DCRs in the NCBFs varied substantially along the height of the building but exceeded 1.0 in many cases, indicating a potential for column buckling. In the 3-story NCBF, the columns were continuous and hence most critical at the first story with DCRs of 2.0 and 1.3 in the paired single diagonal and chevron CBFs, respectively. In the 9-story NCBF, the columns were spliced at stories 2, 4, 6, and 8, and this resulted in varying DCRs over the height of the building which were not always largest at the base. These DCRs reached a maximum of 2.8 in the paired single diagonal CBF and 1.3 in the chevron CBF. The large DCRs in the 9-story paired single diagonal were driven by an unbalanced force at the central column similar to the chevron beam case, since the braces here were oriented in a multi-story, multi-bay chevron configuration.

The SCBF buildings were assumed to have no connection deficiencies since these were designed with modern, capacity-based and ductile design provisions (AISC 2017a). However, the NCBF bracing connections were characteristic of those identified in the infrastructure review. Even though the 1/3 allowable stress increase was not applied in connection design, the buildings had significant connection deficiencies. The brace-to-gusset weld was not sized to develop the strength of the brace ($DCR > 0.75$), the brace end was typically offset 2 inches from the nearest beam or column flange resulting in little or no rotational clearance ($L_{clear} < 8t_p$), and the gusset-plate interface welds were not sized to develop the strength of the plate ($DCR > 0.75$ using the BDP). The brace-to-gusset weld DCRs and gusset-plate interface weld fracture rotations (θ_f) determined using Eq. 4.11 for these buildings are shown in Table 5.7. The fracture rotations are shown in radians and normalized by the approximate gusset-plate rotation at 2% story drift, which is the allowable design story drift for most CBFs in *ASCE/SEI 7-16* (ASCE 2017a). The gusset-plate rotation was approximated assuming the brace axial deformation, δ, is related to the gusset-plate rotation, θ, by $\delta = L\theta^2/2$, as described in Chapter 4.

5.2.2 Building Modeling Approach

Figure 5.5 shows the general modeling approach for the buildings analyzed in this study. Note that CBFs for each building were analyzed independently as planar frames although they share the same floor plan. To reduce computational expense, only a portion of each seismic-force-resisting system was modeled; these model regions are indicated by the circled bays in Fig. 5.4. The shaded regions in Figs. 5.4a and 5.4b indicate the tributary area of the modeled seismic-force-resisting system. The mass, gravity load, strength, and stiffness of the model were consistent with this tributary area. Mass and gravity load was based on the load combination $1.05D + 0.25L$ specified in *FEMA P695* (FEMA 2009), where D and L are the nominal dead and live loads. The buildings were modeled with a modal damping ratio, ξ, of 2% where the total damping matrix, $\mathbf{c}$, is given by Eq. 5.6. This damping ratio is consistent with commonly used values for nonlinear dynamic analysis (FEMA 2009). The total number of modes damped (N in Eq. 5.6) was equal to the number of stories.

$$\mathbf{c} = \mathbf{m}\left[\sum_{n=1}^{N} \frac{2\xi_n\omega_n}{M_n}\phi_n\phi_n^T\right]\mathbf{m} \tag{5.6}$$

The building models implemented the proposed modeling approaches in Chapter 4, including the following:

- Braces were modeled with distributed-plasticity, displacement-based elements (DP-DBEs) with fiber sections and with the new load-history-dependent maximum strain range (MSR) fracture model (Eq. 4.2),

- Gusset-plate axial and flexural yielding was modeled with nonlinear springs within a zero-length element at each brace end,

- Brace-to-gusset weld and gusset-plate interface weld fracture were modeled assuming Type-B behavior in the NCBFs (no connection failure modes were modeled in the SCBFs),

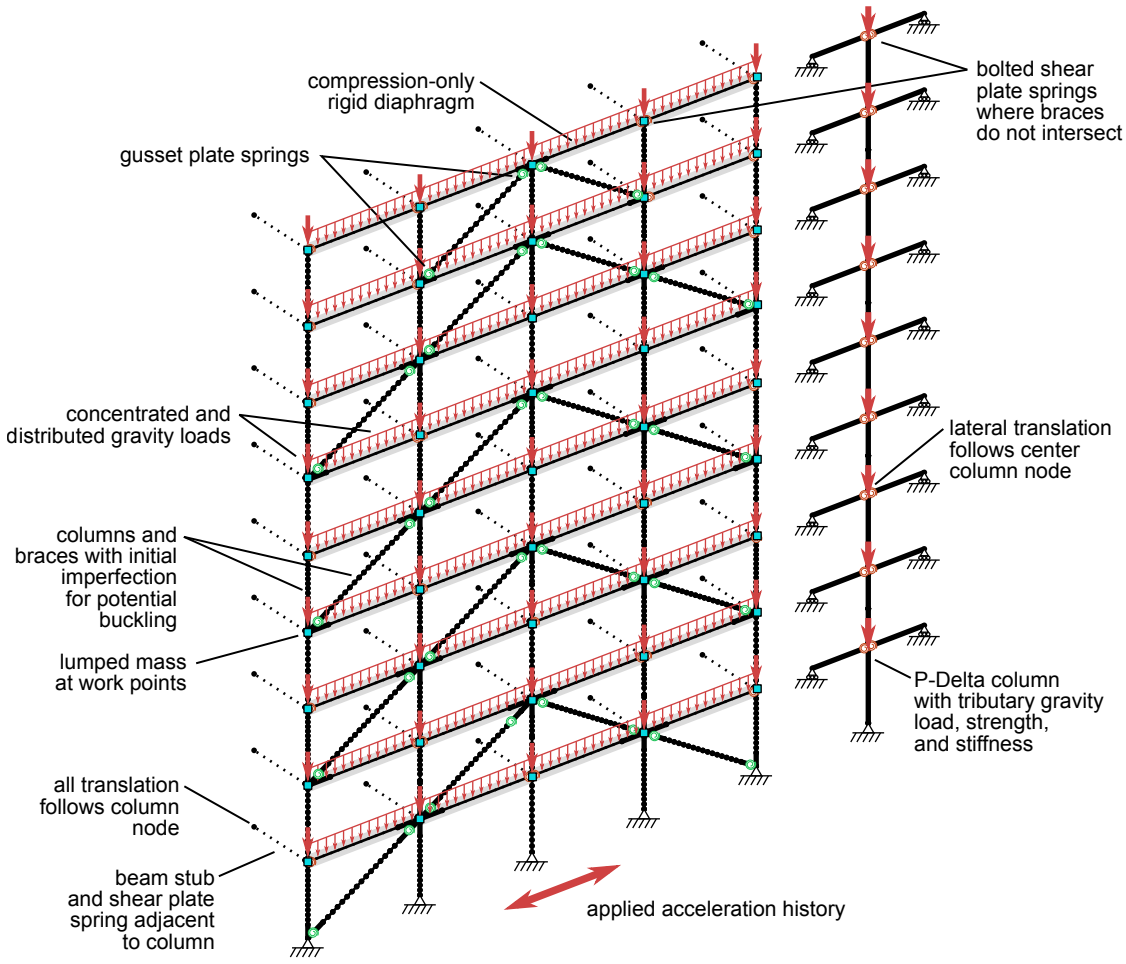

Figure 5.5: Example model for response-history analysis

- Beams and columns were modeled with distributed-plasticity, force-based elements with fiber sections; stiff (e.g., with elastic modulus of $E \times 10^4$), elastic elements were used to offset the beams and columns from the work points to account for the depth of the adjacent cross sections and gusset-plate geometry,

- Beams were modeled with 1 element between work points, and

- Columns were discretized with 12 elements with an initial imperfection amplitude of

$H/1000$, where H is the story height, to initiate buckling.

The building diaphragm was modeled as corotational truss elements between all work points. These elements were elastic but with variable stiffness depending on the direction of loading to simulate the effects of the concrete floor slab. In compression, the concrete elastic modulus, E_c was based on the strength of the slab ($E_c = 57,000\sqrt{f'_c}$ for f'_c in psi (ACI 2014)). Hence, when the beam was in compression, most of the axial force was transmitted through slab.

The concrete elastic modulus in tension was specified as $E_c \times 10^{-6}$. The tensile strength of the slab was neglected. As such, nearly all the axial force in tension was transmitted through the steel. The truss-element area was based on the effective slab width determined from the *Specification* (AISC 2017c) and average slab depth (accounting for ribs in the metal deck). The buildings in this study were designed with composite slabs with a total depth of 6 inches and using 3-inch metal decking. The concrete was modeled with a compressive strength of 6 ksi, which would be stronger than normally specified in older contruction; however, this value was assumed to represent expected compressive strength.

All beam-to-column connections which were not adjacent to gusset plates were composite bolted shear plates (i.e., the positive moment resistance was enhanced by the slab). Previous research on SCBFs found that the aggregated strength and stiffness provided by these connections may prevent collapse, and therefore modeling this behavior is important (Hsiao et al. 2013b). These connections were modeled here as nonlinear rotational springs following the recommendations of Liu and Astaneh-Asl (2004). Moment-rotation behavior was modeled with the *Pinching4* material in *OpenSees* to simulate bolt slip, increased strength in positive bending provided by the composite slab above the connection, concrete crushing, connection yielding (e.g., bolt-hole elongation or plate yielding), and connection fracture due to binding of the beam and column flanges. Figure 5.6 shows an example of this behavior as modeled in *OpenSees*.

Beam stubs simulating framing transverse to the CBFs were modeled to provide more

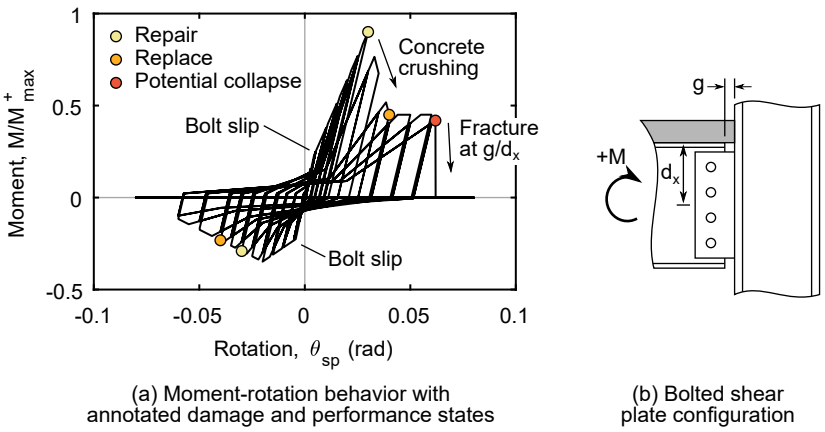

(a) Moment-rotation behavior with annotated damage and performance states

(b) Bolted shear plate configuration

Figure 5.6: Bolted shear plate connection model

realistic boundary conditions for the columns, which were vulnerable to buckling in the NCBF building. The stubs were modeled to the beam inflection point (i.e., half the total length) and attached to the column with nonlinear rotational springs representing composite bolted shear plate moment-rotation behavior as described above.

A leaning column was modeled to simulate P-Delta effects induced by gravity loads in the framing tributary to the modeled braced frame. The strength and stiffness of the gravity system was represented in the building models, as this reserve capacity is important for collapse prevention (Hsiao et al. 2013b). The columns were modeled with multiple nonlinear beam-column elements in parallel. These elements had fiber sections with elastic moduli and yield stresses scaled to represent all similar columns in the gravity system tributary to the seismic-force-resisting system being modeled. Beam stubs were modeled using a similar approach (i.e., multiple nonlinear beam-column elements in parallel) and, as with the transverse beam stubs, they were half the total length of the beam and connected to the columns with nonlinear rotational springs representing composite bolted shear plate beam-to-column connections. The lateral displacements of the leaning column were constrained to follow those of the center column of the braced frame.

5.3 Input Ground-Motion Suites

5.3.1 Ground-Motion Suite Selection

Each building was subjected to a suite of ground motions representing multiple discrete seismic hazard levels for the site of interest and evaluated using a multiple-stripe analysis framework (Baker 2015). The Uniform Hazard Spectrum (UHS) at the 1%/50-year, 2%/50-year, 5%/50-year, 10%/50-year, and 50%/30-year probabilities of exceedance define the seismic hazard levels considered here to capture a range of salient levels of seismic performance. These UHS (dotted lines in Fig. 5.7) were computed from hazard curves generated for the site using the USGS National Seismic Hazard Mapping Project Code with the 2014 edition of the Conterminous US National Seismic Hazard Model (USGS 2017). This hazard model is also used to produce the *ASCE 7-16* design spectra (ASCE 2017a), and thus the SCBFs were designed and analyzed with a consistent hazard.

The probability of exceedance for each hazard level is related to *annual* probability of exceedance (denoted P_1 here but often referred to as λ in the literature; λ is not used here since it has already been defined as the local slenderness ratio here) and return period ($1/P_1$) assuming a Poisson process. For a probability of exceedance P_N in an N-year time span, the annual probability of exceedance is given by Eq. 5.7. Return periods are computed for each hazard level in Table 5.8 and are used throughout this document to simplify the discussion.

$$P_1 = -\frac{\ln(1 - P_N)}{N} \tag{5.7}$$

To facilitate discussion and interpretation of the results, the aggregated results from each suite of ground motions were assumed to approximate the complete seismic hazard for a given return period. For example, a suite in which 10% of the ground motions result in potential collapse is interpreted as a 10% probability of potential collapse for that hazard level. In reality, there is greater uncertainty associated with both the seismic hazard and building response that is not considered here, but this provides a convenient framework for

comparing results between buildings.

5.3.2 Ground-Motion Selection and Scaling

For each hazard level, 30 ground-motion records from the PEER NGA-West2 Database (Ancheta et al. 2013) were selected and scaled to match the corresponding UHS, as shown in Fig. 5.7 for a building with an analytical fundamental period of 0.43 s (e.g., for a 3-story building) and Fig. 5.8 for a building with an analytical fundamental period of 1.54 s (e.g., for a 9-story building). Note that these fundamental periods are the minimum and maximum values for the buildings evaluated in this document. The full ground-motion sets are listed in Appendix C. Candidate ground-motion records were limited to events with magnitude and distance consistent with the range of those considered in the probabilistic seismic hazard analysis used to generate the UHS, and no more than two records from the same event were selected for a given hazard level to avoid event bias. A record geometric mean spectrum was computed for each pair of horizontal ground-motion components, and scale factors were optimized to minimize the error function given by:

$$f_{error}(T_1) = \sum_{i=1}^{n} w_i \left(\left(\prod_{j=1}^{m} \kappa_j S_{a,ij} \right)^{\frac{1}{m}} - S_{a,i}^{\text{UHS}} \right)^2 + \sum_{i=1}^{n} \sum_{j=1}^{m} w_i \left(\kappa_j S_{a,ij} - S_{a,i}^{\text{UHS}} \right)^2 \tag{5.8}$$

$$w_i = \begin{cases} w_{max} + (w_{min} - w_{max}) \frac{\ln c_i}{\ln c_1} & \text{for } c_1 \leq c_i \leq 1 \\ w_{max} + (w_{min} - w_{max}) \frac{\ln c_i}{\ln c_n} & \text{for } 1 < c_i \leq c_n \end{cases} \tag{5.9}$$

where $S_{a,ij}$ is the geometric mean spectral acceleration at period $c_i T_1$ for record j, $S_{a,i}^{\text{UHS}}$ is the UHS spectral acceleration at period $c_i T_1$, w_i is the weight factor at period $c_i T_1$, and $\kappa_j S$ is the scale factor for record j. Note that Eq. 5.9 describes how the weight factor varies relative to the fundamental period, T_1 (i.e, the case where $c_i = 1$). The weight factor is largest (w_{max}) at T_1 and decays logarithmically to w_{min} at the terminal periods for optimization, $c_1 T_1$ and $c_n T_1$. In this study, the ground motions are scaled using c_1 of 0.5, c_n of 5, w_{max} of 1,000,

and w_{min} of 1. A relatively large value of c_n was selected to ensure the ground motions have sufficient intensity at post-buckling and post-fracture structural periods. This optimization is performed for each of the five hazard levels and at all fundamental periods of interest (i.e., the scale factors are recomputed for each building analyzed).

Figure. 5.9 shows the distribution of scale factors used at each hazard level and for each building height using a box plot. From left to right, each point in the box plot represents the minimum, lower quartile, median, upper quartile, and maximum values. Data greater than approximately 2.7 standard deviations from the median are considered outliers and are plotted individually with '+' symbols. Each ground-motion scale factor used to generate the plots was the average for the period ranges shown, which are representative of all three- and nine-story buildings analyzed in this document.

The scale factors used here for longer return periods tend to be larger and more variable. This is due to the paucity of recordings of ground motions associated with very strong but infrequent earthquakes. In addition, the scale factors are larger on average for the nine-story buildings (Fig. 5.9b) because the unscaled ground motions generally had lower spectral accelerations at longer periods. While ground-motion scaling does not have a physical basis, the multiple-stripe analysis approach used here was expected to provide a more reasonable approximation of seismic demand than incremental dynamic analysis, where a single set of ground motions would be scaled up until the structure is determined to have collapsed.

Figure 5.7b shows the record geometric mean spectra, set geometric mean spectrum, and UHS for the 5%/50-year probability of exceedance (975-year return period) hazard level and scaled for a fundamental period of 0.43 s. Note that there is considerable variability in the spectral content of the individual ground-motion records for the same hazard level, but the motions capture the UHS intensity on average. Modified design spectra based upon *UBC-79* and *ASCE/SEI 7-16* are superimposed in Fig. 5.7b. These spectra are multiplied by the SCBF response modification factor ($R = 6$) for comparison purposes; for the *ASCE/SEI 7-16* spectrum this represents the $\frac{2}{3}MCE_R$ spectrum. The intensity of the 5%/50-year ground-motion set for this site is, on average, below the *ASCE/SEI 7-16* design level regardless

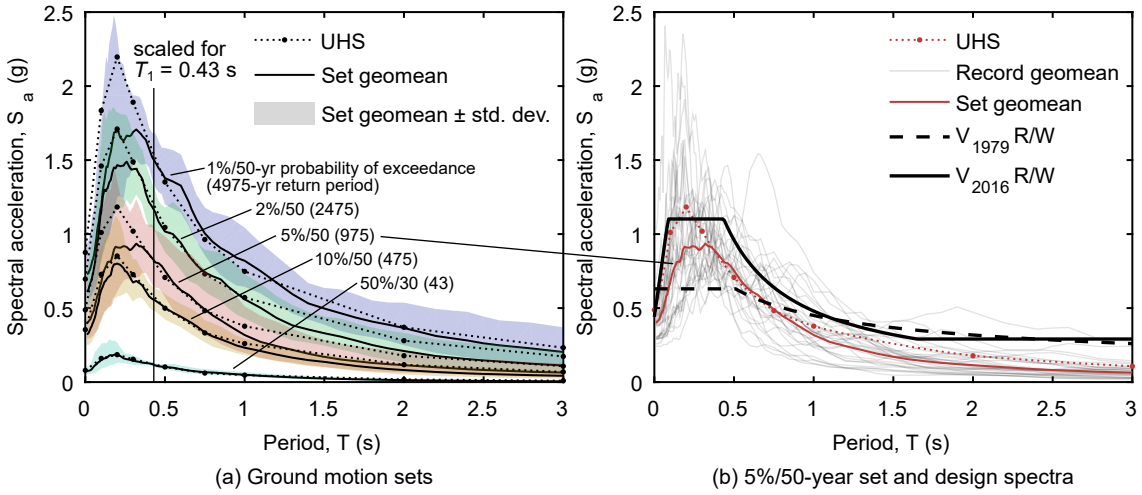

Figure 5.7: Uniform-hazard and input ground-motion response spectra with scaling shown for $T_1 = 0.43$ s

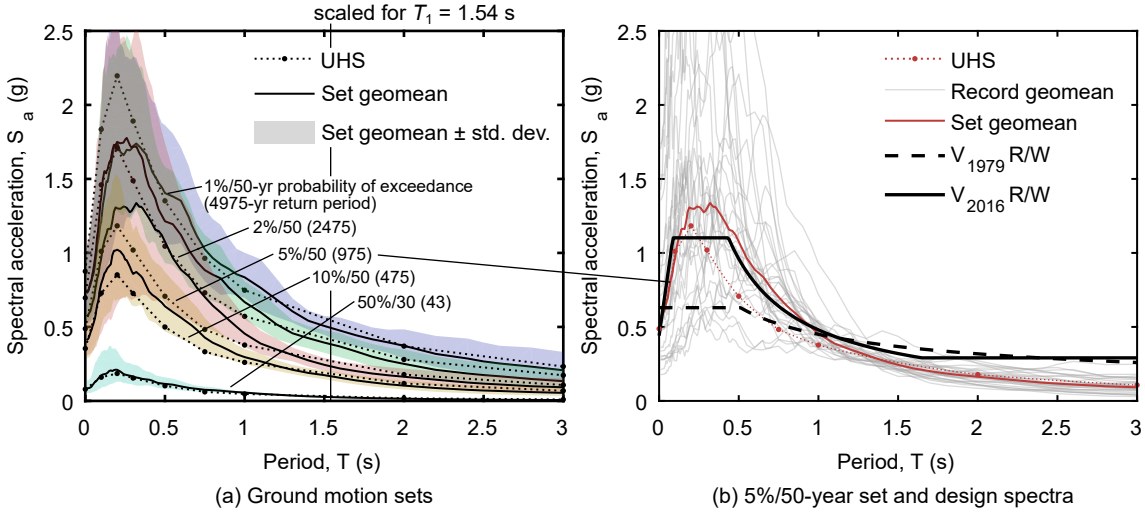

Figure 5.8: Uniform-hazard and input ground-motion response spectra with scaling shown for $T_1 = 1.54$ s

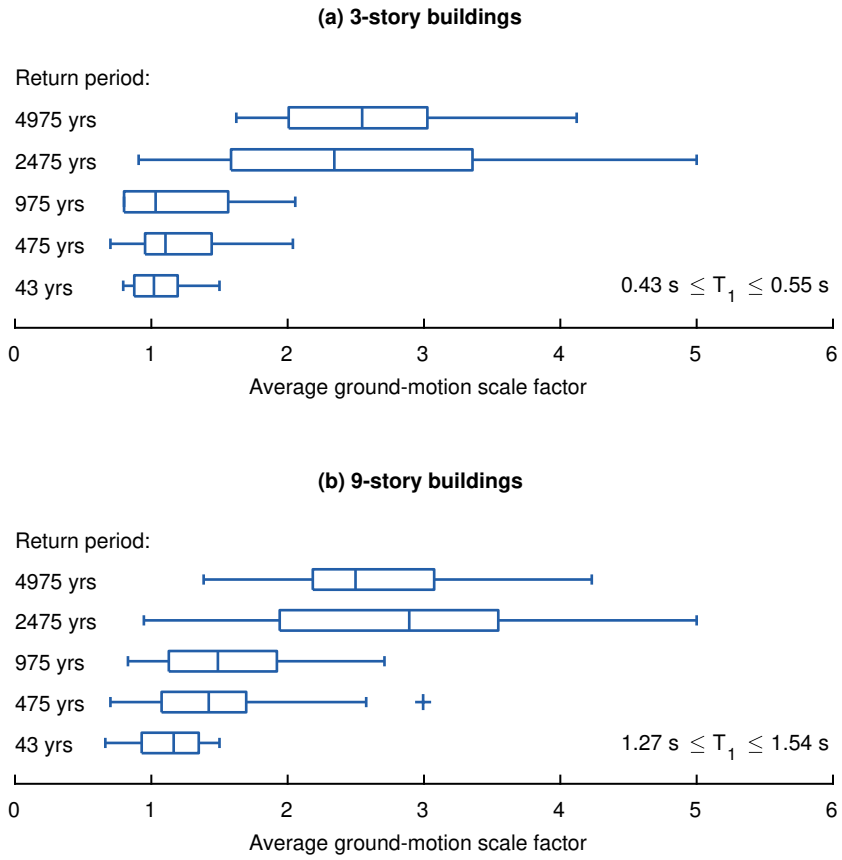

Figure 5.9: Distribution of average ground-motion scale factors for (a) 3-story buildings and (b) 9-story buildings

of period; thus, SCBF damage at this hazard level would be expected to be limited. The *UBC-79* spectrum suggests that NCBFs may sustain significant damage at shorter periods but not necessarily at longer periods. Hence, different levels of damage are expected for this ground-motion set depending on building height and vintage.

Figure 5.8b shows an analogous comparison between the geometric mean spectra, the 5%/50-year UHS, and the design spectra for a fundamental period of 1.54 s. The set geometric mean spectrum shows that the ground-motion intensity is well above the UHS and

design intensity for short periods while the spectra match well at the fundamental period. This issue could be resolved by selecting new ground motions for buildings with longer fundamental periods, but the same ground-motion sets (not scale factors) were used for each building in this study to facilitate comparison.

5.4 Component Performance-State Expressions

Component and frame performance-state definitions are proposed here to provide a quantitative approach for evaluating seismic performance. These performance-state expressions, shown in Table 5.9, are similar in functionality to acceptance criteria in *ASCE/SEI 41-17* (ASCE 2017b); they are both based on engineering demand parameters (EDPs) but have two key differences in their implementation. First, the performance-state definitions here are related to component-level damage states and their direct effects on system behavior, whereas *ASCE/SEI 41-17* uses component EDPs to collectively determine if the system performance objective is met. The performance states considered here include (1) component repair, (2) component replacement, and (3) potential collapse. Second, the damage states are linked to specific repair measures, except in the case of potential collapse.

The performance states defined and evaluated in this research consider multiple damage states within the components labeled in Fig. 5.10, including brace-gusset assemblies, columns vulnerable to buckling, beams vulnerable to yielding under combined axial-flexural demands in the chevron configuration, and composite bolted shear-plate gravity connections. These definitions are developed in this section based on observations from component and subassemblage testing.

5.4.1 Brace-Gusset Assembly

Damage to the brace and gusset plate assemblies typical to most CBFs is important since these components work together to resist the majority of the system's lateral forces. The brace, brace-to-gusset connection, and gusset-to-frame connections can all sustain damage and hence compromise lateral resistance, as has been observed in many tests of NCBFs (see

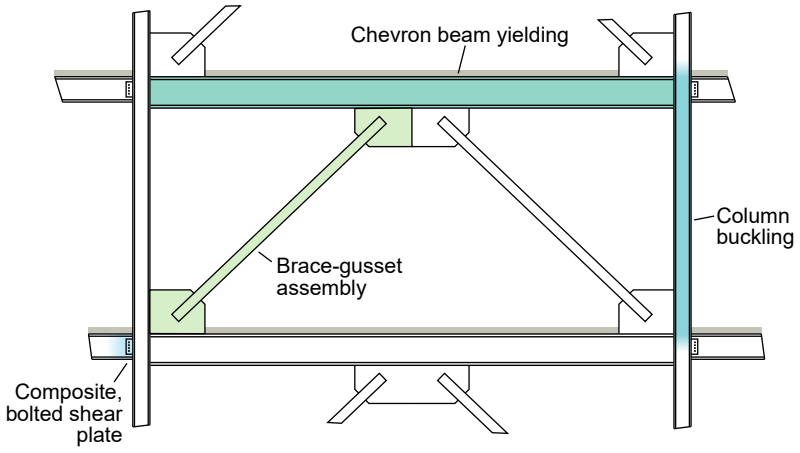

Figure 5.10: CBF with labeled performance-state components

Chapter 3).

Yielding of components (e.g., brace yielding or gusset-plate Whitmore yielding in tension) are ductile actions which do not degrade lateral resistance or directly necessitate repair. In addition, brace buckling only requires structural repair if the deformations are severe enough, though some cosmetic, nonstructural repair may be performed.

Tearing or fracture of components within the brace-gusset assembly, including the brace, brace-to-gusset weld, and gusset-plate interface weld, constitutes significant damage which requires repair. Components which have fractured or are near fracture require replacement; it is expected that the entire brace-gusset assembly would need to be replaced in this scenario.

The brace should be replaced either when local cupping deformation has developed or the brace has torn or fractured at its midspan. Brace fracture is explicitly modeled in this work using the maximum strain range (MSR) approach described in Chapter 4 and can thus be readily detected, but local cupping is not simulated. Therefore, local cupping is evaluated *a posteriori* based on sustained brace axial deformation. Data from six tests of NCBF subassemblages with rectangular HSS braces, shown in Table 5.10, were used to calibrate Eq. 5.10, which predicts the initiation of local cupping based on deformation *range* (i.e.,

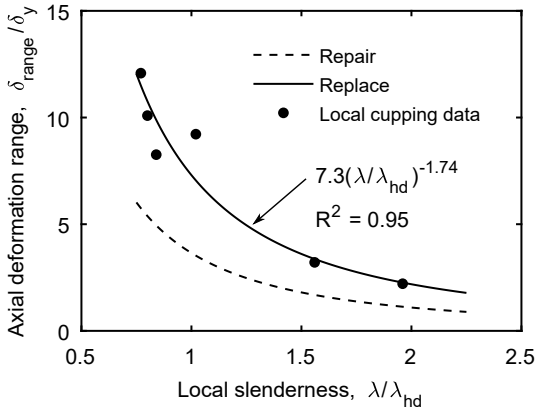

Figure 5.11: Brace performance states

the sum of the absolute tensile and compressive deformations). The braces were selected to cover a broad range of λ/λ_{hd} ratios, since locally slender braces are prone to develop local cupping at smaller deformations, leading to premature brace fracture. Figure 5.11 shows the relationship between local slenderness ratio and the deformation range at the initiation of local cupping for the test data and Eq. 5.10.

$$\frac{\delta_{range,lc}}{\delta_y} = 7.3\left(\frac{\lambda}{\lambda_{hd}}\right)^{-1.74} \tag{5.10}$$

Braces with deformation ranges exceeding Eq. 5.10 are expected to have developed local cupping and thus require replacement. A less severe "repair" performance-state threshold is defined by multiplying Eq. 5.10 by 0.5, which is consistent with acceptance criteria definitions in *ASCE/SEI 41-17* (ASCE 2017b). This threshold is depicted by the dashed curve in Fig. 5.11. At this stage, tearing of the gusset-plate interface welds may occur and require repair by backgouging and reforming the welds.

Connection fracture is explicitly modeled in this work, and fracture criteria for brace-to-gusset weld and gusset-plate interface weld failure modes have been described in Chapter 4. These failure modes disconnect the brace from the frame fully (Type-B behavior) or partially

(Type-C behavior) and thus the entire brace-gusset assembly would likely need to be replaced.

5.4.2 Column

Damage to columns due to buckling is serious and may lead to collapse of the floor system or building. Repair and potential collapse performance states are defined here based on nonlinear analysis of wide-flange sections under cyclic, compressive loading. The nonlinear analyses were extensions of the *OpenSees* simulation of Test 2 from Lamarche and Tremblay (2011), illustrated in Fig. 4.11, and were performed to determine the compressive strength degradation of columns with other wide-flange cross sections. A series of 13-ft W10 (W10×39, W10×49, and W10×68) and 15-ft W12 (W12×40, W12×50, W12×65, W12×79, W12×87, W12×96, W12×106, W12×170, and W12×190) sections were investigated, since these represented columns in the NCBF archetypes. The columns were loaded with protocols similar to that used by Lamarche and Tremblay (2011).

Figure 5.12 shows force-displacement curves for each column with respect to axial deformation, δ (normalized by height, H), and midheight deflection, z (normalized by flange width, b_f). These plots show that the force-axial deformation relationship varies between cross sections but the force-midheight deflection relationship is consistent regardless of cross section. Therefore, midheight deflection is used to define the repair and potential collapse performance states.

The analyses show that compressive resistance degrades rapidly after buckling initiates, and thus almost any degree of buckling requires repair to restore or increase the strength of the member. At z/b_f of 0.1, the compressive resistance of the columns analyzed was between 93 and 98% of P_{cr}. The column could be strengthened by reinforcing the it with steel plates or encasing it in concrete. A replacement performance state is not defined here, since column replacement is not expected to be practical and thus would heavily depend on external factors (e.g., economic viability, total extent of damage in building, etc.). However, a threshold for potential collapse is defined when compressive resistance has degraded severely such that it compromises stability of the vertical-load-resisting system. A threshold of $z/b_f > 1$ is used

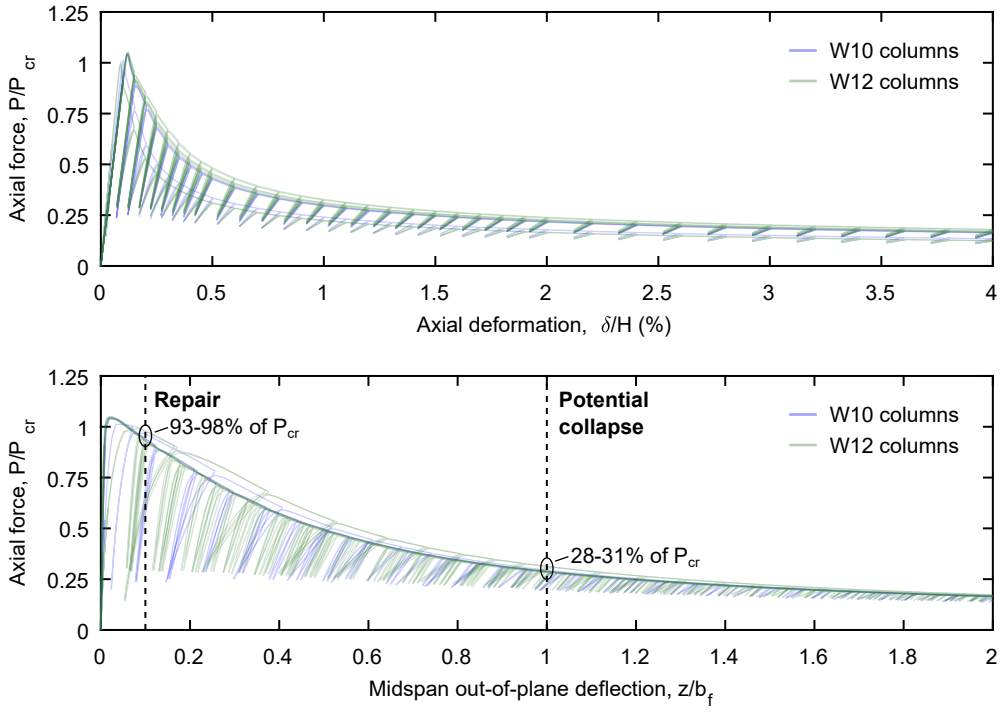

Figure 5.12: Column axial force degradation curves and performance states

here, which corresponds to approximately 70% strength degradation.

5.4.3 Chevron Beam

Chevron NCBFs which develop a yielding-beam mechanism are expected to sustain damage to the beam at larger deflections under the unbalanced brace forces. Experimental research on chevron NCBFs has documented minor beam damage, as in the test of Specimen TNCBF2-D-HSS shown in Fig. 5.13 when the beam deflection was 0.8% of the length (i.e., $\Delta_{bm}/L_{bm} = 0.8\%$). Slight yielding was observed at the beam ends near the fully restrained beam-to-column connections, but this was minor and would not require repair. As indicated in the crack diagram in Fig. 5.13b, significant damage to the slab was sustained, which could indicate degradation of composite action between the steel and concrete.

In view of the observed damage, a repair performance state is defined at Δ_{bm}/L_{bm} of

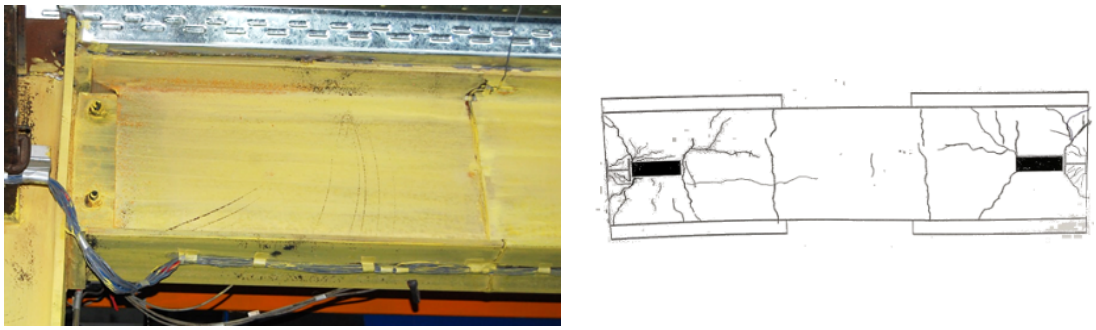

(a) Yielding at beam end

(b) Crack diagram for concrete slab

Figure 5.13: Observed beam damage in Specimen TNCBF2-D-HSS at 0.8% beam deflection

1.5%, approximately twice the maximum deflection of Specimen TNCBF2-D-HSS. At these deflections, local buckling may have occurred and, if the deflections are significant, residual beam deflection may be a serviceability concern. These issues could be mitigated by heat-straightening the locally buckled areas and leveling the slab with grout. As with the columns, a replacement performance state is not defined since this was not deemed to be a practical repair.

A beam "potential collapse" performance state is not considered here but could be associated with failure of the beam-to-column connection–an issue which is addressed for gravity connections below.

5.4.4 Composite, Bolted Shear Plate

Damage to beam-to-column connections in the building gravity system is a significant concern since they must develop the rotational demands due to lateral drift. Typical buildings have numerous beam-to-column connections and thus any level of damage to them may result in an extensive, costly repair. One of the most commonly used beam-to-column connections is the bolted shear plate connection. These connections are designed as simple connections but can have significant moment capacities, especially if they engage adjacent, composite

concrete slabs (Liu and Astaneh-Asl 2000).

Composite, bolted shear-plate connections are considered in this work. Figure 5.6 shows the numerically simulated moment-rotation behavior of a typical composite, bolted shear-plate connection with annotated performance-state markers. This connection is explicitly modeled and its performance states correspond directly to simulated deterioration of the connection strength (Liu and Astaneh-Asl 2004). Liu (2000) provides a full summary of damage with respect to rotation demand.

Bolt slip and plate yielding is expected at small rotations and do not require repair. Repair and replacement performance states are associated primarily with bolt or bolt-hole deformation and concrete crushing. At 0.03 radians, bolt and bolt-hole deformation would be expected to be significant, and this action is associated with a small loss of moment resistance. This damage could be repaired by replacing the bolts if they are deformed. Under more severe damage at 0.04 radians of rotation, replacement of the bolts and plate would be a likely repair due to severe bolt and bolt-hole deformation. Significant concrete crushing also occurs at such large rotations, which may necessitate repair of the slab for cosmetic reasons and to restore some positive moment resistance. The ultimate damage state of the bolted shear plate is fracture in the plate or bolts. This fracture is a result of the large demands due to binding of the beam and column flanges and is thus a function of the gap between the flanges (g) and the depth to the bolt group center of gravity (d_x). Since the vertical-load-resisting system is compromised upon fracture, this is considered a potential collapse performance state.

Table 5.6: 9-Story NCBF and SCBF Building Column Sizes

Story	Section (DCR[a])				
	A-1	A-2	A-3	B-1	B-2
9-story NCBF					
9	W12×40 (0.1)	W12×40	W12×40 (0.8)	W12×40 (0.4)	W12×40
8	W12×40 (0.1)	W12×40	W12×40 (1.9)	W12×40 (1.0)	W12×40
7	W12×45 (0.2)	W12×50	W12×50 (1.6)	W12×65 (0.8)	W12×72
6	W12×45 (1.1)	W12×50	W12×50 (2.7)	W12×65 (1.2)	W12×72
5	W12×79 (0.5)	W12×65	W12×65 (1.7)	W12×106 (1.0)	W12×106
4	W12×79 (1.1)	W12×65	W12×65 (2.4)	W12×106 (1.3)	W12×106
3	W12×120 (0.7)	W12×79	W12×79 (2.0)	W12×170 (1.0)	W12×136
2	W12×120 (1.1)	W12×79	W12×79 (2.8)	W12×170 (1.2)	W12×136
1	W12×120 (1.1)	W12×96	W12×96 (2.3)	W12×190 (1.2)	W12×152
9-story SCBF					
9	W12×45 (0.1)	W12×45	W12×96 (0.3)	W12×50 (0.3)	W12×40
8	W12×45 (0.1)	W12×45	W12×96 (0.6)	W12×50 (0.8)	W12×40
7	W12×45 (0.2)	W12×45	W12×120 (0.5)	W12×96 (0.4)	W12×53
6	W12×45 (0.6)	W12×45	W12×120 (0.8)	W12×96 (0.7)	W12×53
5	W12×96 (0.2)	W12×96	W12×170 (0.6)	W12×136 (0.6)	W12×72
4	W12×96 (0.4)	W12×96	W12×170 (0.8)	W12×136 (0.8)	W12×72
3	W12×96 (0.4)	W12×96	W12×230 (0.6)	W12×210 (0.6)	W12×96
2	W12×96 (0.6)	W12×96	W12×230 (0.8)	W12×210 (0.8)	W12×96
1	W12×96 (0.6)	W12×96	W12×230 (0.8)	W12×230 (0.8)	W12×106

Note: Example column locations shown; same sections for typical column locations.
[a]DCR shown in parentheses if column is part of CBF and develops excessive compressive forces under expected brace forces

Table 5.7: Archetype NCBF Connection Deficiencies

Story	Brace-to-gusset weld DCR	Gusset-plate interface weld fracture rotation, θ_f (rad)	Approx. gusset-plate rotation at 2% drift, $\theta_{2\%}$ (rad)	$\theta_{2\%}/\theta_f$
3-story paired single diagonal				
3	1.30	0.156	0.143	0.92
2	1.76	0.154	0.144	0.93
1	1.84	0.110	0.141	1.28
3-story chevron				
3	1.26	0.130	0.155	1.19
2	1.76	0.118	0.155	1.31
1	1.32	0.092	0.151	1.64
9-story paired single diagonal				
9	1.59	0.243	0.147	0.60
8	1.25	0.132	0.147	1.09
7	1.33	0.061	0.147	2.42
6	1.33	0.061	0.147	2.42
5	1.34	0.054	0.148	2.77
4	1.34	0.054	0.148	2.77
3	1.34	0.061	0.148	2.44
2	1.62	0.061	0.148	2.44
1	1.62	0.061	0.144	1.96
9-story chevron				
9	1.19	0.106	0.155	1.46
8	1.51	0.086	0.155	1.81
7	1.36	0.080	0.155	1.94
6	1.26	0.087	0.155	1.78
5	1.26	0.077	0.155	2.01
4	1.11	0.086	0.156	1.82
3	1.11	0.081	0.156	1.93
2	1.11	0.088	0.156	1.77
1	1.11	0.085	0.154	1.80

Table 5.8: Hazard-Level Descriptions

Probability of exceedance	Return period (yr)	Comment
1%/50-yr	4975	Extreme hazard level intended to help characterize collapse performance
2%/50-yr	2475	Maximum Considered Earthquake (MCE) in *ASCE 7-16* (note that the MCE_R is adjusted from this hazard level)
5%/50-yr	975	Approximation of design-level earthquake ($\frac{2}{3}MCE_R$) for Seattle in *ASCE 7-16*
10%/50-yr	475	Intermediate-level earthquake often used in prior work (e.g., FEMA (2000))
50%/30-yr	43	Seviceability-level earthquake where most structures remain essentially elastic

Table 5.9: Performance-State Expressions

Characteristic	Performance state			
	No structural repair	Component repair	Component replacement	Potential collapse
Brace-gusset assembly				
Demand limit	–	$\frac{\delta_{range}}{\delta_y} > 3.7\left(\frac{\lambda}{\lambda_{hd}}\right)^{-1.74}$	$\frac{\delta_{range}}{\delta_y} > 7.3\left(\frac{\lambda}{\lambda_{hd}}\right)^{-1.74}$ –or– $MSR > MSR_f$ –or– $\theta_{gp} > \theta_{gp,f}$ –or– $\Delta_{weld} > \Delta_u$	–
Expected damage	Yielding of gusset plates	Tearing of gusset-plate interface welds	Local cupping of brace at midspan –or– Tearing and/or fracture of brace at midspan –or– Fracture of gusset-plate interface weld(s) –or– Fracture of brace-to-gusset weld	–
Repair measure	Heat-straighten gusset plate	Repair gusset-plate interface welds	Replace brace and gusset plates	–
Column (buckling)				
Demand limit	–	$\frac{z}{b_f} > 0.1$	–	$\frac{z}{b_f} > 1$
Expected damage	–	Visible buckling of column	–	Severe buckling of column and potential instability under gravity loads
Repair measure	–	Reinforce or encase column to increase resistance	–	–
Beam (chevron configuration)				
Demand limit	–	$\frac{\Delta_{bm}}{L_{bm}} > 1.5\%$	–	–
Expected damage	Beam yielding	Local buckling and residual deflection	–	–
Repair measure	–	Heat-straighten regions with local buckling and level slab	–	–
Composite, bolted shear plate (gravity connection)				
Demand limit	–	$\theta_{sp} > 0.03$ rad	$\theta sp > 0.04$ rad	$\theta_{sp} > \theta_{sp,f}$ –or– $\frac{\Delta_{story}}{H} > 8\%$
Expected damage	Bolt slip and plate yielding	Bolt/bolt-hole deformation	Severe bolt/bolt-hole deformation, concrete crushing	Binding of beam and column flanges; fracture of shear plate, weld, or bolts –or– Severe yielding and potential tearing of columns adjacent to connection
Repair measure	–	Replace bolts	Replace shear plate and bolts	–

Table 5.10: Brace Local Cupping Initiation Data

Specimen	Brace	L (mm)	E/F_y	$\lambda = b/t$	λ_{hd}	λ/λ_{hd}	δ_y (%)	$\delta_{range,lc}$ (%)
NCBF-2E	HSS7×7×1/4	4232	450	27.0	13.8	1.96	0.22	0.49
NCBF-3E	HSS6×6×1/4	4249	494	22.7	14.4	1.57	0.20	0.65
NCBF-8I	HSS6×4×3/8	3627	459	14.2	13.9	1.02	0.22	2.01
NCBF-9O	HSS5×5×3/8	4440	468	11.3	14.1	0.80	0.21	2.16
NCBF-4O-W	HSS5×5×3/8	4244	506	11.3	14.6	0.77	0.20	2.39
NCBF-8O-W	HSS5×5×3/8	4173	430	11.3	13.5	0.84	0.23	1.92

Chapter 6
SEISMIC PERFORMANCE OF BENCHMARK BUILDINGS

Quantifying the vulnerability of NCBFs relative to SCBFs is important to understanding potential seismic retrofit needs. The building models and multiple-stripe analysis framework discussed in Chapter 5 were implemented in *OpenSees* to achieve this objective by benchmarking NCBF and SCBF seismic performance using nonlinear response-history analysis. These analyses were conducted using high-performance computing resources at the Texas Advanced Computing Center provided through DesignSafe-CI (NSF Grant No. CMMI-1520817, NHERI Cyberinfrastructure) (Rathje et al. 2017). A brief review of the study-building characteristics is provided here, and the NCBF building deficiencies are reframed with respect to the retrofit priority established from the experimental research in Chapter 3. Then, the results of the analyses are discussed, including nonconvergence issues encountered, drift and base-shear demand, damage progression, and performance evaluation.

6.1 Study Overview

The three- and nine-story NCBF and SCBF buildings described in Chapter 5 were modeled in *OpenSees* and subjected to five ground-motion suites representing hazard return periods between 43 and 4,975 years. These buildings are intended to represent code-compliant buildings based on either *UBC-79* (ICBO 1979) or *ASCE/SEI 7-16* (ASCE 2017a) and are hence referred to as benchmark buildings. As such, the benchmark NCBFs were not designed to target a specific deficiency and had locally slender HSS braces ($\lambda/\lambda_{hd} > 1.0$), nonductile brace and gusset-plate connections, and relatively weak beams and columns compared to modern, capacity-based design requirements. These deficiencies are described in detail in Chapter 5 and summarized in Table 6.1. The benchmark SCBFs fully met the requirements

of the current *Seismic Provisions* (AISC 2017a).

Table 6.1: Benchmark Analysis Matrix

Building	Brace local slenderness ratio, λ/λ_{hd}	Brace-to-gusset weld fracture DCR	Gusset-plate interface weld fracture rotation, θ_f (rad)	Column buckling DCR[a]	Chevron beam yielding DCR
NCBF					
3-story paired single diagonal	1.6–2.0	1.3–1.8	0.11–0.16	0.5–2.0	–
3-story chevron	1.6–1.8	1.3–1.8	0.092–0.13	0.3–1.3	2.2–2.5
9-story paired single diagonal	1.6–2.2	1.3–1.6	0.061–0.24	0.1–2.8	–
9-story chevron	1.7–2.2	1.1–1.5	0.077–0.11	0.4–1.3	1.5–2.7
SCBF					
3-story paired single diagonal	0.8–0.9	< 0.75	N/A	0.2–0.7	–
3-story chevron	0.8–0.9	< 0.75	N/A	0.2–0.8	0.5–0.7
9-story paired single diagonal	0.7–0.9	< 0.75	N/A	0.1–0.8	–
9-story chevron	0.7–0.9	< 0.75	N/A	0.3–0.8	0.1–0.8

[a]Experimental retrofit priority not investigated
Experimental retrofit priority:
■ High
■ Moderate

In the experimental research described in Chapter 3, a retrofit priority was developed to provide preliminary guidance for identifying key deficiencies. This retrofit priority is reproduced in Table 6.2, and moderate- and high-priority deficiencies are highlighted in Table 6.1. The gusset-plate interface weld fracture DCR and elliptical clearance retrofit priorities are combined in Table 6.2 using Eq. 4.11 to formulate this deficiency in terms of fracture rotation (θ_f), since this is used as the gusset-plate interface weld fracture criterion in the numerical models. Note that the benchmark NCBFs do not have secondary yielding mechanisms, and thus gusset-plate interface weld fracture results in Type-B behavior. The effects of a secondary yielding mechanism are investigated parametrically in Chapter 7.

As Table 6.1 indicates, the benchmark NCBF buildings all have brace local slenderness and connection deficiencies which are severe enough to be considered high priorities for retrofit based on analysis of experimental results. These deficiencies result in distinct, premature failure modes based on different criteria (brace strain range, brace-to-gusset weld

Table 6.2: Retrofit Priority

Criterion	Low	Moderate	High
Yielding mechanisms			
Whitmore yielding (30°)	DCR $\leq$ 1.3	(DCR $>$ 1.3)	
Chevron beam yielding	DCR $\leq$ 2.3	(DCR $>$ 2.3)	
Failure modes			
Brace-to-gusset-plate weld fracture	DCR $\leq$ 0.8	0.8 $<$ DCR $\leq$ 1.0	DCR $>$ 1.0
Gusset-plate interface weld fracture	$\theta_f \geq 0.18$	$0.11 \leq \theta_f < 0.18$	$\theta_f < 0.11$
Geometric limits			
Rectangular HSS brace local slenderness	$\lambda/\lambda_{hd} \leq 1.2$	$1.2 < \lambda/\lambda_{hd} \leq 1.6$	$\lambda/\lambda_{hd} > 1.6$

deformation, and gusset-plate rotation). As a result, it is unclear which deficiencies control the nonlinear dynamic response of a given structure. The chevron NCBFs have beam DCRs above the low-priority retrofit level, but it is unclear from the experimental work if these DCRs are moderate- or high-priorities for retrofit. Quantifying the seimsic vulnerability of existing NCBFs relative to SCBFs and clarifying retrofit-priority limits are expected outcomes of this work.

6.2 Analysis Nonconvergence

The benchmark NCBF building models were especially prone to nonconvergence prior to the development of any of the potential-collapse performance states when subjected to strong ground motions. This was due in part to the complexity of the benchmark NCBF models, which were required to simulate buckling of braces and weak columns, fracture of braces, fracture of brace-to-gusset welds, and fracture of gusset-plate interface welds. These phenomena result in large, rapid changes in strength and stiffness that can lead to numerical instability. Table 6.3 reports the percentage of analyses which did not converge at each hazard level for each building archetype. The 9-story benchmark NCBFs had the highest rates of nonconvergence, which may be attributed to the computational difficulty of analyzing such large models in *OpenSees*. For reference, the 3- and 9-story paired single diagonal

Table 6.3: Nonconvergence Summary

Return period (yr)	Nonconverged analyses (%)	
	NCBF	SCBF
3-story paired single diagonal		
43	0	0
475	0	0
975	0	0
2475	0	0
4975	2	0
3-story chevron		
43	0	0
475	12	0
975	18	0
2475	17	0
4975	12	0
9-story paired single diagonal		
43	0	0
475	35	0
975	80	0
2475	95	0
4975	98	3
9-story chevron		
43	0	0
475	5	0
975	23	0
2475	37	0
4975	33	0

NCBF model had 375 and 1,469 nodes, respectively, and each node has 6 potential degrees of freedom.

In some cases, nonconvergence arises due to dynamic instability and collapse of the structure. However, all cases of nonconvergence do not imply structural collapse. Modeling and analysis decisions, including element formulation, structural damping scheme, nonlinear solution algorithm, convergence criteria (test type, tolerance, and maximum number of iterations), integration scheme, and others all potentially affect nonconvergence. Since the data from nonconverged analyses cannot be easily or confidently interpreted to characterize per-

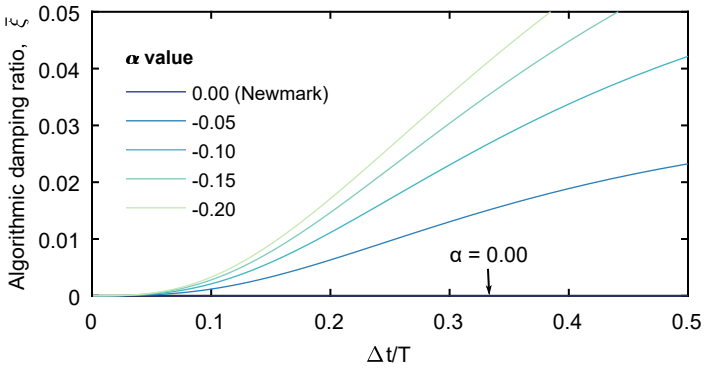

Figure 6.1: Algorithmic damping ratio using the HHT integration method

formance, cases of nonconvergence are reported alongside the potential collapse performance state.

Some analyses did not converge prior to the development of strong ground acceleration within less than 0.5 seconds from the start of the record. This nearly instantaneous numerical instability was observed on high-performance computing (HPC) resources, but identical analyses performed on desktop computers completed successfully. To aid numerical stability on HPC resources, a small amount of numerical damping was introduced using the Hilber-Hughes-Taylor (HHT) integration scheme (Hilber et al. 1977). The HHT method is a generalization of the Newmark method, which has no numerical damping and was used preferentially throughout this study unless early numerical instability was encountered.

The HHT method introduces numerical damping at higher modes but not lower modes. Figure 6.1 shows the algorithmic damping ratio, $\bar{\xi}$, with respect to the time-step-to-period ratio ($\Delta t/T$). The algorithmic damping ratio is asymptotic to zero for small $\Delta t/T$ and therefore the damping ratio is lower for longer periods. For negative values of α, a parameter of the HHT method, the algorithmic damping ratio increases with $\Delta t/T$.

An appropriate α value for this study was required to be large enough to provide numerical stability but small enough to avoid drastically affecting structural response. A trial α value of -0.05 was investigated using the 9-story paired single diagonal SCBF archetype building

subjected to the 475-yr and 2,475-yr ground-motion suites. The use of the HHT method eliminated all early numerical instability issues for this building (4 cases at the 475-yr level and 8 cases at the 2,475-yr level).

Figure 6.2 shows the difference in maximum story drift for all ground motions which converged and did not reach the potential collapse performance state when employing the Newmark and HHT methods. The difference in maximum story drift was negligible for the 475-yr ground motions. At the 2,475-yr hazard level, the difference in maximum story drift was less than 0.14% in all but one ground motion. The first-story drift response history for this ground motion (RSN 5818) is shown in Fig. 6.3. The first-story response was identical up to about 17 seconds, after which the response was similar but shifted lower by approximately 1.5% story drift when using the HHT method. This shift did not correspond to any change in component performance state. Overall, the difference in response between the Newmark and HHT methods was judged to be appropriately small to justify the use of an α value of -0.05.

6.3 Drift and Base-Shear Demand

6.3.1 Maximum Story Drift

Table 6.4 provides median (50th percentile) and 84th percentile statistics for the maximum story drift reported in the buildings at each hazard level. The median of the maximum story drifts for each ground-motion suite are shown in graphical form in Fig. 6.4. If the data are normally distributed, the median is equal to the mean and the 84th percentile is one standard deviation larger than the mean. The true mean and standard deviations are not reported, since these values would be skewed by collapse data. Story drifts larger than 8% are reported as "C" in the table, since this threshold is associated with potential collapse; the models are not validated for such large deformations, and experiments provide no evidence that such deformations can be tolerated. Story drifts are reported as "NC" for cases where 50th or 84th percentile include nonconvergence. If both potential collapse and nonconvergence cases

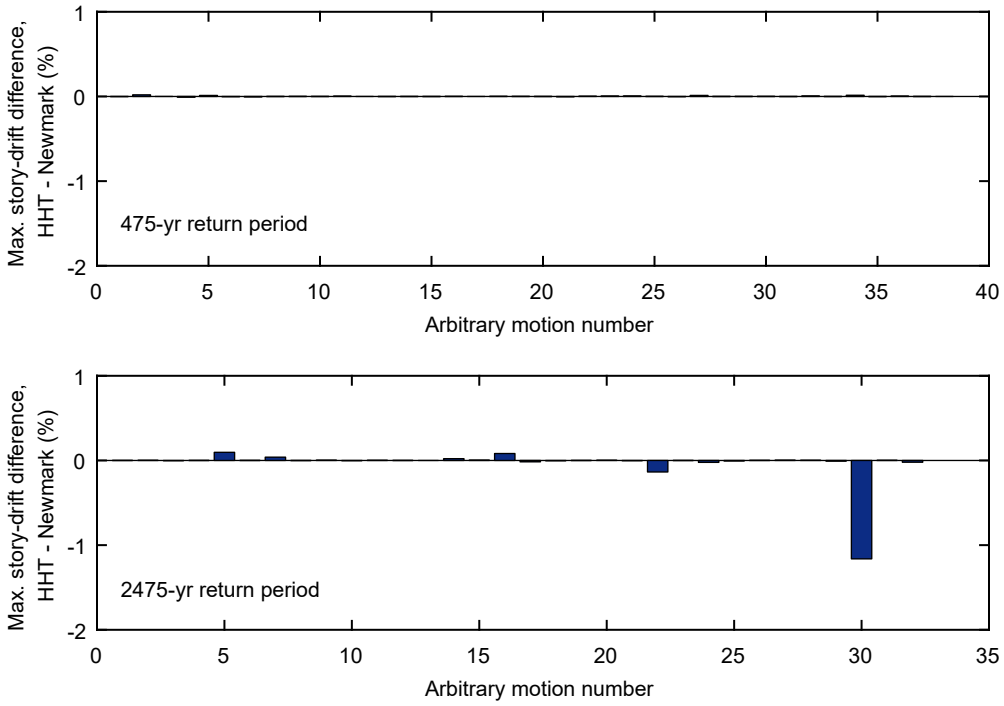

Figure 6.2: Difference in maximum story drift using Newmark and HHT integration methods

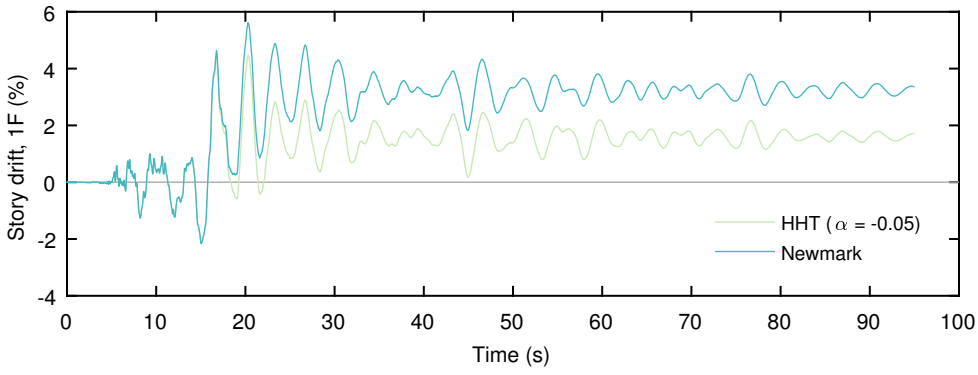

Figure 6.3: First-story response of 9-story paired single diagonal SCBF using Newmark and HHT integration methods

fall within the 50th or 84th percentile, the story drift is reported as "C/NC."

The ratio of the median NCBF and SCBF story drifts are shown in Table 6.4 to relate the average deformation demands for the two systems. As expected, the maximum story drifts were generally higher in the NCBF buildings (ratio greater than unity), especially at more severe hazard levels. Notably, more than half of the NCBFs either reached the potential collapse performance state or had nonconvergence at the 2,475-yr return period and above. At lower hazard levels, the largest difference in story drift between the NCBFs and SCBFs occurred in the 9-story chevron frames, where the maximum story drift was 5 times higher on average for the 975-yr return-period ground motions.

6.3.2 Vertical Distribution of Drift

Work by previous researchers has shown that NCBFs are vulnerable to soft-story collapse (e.g., Balazadeh-Minouei et al. (2018a)), and hence the vertical distribution of story drift is important to quantify for the benchmark buildings. Figures 6.5 and 6.6 plot the story-drift distribution for the 3- and 9-story buildings, respectively, for each ground motion at the 2,475-yr return-period hazard level. The median and 84th percentile drift at each story is highlighted, and cases of nonconvergence are excluded from these plots.

In the 3-story benchmark NCBF- and SCBF-building results shown in Fig. 6.5, drift was almost entirely concentrated in the first story. On average, the story drifts exceeded the threshold for the potential-collapse performance state (8%) in the NCBFs, indicating a high probability of soft-story collapse at this hazard level. The SCBFs were less vulnerable to collapse, as the 84th-percentile story drifts did not exceed 8%. However, several ground motions caused soft-story collapse of the chevron SCBF.

The nine-story NCBF and SCBF buildings were also vulnerable to the formation of soft stories, as shown in Fig. 6.6. Due to the high percentage of analyses which did not converge for the nine-story paired single diagonal NCBF, the drift distribution could not be determined. Drift in the nine-story chevron NCBF was primarily concentrated at the first and ninth stories. Most instances of soft-story collapse occurred at the first story; only one

Table 6.4: Maximum Story-Drift Statistics

Return period (yr)	Maximum story drift (%)				
	NCBF		SCBF		Comparison
	Median	84th percentile	Median	84th percentile	$\frac{\text{Median}_{\text{NCBF}}}{\text{Median}_{\text{SCBF}}}$
3-story paired single diagonal					
43	0.10	0.14	0.10	0.14	1.02
475	1.46	2.36	0.56	0.71	2.59
975	2.41	C	0.89	1.33	2.72
2475	C	C	1.68	2.92	–
4975	C	C	4.30	C	–
3-story chevron					
43	0.13	0.18	0.10	0.13	1.33
475	0.94	C/NC	0.64	0.95	1.47
975	2.12	C	1.06	2.82	2.00
2475	C	C	3.63	5.48	–
4975	C	C	7.46	C	–
9-story paired single diagonal					
43	0.10	0.13	0.11	0.13	0.92
475	0.68	NC	0.67	0.86	1.00
975	NC	NC	1.06	1.48	–
2475	NC	NC	1.53	2.27	–
4975	NC	NC	5.13	C	–
9-story chevron					
43	0.08	0.10	0.08	0.10	0.99
475	1.25	2.99	0.57	0.76	2.19
975	4.58	4.42	0.92	1.37	4.96
2475	C/NC	C	1.42	3.42	–
4975	C	C	5.75	C	–

C = Potential collapse; NC = Nonconvergence; C/NC = Potential collapse or nonconvergence

ground-motion caused soft-story collapse of the ninth story. The nine-story SCBFs had more uniform vertical distribution of story drift than their three-story counterparts, but both the paired single diagonal and chevron archetypes had instances of soft-story collapse at the first story.

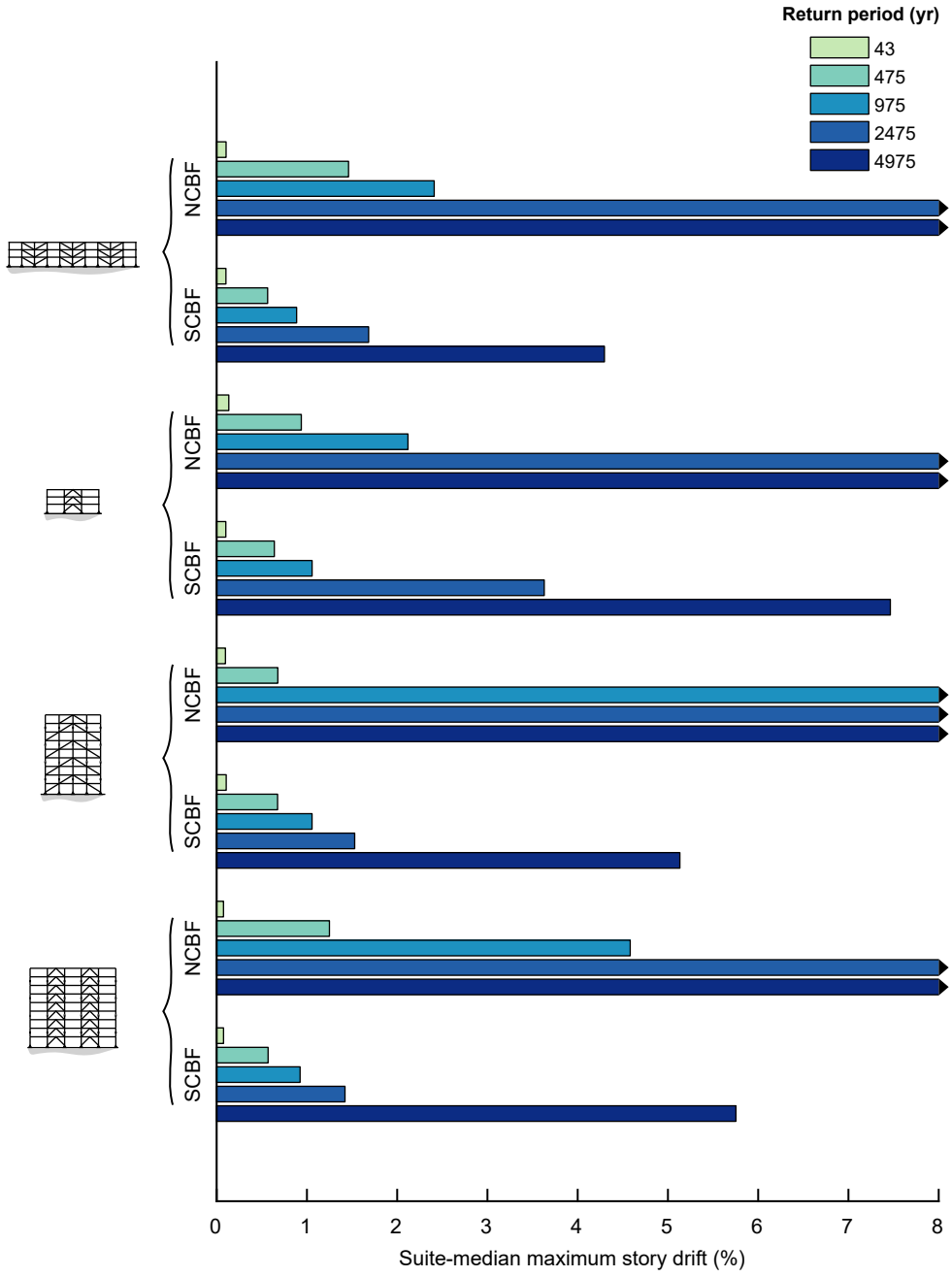

Figure 6.4: Median of maximum story drift at each hazard level

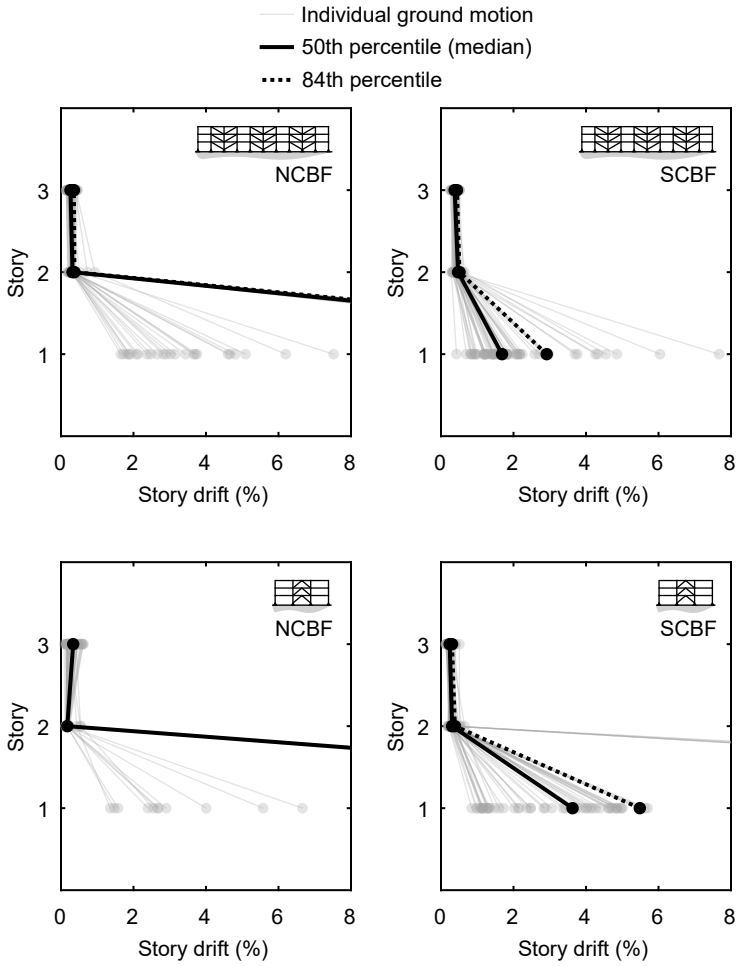

Figure 6.5: Story-drift distribution in three-story archetype buildings for 2475-year hazard

6.3.3 Deflection Amplification Factors

In modern seismic design using the Equivalent Lateral Force (ELF) procedure in *ASCE/SEI 7-16*, story drifts must not exceed the specified limit, which is usually 2.0 to 2.5% for SCBFs in Risk Category I or II (ASCE 2017a). These story drifts are clearly in the inelastic range but are checked using elastic analysis of the structure under the ELF procedure forces. The elastic story drifts, Δ_e, from this analysis are multiplied by a deflection amplification factor, C_d, and compared to the limiting story drift to check the design. The C_d value for SCBFs

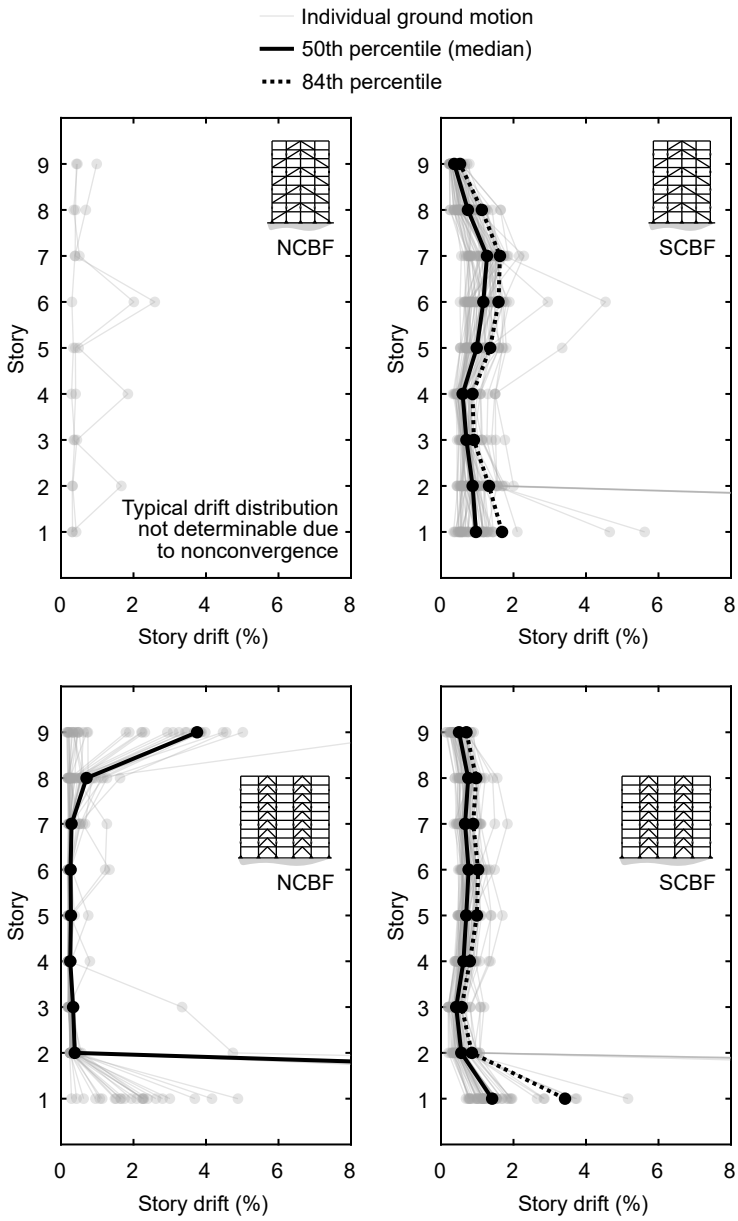

Figure 6.6: Story-drift distribution in nine-story archetype buildings for 2475-year hazard

is 5 in *ASCE/SEI 7-16*, but prior work by Hsiao et al. (2013b) showed that the actual relative drift demands at the 2,475-yr hazard level (i.e., MCE shaking) may be much larger on average, corresponding to deflection amplification factors on the order of 15 to 20 for 3-

and 9-story SCBFs.

To build upon this prior work and evaluate the relative drift demands of the benchmark NCBFs, similar deflection amplification factors are reported in Table 6.5, where, Δ_{max} is the maximum story drift computed from response-history analysis at the 2,475-yr hazard level and Δ_e is the story drift computed from elastic analysis under the modern design forces. The same forces were used to calculate Δ_e for the NCBFs and SCBFs, since these archetypes have identical seismic weights and geometries, resulting in the same approximate period for design.

As noted in Table 6.5, more than 50% of the ground motions at this hazard level resulted in potential collapse or nonconvergence for the benchmark NCBFs. Therefore, median deflection amplification factors could not be computed for these structures. However, Fig. 6.7 shows empirical cumulative probability functions for Δ_{max}/Δ_e for these buildings, and it can be seen that the drift demands result in amplification factors well above those for the SCBFs.

With the exception of the 9-story paired single diagonal building, median deflection amplification factors for the SCBFs were similar in order of magnitude to those reported by Hsiao et al. (2013b): between 13 and 26. The 9-story paired single diagonal SCBF had abnormally large amplification factors because the elastic story drift was very small (0.01%) on the ninth story, but this story sustained inelastic deformations at the 2,475-yr return period. Further, this factor is misleading since the 9th story's inelastic deformations were less than those of all other stories on average.

6.3.4 Overstrength Factors

The overstrength factor, Ω_0, describes lateral resistance relative to the design demands (a force analog to C_d). In *ASCE 7-16*, Ω_0 is specified as 2 for SCBFs (ASCE 2017a). Hsiao et al. (2013b) also computed overstrength factors for SCBFs, which were between 2.0 and 2.5 at the base of the 3- and 9-story buildings. Base-shear overstrength factors were computed for the benchmark NCBF and SCBF buildings here at the 2,475-yr hazard level and are shown

Table 6.5: Analysis Story-Drift Demands

Story	NCBF			SCBF		
	Δ_e (%)	Median Δ_{max} (%)	Median Δ_{max}/Δ_e	Δ_e (%)	Median Δ_{max} (%)	Median Δ_{max}/Δ_e
3-story paired single diagonal						
3	0.10	C/NC	C/NC	0.08	0.38	5.0
2	0.14	C/NC	C/NC	0.10	0.47	4.7
1	0.15	C/NC	C/NC	0.12	1.68	14
3-story chevron						
3	0.13	C/NC	C/NC	0.09	0.24	2.8
2	0.15	C/NC	C/NC	0.12	0.31	2.5
1	0.19	C/NC	C/NC	0.14	3.63	26
9-story paired single diagonal						
9	0.02	C/NC	C/NC	0.01	0.37	56
8	0.04	C/NC	C/NC	0.05	0.80	17
7	0.12	C/NC	C/NC	0.15	1.34	8.7
6	0.08	C/NC	C/NC	0.11	1.17	11
5	0.13	C/NC	C/NC	0.18	0.99	5.5
4	0.11	C/NC	C/NC	0.13	0.60	4.6
3	0.14	C/NC	C/NC	0.17	0.70	4.0
2	0.11	C/NC	C/NC	0.16	0.87	5.4
1	0.09	C/NC	C/NC	0.12	0.97	8.0
9-story chevron						
9	0.05	C/NC	C/NC	0.04	0.53	13
8	0.07	C/NC	C/NC	0.08	0.81	9.9
7	0.08	C/NC	C/NC	0.09	0.68	7.3
6	0.09	C/NC	C/NC	0.12	0.81	6.9
5	0.10	C/NC	C/NC	0.13	0.73	5.7
4	0.10	C/NC	C/NC	0.14	0.62	4.5
3	0.11	C/NC	C/NC	0.11	0.42	3.8
2	0.12	C/NC	C/NC	0.11	0.56	5.0
1	0.12	C/NC	C/NC	0.12	1.41	12

Note: Δ_e = Story drift from elastic analysis under design ELFs from *ASCE 7-16*; Δ_{max} = Maximum story drift from response-history analysis for 2,475-year hazard; C/NC = Collapse or nonconvergence

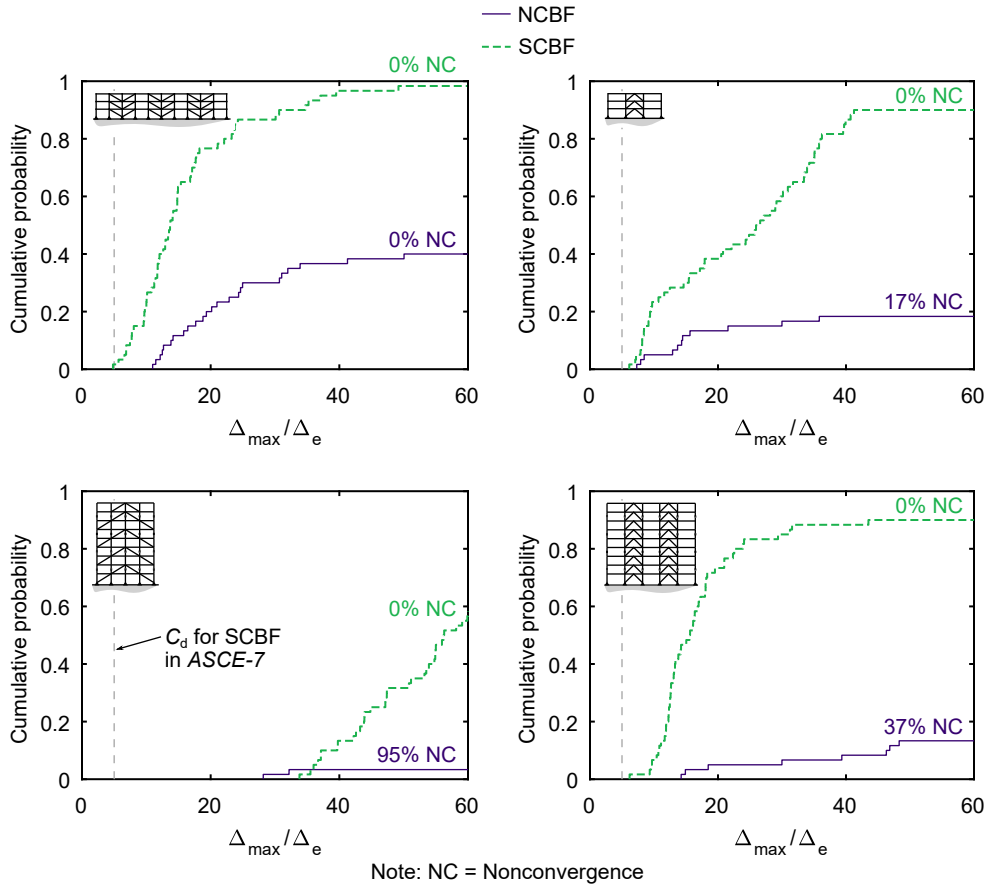

Figure 6.7: Deflection amplification factors for the 2,475-year hazard

in Table 6.6 and Figure 6.8. For the NCBFs, the maximum base shear from the response-history analyses were normalized by both the *UBC-79* (ICBO 1979) and *ASCE/SEI 7-16* (ASCE 2017a) base shears, respectively referred to as V_{1979} and V_{2016}. As noted above, the design base shear in *ASCE/SEI 7-16* would be identical for the NCBF and SCBF buildings based on the ELF procedure.

The 3-story NCBF buildings were substantially weaker than their SCBF counterparts (50 to 60% of the SCBF strength), which is attributable to the large difference in short-period (less than 1 second) design spectral accelerations in *UBC-79* and *ASCE/SEI 7-16* (see Fig. 5.7). In contrast, there was little difference in the 9-story NCBF and SCBF strengths,

Table 6.6: Analysis Base-Shear Demands

Archetype	V_{1979} (kN)	V_{2016} (kN)	NCBF			SCBF	
			Median V_{max} (kN)	Median V_{max}/V_{1979}	Median V_{max}/V_{2016}	Median V_{max} (kN)	Median V_{max}/V_{2016}
3-story paired single diagonal	2589	4528	8091	3.1	1.8	14087	3.1
3-story chevron	2589	4528	4479	1.7	0.99	9492	2.1
9-story paired single diagonal	4595	4065	11507	2.5	2.8	10929	2.7
9-story chevron	4595	4065	11436	2.5	2.8	11520	2.8

Note: V_{max} = Maximum base shear from response-history analysis for 2,475-year hazard; nonconvergence cases excluded when computing median

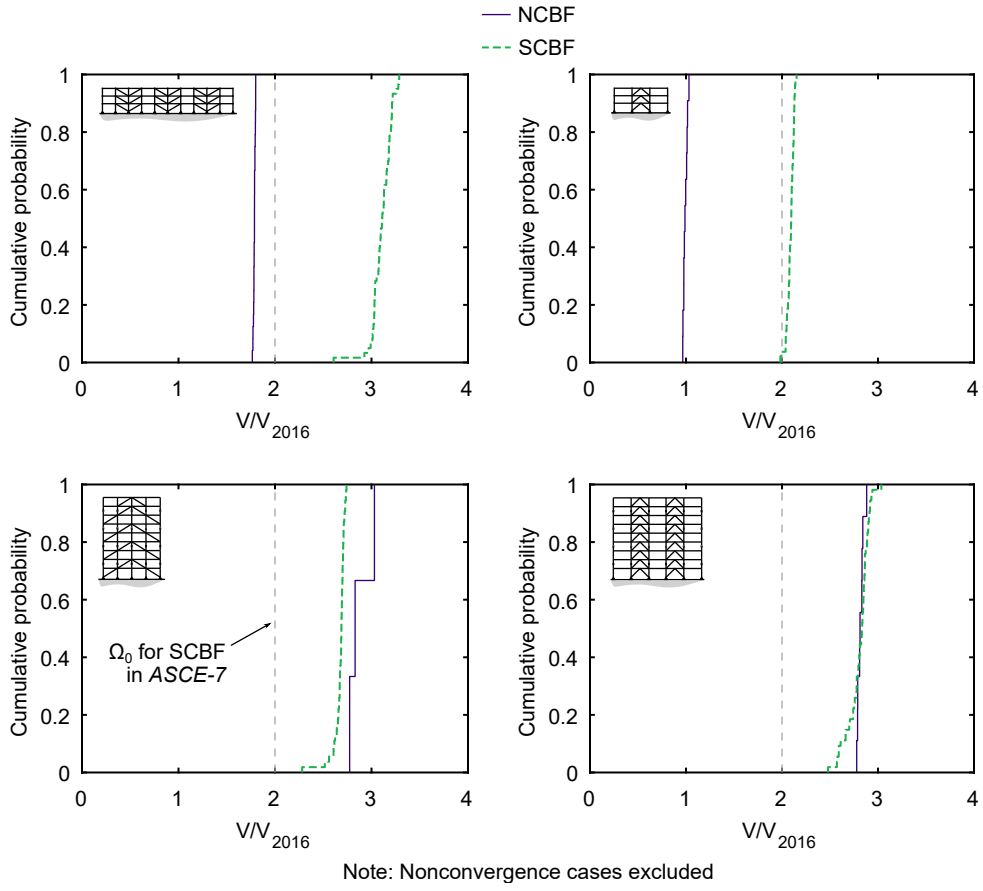

Figure 6.8: Base-shear overstrength factors for 2475-year hazard

which is due to the close similarity of the corresponding design spectra at longer periods (at least 1 second).

The overstrength of the NCBF buildings were betwween 1.7 and 3.1 with respect to *UBC-79* base shear due to the 5/4 increase in design base shear required for CBFs, the large factor of safety applied for brace buckling resistance, and material overstrength. The NCBFs could also develop (or very nearly develop in the case of the 3-story chevron) the design strength from *ASCE/SEI 7-16* (ASCE 2017a). The SCBFs had similar overstrength relative to their respective building codes, sustaining 2.1 to 3.1 times V_{2016}. These values are larger than Ω_0 and consistent with the findings from Hsiao et al. (2013b) for SCBFs.

6.4 Damage Progression

Individual building response histories are plotted in Figs. 6.9 and 6.10 to understand damage progression in the benchmark buildings, including the sequence of yielding and failure. Each plot compares NCBF and SCBF response for the ground motions scaled to the 2,475-yr hazard level. Only the first-story drift history and first-story hysteresis are shown, since Figs. 6.5 and 6.6 showed that damage tended to concentrate on the first story.

Figure 6.9 shows the highly nonductile response of the 3-story paired single diagonal NCBFs, which both reached the potential collapse performance state. The paired single diagonal frame had brace-to-gusset weld fracture and gusset-plate interface weld fracture, while the chevron frame had gusset-plate interface weld fracture and brace fracture. In both 3-story NCBFs, these fracture events occurred in quick succession. The 3-story SCBFs developed the intended failure mode: delayed brace fracture.

The 9-story NCBFs had very different behavior from the 3-story NCBFs. First, the 9-story paired single diagonal building did not converge under the selected ground motion, which was common for this building and ground-motion intensity. Second, the 9-story chevron building had relatively ductile behavior after brace-to-gusset weld fracture because the relatively weak beam (DCR of 1.6) limited tensile demand in the opposing brace and prevented a second failure mode from developing. The relatively full hysteresis for the NCBF

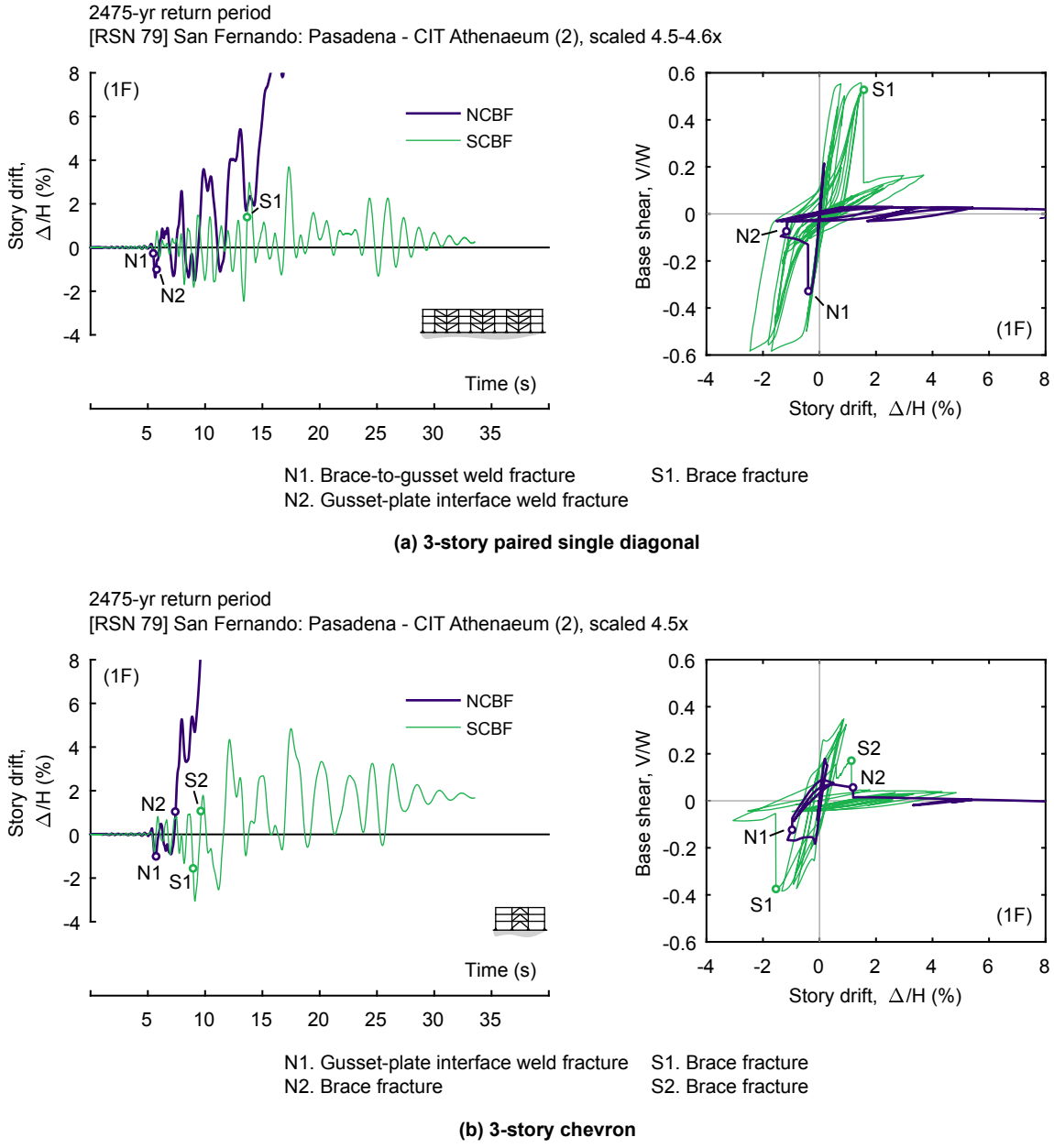

Figure 6.9: Example response history and hysteresis for 3-story NCBF and SCBF buildings

in Fig. 6.10b is due to beam yielding in this secondary, long-link-EBF mechanism. From Table 6.1, the brace-to-gusset weld DCRs were somewhat lower in the 9-story chevron compared to the other buildings, which also helped mitigate connection fracture.

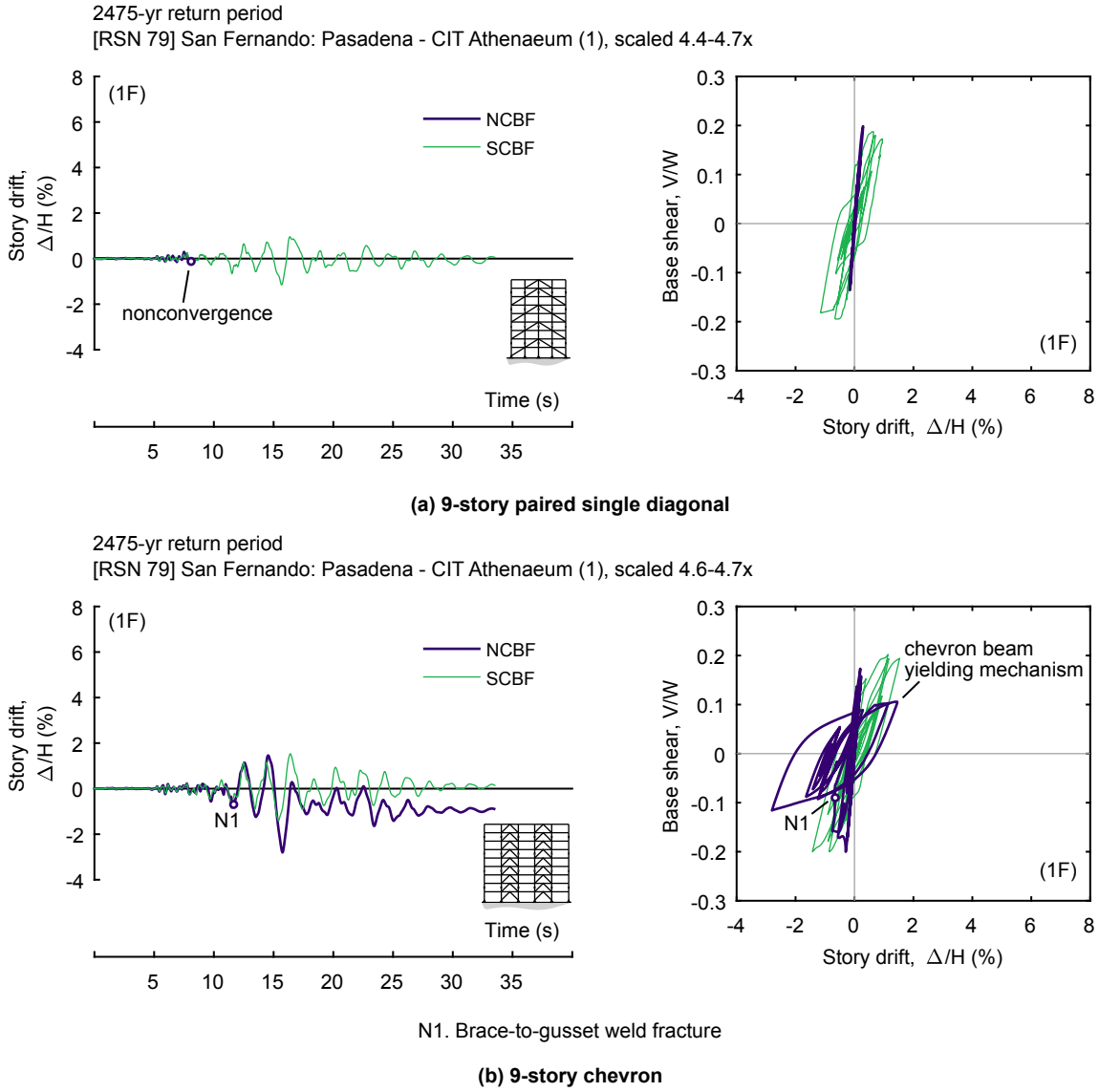

Figure 6.10: Example response history and hysteresis for 9-story NCBF and SCBF buildings

None of the SCBFs shown in Figs. 6.9 or 6.10 reached the potential collapse performance state for the selected ground motions, though brace buckling was evident in each. The intended failure mode of delayed brace fracture occurred at the first story of the 3-story SCBFs.

6.5 Performance Evaluation

Figure 6.11 shows the probabilities of exceedance of brace-gusset assembly damage states for the eight systems (three- or nine-story buildings, paired single diagonal or chevron, and NCBF or SCBF). The small building elevation drawings in the figures key the plots on each row to the corresponding building height and brace configuration. The buildings were essentially elastic at the 43-year return-period hazard level, with median story drifts no larger than 0.14% in any of the buildings as shown in Table 6.4. The NCBF buildings had locally slender braces (Table 5.3) and multiple connection deficiencies (Table 6.1), which corresponded to very high probabilities of brace-gusset assembly repair (nearly 100%) and replacement (greater than 52%) at ground-motion return periods of at least 475 years. This indicates the NCBFs are prone to significant damage in less severe but more frequent earthquakes. On the other hand, the probability of brace-gusset assembly replacement damage was not appreciable in the SCBF buildings until the 975-year return-period hazard level. Note also that the SCBFs have significant differences between probabilities of brace-gusset assembly repair and replace damage states while the NCBFs do not; this indicates that the brace-gusset assembly failure mode (i.e., delayed brace fracture in SCBFs) is relatively ductile compared to the brittle NCBF brace and connection failure modes.

Figure 6.12 shows performance-state probabilities of exceedance for the columns in each of the buildings. Column buckling was rare in the chevron NCBFs despite having DCRs greater than 1.0 (Tables 5.5 and 5.6), since the relatively weak beams limited the axial demands on the column through the yielding-beam mechanism. Column buckling was most prevalent in the 9-story paired single diagonal SCBF even though the columns were designed to develop the expected brace forces. This particular frame had braces oriented in a multi-story, multi-bay chevron configuration. The central column in this configuration is susceptible to large unbalanced brace forces, similar to a beam in a chevron CBF. Even so, ths magnitude of buckling was not severe enough in the SCBF to reach the potential collapse damage state.

Figure 6.13 provides performance-state probabilties of exceedance for shear plates. Shear

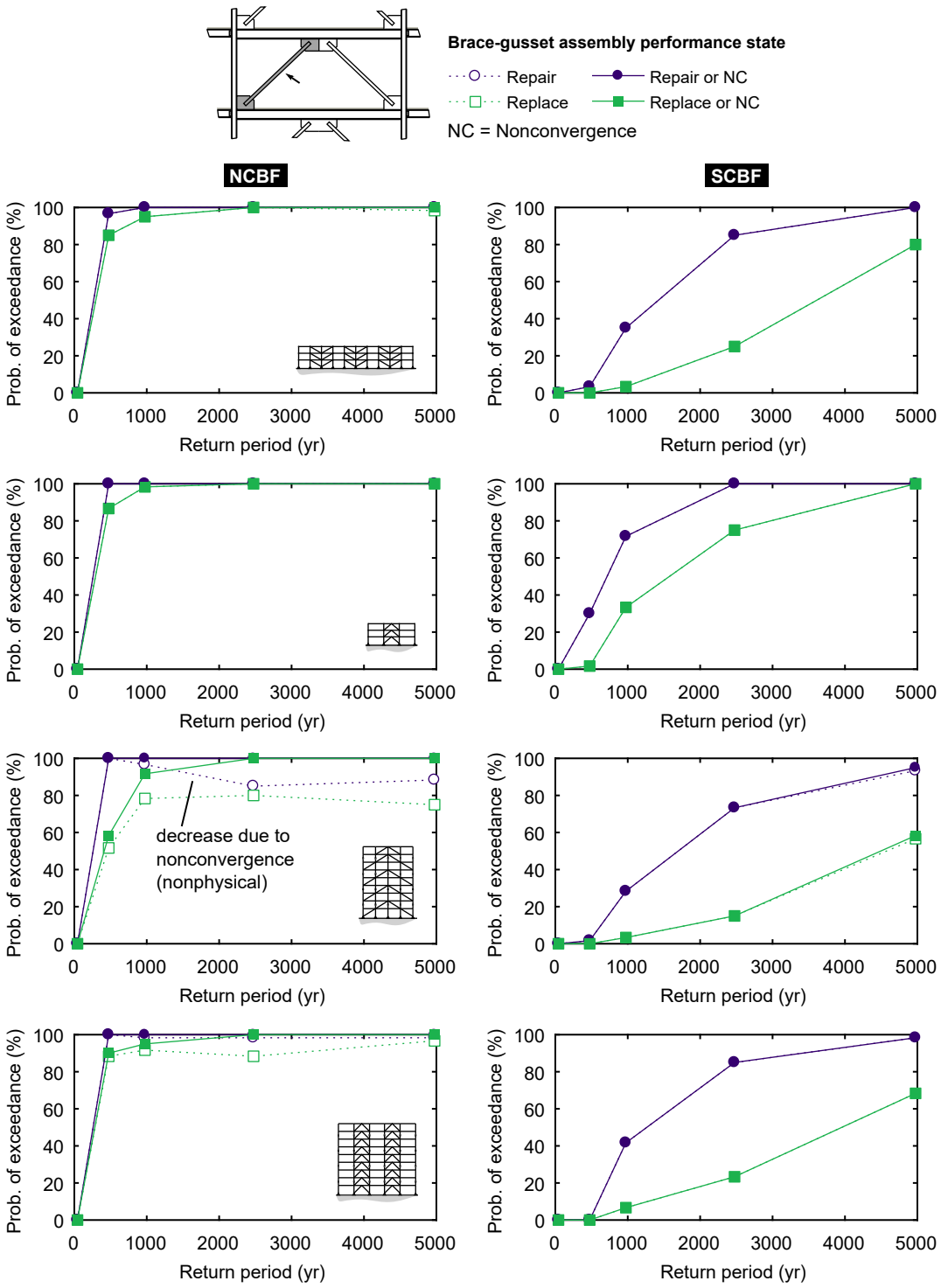

Figure 6.11: Probability of exceedance of brace-gusset assembly damage states for NCBF and SCBF buildings

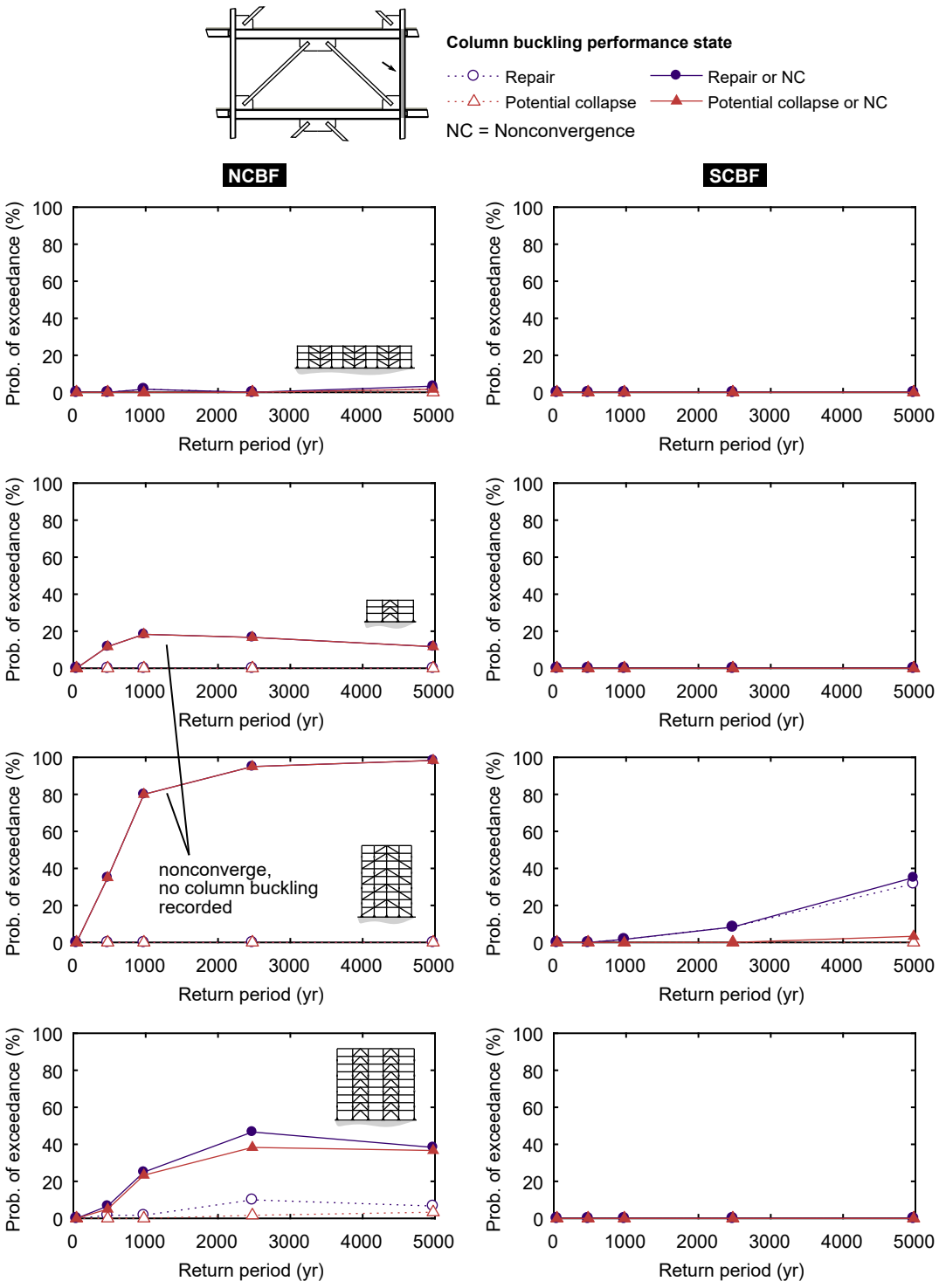

Figure 6.12: Probability of exceedance of column damage states for NCBF and SCBF buildings

plate rotations are related to story drift demands, which are summarized in Table 6.4. The probabilities of potential collapse due to shear-plate fracture (or excessive story drift) were significantly higher in the NCBFs versus the SCBFs. Note also that, for both system types, the difference in probabilities of repair, replace, and potential collapse damage states tended to be low.

Figure 6.14 combines the collapse data based on the shear-plate (drift) and column demands. Recall that a large number of analyses of the 9-story paired single diagonal building did not converge, and these are noted here. The anticipated probability of collapse in *ASCE/SEI 7-16* is 10% under the risk-adjusted maximum considered earthquake (MCE_R), which is similar in intensity to the 2,475-yr return period. Based on the performance-state definitions, all SCBFs met this criteria for acceptable performance with exactly 10% probability of potential collapse for all but the 3-story paired single diagonal building, which had 0%. The probabilities of collapse in the NCBFs exceeded the SCBF probabilities and the code-targeted reliability by very large margins based on the analyses which converged alone (48 to 65% probability of potential collapse at the 2,475-yr hazard level). Further, the NCBFs are prone to potential collapse in more frequent but less severe earthquakes. For example, the 3-story chevron NCBF had a 25% probability of exceeding the potential collapse damage state due to excessive drift at the 975-yr return period.

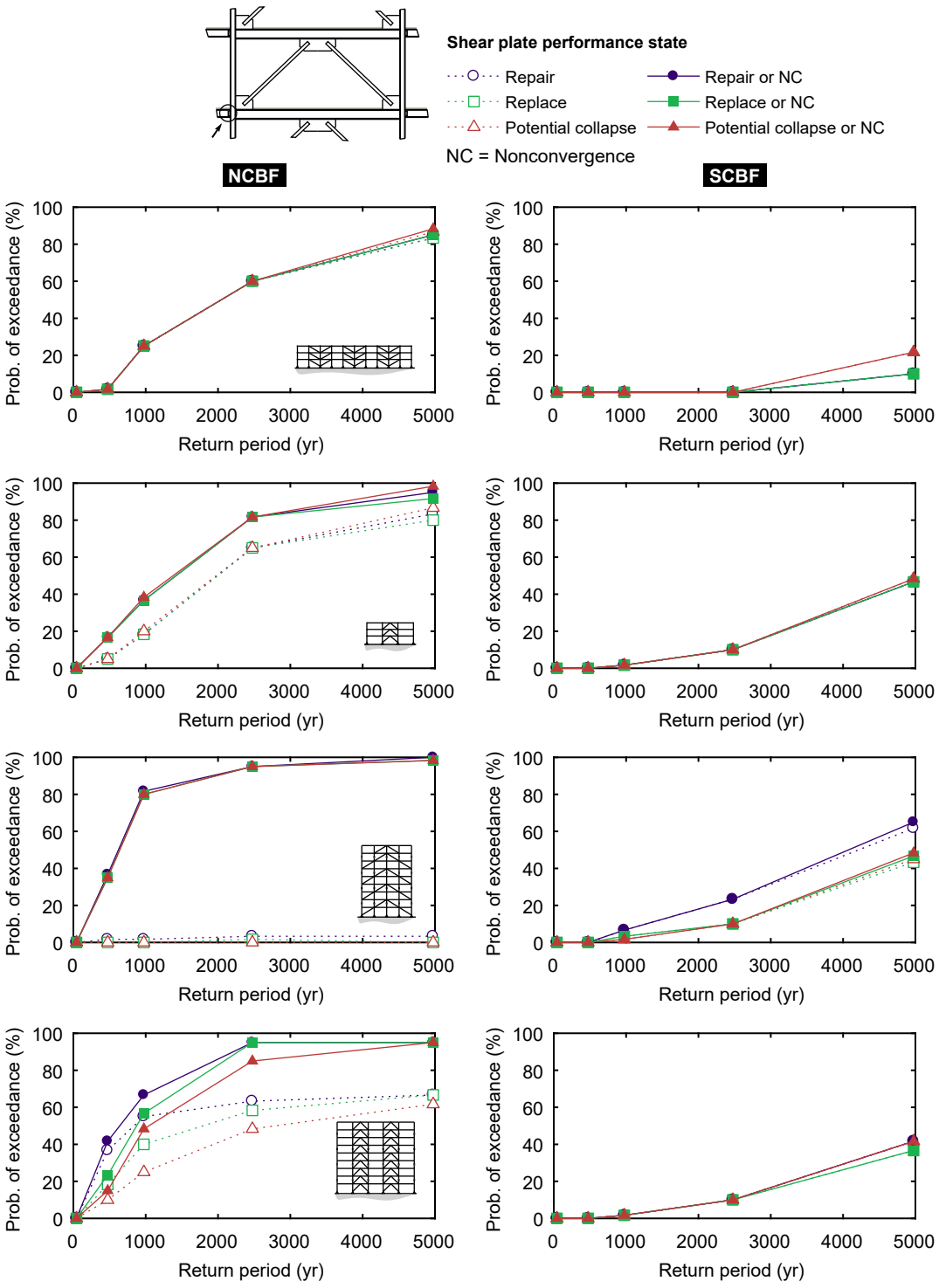

Figure 6.13: Probability of exceedance of shear-plate damage states for NCBF and SCBF buildings

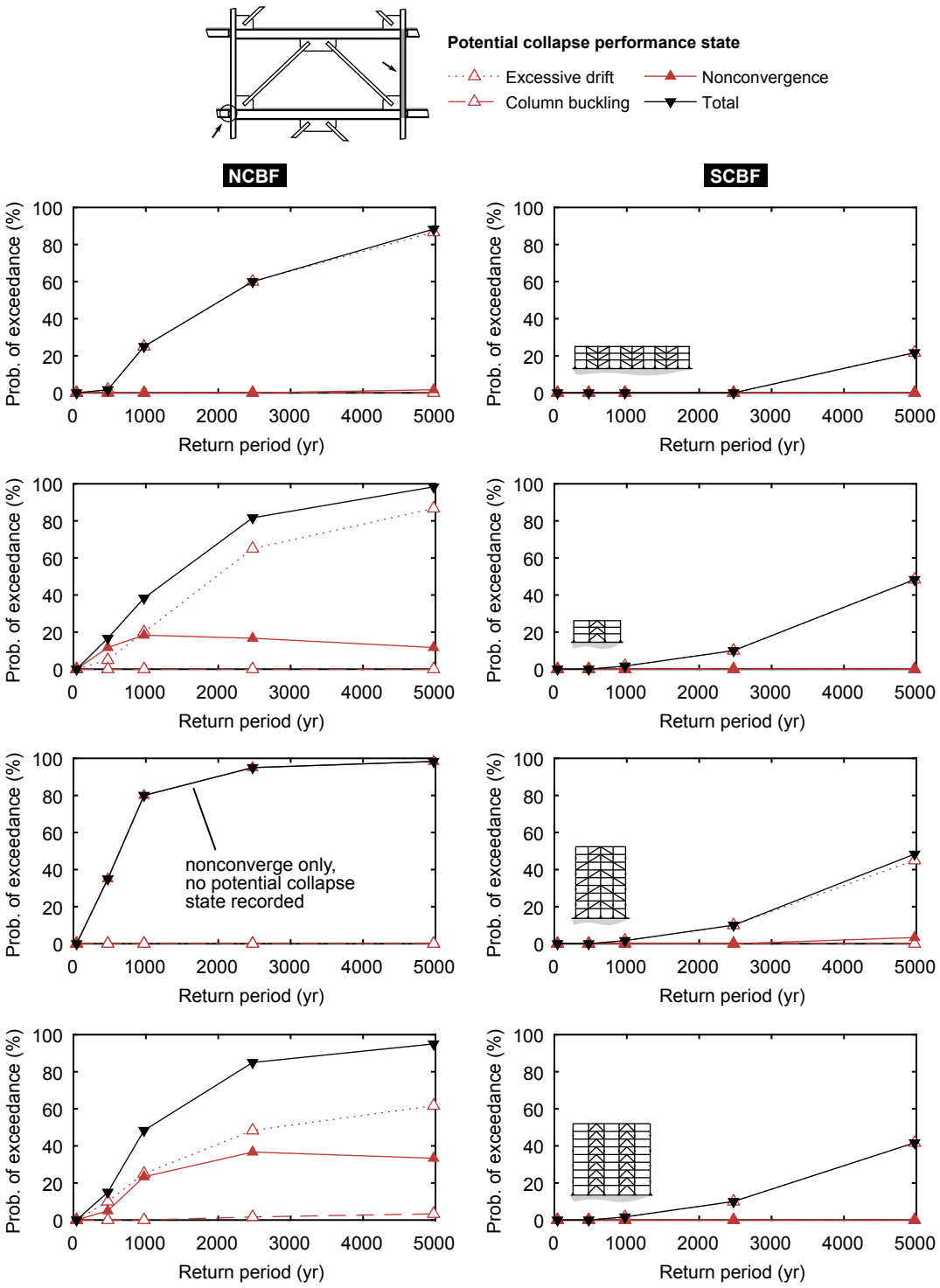

Figure 6.14: Probability of exceedance of potential collapse damage states for NCBF and SCBF buildings

Chapter 7

IMPACTS OF COMPONENT DEFICIENCIES ON SEISMIC PERFORMANCE

In the preceding chapter, existing NCBFs were identified as vulnerable systems with respect to potential damage, including collapse. These buildings had multiple deficiencies, including braces with high local slenderness ratios, connections with limited strength and ductility, beams susceptible to yielding, and columns with the potential for buckling. However, NCBFs do not necessarily have each of these deficiencies and some deficiencies may result in more severe behavior compared to others; thus, it is important to understand the impacts individual deficiencies on building performance. Knowledge of deficiency impact can also be used to develop targeted retrofit schemes which minimize the vulnerability of the most critical failure modes. This chapter uses focused evaluation of different deficiencies to advance this understanding. Specifically, the effects of brace local slenderness, brace-to-gusset weld strength, gusset-plate interface weld rotational capacity, and secondary yielding mechanisms are investigated using NCBF buildings modified from Chapter 5.

7.1 Study Overview

The component-deficiency studies presented in this chapter utilized the benchmark NCBF buildings with modifications to investigate the effects four primary parameters:

1. Brace local slenderness ratio,

2. Brace-to-gusset weld strength,

3. Gusset-plate interface weld fracture rotation without a secondary yielding mechanism (i.e., Type-B behavior), and

4. Gusset-plate interface weld fracture rotation with a secondary yielding mechanisms (i.e., Type-C behavior).

Table 7.1 summarizes the analysis matrix for each deficiency studied. Deficiencies classified as moderate and high retrofit priorities based on the experimental retrofit priority given in Table 6.2 are highlighted. Brace local slenderness was investigated using the benchmark NCBF brace sections in Table 5.3 in their original conditions (λ/λ_{hd} between 1.6 and 2.2) or filled with concrete to improve their fracture life (λ/λ_{hd} effectively equal to 1.0 or below), which was successfully tested as a retrofit in the experimental research described in Chapter 3. The concrete was assumed to be blocked out before the gusset plate to avoid increasing brace strength and hence demands on the adjacent connections; in addition, this facilitated comparison to the existing building performance because the elastic lateral resistance was unchanged. The buildings in this study correspond to model groups 1 and 6 in Table 7.1, since the brace-to-gusset weld fracture DCR was 0.75 and gusset-plate interface weld fracture was not modeled. Since concrete in-fill is a retrofit, the buildings with concrete-filled braces are referred to as "NCBF-R" buildings in the discussion below.

The effects of deficient brace-to-gusset welds were investigated for DCRs between 0.75 and 1.75 as shown for model groups 1 through 10 in Table 7.1. These DCRs were constant along the building height and modeled by adjusting the weld leg size to produce the targeted DCR. Both NCBF and NCBF-R buildings with these DCRs were evaluated, and gusset-plate interface weld fracture was not modeled.

Gusset-plate interface weld fracture was studied without a secondary yielding mechanism (i.e., Type-B behavior) for fracture rotations, θ_f, between 0.075 and 0.200 radians. The buildings in this study corresponded to model groups 11 through 22. As in the brace-to-gusset weld deficiency study, the deficiency severity was constant along the building height and its effects were investigated for the NCBF and NCBF-R buildings.

A second study with gusset-plate interface weld fracture evaluated the impact of secondary yielding mechanisms (i.e., Type-C behavior) with deformation capacities between

Table 7.1: Component Deficiency Analysis Matrix

Model group	Brace local slenderness ratio, λ/λ_{hd}	Brace-to-gusset weld fracture DCR	Gusset-plate interface weld fracture rotation, θ_f (rad)	Secondary yielding mechanism deformation capacity, δ_f (mm)
Brace-to-gusset weld deficiency study				
1	1.6–2.2	0.75	N/A	0.0
2		1.00		
3		1.25		
4		1.50		
5		1.75		
6	< 1.0 (concrete fill)	0.75	N/A	0.0
7		1.00		
8		1.25		
9		1.50		
10		1.75		
Gusset-plate interface weld deficiency (Type B) study				
11	1.6–2.2	< 0.75	0.200	0.0
12			0.175	
13			0.150	
14			0.125	
15			0.100	
16			0.075	
17	< 1.0 (concrete fill)	< 0.75	0.200	0.0
18			0.175	
19			0.150	
20			0.125	
21			0.100	
22			0.075	
Gusset-plate interface weld deficiency (Type C) study				
23	< 1.0 (concrete fill)	< 0.75	0.175	12.7 (0.5 in)
24				25.4 (1.0 in)
25				38.1 (1.5 in)
26				50.8 (2.0 in)
27			0.075	12.7 (0.5 in)
28				25.4 (1.0 in)
29				38.1 (1.5 in)
30				50.8 (2.0 in)

Experimental retrofit priority:
■ High
■ Moderate

12.7 mm (0.5 in) and 50.8 mm (2.0 in). As shown for model groups 23 through 30 in Table 7.1, only fracture rotations of 0.075 and 0.175 radians were investigated; these corresponded to high- and moderate-priority retrofits based on Table 6.2. The brace local slenderness deficiency was also not investigated as part of this study in order to focus on the secondary yielding mechanism.

To isolate the effects of the brace and connection deficiencies noted above, the NCBF buildings introduced in Chapter 5 (see Fig. 5.4) were redesigned to mitigate weak beam and column deficiencies. The new beams and columns were sized as ASTM A36 members to resist the expected brace forces under the buckling and post-buckling load cases in the *Seismic Provisions* (AISC 2017a). Resistance factors were used in the designs, and therefore their corresponding DCRs were below 0.9. The updated beam and column shapes for the "compliant-frame" NCBFs are provided in Tables 7.2 and 7.3. Note that the braces and gravity-force-resisting system members in each building were not changed.

7.2 Effects of Brace Local Slenderness

Previous work has shown that premature brace fracture is a common failure mode for existing NCBF buildings. This phenomenon has been observed in past earthquakes (Kelly et al. 2000) and the effects of local slenderness on the development of local cupping and fracture have been well quantified through experimental research (Goel 1992). The NCBF buildings analyzed in this study had brace local slenderness ratios which reflected common values computed in the infrastructure review, λ/λ_{hd} between 1.6 and 2.2. These braces were classified as high priorities for retrofit based on experimental research, and thus a concrete-filled brace retrofit was evaluated in the NCBF-R buildings.

Figure 7.1 shows the probability of brace-gusset assembly damage for the sets of NCBF and NCBF-R buildings without connection deficiencies. Thus, these brace-gusset assembly performance states were all derived from the brace demands. Recall that the brace local cupping damage state is based on λ/λ_{hd} in Table 5.9. To evaluate damage to the concrete-filled brace, λ/λ_{hd} values were back-calculated from the $MSR_{f,disp}$ prediction equation (Eq. 4.2)

Table 7.2: Compliant-Frame NCBF Building Beam Sizes

Story	Section (iDCR[a])				
	B1	B2	B3	B4	B5
3-story strong-frame NCBF					
3	W16×45	W16×25	W21×201 (0.6)	W21×55	–
2	W16×67	W16×31	W21×201 (0.6)	W21×73	–
1	W16×67	W16×31	W21×201 (0.6)	W21×73	–
9-story strong-frame NCBF					
9	W18×65	W18×65	W18×35	W24×146 (0.8)	W21×83
8	W18×86	W18×86	W18×35	W24×207 (0.6)	W21×83
7	W18×65	W18×65	W18×35	W24×192 (0.5)	W21×83
6	W18×86	W18×86	W18×35	W24×250 (0.6)	W21×83
5	W18×65	W18×65	W18×35	W24×192 (0.3)	W21×83
4	W18×86	W18×86	W18×35	W24×229 (0.3)	W21×83
3	W18×65	W18×65	W18×35	W24×176 (0.6)	W21×83
2	W18×86	W18×86	W18×35	W24×176 (0.6)	W21×83
1	W18×65	W18×65	W18×35	W24×162 (0.7)	W21×83

[a]iDCR shown in parentheses if beam is part of chevron CBF

using the lower-bound MSR_f for concrete-filled braces (0.0505).

It can be seen from Fig. 7.1 that the probability of exceedance of the brace-gusset assembly performance states did not vary significantly between the NCBF buildings. The probability of exceeding the repair performance state was nearly 100% for the 475-yr hazard level and above. The replacement performance state had a probability of exceedance of at least 90% at the 975-yr hazard level and above. The largest variation occurred for the replacement performance state at the 475-yr hazard level, where the paired single diagonal and chevron NCBFs had respective probabilities of exceedance of 47–60% and 75–93%, respectively.

Brace-gusset assembly performance was significantly improved in the NCBF-R buildings, where the probabilities of exceeding the repair and replace performance states were essentially 0% at the 475-yr hazard level. In addition, the performance at more severe hazard levels met or exceeded that of the benchmark SCBFs shown in Fig. 6.11. Similar to the NCBF build-

Table 7.3: Compliant-Frame NCBF Building Column Sizes

Story	Section (DCR[a])				
	C1	C2	C3	C4	C5
3-story strong-frame NCBF					
3	W10×77 (0.2)	W10×33	W10×77 (0.2)	W10×49	W10×33
2	W10×77 (0.5)	W10×33	W10×77 (0.5)	W10×49	W10×33
1	W10×77 (0.9)	W10×33	W10×77 (0.8)	W10×49	W10×33
9-story strong-frame NCBF					
9	W12×40 (0.1)	W12×40	W12×72 (0.4)	W12×50 (0.3)	W12×40
8	W12×40 (0.2)	W12×40	W12×72 (0.9)	W12×50 (0.9)	W12×40
7	W12×53 (0.2)	W12×50	W12×120 (0.6)	W12×96 (0.6)	W12×72
6	W12×53 (0.9)	W12×50	W12×120 (0.9)	W12×96 (0.9)	W12×72
5	W12×106 (0.4)	W12×65	W12×190 (0.6)	W12×170 (0.7)	W12×106
4	W12×106 (0.8)	W12×65	W12×190 (0.9)	W12×170 (0.9)	W12×106
3	W12×152 (0.6)	W12×79	W12×252 (0.7)	W12×252 (0.7)	W12×136
2	W12×152 (0.9)	W12×79	W12×252 (0.9)	W12×252 (0.9)	W12×136
1	W12×152 (0.9)	W12×96	W12×279 (0.8)	W12×279 (0.9)	W12×152

[a]DCR shown in parentheses if column is part of CBF and develops excessive compressive forces under expected brace forces

ings above, the chevron NCBF-R buildings had greater potential for brace-gusset assembly damage with 47–52% probability of exceedance of the replace performance state versus only 0–15% for their paired single diagonal counterparts.

The probabilities of exceeding the column repair and potential collapse performance states are shown in Fig. 7.2. The paired single diagonal NCBF buildings were most vulnerable to column buckling, with probabilities of exceedance of 3–17% for the repair performance state at the 2,475-yr hazard level. The equivalent NCBF-R buildings had lower repair probabilities of exceedance (0–7%), which suggests that the larger brace deformation capacities helped mitigate column buckling. None of the columns sustained post-buckling deformations exceeding the potential collapse threshold.

Figure 7.3 illustrates the probabilities of exceedance for the shear-plate performance states. As was found in the benchmark NCBF and SCBF buildings, probability-of-exceedance

differences between performance states was relatively small due to the tight performance-state limits for these connections. Consequently, the shear-plate potential collapse performance state is perhaps the most compelling for this component and is plotted as the "excessive drift" criteria in Fig. 7.4. The NCBF buildings had high probabilities of potential collapse at the 2,475-yr hazard level (32–57%) but this vulnerability was dramatically reduced in the NCBF-R buildings (0–22%) due to the concrete fill. In fact, the paired single diagonal NCBF-R buildings met the anticipated collapse probability for new buildings designed with *ASCE/SEI 7-16* (ASCE 2017a). This is especially significant because the 3-story NCBF-R building was substantially weaker than required in new construction of an SCBF.

7.3 Effects of Brace-to-Gusset Weld Deficiencies

The previous set of analyses show the importance of brace local slenderness on seismic performance through a concrete-filled brace retrofit, but most NCBFs have connection deficiencies which may preclude brace fracture. The effects of one such deficiency, brace-to-gusset weld fracture, were evaluated parametrically for DCRs (Eq. 4.7) between 0.75 and 1.75. Over half of the buildings surveyed as part of the NCBF infrastructure review had undersized brace-to-gusset welds, and DCRs as large as 1.6 were reported. Both NCBF and NCBF-R buildings were analyzed with these deficiencies, since the latter effectively isolates the connection deficiency to directly evaluate its effects.

Figure 7.5 shows the brace-gusset assembly performance at each hazard level, building, and range of DCRs investigated. The probability of exceedance of the brace-gusset assembly replace state was similar for the NCBF buildings regardless of brace-to-gusset weld DCR. At low DCRs, the locally slender braces fracture prematurely, and at high DCRs, the brace-to-gusset welds fracture prematurely; hence, replacement of the brace would be necessary in both cases.

When the braces were filled with concrete in the NCBF-R buildings, mitigating premature brace fracture, the probability of exceeding the replace state varied significantly at all hazard

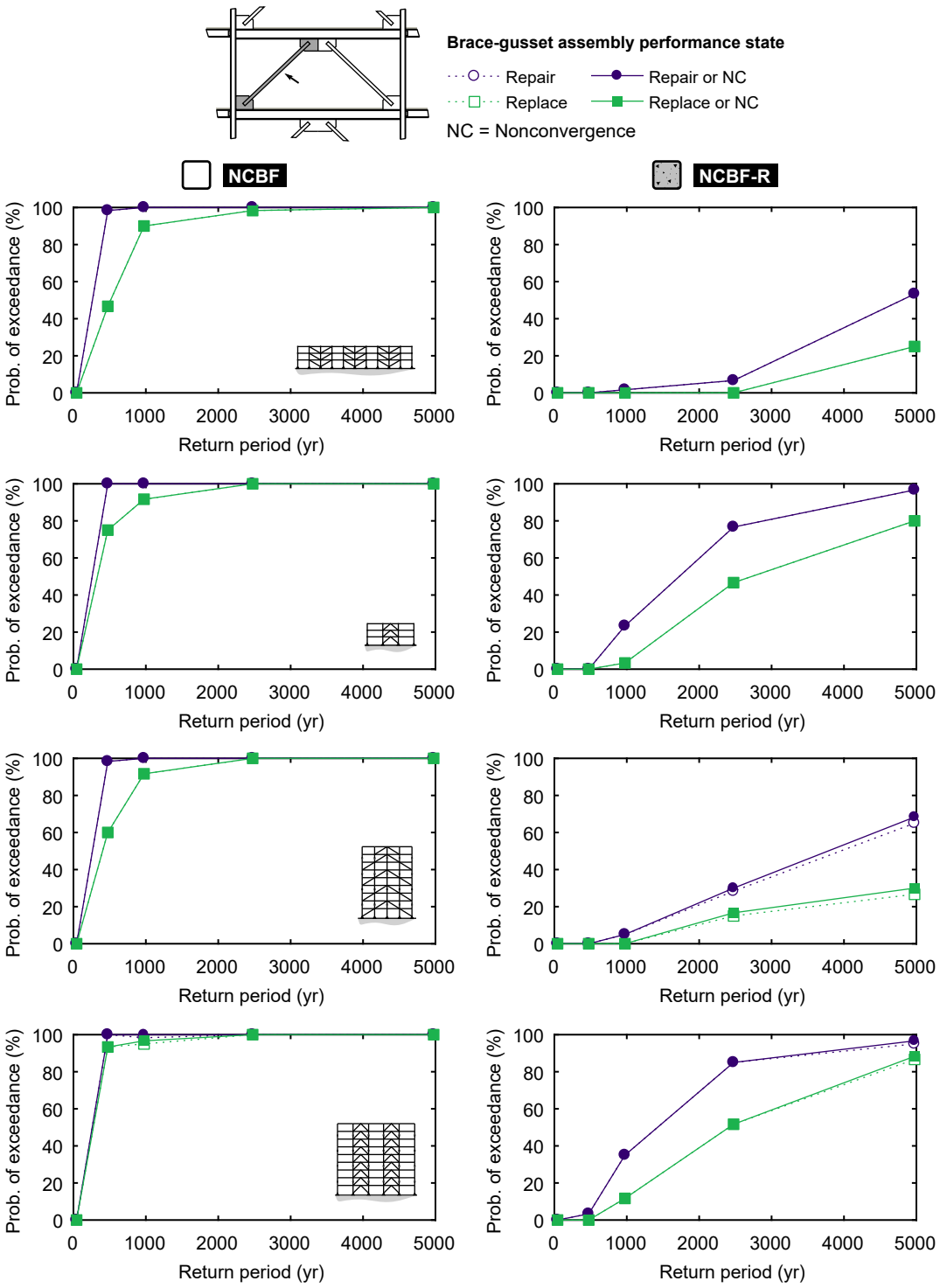

Figure 7.1: Probability of exceedance of brace-gusset assembly damage states for NCBF and NCBF-R buildings without connection deficiencies

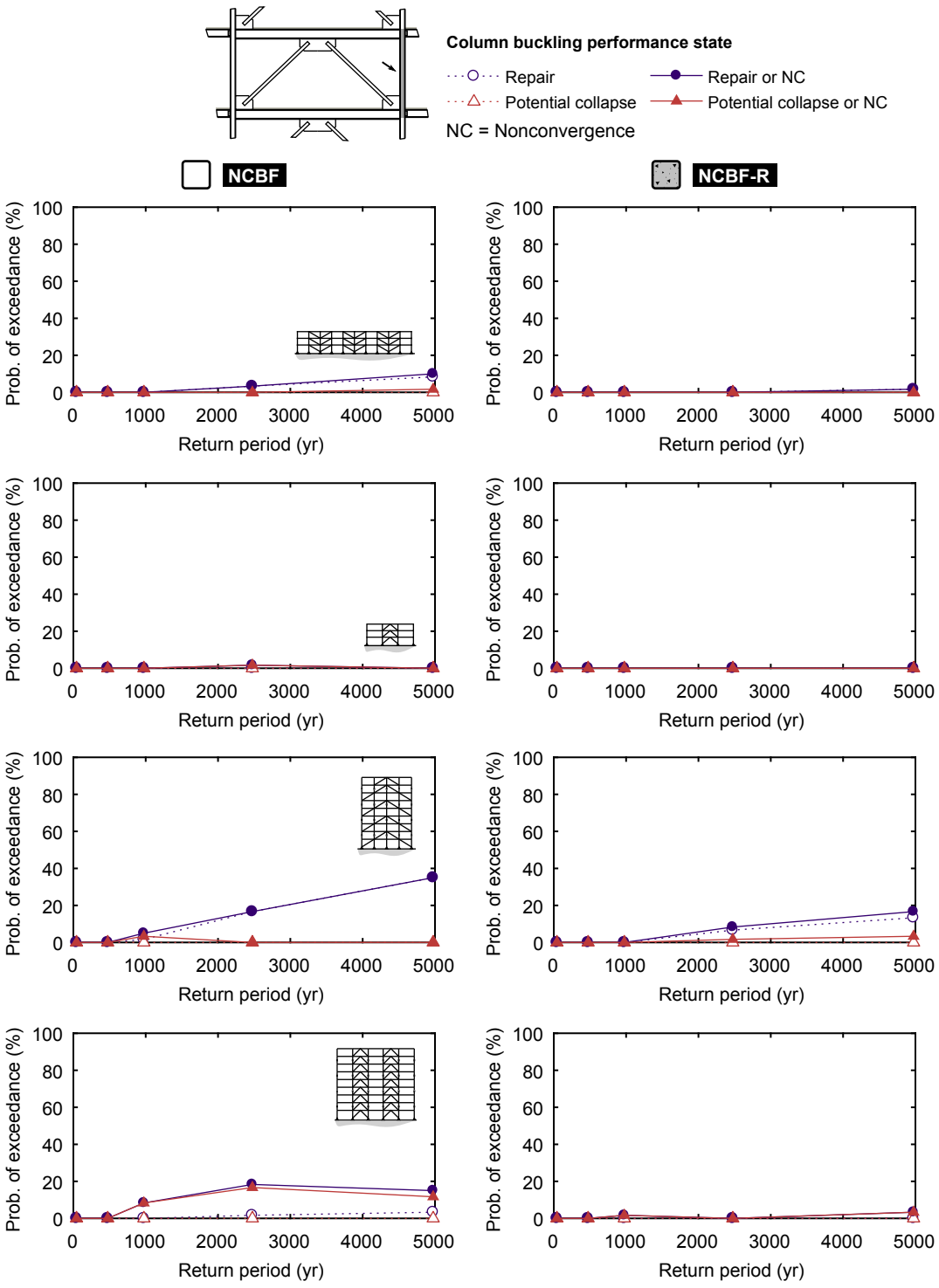

Figure 7.2: Probability of exceedance of column damage states for NCBF and NCBF-R buildings without connection deficiencies

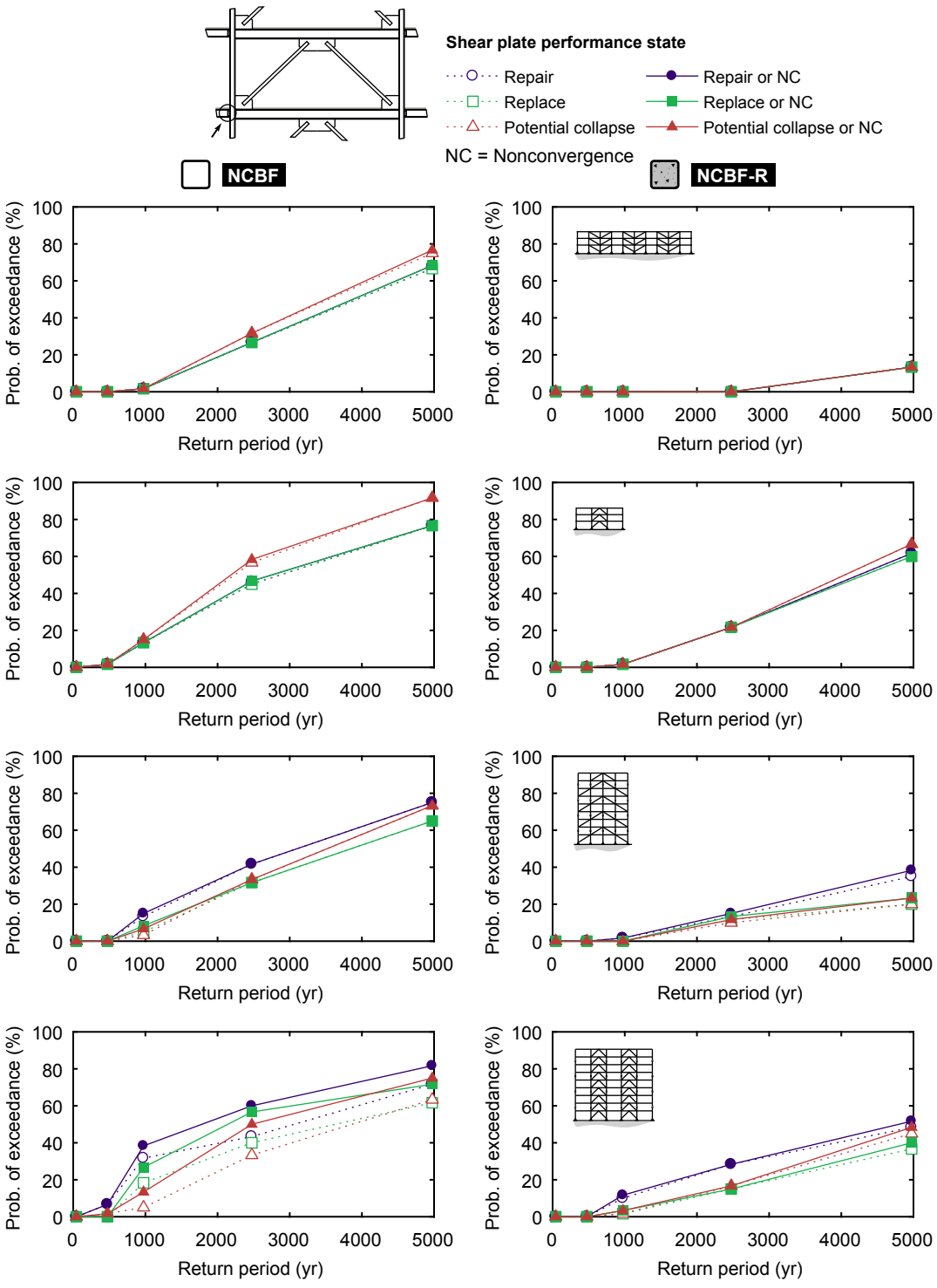

Figure 7.3: Probability of exceedance of shear-plate damage states for NCBF and NCBF-R buildings without connection deficiencies

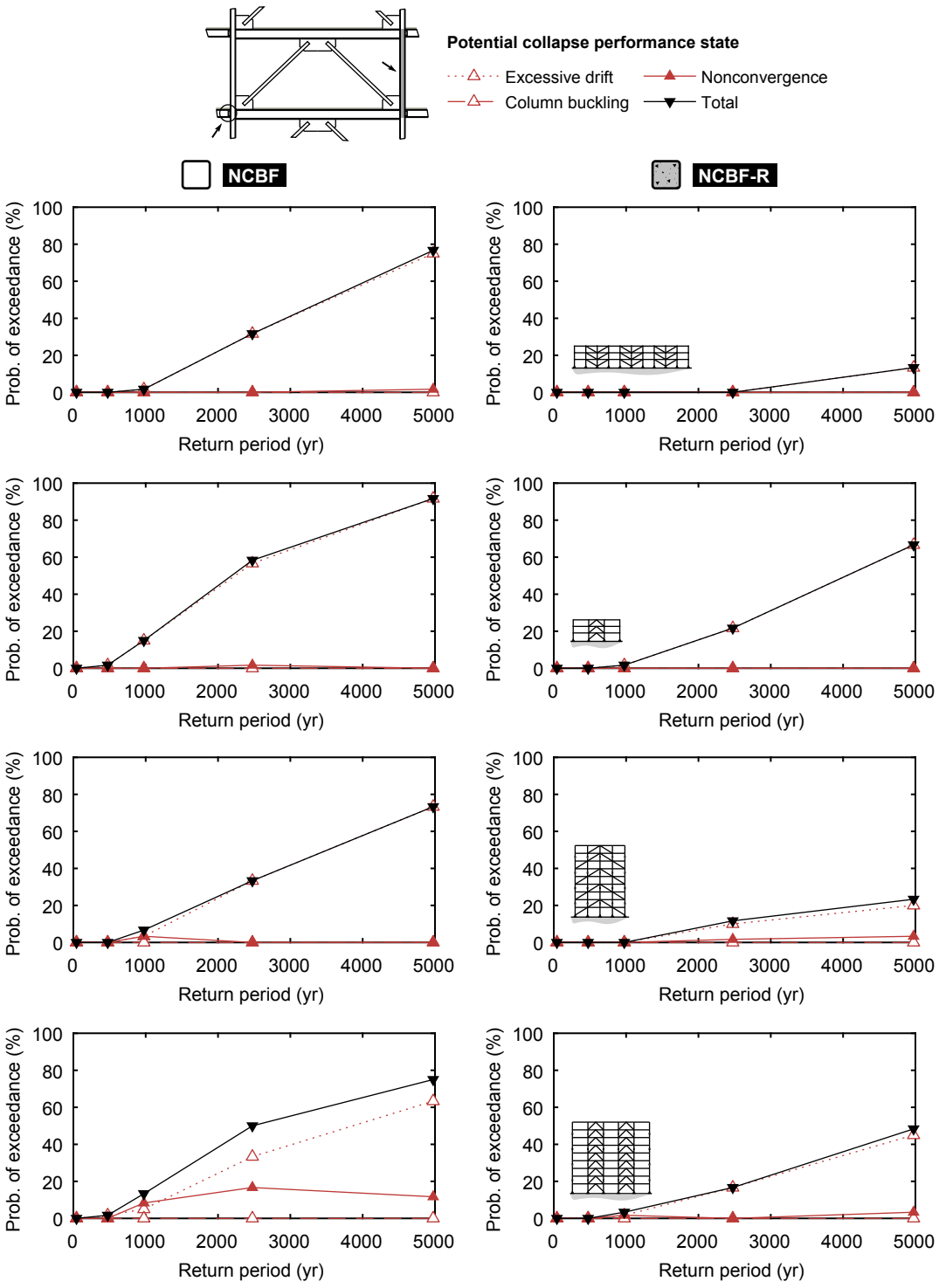

Figure 7.4: Probability of exceedance of potential collapse damage states for NCBF and NCBF-R buildings without connection deficiencies

levels. For DCRs of 1.50 and 1.75, brace-gusset assembly performance was similar to the NCBF building case, as brace-to-gusset weld fracture dominates the behavior. Compared to a DCR of 1.75, a DCR of 1.25 reduced the probability of brace-gusset assembly replacement from 78–92% to 10–50% at the 475-yr hazard level, though performance at the 2,475-yr hazard level was essentially unchanged. Performance of the brace-gusset assembly at the 2,475-yr hazard level was only improved for DCRs of 1.00 and below, where the probability of exceeding the replace performance state was between 0 and 52%.

Probabilities of exceedance for the column repair state are shown in Fig. 7.6. The 9-story paired single diagonal NCBF and NCBF-R buildings were again the most vulnerable building types for column buckling. In the NCBF building, the probability of exceeding the column repair state was largest when the brace-to-gusset weld DCR was 0.75. At the 2,475-yr hazard level, the probability of exceeding the column repair was 0–17% for a weld DCR of 0.75 and 0-7% for a weld DCR of 1.75. Thus, premature brace-to-gusset weld fracture reduced the compressive-force demands on the columns. This trend was not clear in the NCBF-R buildings, however.

Figure 7.7 shows the potential collapse performance for these buildings, which follows similar trends to the brace-gusset assembly performance. The effect of brace-to-gusset weld DCR is relatively small for the NCBF buildings, but significant in the NCBF-R buildings since premature brace fracture was eliminated. Figure 7.8 illustrates these effects at the 2,475-yr hazard level, where it can be seen that a DCR of 0.75 had lower probabilities of potential collapse (0-21%) versus a DCR of 1.00 (3–52%) and significantly lower probabilities of potential collapse versus a DCR of 1.75 (40–58%).

7.4 Effects of Gusset-Plate Interface Weld Deficiencies

Fracture of the weld(s) connecting the gusset plate to the frame was a commonly observed failure mode in experiments of NCBFs and all buildings in the infrastructure review with such connections had undersized welds based on the BDP (Eq. 4.10; Roeder et al. (2011b)), inadequate rotational clearance in the gusset plate to accommodate brace end rotation,

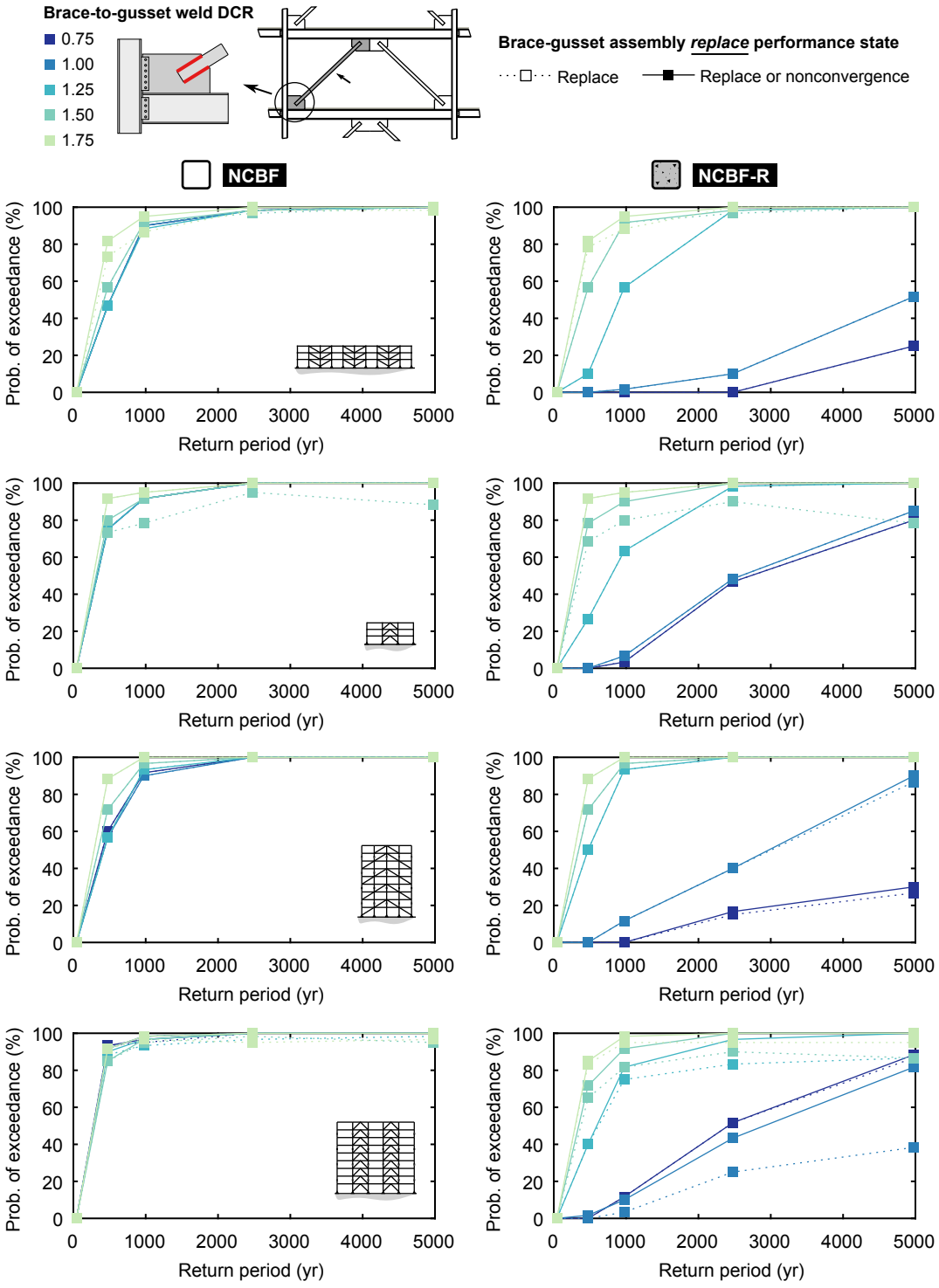

Figure 7.5: Probability of exceedance of brace-gusset assembly "replace" performance state for NCBF and NCBF-R buildings with various brace-to-gusset weld DCRs

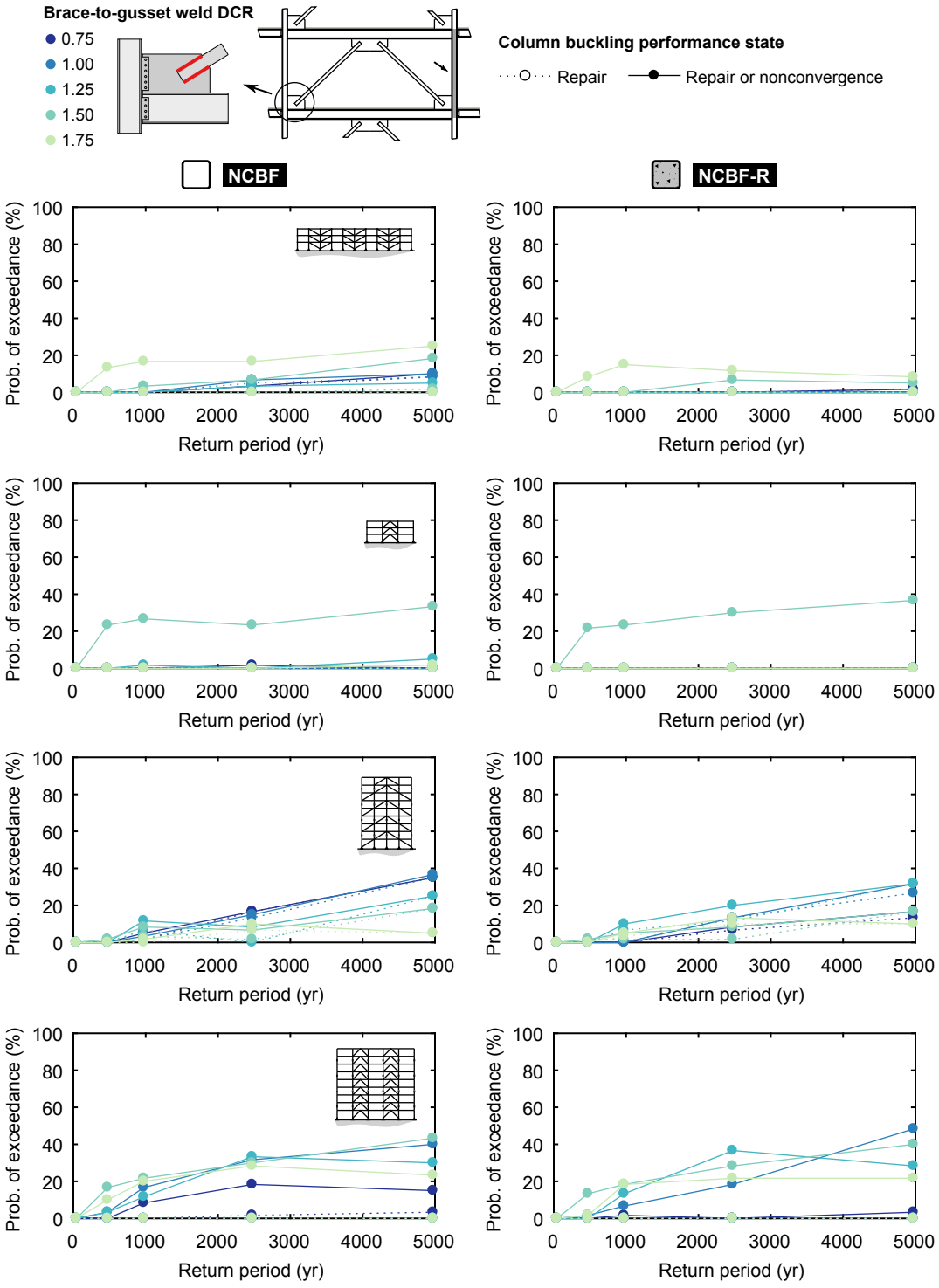

Figure 7.6: Probability of exceedance of column "repair" performance state for NCBF and NCBF-R buildings with various brace-to-gusset weld DCRs

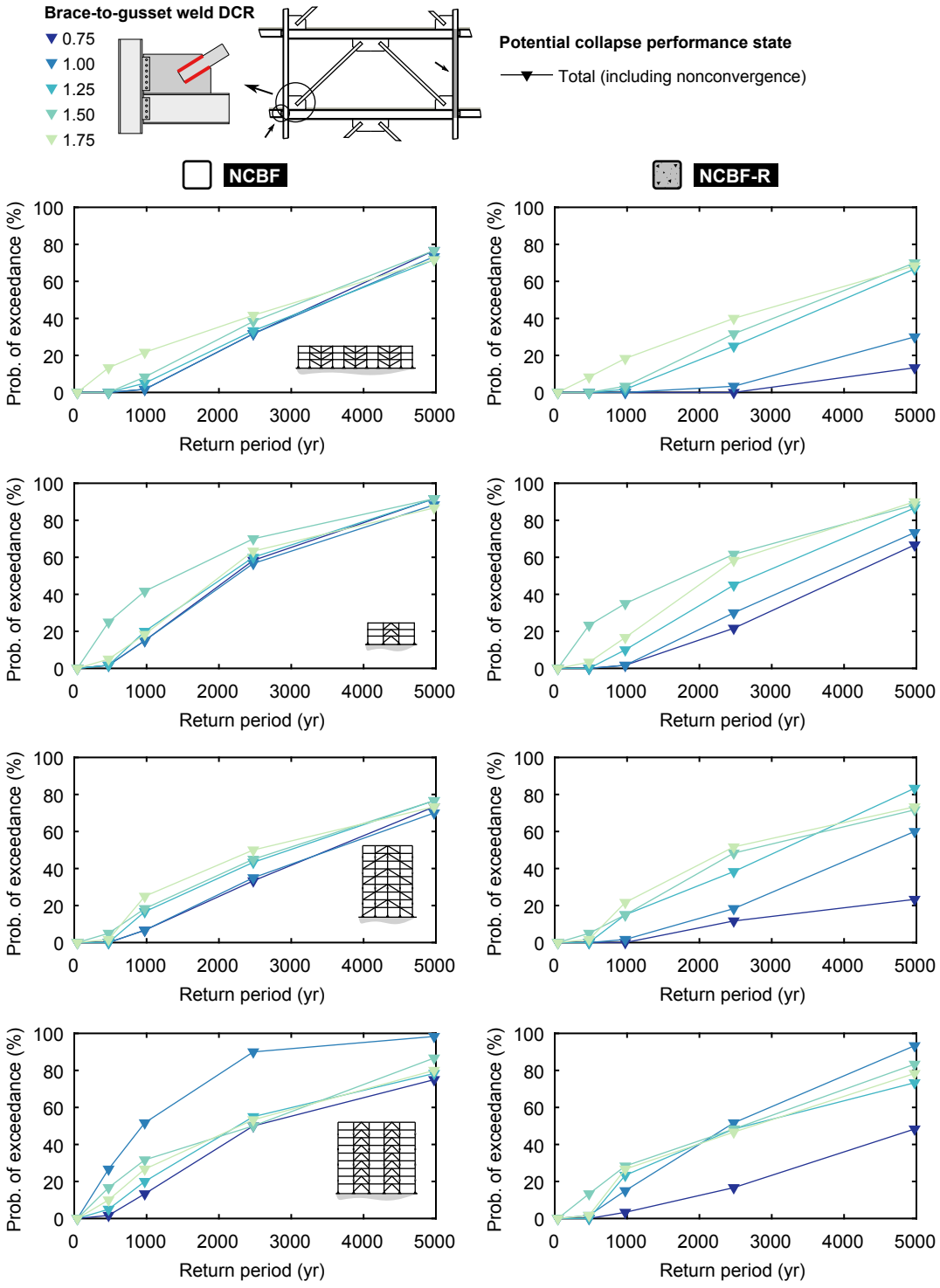

Figure 7.7: Probability of exceedance of all potential collapse performance states (including nonconvergence) for NCBF and NCBF-R buildings with various brace-to-gusset weld DCRs

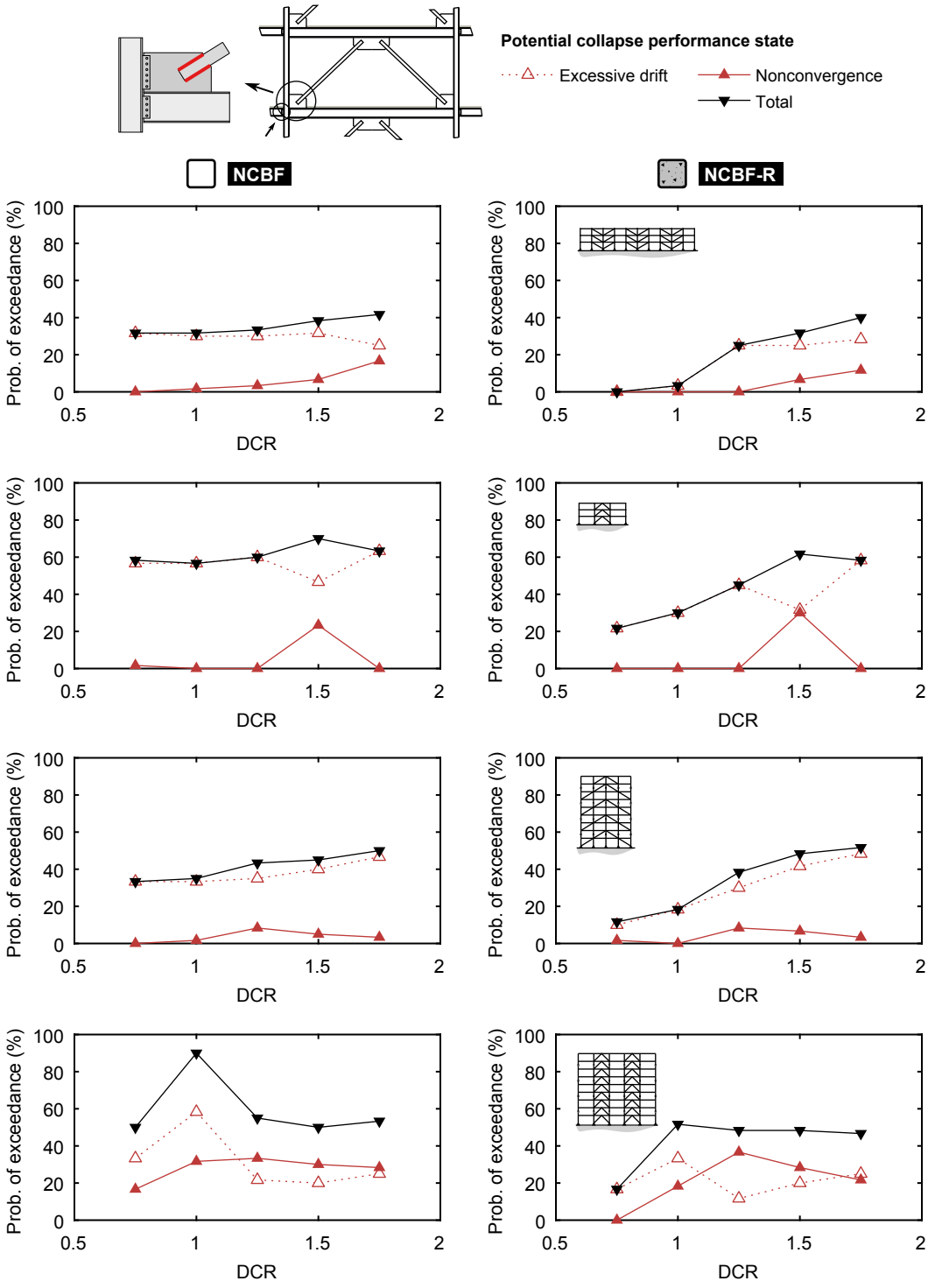

Figure 7.8: Probability of exceedance of potential collapse performance states at 2,475-yr return-period hazard level for NCBF and NCBF-R buildings with various brace-to-gusset weld DCRs

and noncompliant filler metal toughness for demand critical welds. To evaluate the effects of premature fracture of gusset-plate interface welds, NCBF and NCBF-R buildings with gusset-plate fracture rotations, θ_f, between 0.075 and 0.200 radians were developed to simulate Type-B behavior as depicted in Fig. 3.21. Then, to evaluate the benefits of a secondary yielding mechanism providing Type-C behavior, NCBF-R buildings with fracture rotations of 0.075 and 0.175 radians were developed.

Depending on the relative strength of yielding mechanisms and failure modes in the remaining connection, the secondary yielding mechanism deformation capacity, δ_f, may be rather large. For example, if bolt-hole elongation is possible, greater than 25 mm of deformation could be achieved through a combination of bolt deformation, bolt rotation, and plate yielding before tearout or bolt fracture occurs. A simplistic approach was used in the Type-C behavior study to evaluate the potential benefit of such secondary yielding mechanisms. The secondary yielding mechanism response was modeled using an axial spring with the *Steel02* constitutive behavior which engaged only after gusset-plate interface weld fracture. The spring had a yield force of 70% of the brace yield strength, an elastic stiffness of $4EA_g/L$, and a fracture deformation between 0 and 51 mm (2 in). The relative yield force and stiffness was consistent with Specimen 4O modeled in Chapter 4 (see Fig. 4.10).

7.4.1 Type-B Behavior

The first gusset-plate interface weld fracture study evaluated Type-B behavior for NCBF and NCBF-R buildings. Figure 7.9 illustrates the probability of exceedance for the brace-gusset assembly replacement performance state. As in the brace-to-gusset weld deficiency study, the severity of the gusset-plate interface weld deficiency had little impact on the probability of brace-gusset assembly replacement in the NCBF buildings due to the potential for premature brace fracture.

The effects of gusset-plate interface weld fracture rotation were clearly seen in the NCBF-R buildings, where this failure mode dominated the response. For a fracture rotation of 0.075 rad, the brace-gusset assembly replacement performance was similar to all of the NCBF

buildings in Fig. 7.9. For all larger fracture rotations, the probability of exceedance of the brace-gusset assembly replacement performance state systematically decreased for each hazard level except the 43-yr return period where the buildings were essentially elastic. The performance improvements were larger for the paired single diagonal NCBF-R buildings, especially at the 2,475-yr hazard level. However, the rotation demands would be expected to be larger in the chevron archetypes with the same story-drift demands since the braces are shorter. That is, the same fracture rotation in both bracing configurations investigated would correspond to different story drifts at fracture.

The trends for column buckling performance (Fig. 7.10) were also similar to the previous brace-to-gusset weld deficiency study. The 9-story paired single diagonal had the largest probability of exceeding the column repair state. In the NCBF buildings, larger fracture rotations led to higher probabilities of exceedance. This trend appeared to reverse in the NCBF-R buildings. However, the relatively high rate of nonconvergence in the 9-story paired single diagonal buildings obstructs clear interpretation of these results.

The probability of exceeding the potential collapse performance state was largely unaffected by fracture rotation in the NCBF, as shown in Fig. 7.11. Note that the variation observed in the 9-story paired single diagonal NCBF is attributed to a large number of cases of nonconvergence; this can be seen for the 2,475-yr hazard level in Fig. 7.12 (the x-axes are reversed in this figure such that the deficiency severity increases from left to right).

The effect of gusset-plate interface weld fracture rotation was greater in the NCBF-R buildings. Excluding the 9-story paired single diagonal, the probability of potential collapse at the 2,475-yr hazard level was 42-58% for a fracture rotation of 0.075 radians but only 7-37% for a fracture rotation of 0.200 radians. Notably, the 3-story paired single diagonal had a 10% probability of potential collapse with a fracture rotation of 0.175 radians at the 2,475-yr hazard level, which meets the performance objective targeted in *ASCE/SEI 7-16* for new construction (ASCE 2017a). It is noted that a fracture rotation of 0.175 radians is less than would be expected for an SCBF, since experiments show that rotations up to about 0.25 radians could be tolerated for these systems (Lumpkin 2009). Thus, it may be possible

to retain a gusset-plate interface weld fracture deficiency of this magnitude while providing acceptable performance.

7.4.2 Type-C Behavior

The second gusset-plate interface weld fracture study evaluated Type-C behavior for NCBF-R buildings with fracture rotations of 0.075 and 0.175 radians. The secondary yielding mechanisms had deformation capacities, δ_f, between 13 and 51 mm (0.5 and 2.0 in). Figure 7.13 plots response histories from one ground motion (RSN 79) at the 2,475-yr hazard level which shows characteristic Type-B behavior ($\delta_f = 0mm$) and Type-C behavior for δ_f equal to 25 and 51 mm. In this illustrative example, the secondary yielding mechanism is shown to prevent the potential collapse performance state based on excessive drift.

The NCBF-R buildings evaluated here with fracture rotations of 0.075 and 0.175 radians are the same as those from the above study on Type-B behavior with the exception of the secondary yielding mechanism. The secondary yieldingmechanism does not affect brace-gusset assembly performance, since the behavior does not engage until after gusset-plate interface weld fracture. Thus, the brace-gusset assembly performance-state probabilities would be the same as those in Fig. 7.9, and the effect of the secondary yielding mechanism is primarily to mitigate damage to other components and prevent collapse.

Figure 7.14 shows the impact of secondary yielding-mechanism deformation capacity on the column repair performance state. The 9-story paired single diagonal NCBF-R buildings were most vulnerable to column buckling damage, but the probability of exceedance of the repair performance state was reduced with larger secondary yielding mechanism deformation capacities where the fracture rotation was 0.075 radians. For δ_f of 13 and 51 mm, the respective column repair-state probabilities of exceedance were 45% and 23% at the 4,975-yr hazard level.

In the buildings with a fracture rotation of 0.175 radians, the overall effects of the secondary yielding mechanism were reduced because gusset-plate interface weld was less likely; this was true with respect to both column and potential collapse performance. Figures 7.15

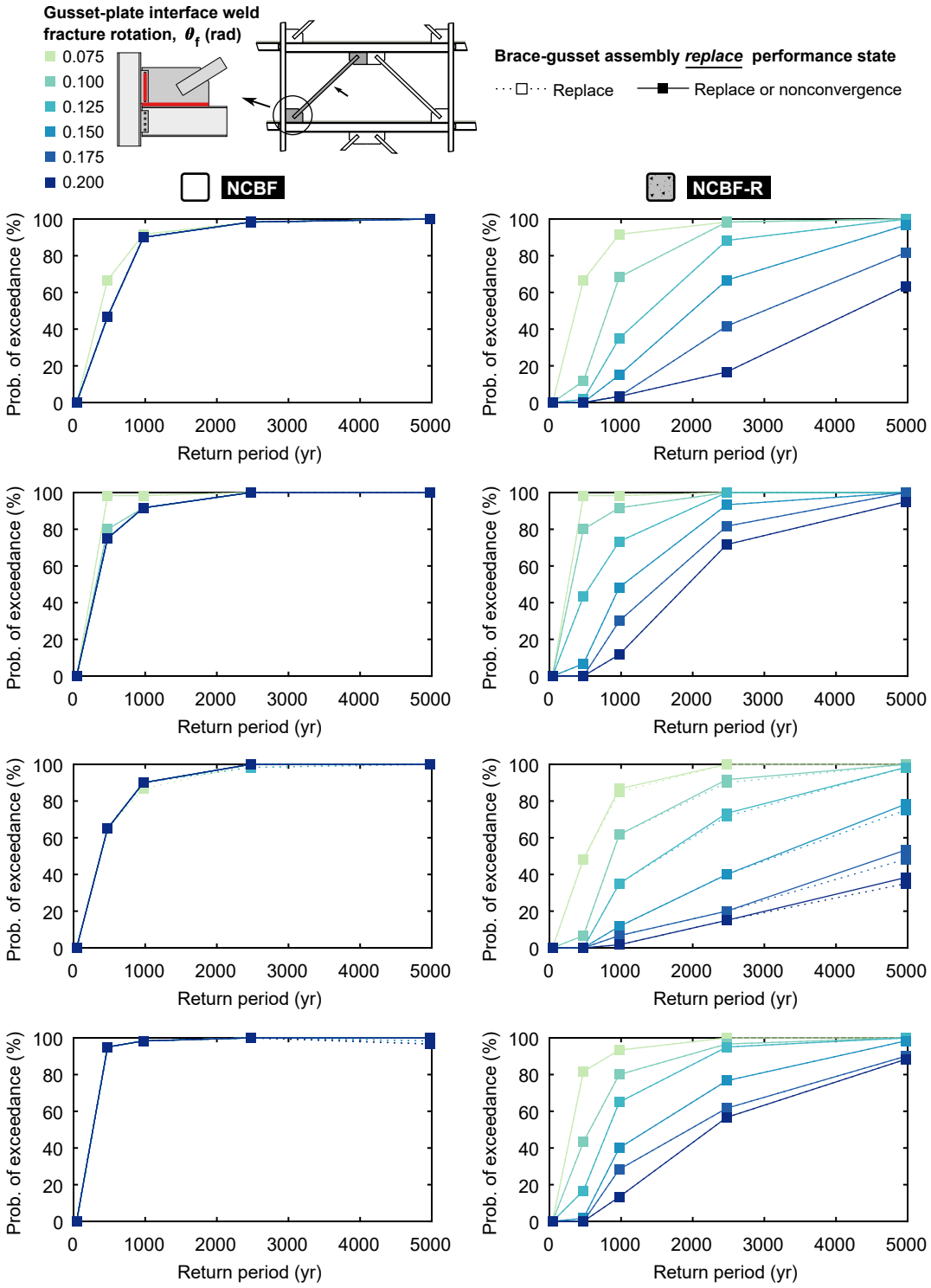

Figure 7.9: Probability of exceedance of brace-gusset assembly "replace" performance state for NCBF and NCBF-R buildings with various gusset-plate interface weld fracture rotations (Type-B behavior)

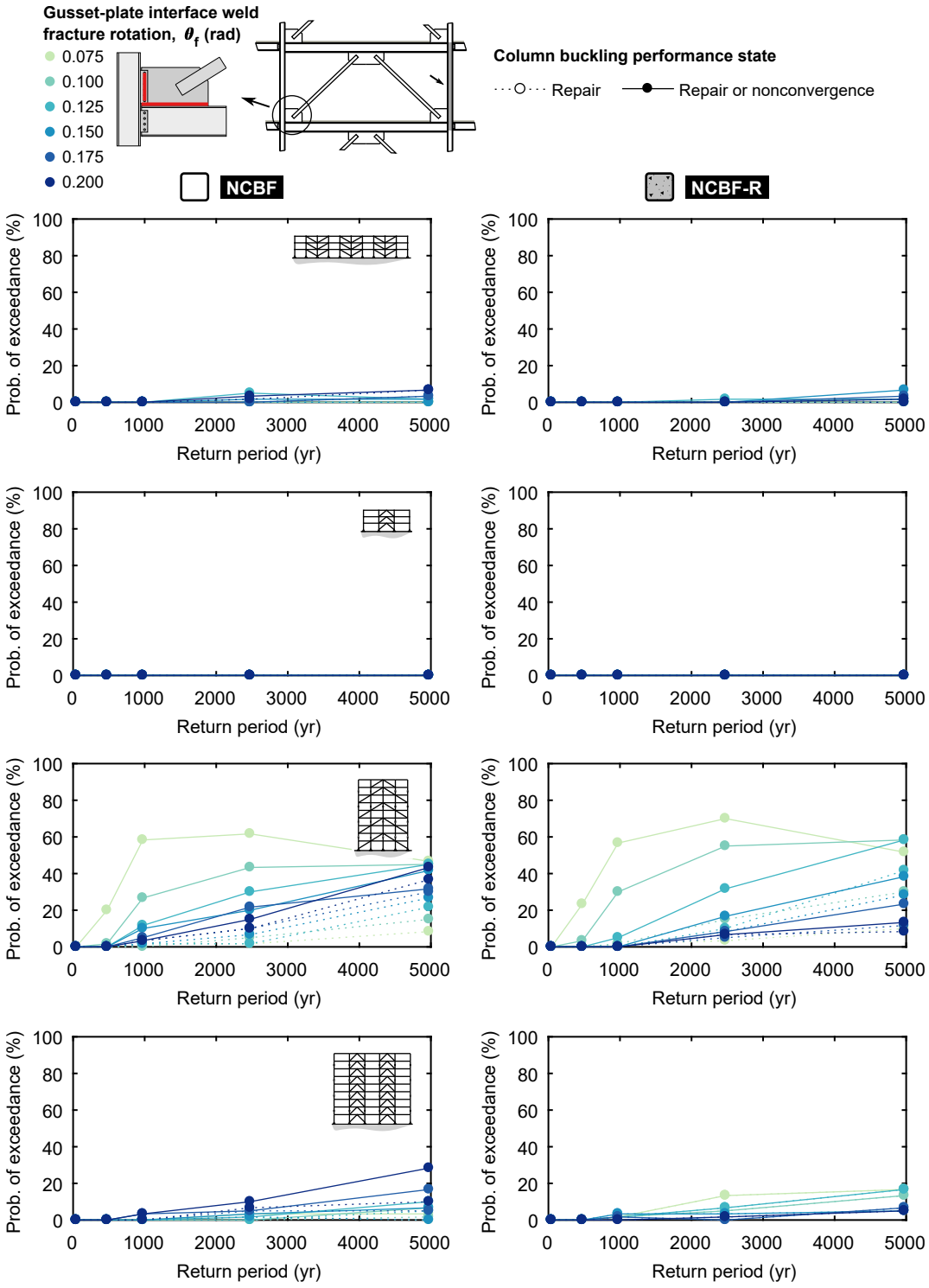

Figure 7.10: Probability of exceedance of column "repair" performance state for NCBF and NCBF-R buildings with various gusset-plate interface weld fracture rotations (Type-B behavior)

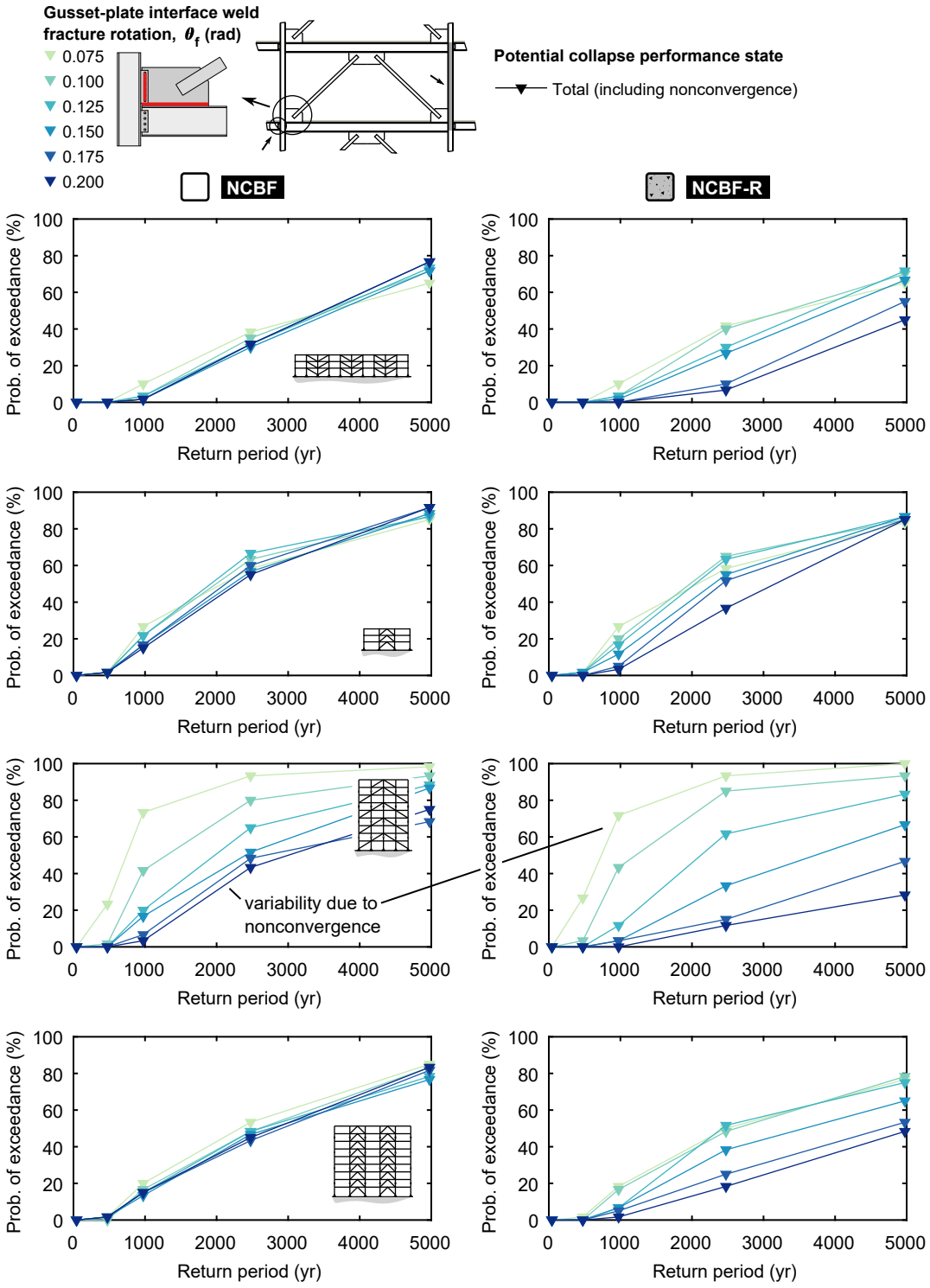

Figure 7.11: Probability of exceedance of all potential collapse performance states (including nonconvergence) for NCBF and NCBF-R buildings with gusset-plate interface weld fracture rotations (Type-B behavior)

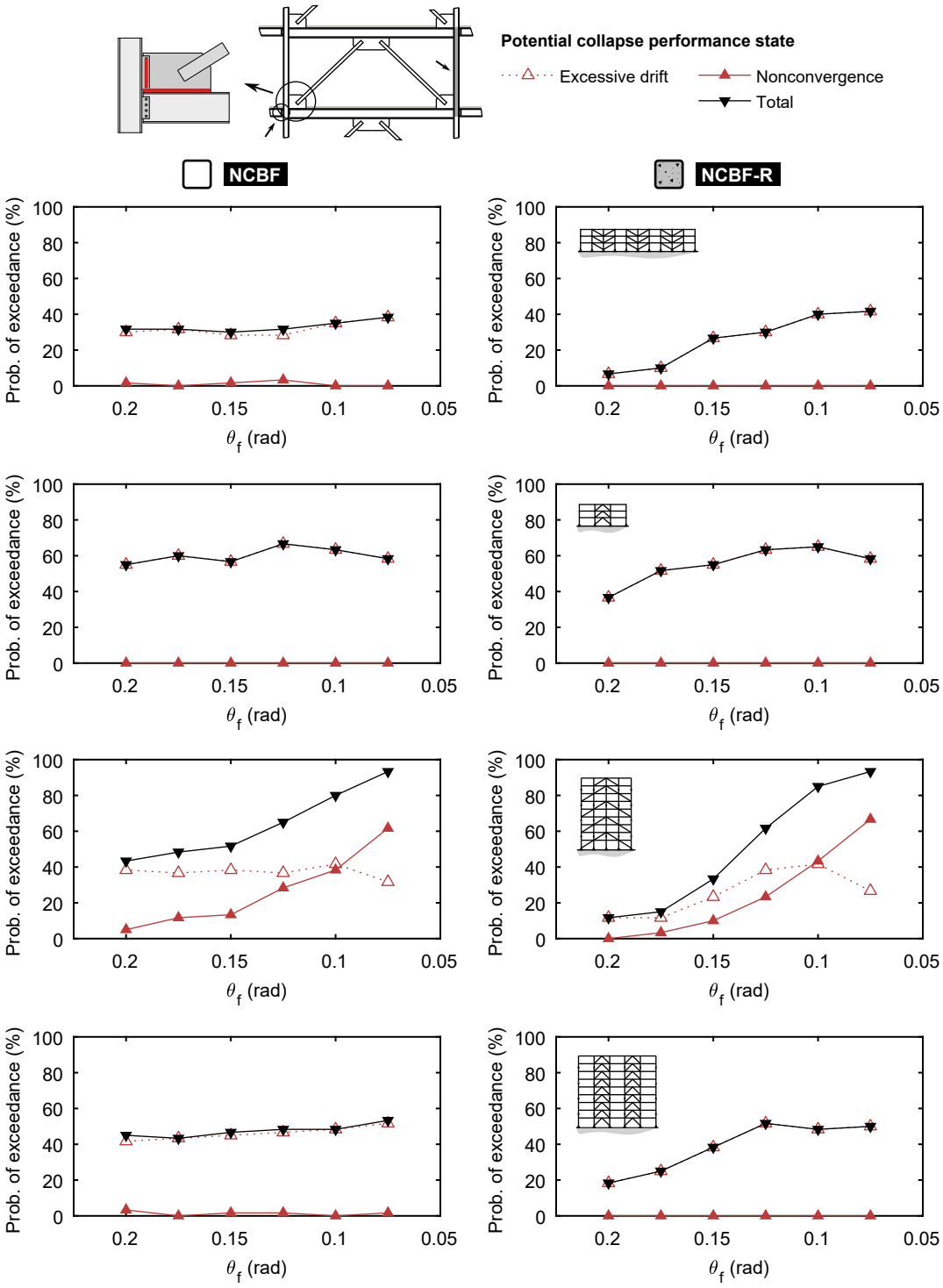

Figure 7.12: Probability of exceedance of potential collapse performance states at 2,475-yr return-period hazard level for NCBF and NCBF-R buildings with various gusset-plate interface weld fracture rotations (Type-B behavior)

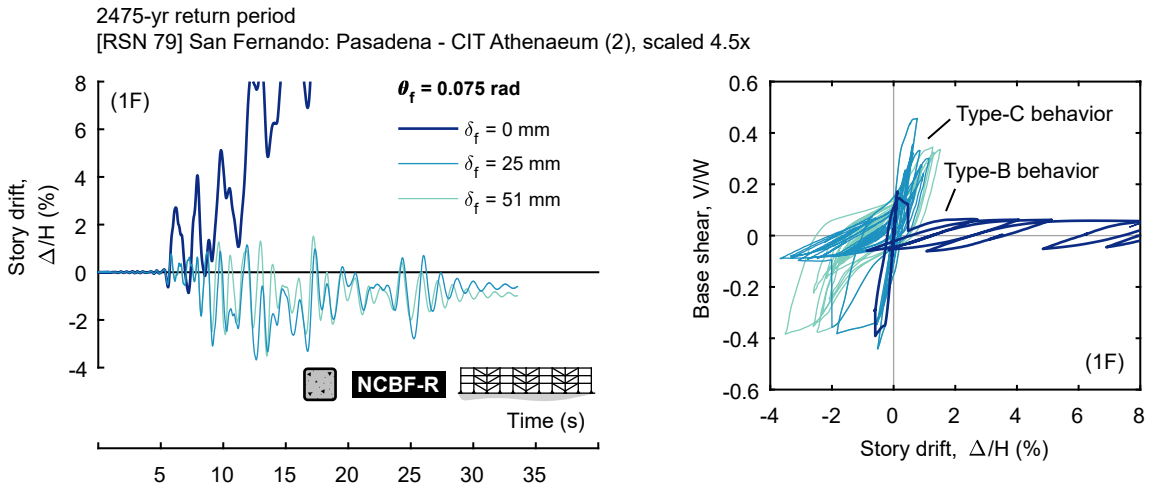

Figure 7.13: Example response history and hysteresis for 3-story NCBF-R buildings with gusset-plate interface weld fracture with a secondar yielding mechanism (Type-C behavior)

and 7.16 show the overall and 2,475-yr potential collapse performance. Secondary yielding-mechanism deformation capacity had a significant impact on collapse probability in the 3-story frames for both rotational capacities investigated. Even a limited amount of yielding in the connection after gusset-plate interface weld fracture drastically reduced the probability of potential collapse. For example, a δ_f of 13 mm (0.5 in), reduced the probability of potential collapse in the 3-story paired single diagonal NCBF-R building with a fracture rotation of 0.075 radians from 10% to 2% at the 475-yr hazard level and from 42% to 20% at the 2,475-yr hazard level.

Figure 7.16 indicates that larger reductions in potential collapse probabilities occurred for larger secondary yielding-mechanism deformation capacities. In particular, if enough secondary yielding-mechanism deformation capacity was available in the buildings with a fracture rotation of 0.075 radians, the potential collapse performance was comparable to that of buildings with a fracture rotation of 0.175 but δ_f of 0. For instance, this effect was achieved with a δ_f equal to 38 mm in the 3-story paired single diagonal buildings.

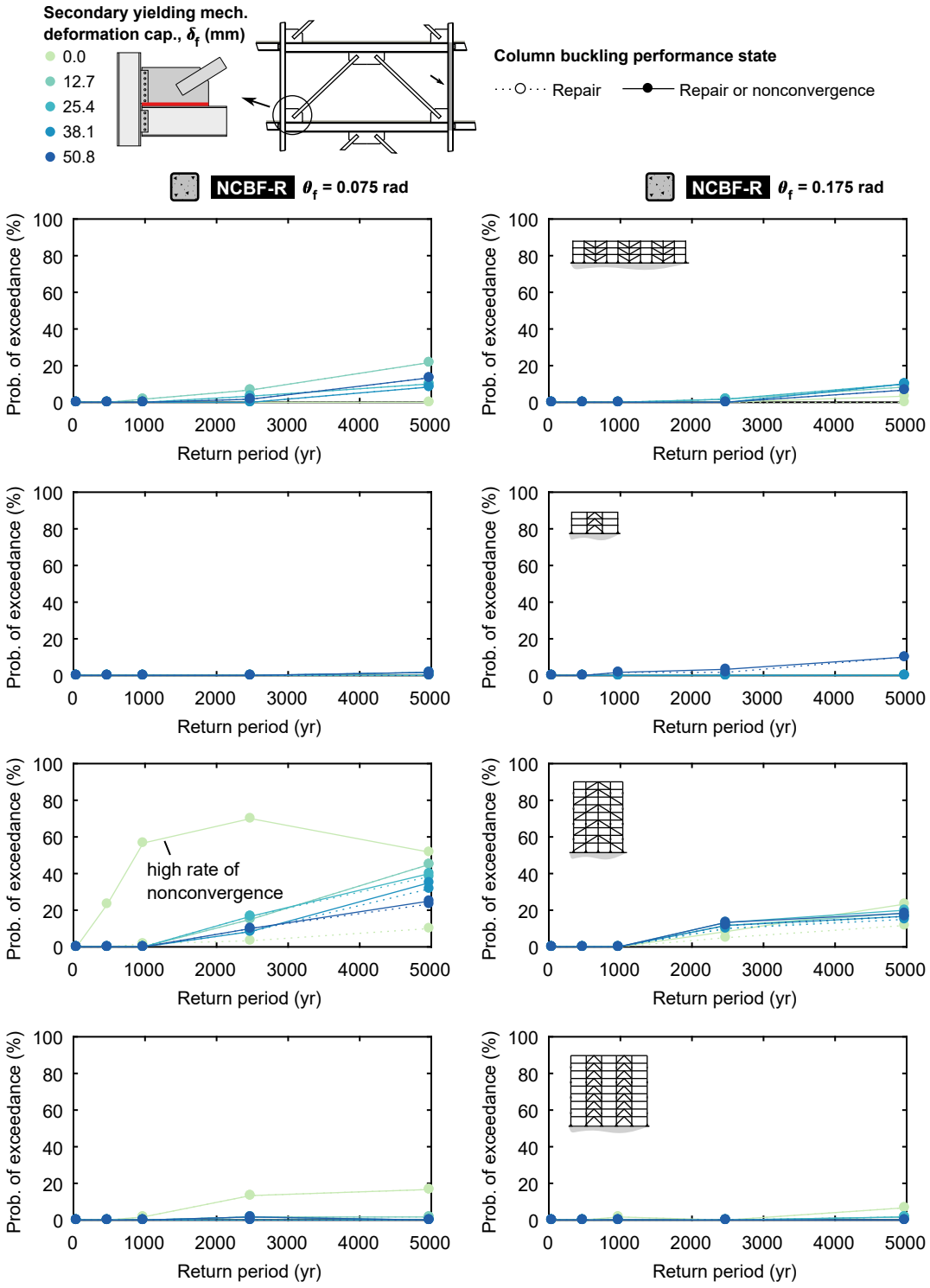

Figure 7.14: Probability of exceedance of column "repair" performance state for NCBF and NCBF-R buildings with various gusset-plate interface weld fracture rotations (Type-C behavior)

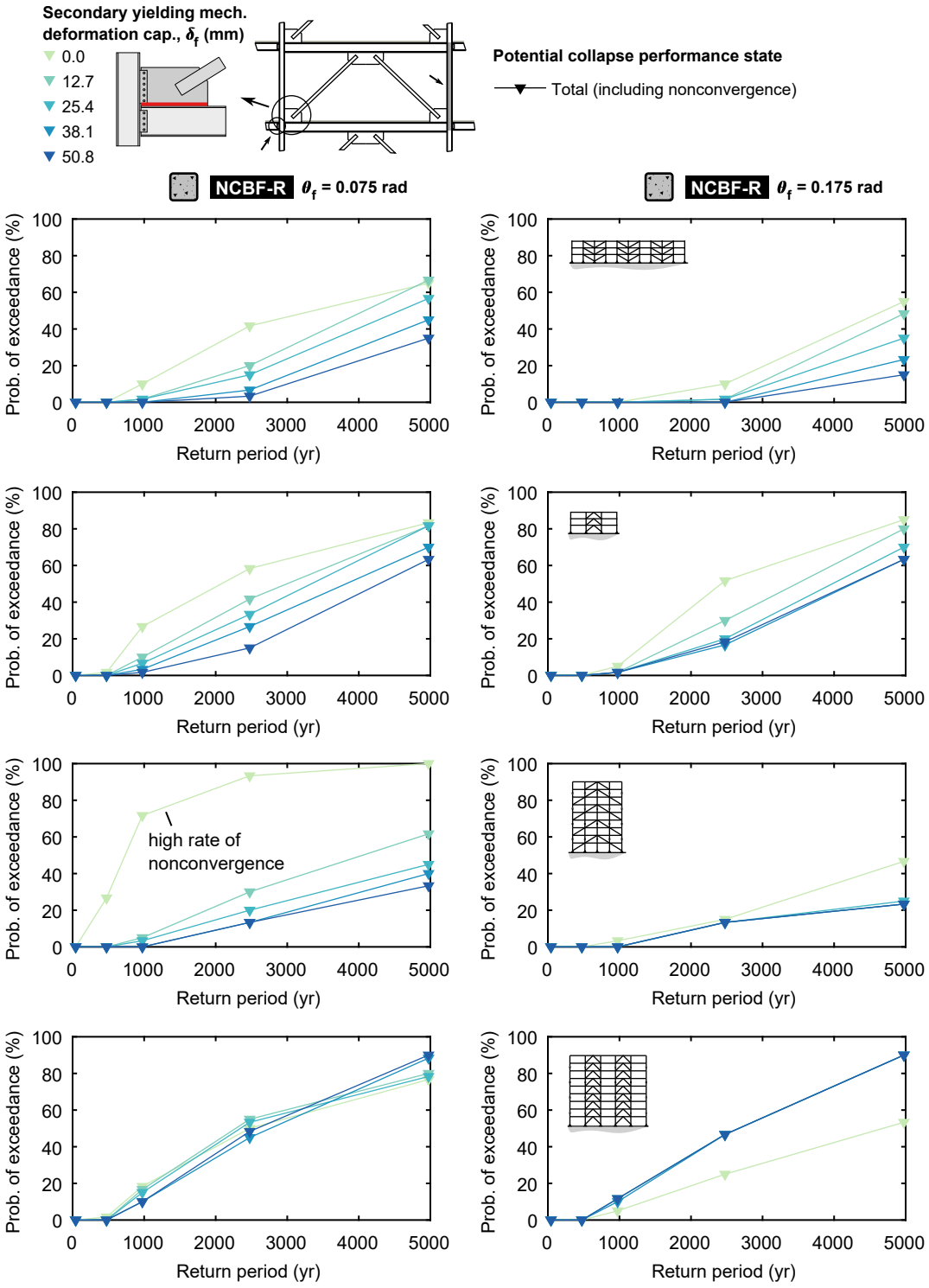

Figure 7.15: Probability of exceedance of all potential collapse performance states (including nonconvergence) for NCBF and NCBF-R buildings with gusset-plate interface weld fracture rotations (Type-C behavior)

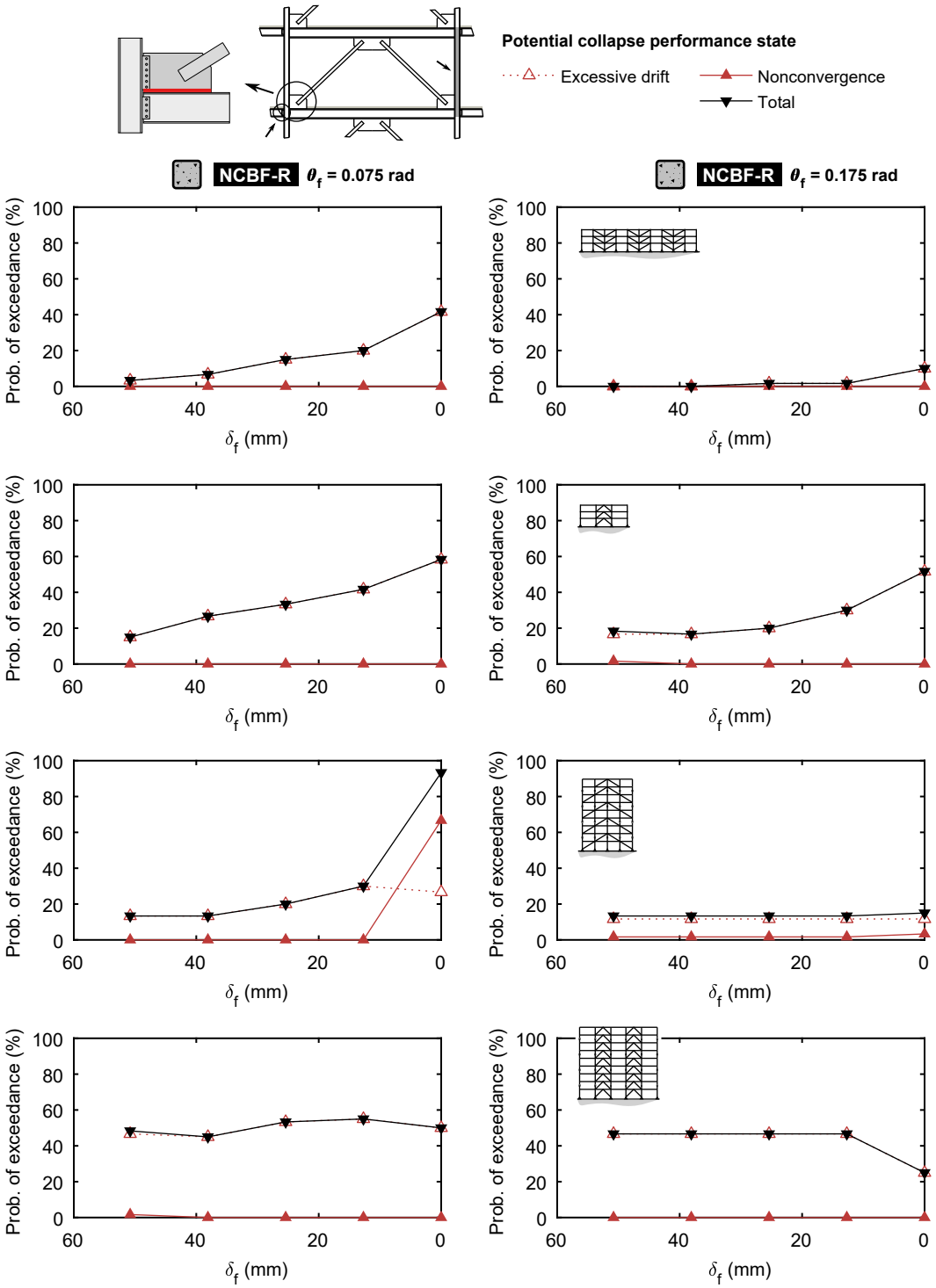

Figure 7.16: Probability of exceedance of potential collapse performance states at 2,475-yr return-period hazard level for NCBF and NCBF-R buildings with various gusset-plate interface weld fracture rotations (Type-C behavior)

7.5 Consequences of Column Buckling

Although the probability of exceeding the column repair performance state was significant in many of the above buildings, the probability of exceeding the column potential collapse performance state was essentially zero. This phenomenon may have been precluded by sidesway collapse or fracture of gravity-system beam-to-column connections due to excessive drift. However, column buckling which is not severe enough to be classified as potential collapse may affect these other collapse mechanisms.

Figure 7.17 aggregates the maximum story drifts and column midheight out-of-plane deflections at the 4,975-yr hazard level for the 3-story paired single diagonal NCBF-R buildings with a gusset-plate interface weld fracture rotation of 0.075 radians and varying secondary yielding mechanism deformation capacities between 0 and 51 mm. These columns were designed to develop the accumulated expected brace forces along the building height but had column repair state probabilities of exceedance between 0 and 22%. This histogram on the right-hand side of the figure shows the distribution of maximum column deflections for all buildings which had story drifts greater than 8%. The figure shows that: (1) column deflections below the repair state threshold ($z/b_f < 0.1$) were common, (2) there is slight correlation between maximum story drift and maximum column deflection, and (3) almost all instances of sidesway collapse had column deflections oat least $0.04b_f$ but no larger than $0.4b_f$. These observations suggest a link between column buckling and the sidesway collapse mechanisms, but their causal relationship (if any) is not obvious from the data. Future work should investigate this phenomenon in greater detail to understand the importance of column strength on collapse performance.

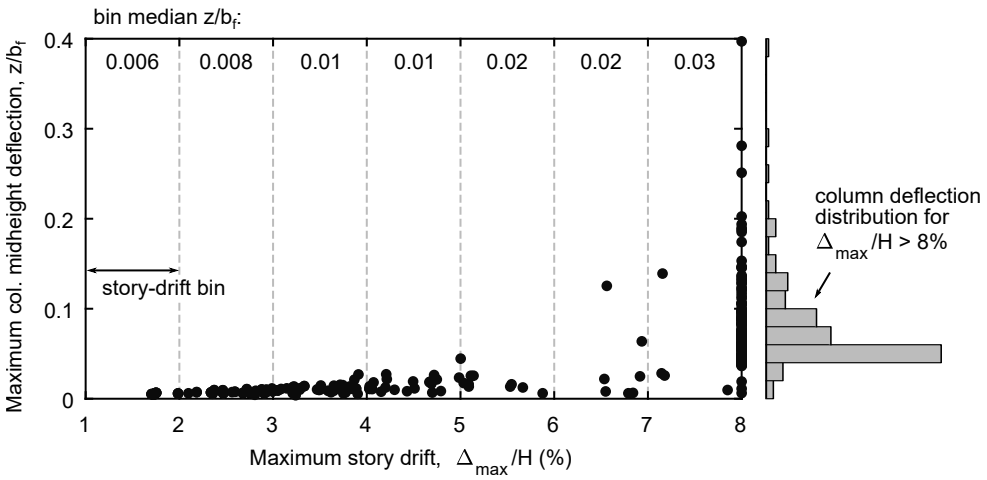

Figure 7.17: Relationship between column midheight deflection and story drift

Chapter 8

SUMMARY, CONCLUSIONS, AND FUTURE WORK

Many potentially nonductile concentrically braced frames (NCBFs) designed prior to about 1988, when significant changes in the seismic design of steel structures were codified (ICBO 1988), remain in use today as offices, hospitals, schools, warehouses, and other structures in regions with high seismic risk. These NCBFs are expected to be weaker than special CBFs (SCBFs) used in current practice and are susceptible to premature failure modes which may limit their strength and deformation capacity, leading to serious damage and potential collapse. The seismic vulnerability of these older buildings has been recognized but not well quantified by the engineering community due to limitations in the understanding of NCBF behavior, particularly due to limited experimental data. In addition, numerical modeling approaches used in typical practice are not generally equipped to accurately simulate the complex yielding and failure sequences possible in NCBFs, limiting the capabilities of seismic performance evaluation.

Characterizing and quantifying the behavior of NCBFs and advancing modeling capabilities is critical to understanding the vulnerability and improving the safety and post-earthquake functionality of these structures through seismic evaluation and retrofit. An NSF-funded research program entitled "NEESR: Collaborative Developments for Seismic Rehabilitation of Vulnerable Braced Frames" was undertaken to address these engineering needs. The research consisted of integrated experimental and numerical research programs. Large-scale testing of existing and retrofitted NCBF subassemblages was performed at the University of Washington Structural Research Laboratory and the National Center for Research on Earthquake Engineering (NCREE) laboratory in Taipei, Taiwan. The test data were used to validate new computational models, which were used with advanced seismic

hazard analysis approaches to quantify existing and retrofitted NCBF seismic performance and provide practical retrofit guidance.

8.1 Summary

The research was conducted in three phases: (1) experimental testing, (2) numerical model development, and (3) building seismic performance evaluation.

The first task of the research program consisted of a review of existing NCBF infrastructure. Twelve (12) drawings of buildings with NCBFs and located in regions with high seismic hazard in the US were reviewed to identify common deficiencies and quantify their severity relative to current design provisions for SCBFs (AISC 2017a). This evaluation included the computation of demand-to-capacity ratios (DCRs) for connection, beam, and column limit states. Analogous ratios were calculated for brace local slenderness (λ/λ_{hd}) and gusset-plate clearance ($8t_p/L_{clear}$) with respect to high-ductility geometric limits. System irregularities were also documented, though these were not studied in this work.

The infrastructure review revealed a variety of deficiencies and connection configurations which were used to design full-scale specimens tested in the second phase of the research. Twenty-two (22) experiments simulating existing and retrofitted NCBFs were conducted at the University of Washington with a focus on brace and connection behavior. Each specimen employed a single rectangular HSS brace which was slotted and welded to gusset plates on both ends. The gusset plates were attached to the frame with connection configurations and deficiencies identified in a review of existing infrastructure, including: continuous, welded shear plates; continuous, bolted shear plates; split, bolted shear plates; bolted double angles; bolted end plates; and integrated gusset-shear plates.

Three (3) of these specimens investigated the behavior of existing NCBFs with locally slender braces, undersized gusset-plate interface welds, and/or undersized brace-to-gusset welds. These deficiencies resulted in premature brace or weld fracture, which limited drift-range capacity to 1.3 to 1.8%. In contrast, SCBFs are expected to reach drift ranges on the order of 5 to 6% prior to significant damage (Roeder et al. 2011b). These concerns

were addressed in experiments of retrofit alternatives by replacing the brace, filling the brace with concrete, and reinforcing deficient welds. Brace replacement schemes using out-of-plane (OOP) buckling, in-plane (IP) buckling, and buckling-restrained braces (BRBs) were tested. In the retrofit specimens, the braces had approximately the same tensile capacities as the theoretical existing braces to avoid increasing force demands on adjacent connections, beams, and columns, and the gusset-plate interface welds were either retained as originally formed or reinforced with bolts or welds.

A second set of experiments simulating existing and repaired chevron NCBFs was conducted at the NCREE laboratory in Taiwan. This study consisted of four (4) experiments of two-story chevron CBFs with weaker beams than permitted for current SCBFs in the *Seismic Provisions* (AISC 2017a). The primary objective of these experiments was to understand the effects and behavior of these weak beams as part of a yielding-beam plastic mechanism. This deficiency was found in all chevron NCBFs in the infrastructure review, and the first-story beam DCRs tested were at the low end of the range of DCRs reported in the infrastructure review. The first specimen had a beam DCR of 2.1 and contextualized the yielding-beam mechanism within an existing NCBF with connection and brace deficiencies similar to those studied in the previous experimental program. After this test was completed, the specimen was repaired twice with (1) square HSS braces intended for IP buckling and (2) wide-flange braces intended for OOP buckling. The final specimen was a more extensive repair in which the components met the requirements of SCBFs with the exception of the first-story beam strength (DCR of 1.2).

The results of the experimental investigations were used to develop a priority for retrofitting NCBFs. This priority included DCR limits for beam yielding, brace-to-gusset weld fracture, gusset-plate interface weld fracture, and shear-plate bolt fracture, brace local slenderness, and gusset-plate elliptical clearance to classify low-, moderate-, and high-priority retrofits. In addition, specimen responses were used to define characteristic behavior types associated with the hierarchy of yielding mechanisms and failure modes within the brace-gusset assembly. These retrofit priority criteria and behavior types were used to design a building study

matrix to investigate their system-level implications under seismic loading.

The second phase of the research program utilized the experimental data to develop computational models capable simulating important NCBF yielding mechanisms and failure modes to analyze the nonlinear dynamic response of existing and retrofitted NCBF buildings. This work built upon the SCBF modeling approach developed by Hsiao et al. (2012, 2013a), which included the use of fiber-based, distributed-plasticity beam-column elements for modeling braces, beams, and columns; multiple brace elements with initial imperfection to simulate buckling; a brace fracture model based on maximum strain range (MSR) of individual fibers; and nonlinear rotational springs at the brace ends to simulate the out-of-plane flexural strength and stiffness of the gusset-plates. The new modeling approaches advanced this work to simulate gusset-plate Whitmore yielding, brace-to-gusset weld fracture, gusset-plate interface weld fracture with and without secondary yielding mechanisms, chevron beam yielding, and column buckling. In addition, the MSR brace-fracture model was modified to capture the effects of load-direction bias and concrete in-fill on fracture life.

These new modeling approaches were implemented in *OpenSees* to quantify the seismic vulnerability of three- and nine-story buildings with paired single diagonal and chevron CBFs using response-history analysis in a multi-stripe analysis framework. The buildings were subjected to five (5) suites of ground motions representing different hazard levels (i.e., different ground-motion intensities) for the building site in Seattle. Damage states for brace-gusset assemblies, beams, columns, and composite bolted shear-plate gravity connections were defined based on experimental data to objectively evaluate the buildings. Different design variations were evaluated, including benchmark NCBFs designed to the *1979 Uniform Building Code* (ICBO 1979) with deficient braces, connections, beams and columns; retrofitted NCBFs with concrete in-fill; parametrically varying connection deficiencies; and reference SCBFs designed to *ASCE/SEI 7-16* (ASCE 2017a).

8.2 Conclusions

8.2.1 Nonlinear Modeling of NCBFs using Line- and Spring-Element Formulations

Fracture Simulation

- The general-purpose *MaxStrainRange* material wrapper can be used to simulate fracture of various components, including braces, brace-to-gusset weld, gusset-plate interface welds, and secondary yielding mechanisms. This material simulates fracture when the MSR of the underlying material exceeds the input value (MSR_f). Its *OpenSees* implementation has been redeveloped from Hsiao et al. (2013a) to provide optional support for (i) tracking global deformation between two nodes, (ii) specifying a lower-bound MSR_f, and (iii) removing elements from the analysis when the fracture criterion is reached.

Rectangular HSS Braces

- Brace fracture should be simulated with the *MaxStrainRange* material using the proposed $MSR_{f,disp}$ prediction equation (Eq. 4.2). To use this equation, rectangular HSS braces should be modeled with 16 displacement-based elements with 4 integration points per element. Brace fracture should be simulated with the *MaxStrainRange* material using Eq. 4.2, which includes a term for the ratio of the maximum brace compressive deformation to the maximum brace tensile deformation. This is tracked in the *MaxStrainRange* material by specifying the end nodes of the brace, which updates the MSR_f at each analysis step.

- Rectangular HSS braces with concrete in-fill should be modeled as above but with an MSR_f no less than 0.0505 to account for the increased fracture life of these braces. This can be simulated with the *MaxStrainRange* material by specifying a lower-bound MSR_f.

Gusset-Plate Connections

- Brace-to-gusset weld fracture should be modeled with an axial spring at the brace end with the nonlinear force-deformation relationship proposed by Lesik and Kennedy (1990). Specimen 1E from the experimental research program had a brace-to-gusset weld DCR of 1.7 and was numerically simulated in *OpenSees* with the Lesik and Kennedy (1990) relationship modeled using the *MultiLinear* constitutive model wrapped with the *MaxStrainRange* material. The behavior was simulated well using a weld size 1.25 times the specified value.

- The out-of-plane fracture rotation, θ_f, of gusset plates with deficient interface welds should be computed as a function of the weld DCR based on the BDP expression and the gusset-plate elliptical clearance relative to the plate thickness (Eq. 4.11). This fracture rotation can be used to explicitly simulate gusset-plate interface weld fracture (e.g., in *OpenSees*) or transformed to an approximate brace compressive deformation limit as $L\theta_f^2/2$, where L is the end-to-end length of the brace.

- Gusset-plate interface weld fracture should be explicitly modeled by wrapping the gusset-plate rotational spring (modeled after Hsiao et al. (2012)) with the *MaxStrain-Range* material. The fracture rotation computed using the proposed prediction equation can be specified as the MSR_f in the material. It is recommended that the reduced stiffness of adjacent beam and column elements after gusset plate fracture is simulated using a stiff, elastic beam-column element in parallel with a nonlinear beam-column element. Upon fracture, the stiff element is removed if its element tag is specified with the *MaxStrainRange* material for that gusset-plate rotational spring.

- Secondary yielding mechanisms which develop after gusset-plate interface weld fracture (Type-C behavior) should be modeled with a stiff, elastic axial spring and nonlinear axial spring in parallel at the brace end. In the initial state, the stiff spring attracts essentially all demand and the nonlinear spring is not engaged. When gusset-plate

interface weld fracture is modeled as above with the *MaxStrainRange* material, the tag of the stiff, elastic axial spring element should be specified to be removed on fracture. Further, the nonlinear axial spring can be wrapped with another *MaxStrainRange* material to simulate fracture of the secondary mechanism.

8.2.2 Seismic Vulnerability and Retrofit Priority

- Based on nonlinear response-history analysis, NCBFs are expected to sustain much larger drift demands than SCBFs. At the 475-yr hazard level, the SCBF buildings analyzed had median story-drift demands of 0.6 to 0.7%, while NCBF buildings which had combinations of brace, connection, beam, and column deficiencies based on *UBC-79* design requirements (ICBO 1979) had median story drifts between 0.7 and 1.5%. At the 2,475-yr hazard level, the SCBF-building median drift demands were between 1.4 and 3.6% but the NCBF buildings reached the potential collapse performance state or did not converge on average. The potential collapse probabilities of exceedance were between 60 and 95% for the NCBF buildings at this hazard level. The corresponding SCBF probabilities of exceedance were no larger than 10%, which is the anticipated collapse reliability in the MCE_R in *ASCE/SEI 7-16* (ASCE 2017a). The SCBF deflection amplification factors based on this hazard level were generally much larger than C_d in *ASCE/SEI 7-16* (median values between 13 and 26 for all but the 9-story paired single diagonal) (ASCE 2017a). Both the NCBFs and SCBFs were vulnerable to drift concentration in a single story, leading to soft-story collapse in large earthquakes. The vertical distribution of drift was more uniform in the 9-story SCBFs than in the other buildings.

- Locally slender rectangular HSS braces with λ/λ_{hd} greater than about 1.6 are high priorities for retrofit. Experiments showed that frames with these braces may only sustain a drift range of about 1.0 to 1.5% before brace fracture. In response-history analysis of NCBF buildings with these deficient braces, the probability of exceedance

of incipient brace fracture was greater than 98% at the 2,475-yr return period. This corresponded to a probability of potential collapse between about 30 and 60% at the same hazard level, which is well above the 10% probability of collapse targeted by *ASCE 7-16* (ASCE 2017a). Rectangular HSS braces with λ/λ_{hd} between 1.2 and 1.6 are considered moderate priorities for retrofit, but braces in this local slenderness range were not investigated using response-history analysis. An experimental specimen with a brace with λ/λ_{hd} equal to 1.2 sustained a drift range of 4% prior to initial tearing at the brace midspan. This is below the drift range expected for SCBFs (Roeder et al. 2011b) but substantially larger than that for braces with λ/λ_{hd} greater than 1.6.

- Brace-to-gusset welds with DCRs greater than about 1.0 are high priorities for retrofit. DCRs of 1.0 and 1.7 were experimentally investigated and the drift range capacity was below 1% in both cases. In building-level analyses, the performance of NCBF buildings with brace-to-gusset weld DCRs above 1.0 was similar to that of NCBFs with braces classified as high-priority retrofits. Specifically, the probability of exceedance was between 83 and 100% for the brace-gusset assembly replace state and between 25 and 48% for the potential collapse performance state for a brace-to-gusset weld DCR of 1.25 at the 2,475-yr return period when this failure mode was isolated. These probabilities of exceedance were generally lower for a brace-to-gusset weld DCR of 1.00 at the same hazard level (10–48% for brace-gusset assembly replacement and 3–52% for potential collapse), and hence a DCR between 0.75 (fully compliant) and about 1.0 is considered a moderate priority for retrofit.

- Gusset-plate interface welds with rotation capacities less than about 0.1 rad are also high priorities for retrofit and share similar response and performance characteristics to high-priority brace and brace-to-gusset weld deficiencies (98 to 100% probability of exceedance of brace-gusset assembly replacement and 42 to 93% probability of exceedance of potential collapse performance states at the 2,475-yr return period). The rotation capacity of welded gusset plates in NCBFs can be approximated using the

weld DCRs based on the BDP and the gusset-plate elliptical clearance using the proposed equation from the modeling recommendations (Eq. 4.11). Gusset-plate interface welds with rotation capacities between about 0.1 and 0.2 rad are moderate priorities for retrofit. Experimentally, gusset-plate interface welds with fracture rotations in this range sustained drift ranges between 2.4 and 3.3% prior to fracture. Response-history analysis showed improved performance over the high-priority cases; notably, the probability of exceedance for the brace-gusset assembly replacement performance state was 0% for a fracture rotation of 0.200 rad versus 48 to 98% for a fracture rotation of 0.075 rad at the 475-yr return period when this failure mode was isolated. These gusset-plate interface weld rotational capcaities may be below those which would be expected for SCBFs but were large enough to mitigate damage in less severe earthquakes.

- Columns in NCBFs and SCBFs which met the capacity-based design strength requirements of the *Seismic Provisions* (AISC 2017a) sustained buckling in several cases. In all building analyses in this document, the probability of exceedance for the *column* potential collapse performance state was only greater than 0% in the benchmark, 9-story chevron NCBF, which had 1.7 and 3.3% probabilities of exceedance at the 2,475- and 4,975-yr return periods, respectively. The probability of exceeding the column repair performance state was as high as about 33% at the 2,475-yr return period. The vulnerability to column buckling was generally largest in the 9-story paired single diagonal buildings, where the central column is subjected to unbalanced brace forces similar to a beam in a chevron CBF. In the benchmark 9-story paired single diagonal SCBF, the probability of exceedance of the column buckling performance state was 8% at the 2,475-yr return period. Although the probability of column deflection exceeding the potential collapse performance state was very low, lesser degrees of column buckling (i.e., $z/b_f < 0.4$) were correlated with potential collapse due to excessive drift. However, it is unclear if this slight column buckling helps precipitate sidesway collapse or is an artifact of the large overall deformation demands leading to sidesway collapse.

8.2.3 Retrofit Recommendations

- Seismic retrofits of NCBFs should follow a balanced design philosophy to retain secondary yielding mechanisms and suppress unwanted failure modes. Specifically, experimental investigation suggested that: (i) a Whitmore angle of 37° should be used for evaluating gusset plate yielding; (ii) gusset-plate interface welds, including weld overlays, should be designed using the BDP to develop the tensile strength of the gusset plate; (iii) bolted connections should be designed to promote bolt-hole elongation by balancing the bolt fracture and bearing (tearout and excessive bearing deformation) limit-state resistances; and (iv) chevron beams with DCRs up to about 2.0 to 2.5 should be permitted. These recommendations apply for the connection configurations tested. In addition, the recommended limits for chevron beam DCRs may differ for other brace sections and beam-end conditions; other research is in progress to improve these recommendations (e.g., Terpstra (2017)).

- Rectangular HSS braces with λ/λ_{hd} greater than 1.0 can be retrofitted with concrete in-fill to improve deformation capacity. This retrofit was successfully tested for an HSS7×7×1/4 brace (λ/λ_{hd} equal to 2.3), where the story-drift range was increased from 1.5 to 4.4%. The concrete fill must be separated from the gusset plate to prevent contact and an increase in brace force, which could place larger demands on the adjacent connections. In response-history analysis, this retrofit was effective in mitigating the probability of potential collapse in the buildings without connection deficiencies (reduction in probability of exceedance from 33–58% to 0–22% at the 2,475-yr return period). This reduction is especially notable because the brace (and hence building) strength was not increased to resist modern design demands. This retrofit is not effective if high-priority connection deficiencies are retained.

- Secondary yielding mechanisms (i.e., item (iii) above) were shown in response-history analysis to significantly reduce the probability of potential collapse at the 975-yr haz-

ard level and above. Even a yielding mechanism with a modest deformation capacity (12.7 mm) decreased the probability of potential collapse at the 2,475-yr hazard level from 42–58% to 20–42%. Further, a gusset-plate with a rotational capacity of 0.075 rad due to interface weld fracture (high priority) but a large secondary yielding mechanism deformation capacity (51 mm) performed similar to a system with a gusset-plate rotational capacity of 0.175 rad (moderate priority). Thus, the system vulnerability due to the gusset-plate interface weld fracture failure mode may be lower if a stable secondary yielding mechanism can form. It is noted that these results have only been validated for a secondary yielding mechanism with full hysteretic behavior and a yield strength equal to 70% of the expected brace capacity in tension.

- IP-buckling brace and BRB retrofits were only investigated experimentally but may be performed to mitigate gusset-plate interface weld fracture due to the high rotational demands with OOP-buckling braces. IP-buckling was difficult to control experimentally with square HSS braces. Therefore, these retrofits should be carefully designed to consider the impact of connection rotational stiffness on buckling direction or employ a brace cross section with radii of gyration that favor IP buckling. BRB retrofits should follow the web-doubler recommendations of Palmer et al. (2016) to mitigate yielding and local deformation in the beam and column adjacent to the connection. This type of retrofit was investigated experimentally but not numerically in this work.

8.3 Future Work

Although the scope of the research presented in this dissertation was large, additional work is needed to fully characterize the seismic performance of NCBFs.

Practical limitations to the experimental research program scope did not permit testing of alternative load histories, which may reveal different connection and system behaviors that are important for NCBFs. For example, net section fracture is known to occur in pulse-like loading characteristic of near-field earthquakes (Yang and Mahin 2005; Roeder et al. 2011b).

Pulse-like, long-duration, or collapse-consistent loading protocols are all candidates for future study. In a similar vein, the input ground motions used for seismic performance evaluation in this study were limited to far-field motions from crustal source mechanisms. While these types of motions are perhaps the most consistent with the fully reversed cyclic, increasing-amplitude loading protocols used in the experiments, ground motions from other sources would likely have characteristics which affect performance including collapse probability.

Several simplifications were made in this work to model gusset-beam-column connection behavior of connections with secondary yielding mechanisms. This intersection is difficult to accurately model using line elements, as in *OpenSees*, due to the complex geometry of the members and highly nonlinear behavior of the connections (e.g., bolt pretension and slip, bolt bearing and rotation, angle yielding, contact, etc.). Fiber models for bolted shear plates and double-angles developed to simulate progressive collapse have been proposed in the literature for gravity beam-to-column connections (Weigand et al. 2016; Weigand 2017), but it is not clear if these models are suitable for gusset-plate connections which have high axial forces.

There are several NCBF deficiencies which have not been studied but likely have significant impacts on system response. As noted in the infrastructure review, many beams and columns had strength deficiencies based on modern capacity-based design requirements. These issues were only investigated in the benchmark NCBF buildings here, but should be investigated using additional parametric studies to better understand their impacts on seismic performance. The performance of NCBFs with columns oriented for weak-axis bending in the plane of the frame may also result in different seismic performance due to the reduced lateral resistance from frame action and alternative gusset-plate connection configurations employed. Uplift and/or fracture of column bases was reported in many NCBFs damaged in past earthquakes (e.g., the 1994 Northridge Earthquake and 1995 Hyogoken-Nanbu Earthquake). This failure mode would clearly affect the dynamic response of the building. In addition, vertical irregularities were identified in many of the buildings in the infrastructure review and could result in damage concentration that leads to collapse.

Lastly, simulating the deficiencies evaluated in this document and others listed here using more realistic, three-dimensional building models which consider the effects of bidirectional loading, flexible diaphragms, weak collectors, and beam and column local buckling could potentially demonstrate greater seismic vulnerability and ultimately improve retrofit guidance for NCBFs.

Appendix A

NOTATION LIST

The notation list in Table A.1 defines variables which are used throughout the document. In some cases, variables are defined in the document manuscript and are necessarily repeated here.

Table A.1: Notation List

Variable	Description
A_g	Gross area
A_{gp}	Gross area of plate
A_{gv}	Gross area in shear
A_{nb}	Net area of brace
A_{nt}	Net area in tension
A_{nv}	Net area in shear
B_w	Whitmore width
$BFFR$	Bolt bearing-to-fracture resistance ratio
C	Coefficient for determining base shear in *UBC-79* (ICBO 1979)
C_d	Deflection amplification factor in *ASCE/SEI 7-16* (ASCE 2017a)
C_s	Seismic response coefficient in *ASCE/SEI 7-16* (ASCE 2017a)
C_u	Coefficient for upper limit on calculated period in *ASCE/SEI 7-16* (ASCE 2017a)
D	Nominal dead load
DCR	Demand-to-capacity ratio
$DCR_{prac.}$	Practical demand-to-capacity ratio for chevron beam yielding
DI	Accumulated damage index in Miner's rule
DI_i	Damage index for full or half cycle in Miner's rule
E	Elastic modulus of steel
E_c	Elastic modulus of concrete
F_{EXX}	Weld filler metal classification strength
F_{cr}	Critical buckling stress computed with F_y
F_{cre}	Critical buckling stress computed with $R_y F_y$
F_t	Concentrated force at roof in *UBC-79* (ICBO 1979)

Continued on next page

Variable	Description
F_u	Nominal tensile strength
$F_{u,meas}$	Measured tensile strength
F_x	Equivalent lateral force at story x
F_y	Nominal yield stress
$F_{y,exp}$	Expected yield stress
$F_{y,meas}$	Measured yield stress
H	Story height
K	Effective length factor
	Horizontal force factor for buildings and other structures in *UBC-79* (ICBO 1979)
L	End-to-end brace length
	Nominal live load
L_{avg}	Whitmore length
L_b	Clear beam length
L_{bm}	Beam length from work point to work point
L_c	Effective bacee length (i.e., KL)
L_{clear}	Elliptical clearance length
L_D	Building length
L_w	Weld length
I	Importance factor in *UBC-79* (ICBO 1979)
I_e	Importance factor in *ASCE/SEI 7-16* (ASCE 2017a)
M_c	Plastic moment of column
M_n	Normal-coordinate generalized mass
M_p	Plastic moment
M_r	Required moment
MSR_f	Maximum strain range at fracture
$MSR_{f,conc}$	MSR_f for concrete-filled braces
$MSR_{f,disp}$	MSR_f for displacement-based brace elements
$MSR_{f,force}$	MSR_f for force-based brace elements
N	Elliptical clearance length normalized by t_p
N_f	Number of constant-amplitude cycles to cause fracture
N_s	Number of shear surfaces
N_w	Number of brace-to-gusset weld legs
P_1	Annual probability of exceedance
P_N	Probability of exceedance in an N-year time span
P_{brw}	Brace-to-gusset weld force
P_c	Expected brace strength in compression

Continued on next page

Variable	Description
P_{cr}	Critical buckling load
$P_{cr,n}$	Critical buckling load of brace at story n
P_h	Resultant horizontal component from unbalanced brace forces
P_t	Expected brace strength in tension
P_v	Resultant vertical component from unbalanced brace forces
P_y	Yield force
R	Response modification factor in *ASCE/SEI 7-16* ASCE (2017a)
R_y	Ratio of expected-to-nominal yield stress
R_t	Ratio of expected-to-nominal tensile strength
S	Site-structure resonance coefficient in *UBC-79* (ICBO 1979)
T	Fundamental period in *UBC-79* (ICBO 1979)
	Period
T_1	Fundamental period in analysis
T_a	Approximate fundamental period in *ASCE/SEI 7-16* (ASCE 2017a)
T_{des}	Design fundamental period
U_{bs}	Block shear coefficient
V	Base shear
V_{1979}	Design base shear in *UBC-79* (ICBO 1979)
V_{2016}	Design base shear in *ASCE/SEI 7-16* (ASCE 2017a)
$V_{bb,n}$	Predicted story shear at story n at initial brace buckling
$V_{fr,n}$	Moment-frame lateral force at story n at initial brace buckling
V_{max}	Maximum base shear
V_{s30}	Time-averaged shear-wave velocity to 30-m soil depth
W	Effective seismic weight
Z	Zone factor in *UBC-79* (ICBO 1979)
b	Rectangular or square HSS brace wall width
	Flange width
$\mathbf{c}$	Damping matrix
d	Rectangular brace wall width
d_x	Depth to bolt group center of gravity
f'_c	Specified concrete compressive strength
g	Gap between beam and column flange
h	Web depth
h_x	Height to story x
m	Coffin-Manson relationship exponent
$\mathbf{m}$	Mass matrix
p	Ratio of fillet-weld deformation to deformation at ultimate load

Continued on next page

Variable	Description
r	Radius of gyration
t	Brace wall thickness
t_f	Flange thickness
t_{kp}	Knife-plate thickness
t_p	Gusset-plate thickness
t_w	Web thickness
w_{br}	Brace-to-gusset fillet-weld leg size
w_p	Gusset-plate interface fillet-weld leg size
w_x	Seismic weight at story x
z	Column midheight deflection in direction of buckling
Δ	Story drift
	Brace-to-gusset weld axial deformation
Δ_{bm}	Beam midspan deflection
Δ_e	Story drift from elastic analysis using equivalent lateral forces
Δ_m	Fillet-weld deformation at ultimate load
Δ_{max}	Maximum story drift
Δ_{story}	Story drift
Δ_u	Fillet-weld deformation at fracture
Δt	Time step
Ω_0	Overstrength factor in *ASCE/SEI 7-16* (ASCE 2017a)
α	Parameter in HHT method
β	Balance factor for BDP limit-state expressions
δ	Axial deformation
	Beam midspan deflection (Chapter 3 only)
$\delta_{c,max}$	Maximum brace compressive deformation
δ_f	Secondary yielding-mechanism axial deformation capacity
δ_{range}	Brace axial deformation range
$\delta_{t,max}$	Maximum brace tensile deformation
δ_y	Axial yield deformation
ε_0	Strain amplitude at which one cycle would result in fracture
ε_{c0}	Concrete strain at maximum compressive stress
ε_i	Strain amplitude in Coffin-Manson relationship
θ	Initial brace angle
	Gusset-plate out-of-plane rotation
$\theta_{2\%}$	Gusset-plate rotation at 2% story drift
θ_i	Fillet-weld load angle
θ_f	Gusset-plate interface weld fracture rotation

Continued on next page

Variable	Description
θ_{gp}	Gusset-plate rotation
θ_n	Initial brace angle at story n
θ_{sp}	Shear-plate rotation
λ	Local slenderness (cross-sectional width-to-thickness) ratio
λ_{hd}	Limiting local slenderness ratio for highly ductile members in *Seismic Provisions* (AISC 2017a)
ξ	Structural damping ratio
ξ_n	Damping ratio at mode n
$\bar{\xi}$	Algorithmic damping ratio
ϕ	Resistance factor for AISC limit-state expressions
ϕ_n	Mode-shape vector for mode n
ω_n	Radial frequency of mode n

Appendix B

OPENSEES SOURCE CODE

This appdendix provides the *OpenSees* source code written in C++ for the *MaxStrain-Range* fracture material.

B.1 MaxStrainRange Header File

```
#pragma once
#define MaxStrainRange_h

#include <UniaxialMaterial.h>
#include <Node.h>

// #define MAT_TAG_MaxStrainRange 5002

class MaxStrainRange : public UniaxialMaterial
{
public:
        MaxStrainRange(int tag,
                UniaxialMaterial &thePreMaterial,
                double limitSR,
                double minStrain,
                double maxStrain,
                double kappa,
                int numEles,
            const Vector &eleTags,
                bool defMode,
                const Vector &nodeTags,
                double floorSR,
                double defCoeff);
        MaxStrainRange();
        ~MaxStrainRange();

        const char *getClassType(void) const { return "MaxStrainRange"; };

```

```
29          int setTrialStrain(double strain, double strainRate = 0.0);
30          double getStrain(void);
31          double getStrainRate(void);
32          double getStress(void);
33          double getTangent(void);
34          double getDampTangent(void);
35          double getInitialTangent(void) {
36                  return theMaterial->getInitialTangent();
37          };
38          double getMaxStrainRange(void);
39          int getFail(void);
40
41          int commitState(void);
42          int revertToLastCommit(void);
43          int revertToStart(void);
44
45          UniaxialMaterial *getCopy(void);
46
47          int sendSelf(int commitTag, Channel &theChannel);
48          int recvSelf(int commitTag, Channel &theChannel, FEM_ObjectBroker &theBroker);
49
50          void Print(OPS_Stream &s, int flag = 0);
51
52          Response *setResponse(const char **argv, int argc, OPS_Stream &s);
53          int getResponse(int responseID, Information &matInformation);
54
55  protected:
56
57  private:
58          UniaxialMaterial *theMaterial;
59
60          // trial values
61          double Tstrain;
62          double Tstress;
63          double Ttangent;
64          double TminS;
65          double TmaxS;
66          double TmaxSR;
67          bool Tfailed;
68
69          // commit values
70          double Cstrain;
```

```
71          double Cstress;
72          double Ctangent;
73          double CminS;
74          double CmaxS;
75          double CmaxSR;
76          bool Cfailed;
77
78          // failure parameters
79          double limitSR;         // strain range that triggers material failure
80          double minStrain;       // negative (compressive, usually) strain that triggers
                material failure
81          double maxStrain;       // positive (tensile, usually) strain that triggers material
                 failure
82          double kappa;           // Ratio of initial stiffness available after fracture
83          double floorSR;         // lower bound on strain range at fracture
84
85          // element removal
86          Domain *theDomain;              // needed to retrieve the element pointer
87          Element *theElement;    // element pointer
88          int numEles;                    // number of elements to be removed
89          Vector eleTags;                 // tags of elements to be removed
90
91          // global deformation tracking
92          Node *iNode;
93          Node *jNode;
94          bool defMode;                   // true if global deformation is being tracked
95          double defCoeff;
96          Vector nodeTags;                // tags of nodes between which global deformation is
                 tracked
97          Vector iCoord;
98          Vector jCoord;
99          Vector iDisp;
100         Vector jDisp;
101         Vector iPos;
102         Vector jPos;
103         double length;                  // initial distance between nodes
104         double Tdef;                    // trial deformation
105         double Cdef;                    // commit deformation
106         double TdefT;                   // trial maximum tensile deformation
107         double TdefC;                   // trial maximum compressive deformation
108         double CdefT;                   // commit maximum tensile deformation
109         double CdefC;                   // commit maximum compressive deformation
```

```
110         double TdefRatio;               // trial compressive-to-tensile deformation ratio
111         double CdefRatio;               // commit compressive-to-tensile deformation ratio
112 };
```

B.2 MaxStrainRange Source File

```
1  #include <elementAPI.h>
2  #include <MaxStrainRange.h>
3
4  #include <Vector.h>
5  #include <Channel.h>
6  #include <math.h>
7  #include <float.h>
8
9  #include <stdlib.h>
10 #include <MaterialResponse.h>
11 #include <Information.h>
12 #include <ID.h>
13 #include <FEM_ObjectBroker.h>
14
15 #include <Domain.h>
16 #include <Node.h>
17 #include <Element.h>
18
19 #include <OPS_Globals.h>
20 #include <OPS_Stream.h>
21
22 #define OPS_Export
23
24 static int numMaxStrainRange = 0;
25
26 OPS_Export void *
27 OPS_MaxStrainRange(void)
28 {
29
30         if (numMaxStrainRange == 0) {
31                 opserr << "MaxStrainRange␣uniaxial␣material␣-␣Written␣by␣Po-Chien␣Hsiao,␣
                        University␣of␣Washington,␣2012\n";
32                 opserr << "\t>␣revised␣Andrew␣D.␣Sen,␣University␣of␣Washington,␣2017\n\n";
33                 numMaxStrainRange = 1;
34         };
```

```
35
36          // pointer to a uniaxial material that will be returned
37          UniaxialMaterial *theMaterial = 0;
38          UniaxialMaterial *thePreMaterial = 0;
39
40          // parse input line for material parameters
41          double minStrain = -1.0e16;
42          double maxStrain = 1.0e16;
43          double kappa = 1.0e-8;
44          double floorSR = 0.0;
45          bool defMode = false;
46          double defCoeff = 0.0;
47
48          Vector eleTags(1);
49          eleTags(0) = 0;
50
51          Vector nodeTags(2);
52          nodeTags(0) = 0;
53          nodeTags(1) = 0;
54
55          int iData[2];           // expecting 2 integers (tag of new material and tag of
                existing material)
56          double dData[1];        // expecting 1 double (limiting strain range)
57
58          int argc = OPS_GetNumRemainingInputArgs();
59          if (argc < 3) {
60                  opserr << "WARNING␣invalid␣uniaxialMaterial␣MaxStrainRange␣$tag␣$preMatTag␣
                        $limitSR␣<-min␣$minStrain>␣<-max␣$maxStrain>" << endln;
61                  return 0;
62          };
63
64          int numData = 2;
65          if (OPS_GetIntInput(&numData, iData) != 0) {
66                  opserr << "WARNING␣invalid␣uniaxialMaterial␣MaxStrainRange␣$tag␣$preMatTag␣
                        ..." << endln;
67                  return 0;
68          }
69
70          thePreMaterial = OPS_GetUniaxialMaterial(iData[1]);
71          if (thePreMaterial == 0) {
72                  opserr << "WARNING␣invalid␣preMatTag␣uniaxialMaterial␣MaxStrainRange␣tag:␣"
                        << iData[0] << endln;
```

```
73                  return 0;
74          };
75
76          numData = 1;
77          if (OPS_GetDoubleInput(&numData, dData) != 0) {
78                  opserr << "WARNING␣invalid␣limitSR␣uniaxialMaterial␣MaxStrainRange␣tag:␣" <<
                         iData[0] << endln;
79                  return 0;
80          };
81
82          argc = OPS_GetNumRemainingInputArgs();
83          while (argc > 1) {
84                  const char *argvLoc = OPS_GetString();
85
86                  numData = 1;
87                  if ((strcmp(argvLoc, "-min") == 0 || strcmp(argvLoc, "-Min") == 0 || strcmp(
                        argvLoc, "-MIN") == 0)) {
88                          if (OPS_GetDouble(&numData, &minStrain) != 0) {
89                                  opserr << "WARNING␣invalid␣min␣uniaxialMaterial␣
                                        MaxStrainRange␣tag:␣" << iData[0] << "\n\t>␣expecting␣
                                        $minStrain" << endln;
90                                  return 0;
91                          };
92                  }
93                  else if ((strcmp(argvLoc, "-max") == 0 || strcmp(argvLoc, "-Max") == 0 ||
                        strcmp(argvLoc, "-MAX") == 0)) {
94                          if (OPS_GetDouble(&numData, &maxStrain) != 0) {
95                                  opserr << "WARNING␣invalid␣max␣uniaxialMaterial␣
                                        MaxStrainRange␣tag:␣" << iData[0] << "\n\t>␣expecting␣
                                        $maxStrain" << endln;
96                                  return 0;
97                          };
98                  }
99                  else if ((strcmp(argvLoc, "-tangentRatio") == 0 || strcmp(argvLoc, "-
                        TangentRatio") == 0 || strcmp(argvLoc, "-TANGENTRATIO") == 0)) {
100                         if (OPS_GetDouble(&numData, &kappa) != 0) {
101                                 opserr << "WARNING␣invalid␣tangentRatio␣uniaxialMaterial␣
                                        MaxStrainRange␣tag:␣" << iData[0] << "\n\t>␣expecting␣
                                        $kappa" << endln;
102                                 return 0;
103                         };
104                 }
```

```
105                 else if ((strcmp(argvLoc, "-floor") == 0 || strcmp(argvLoc, "-Floor") == 0
                        || strcmp(argvLoc, "-FLOOR") == 0)) {
106                     if (OPS_GetDouble(&numData, &floorSR) != 0) {
107                             opserr << "WARNING␣invalid␣tangentRatio␣uniaxialMaterial␣
                                MaxStrainRange␣tag:␣" << iData[0] << "\n\t>␣expecting␣
                                $floor" << endln;
108                             return 0;
109                     };
110                 }
111                 else if ((strcmp(argvLoc, "-defCoeff") == 0 || strcmp(argvLoc, "-DefCoeff")
                        == 0 || strcmp(argvLoc, "-DEFCOEFF") == 0)) {
112                     if (OPS_GetDouble(&numData, &defCoeff) != 0) {
113                             opserr << "WARNING␣invalid␣tangentRatio␣uniaxialMaterial␣
                                MaxStrainRange␣tag:␣" << iData[0] << "\n\t>␣expecting␣
                                $defCoeff" << endln;
114                             return 0;
115                     };
116                 }
117                 else if ((strcmp(argvLoc, "-nodeTags") == 0 || strcmp(argvLoc, "-NodeTags")
                        == 0 || strcmp(argvLoc, "-NODETAGS") == 0 || strcmp(argvLoc, "-nodetags"
                        ) == 0)) {
118                     int numNodes = 2;
119                     int *nTags = new int[numNodes];
120                     defMode = true;
121                     if (OPS_GetIntInput(&numNodes, nTags) != 0) {
122                             opserr << "WARNING␣invalid␣nodeTags␣uniaxialMaterial␣
                                MaxStrainRange␣tag:␣" << iData[0] << "\n\t␣>␣expecting␣
                                $nodeTag1␣$nodeTag2" << endln;
123                     };
124                     nodeTags(0) = nTags[0];
125                     nodeTags(1) = nTags[1];
126                     opserr << "NOTE:␣MaxStrainRange␣tag␣" << iData[0] << "␣will␣track␣
                            deformation␣between␣node␣tags␣" << nodeTags(0) << "␣and␣" <<
                            nodeTags(1) << endln;
127                 }
128                 else if ((strcmp(argvLoc, "-eleTag") == 0 || strcmp(argvLoc, "-EleTag") == 0
                         || strcmp(argvLoc, "-ELETAG") == 0 || strcmp(argvLoc, "-eletag") == 0))
                         {
129                     int numEles = OPS_GetNumRemainingInputArgs();
130                     int *eTags = new int[numEles];
131                     if (OPS_GetIntInput(&numEles, eTags) != 0) {
132                             opserr << "WARNING␣invalid␣eleTags␣uniaxialMaterial␣
```

```
                                        MaxStrainRange␣tag:␣" << iData[0] << "\n\t␣>␣expecting␣
                                        $eleTag1␣$eleTag2␣..." << endln;
133                         };
134                         eleTags.resize(numEles);
135                         for (int i = 0; i < numEles; i++) {
136                                 eleTags(i) = eTags[i];
137                                 opserr << "CAUTION:␣MaxStrainRange␣tag␣" << iData[0] << "␣
                                        will␣remove␣element␣tag␣" << eleTags(i) << "␣on␣failure"
                                         << endln;
138                         };
139                 }
140                 else {
141                         opserr << "WARNING␣invalid␣option:␣" << argvLoc << "␣
                                    uniaxialMaterial␣tag:␣" << iData[0] << endln;
142                         return 0;
143                 };
144
145                 argc = OPS_GetNumRemainingInputArgs();
146         };
147
148         // parsing successful, allocate the material
149         int numEles = eleTags.Size();
150         theMaterial = new MaxStrainRange(iData[0], *thePreMaterial, dData[0], minStrain,
                maxStrain, kappa, numEles, eleTags, defMode, nodeTags, floorSR, defCoeff);
151
152         if (theMaterial == 0) {
153                 opserr << "WARNING␣could␣not␣create␣uniaxialMaterial␣of␣type␣MaxStrainRange\
                        n";
154                 return 0;
155         };
156
157         return theMaterial;
158 };
159
160 MaxStrainRange::MaxStrainRange(int tag,
161         UniaxialMaterial &material,
162         double _limitSR,
163         double _minStrain,
164         double _maxStrain,
165         double _kappa,
166         int _numEles,
167     const Vector &_eleTags,
```

```
168         bool _defMode,
169         const Vector &_nodeTags,
170         double _floorSR,
171         double _defCoeff)
172         :UniaxialMaterial(tag, MAT_TAG_MaxStrainRange),
173         theMaterial(0),
174         limitSR(_limitSR),
175         minStrain(_minStrain),
176         maxStrain(_maxStrain),
177         kappa(_kappa),
178         numEles(_numEles),
179         eleTags(_eleTags),
180         defMode(_defMode),
181         nodeTags(_nodeTags),
182         floorSR(_floorSR),
183         defCoeff(_defCoeff) {
184
185         theMaterial = material.getCopy();
186         if (theMaterial == 0) {
187                 opserr << "MaxStrainRange::MaxStrainRange -- failed to get copy of
                        previously defined material\n";
188                 exit(-1);
189         };
190
191         Tstrain = Cstrain = theMaterial->getStrain();
192         Tstress = Cstress = theMaterial->getStress();
193         Ttangent = Ctangent = theMaterial->getTangent();
194
195         // material history variables
196         TminS = CminS = 0.0;
197         TmaxS = CmaxS = 0.0;
198         TmaxSR = CmaxSR = 0.0;
199         Tfailed = Cfailed = false;
200
201         // element history variables
202         Tdef = Cdef = 0.0;
203         TdefT = CdefT = 0.0;
204         TdefC = CdefC = 0.0;
205         TdefRatio = CdefRatio = 1.0;
206         if (defMode) {
207                 Domain *theDomain = 0;
208                 theDomain = OPS_GetDomain();
```

```
209                 iNode = theDomain->getNode(nodeTags(0));
210                 jNode = theDomain->getNode(nodeTags(1));
211                 iCoord = iNode->getCrds();
212                 jCoord = jNode->getCrds();
213                 length = sqrt(pow(jCoord(0) - iCoord(0), 2) + pow(jCoord(1) - iCoord(1), 2)
                        + pow(jCoord(2) - iCoord(2), 2));
214         };
215 };
216
217 MaxStrainRange::MaxStrainRange()
218         :UniaxialMaterial(0, MAT_TAG_MaxStrainRange),
219         theMaterial(0),
220         limitSR(0.0),
221         minStrain(0.0),
222         maxStrain(0.0),
223         kappa(0.0),
224         numEles(0),
225         eleTags(0),
226         defMode(false),
227         nodeTags(0),
228         floorSR(0.0),
229         defCoeff(0.0) {
230         Tstrain = Cstrain = 0.0;
231         Tstress = Cstress = 0.0;
232         Ttangent = Ctangent = 0.0;
233         TminS = CminS = 0.0;
234         TmaxS = CmaxS = 0.0;
235         TmaxSR = CmaxSR = 0.0;
236         Tfailed = Cfailed = false;
237         Tdef = Cdef = 0.0;
238         TdefT = CdefT = 0.0;
239         TdefC = CdefC = 0.0;
240         TdefRatio = CdefRatio = 1.0;
241 };
242
243 MaxStrainRange::~MaxStrainRange()
244 {
245         if (theMaterial) {
246                 delete theMaterial;
247         };
248 };
249
```

```
250 int
251 MaxStrainRange::setTrialStrain(double strain, double strainRate)
252 {
253         TminS = CminS;
254         TmaxS = CmaxS;
255         TmaxSR = CmaxSR;
256         Tfailed = Cfailed;
257         //Ttangent = Ctangent;
258         //Tstress = Cstress;
259         Tstrain = strain;
260         //theMaterial->revertToLastCommit();
261
262         // check if failed previously; if element tag is defined, remove the element
263         if (Cfailed) {
264                 if (numEles > 0) {
265                         int nEles = 0;
266                         Domain *theDomain = 0;
267                         theDomain = OPS_GetDomain();
268                         while (nEles < numEles) {
269                                 Element *theElement = 0;
270                                 int curTag = eleTags(nEles);
271                                 theElement = theDomain->getElement(curTag);
272                                 Element *theEle = theDomain->removeElement(curTag);
273                                 nEles++;
274                         };
275                         return 0;
276                 } else {
277                         //Ttangent = kappa*theMaterial->getInitialTangent();
278                         //Tstress = 0.0; // Ttangent*Tstrain;
279                         Tfailed = true;
280                         return 0;
281                 };
282         };
283
284         int res = theMaterial->setTrialStrain(Tstrain, strainRate);
285         if (res == 0) {
286                 Tstress = theMaterial->getStress();
287                 //Ttangent = theMaterial->getTangent();
288         } else {
289                 exit(-1);
290         };
291
```

```
292         if (Tstrain < TminS) {
293                 TminS = Tstrain;
294         }
295         else if (Tstrain > TmaxS) {
296                 TmaxS = Tstrain;
297         };
298         TmaxSR = TmaxS - TminS;
299 
300         if (defMode) {
301                 iDisp = iNode->getDisp();
302                 jDisp = jNode->getDisp();
303                 iPos = iCoord + iDisp;
304                 jPos = jCoord + jDisp;
305                 Tdef = sqrt(pow(jPos(0) - iPos(0), 2) + pow(jPos(1) - iPos(1), 2) + pow(jPos
                        (2) - iPos(2), 2)) - length;
306 
307                 if (Tdef > TdefT) {
308                         TdefT = Tdef;
309                 }
310                 else if (Tdef < TdefC) {
311                         TdefC = Tdef;
312                 };
313 
314                 TdefRatio = fmax(-TdefC / TdefT, 0.25);
315         };
316 
317         if (Tstrain >= maxStrain || Tstrain <= minStrain || (TmaxSR >= fmax(floorSR, limitSR
                *pow(TdefRatio, defCoeff)) && Tstress > DBL_EPSILON)) {
318                 Tfailed = true;
319                 /*if (!failMode) {
320                         Ttangent = kappa*theMaterial->getInitialTangent();
321                         Tstress = Ttangent*Tstrain;
322                 };*/
323         }
324         else {
325                 Tfailed = false;
326         };
327 
328         return 0;
329 };
330 
331 double
```

```
MaxStrainRange::getStress(void)
{
        if (Tfailed) {
                return 0.0;
        }
        else {
                return theMaterial->getStress();
        };
};

double
MaxStrainRange::getTangent(void)
{
        if (Tfailed) {
                return kappa*theMaterial->getInitialTangent();
        }
        else {
                return theMaterial->getTangent();
        };
};

double
MaxStrainRange::getDampTangent(void)
{
        if (Tfailed) {
                return kappa*theMaterial->getDampTangent();
        }
        else {
                return theMaterial->getDampTangent();
        };
};

double
MaxStrainRange::getStrain(void)
{
        return theMaterial->getStrain();;
};

double
MaxStrainRange::getStrainRate(void)
{
        return theMaterial->getStrainRate();
```

```
374 };
375
376 double
377 MaxStrainRange::getMaxStrainRange(void)
378 {
379         return TmaxSR;
380 };
381
382 int
383 MaxStrainRange::getFail(void)
384 {
385         if (Tfailed) {
386                 return 1;
387         }
388         else {
389                 return 0;
390         };
391 };
392
393 int
394 MaxStrainRange::commitState(void)
395 {
396         Cstrain = Tstrain;
397         Cstress = Tstress;
398         Ctangent = Ttangent;
399
400         if (Cfailed == false && Tfailed == true) {
401                 opserr << "MaxStrainRange␣material␣" << this->getTag() << "␣failed␣at␣MSR␣of
                        ␣" << TmaxSR << endln;
402         };
403
404         Cfailed = Tfailed;
405         CminS = TminS;
406         CmaxS = TmaxS;
407         CmaxSR = TmaxSR;
408         if (defMode) {
409                 Cdef = Tdef;
410                 CdefT = TdefT;
411                 CdefC = TdefC;
412                 CdefRatio = TdefRatio;
413         };
414         if (Cfailed) {
```

```
415                 CmaxSR = limitSR;
416                 return 0;
417         }
418         else {
419                 return theMaterial->commitState();
420         };
421 };
422
423 int
424 MaxStrainRange::revertToLastCommit(void)
425 {
426         if (Cfailed) {
427                 return 0;
428         }
429         else {
430                 Tstrain = Cstrain;
431                 Tstress = Cstress;
432                 //Ttangent = Ctangent;
433                 TminS = CminS;
434                 TmaxS = CmaxS;
435                 TmaxSR = CmaxSR;
436                 Tfailed = Cfailed;
437
438                 if (defMode) {
439                         Tdef = Cdef;
440                         TdefT = CdefT;
441                         TdefC = CdefC;
442                         TdefRatio = CdefRatio;
443                 };
444
445                 return theMaterial->revertToLastCommit();
446         };
447 };
448
449 int
450 MaxStrainRange::revertToStart(void)
451 {
452         Tstrain = Cstrain = 0.0;
453         int res = theMaterial->revertToStart();
454         if (res == 0) {
455                 Tstress = Cstress = theMaterial->getStress();
456                 Ttangent = Ctangent = theMaterial->getTangent();
```

```
457         } else {
458                 exit(-1);
459         };
460         TminS = CminS = 0.0;
461         TmaxS = CmaxS = 0.0;
462         TmaxSR = CmaxSR = 0.0;
463         Tfailed = Cfailed = false;
464
465         Tdef = Cdef = 0.0;
466         TdefT = CdefT = 0.0;
467         TdefC = CdefC = 0.0;
468         TdefRatio = CdefRatio = 1.0;
469         return 0;
470 };
471
472 UniaxialMaterial *
473 MaxStrainRange::getCopy(void)
474 {
475         MaxStrainRange *theCopy = new MaxStrainRange(this->getTag(), *theMaterial, limitSR,
                minStrain, maxStrain, kappa, numEles, eleTags, defMode, nodeTags, floorSR,
                defCoeff);
476         theCopy->Tstrain = this->Tstrain;
477         theCopy->Tstress = this->Tstress;
478         theCopy->Ttangent = this->Ttangent;
479         theCopy->TminS = this->TminS;
480         theCopy->TmaxS = this->TmaxS;
481         theCopy->TmaxSR = this->TmaxSR;
482         theCopy->Tfailed = this->Tfailed;
483         theCopy->Tdef = this->Tdef;
484         theCopy->TdefT = this->TdefT;
485         theCopy->TdefC = this->TdefC;
486         theCopy->TdefRatio = this->TdefRatio;
487         theCopy->Cstrain = this->Cstrain;
488         theCopy->Cstress = this->Cstress;
489         theCopy->Ctangent = this->Ctangent;
490         theCopy->CminS = this->CminS;
491         theCopy->CmaxS = this->CmaxS;
492         theCopy->CmaxSR = this->CmaxSR;
493         theCopy->Cfailed = this->Cfailed;
494         theCopy->Cdef = this->Cdef;
495         theCopy->CdefT = this->CdefT;
496         theCopy->CdefC = this->CdefC;
```

```
497         theCopy->CdefRatio = this->CdefRatio;
498         return theCopy;
499 };
500 
501 int
502 MaxStrainRange::sendSelf(int cTag, Channel &theChannel)
503 {
504         int dbTag = this->getDbTag();
505 
506         static ID dataID(3);
507         dataID(0) = this->getTag();
508         dataID(1) = theMaterial->getClassTag();
509         int matDbTag = theMaterial->getDbTag();
510         if (matDbTag == 0) {
511                 matDbTag = theChannel.getDbTag();
512                 theMaterial->setDbTag(matDbTag);
513         };
514         dataID(2) = matDbTag;
515         if (theChannel.sendID(dbTag, cTag, dataID) < 0) {
516                 opserr << "MaxStrainRange::sendSelf() -- failed to send the ID\n";
517                 return -1;
518         };
519 
520         static Vector dataVec(19);
521         dataVec(0) = limitSR;
522         dataVec(1) = minStrain;
523         dataVec(2) = maxStrain;
524         dataVec(3) = kappa;
525         dataVec(4) = numEles;
526         dataVec(5) = CminS;
527         dataVec(6) = CmaxS;
528         dataVec(7) = CmaxSR;
529         if (Cfailed) {
530                 dataVec(8) = 1.0;
531         }
532         else {
533                 dataVec(8) = 0.0;
534         };
535         dataVec(9) = Cstrain;
536         dataVec(10) = Cstress;
537         dataVec(11) = Ctangent;
538         if (defMode) {
```

```
539                 dataVec(12) = 1.0;
540         }
541         else {
542                 dataVec(12) = 0.0;
543         };
544         dataVec(13) = Cdef;
545         dataVec(14) = CdefT;
546         dataVec(15) = CdefC;
547         dataVec(16) = CdefRatio;
548         dataVec(17) = floorSR;
549         dataVec(18) = defCoeff;
550
551         if (theChannel.sendVector(dbTag, cTag, dataVec) < 0) {
552                 opserr << "MaxStrainRange::sendSelf() - failed to send the Vector\n";
553                 return -2;
554         };
555
556         if (theChannel.sendVector(dbTag, cTag, eleTags) < 0) {
557                 opserr << "MaxStrainRange::sendSelf() - failed to send the eleTags\n";
558                 return -4;
559         }
560
561         if (theChannel.sendVector(dbTag, cTag, nodeTags) < 0) {
562                 opserr << "MaxStrainRange::sendSelf() - failed to send the nodeTags\n";
563                 return -5;
564         }
565
566         if (theMaterial->sendSelf(cTag, theChannel) < 0) {
567                 opserr << "MaxStrainRange::sendSelf() - failed to send the material\n";
568                 return -3;
569         };
570         return 0;
571 };
572
573 int
574 MaxStrainRange::recvSelf(int cTag, Channel &theChannel, FEM_ObjectBroker &theBroker)
575 {
576         int dbTag = this->getDbTag();
577
578         static ID dataID(3);
579         if (theChannel.recvID(dbTag, cTag, dataID) < 0) {
580                 opserr << "MaxStrainRange::recvSelf() - failed to get the ID\n";
```

```
581                 return -1;
582         };
583         this->setTag(int(dataID(0)));
584 
585         // since there is no way to change the material, don't have to check the classTag of
                the material
586         if (theMaterial == 0) {
587                 int matClassTag = int(dataID(1));
588                 theMaterial = theBroker.getNewUniaxialMaterial(matClassTag);
589                 if (theMaterial == 0) {
590                         opserr << "MaxStrainRange::recvSelf() -- failed to create material
                            with classTag " << dataID(0) << endln;
591                         return -2;
592                 };
593         };
594         theMaterial->setDbTag(dataID(2));
595 
596         static Vector dataVec(19);
597         if (theChannel.recvVector(dbTag, cTag, dataVec) < 0) {
598                 opserr << "MaxStrainRange::recvSelf() -- failed to get the Vector\n";
599                 return -3;
600         };
601         limitSR = dataVec(0);
602         minStrain = dataVec(1);
603         maxStrain = dataVec(2);
604         kappa = dataVec(3);
605         numEles = dataVec(4);
606         CminS = dataVec(5);
607         CmaxS = dataVec(6);
608         CmaxSR = dataVec(7);
609         if (dataVec(8) == 1.0) {
610                 Cfailed = true;
611         }
612         else {
613                 Cfailed = false;
614         };
615         Cstrain = dataVec(9);
616         Cstress = dataVec(10);
617         Ctangent = dataVec(11);
618         if (dataVec(12) == 1.0) {
619                 defMode = true;
620         }
```

```
621         else {
622                 defMode = false;
623         };
624         Cdef = dataVec(13);
625         CdefT = dataVec(14);
626         CdefC = dataVec(15);
627         CdefRatio = dataVec(16);
628         floorSR = dataVec(17);
629         defCoeff = dataVec(18);
630
631         Tstrain = Cstrain;
632         Tstress = Cstress;
633         Ttangent = Ctangent;
634         Tfailed = Cfailed;
635         TminS = CminS;
636         TmaxS = CmaxS;
637         TmaxSR = CmaxSR;
638
639         Tdef = Cdef;
640         TdefT = CdefT;
641         TdefC = CdefC;
642         TdefRatio = CdefRatio;
643
644         eleTags.resize(numEles);
645         if (theChannel.recvVector(dbTag, cTag, eleTags) < 0) {
646                 opserr << "MaxStrainRange::recvSelf()␣-␣failed␣to␣get␣the␣eleTags\n";
647                 return -5;
648         };
649
650         if (theChannel.recvVector(dbTag, cTag, nodeTags) < 0) {
651                 opserr << "MaxStrainRange::recvSelf()␣-␣failed␣to␣get␣the␣nodeTags\n";
652                 return -6;
653         };
654
655         if (theMaterial->recvSelf(cTag, theChannel, theBroker) < 0) {
656                 opserr << "MaxStrainRange::recvSelf()␣--␣failed␣to␣get␣the␣material\n";
657                 return -4;
658         };
659         return 0;
660 };
661
662 void
```

```
663 MaxStrainRange::Print(OPS_Stream &s, int flag)
664 {
665         s << "MaxStrainRange␣tag:␣" << this->getTag() << endln;
666         s << "\tMaterial:␣" << theMaterial->getTag() << endln;
667 };
668
669
670 Response*
671 MaxStrainRange::setResponse(const char **argv, int argc, OPS_Stream &theOutput)
672 {
673         Response *theResponse = 0;
674
675         theOutput.tag("UniaxialMaterialOutput");
676         theOutput.attr("matType", this->getClassType());
677         theOutput.attr("matTag", this->getTag());
678
679         // maximum strain range (msr)
680         if (strcmp(argv[0], "maxSR") == 0 || strcmp(argv[0], "MaxSR") == 0 || strcmp(argv
                [0], "MAXSR") == 0 || strcmp(argv[0], "maxsr") == 0) {
681                 theOutput.tag("ResponseType", "UnknownResponse");
682                 theResponse = new MaterialResponse(this, 1, this->getMaxStrainRange());
683         }
684         else if (strcmp(argv[0], "strain") == 0) {
685                 theOutput.tag("ResponseType", "eps11");
686                 theResponse = new MaterialResponse(this, 2, this->getStrain());
687         }
688         else if (strcmp(argv[0], "stress") == 0) {
689                 theOutput.tag("ResponseType", "sig11");
690                 theResponse = new MaterialResponse(this, 3, this->getStress());
691         }
692         else if (strcmp(argv[0], "stressAndStrain") == 0) {
693                 theOutput.tag("ResponseType", "sig11");
694                 theOutput.tag("ResponseType", "eps11");
695                 theResponse = new MaterialResponse(this, 4, Vector(2));
696         }
697         else if (strcmp(argv[0], "fail") == 0) {
698                 theOutput.tag("ResponseType", "UnknownResponse");
699                 theResponse = new MaterialResponse(this, 5, this->getFail());
700         };
701
702         theOutput.endTag();
703         return theResponse;
```

```
};

int
MaxStrainRange::getResponse(int responseID, Information &matInfo)
{
        static Vector stressAndStrain(2);

        switch (responseID) {
        case 1:
                matInfo.setDouble(this->getMaxStrainRange());
                return 0;
        case 2:
                matInfo.setDouble(this->getStrain());
                return 0;
        case 3:
                matInfo.setDouble(this->getStress());
                return 0;
        case 4:
                stressAndStrain(0) = this->getStress();
                stressAndStrain(1) = this->getStrain();
                matInfo.setVector(stressAndStrain);
                return 0;
        case 5:
                matInfo.setInt(this->getFail());
                return 0;

        default:
                return -1;
        };
};
```

Appendix C

INPUT GROUND MOTIONS

Tables C.1 through C.5 document the ground motions used in each hazard-level suite defined in Chapter 5. These ground motions were selected from the PEER NGA-West2 Database (Ancheta et al. 2013), and the Record Sequence Numbers (RSNs) correspond to their identifiers in the database. In the response-history analyses presented in Chapters 6 and 7, these ground motions were scaled using the methodology described in Chapter 5.

Table C.1: Ground-Motion Set for 50%/30-Year (43-Year Return Period) Hazard Level

RSN	Earthquake	Station
135	Santa Barbara	Cachuma Dam Toe
215	Livermore-01	San Ramon Fire Station
224	Livermore-02	San Ramon Fire Station
238	Mammoth Lakes-03	Long Valley Dam (L Abut)
241	Mammoth Lakes-04	Long Valley Dam (Downst)
399	Coalinga-04	Oil Fields Fire Station - FF
414	Coalinga-05	Sulphur Baths (temp)
479	Lazio-Abruzzo, Italy	Isernia-Sant'Agapito
545	Chalfant Valley-01	Bishop - Paradise Lodge
696	Whittier Narrows-01	Sun Valley - Sunland
698	Whittier Narrows-01	Sylmar - Olive View Med FF
1671	Northridge-03	Pacoima Kagel Canyon
1683	Northridge-05	Castaic - Old Ridge Route
2253	Chi-Chi, Taiwan-02	HWA049
2420	Chi-Chi, Taiwan-02	TCU122
3553	Fruili, Italy-03	Tarcento
3607	Lazio-Abruzzo, Italy	San Agapito
4075	Parkfield-02, CA	PARKFIELD - WORK RANCH
4278	Friuli (aftershock 9), Italy	San Rocco
4314	Umbria-03, Italy	Citta Di Castello-Regnano
4328	Potenza, Italy	Brienza
4329	Potenza, Italy	Rionero In Vulture
4331	Sicilia-Orientale, Italy	Sortino
4366	Umbria Marche (aftershock 1), Italy	Gubbio-Piana
4410	Umbria Marche (aftershock 17), Italy	Gubbio-Piana
4550	L'Aquila (aftershock 2), Italy	L'Aquila - V. Aterno - M. Pettino
4553	L'Aquila (aftershock 2), Italy	L'Aquila - V. Aterno -F. Aterno
8709	40204628	Lick Observatory, Mt. Hamiliton, CA, USA
8823	14383980	Olinda
8895	14383980	Rancho Cucamonga - Hwy 30 & Amethyst

Table C.2: Ground-Motion Set for 10%/50-Year (475-Year Return Period) Hazard Level

RSN	Earthquake	Station
15	Kern County	Taft Lincoln School
57	San Fernando	Castaic - Old Ridge Route
164	Imperial Valley-06	Cerro Prieto
231	Mammoth Lakes-01	Long Valley Dam (Upr L Abut)
265	Victoria, Mexico	Cerro Prieto
288	Irpinia, Italy-01	Brienza
313	Corinth, Greece	Corinth
340	Coalinga-01	Parkfield - Fault Zone 16
534	N. Palm Springs	San Jacinto - Soboba
548	Chalfant Valley-02	Benton
564	Kalamata, Greece-01	Kalamata (bsmt)
587	New Zealand-02	Matahina Dam
739	Loma Prieta	Anderson Dam (Downstream)
811	Loma Prieta	WAHO
990	Northridge-01	LA - City Terrace
1006	Northridge-01	LA - UCLA Grounds
2655	Chi-Chi, Taiwan-03	TCU122
2658	Chi-Chi, Taiwan-03	TCU129
3750	Cape Mendocino	Loleta Fire Station
3943	Tottori, Japan	SMN015
3979	San Simeon, CA	Cambria - Hwy 1 Caltrans Bridge
4031	San Simeon, CA	Templeton - 1-story Hospital
4139	Parkfield-02, CA	PARKFIELD - UPSAR 02
4148	Parkfield-02, CA	PARKFIELD - UPSAR 12
4229	Niigata, Japan	NIGH12
4455	Montenegro, Yugoslavia	Herceg Novi - O.S.D. Paviviv
4873	Chuetsu-oki, Japan	Kashiwazaki City Takayanagicho
4882	Chuetsu-oki, Japan	Ojiya City
5478	Iwate, Japan	AKT023
5678	Iwate, Japan	MYGH02

Table C.3: Ground-Motion Set for 5%/50-Year (975-Year Return Period) Hazard Level

RSN	Earthquake	Station
57	San Fernando	Castaic - Old Ridge Route
139	Tabas, Iran	Dayhook
164	Imperial Valley-06	Cerro Prieto
265	Victoria, Mexico	Cerro Prieto
289	Irpinia, Italy-01	Calitri
495	Nahanni, Canada	Site 1
587	New Zealand-02	Matahina Dam
741	Loma Prieta	BRAN
796	Loma Prieta	SF - Presidio
901	Big Bear-01	Big Bear Lake - Civic Center
963	Northridge-01	Castaic - Old Ridge Route
986	Northridge-01	LA - Brentwood VA Hospital
1111	Kobe, Japan	Nishi-Akashi
1524	Chi-Chi, Taiwan	TCU095
1545	Chi-Chi, Taiwan	TCU120
3745	Cape Mendocino	Butler Valley Station 2
3750	Cape Mendocino	Loleta Fire Station
3947	Tottori, Japan	SMNH01
3964	Tottori, Japan	TTR007
4031	San Simeon, CA	Templeton - 1-story Hospital
4218	Niigata, Japan	NIG028
4223	Niigata, Japan	NIGH06
4455	Montenegro, Yugoslavia	Herceg Novi - O.S.D. Paviviv
4456	Montenegro, Yugoslavia	Petrovac - Hotel Olivia
4882	Chuetsu-oki, Japan	Ojiya City
4891	Chuetsu-oki, Japan	Iizuna Imokawa
5656	Iwate, Japan	IWTH24
5778	Iwate, Japan	Matsuyama City
6915	Darfield, New Zealand	Heathcote Valley Primary School
6980	Darfield, New Zealand	WAKC

Table C.4: Ground-Motion Set for 2%/50-Year (2,475-Year Return Period) Hazard Level

RSN	Earthquake	Station
15	Kern County	Taft Lincoln School
57	San Fernando	Castaic - Old Ridge Route
79	San Fernando	Pasadena - CIT Athenaeum
164	Imperial Valley-06	Cerro Prieto
265	Victoria, Mexico	Cerro Prieto
340	Coalinga-01	Parkfield - Fault Zone 16
564	Kalamata, Greece-01	Kalamata (bsmt)
769	Loma Prieta	Gilroy Array #6
811	Loma Prieta	WAHO
963	Northridge-01	Castaic - Old Ridge Route
1012	Northridge-01	LA 00
1350	Chi-Chi, Taiwan	ILA067
1546	Chi-Chi, Taiwan	TCU122
1618	Duzce, Turkey	Lamont 531
1633	Manjil, Iran	Abbar
1762	Hector Mine	Amboy
2655	Chi-Chi, Taiwan-03	TCU122
3269	Chi-Chi, Taiwan-06	CHY029
3750	Cape Mendocino	Loleta Fire Station
3759	Landers	Whitewater Trout Farm
3943	Tottori, Japan	SMN015
4031	San Simeon, CA	Templeton - 1-story Hospital
4132	Parkfield-02, CA	Parkfield - Vineyard Cany 2E
4213	Niigata, Japan	NIG023
4229	Niigata, Japan	NIGH12
4841	Chuetsu-oki, Japan	Joetsu Yasuzukaku Yasuzuka
4873	Chuetsu-oki, Japan	Kashiwazaki City Takayanagicho
5656	Iwate, Japan	IWTH24
5818	Iwate, Japan	Kurihara City
6948	Darfield, New Zealand	OXZ

Table C.5: Ground-Motion Set for 1%/50-Year (4,975-Year Return Period) Hazard Level

RSN	Earthquake	Station
6	Imperial Valley-02	El Centro Array #9
15	Kern County	Taft Lincoln School
164	Imperial Valley-06	Cerro Prieto
265	Victoria, Mexico	Cerro Prieto
313	Corinth, Greece	Corinth
367	Coalinga-01	Pleasant Valley P.P. - bldg
564	Kalamata, Greece-01	Kalamata (bsmt)
730	Spitak, Armenia	Gukasian
755	Loma Prieta	Coyote Lake Dam - Southwest Abutment
787	Loma Prieta	Palo Alto - SLAC Lab
850	Landers	Desert Hot Springs
995	Northridge-01	LA - Hollywood Stor FF
1042	Northridge-01	N Hollywood - Coldwater Can
1107	Kobe, Japan	Kakogawa
1158	Kocaeli, Turkey	Duzce
1495	Chi-Chi, Taiwan	TCU055
1546	Chi-Chi, Taiwan	TCU122
1633	Manjil, Iran	Abbar
1794	Hector Mine	Joshua Tree
4031	San Simeon, CA	Templeton - 1-story Hospital
4213	Niigata, Japan	NIG023
4860	Chuetsu-oki, Japan	Sanjo Shinbori
5663	Iwate, Japan	MYG004
5813	Iwate, Japan	Mizusawaku Interior O ganecho
5827	El Mayor-Cucapah, Mexico	MICHOACAN DE OCAMPO
5975	El Mayor-Cucapah, Mexico	Calexico Fire Station
6059	Big Bear-01	Morongo Valley Fire Station
6889	Darfield, New Zealand	Christchurch Hospital
6893	Darfield, New Zealand	DFHS
8124	Christchurch, New Zealand	Riccarton High School

BIBLIOGRAPHY

ACI (2014). "Building Code Requirements for Structural Concrete and Commentary." *ACI 318-14*, American Concrete Institute, Farmington Hills, MI.

AIJ (1995a). "Investigation of the disaster due to the Hyogo-Ken Nanbu earthquake – The urgent meeting report." *Report no.*, Architectural Institute of Japan, Tokyo, Japan.

AIJ (1995b). "Performance of steel buildings during the 1995 Hyogoken-Nanbu earthquake." *Report no.*, Architectural Institute of Japan, Tokyo, Japan.

AISC (1997). "Seismic Provisions for Structural Steel Buildings." *ANSI/AISC 341-97*, American Institute of Steel Construction, Chicago, IL.

AISC (2010a). "Seismic Provisions for Structural Steel Buildings." *ANSI/AISC 341-10*, American Institute of Steel Construction, Chicago, IL.

AISC (2010b). "Specification for Structural Steel Buildings." *ANSI/AISC 360-10*, American Institute of Steel Construction, Chicago, IL.

AISC (2016). "Code of Standard Practice for Steel Buildings and Bridges." *ANSI/AISC 303-16*, American Institute of Steel Construction, Chicago, IL.

AISC (2017a). "Seismic Provisions for Structural Steel Buildings." *ANSI/AISC 341-16*, American Institute of Steel Construction, Chicago, IL.

AISC (2017b). "Seismic Provisions for Structural Steel Buildings." *ANSI/AISC 341-16*, American Institute of Steel Construction, Chicago, IL.

AISC (2017c). "Specification for Structural Steel Buildings." *ANSI/AISC 360-16*, American Institute of Steel Construction, Chicago, IL.

AISC (2017d). *Steel Construction Manual*. American Institute of Steel Construction, Chicago, IL.

Ancheta, T. D., Darragh, R. B., Stewart, J. P., Seyhan, E., Silva, W. J., Chiou, B. S. J., Wooddell, K. E., Graves, R. W., Kottke, A. R., Boore, D. M., Kishida, T., and Donahue, J. L. (2013). "PEER NGA-West2 Database." *Report no.*, Pacific Earthquake Engineering Research Center, Berkeley, CA.

ASCE (2010). "Minimum Design Loads and Associated Criteria for Buildings and Other Structures." *ASCE/SEI 7-10*, American Society of Civil Engineers, Reston, VA.

ASCE (2017a). "Minimum Design Loads and Associated Criteria for Buildings and Other Structures." *ASCE/SEI 7-16*, American Society of Civil Engineers, Reston, VA.

ASCE (2017b). "Seismic Evaluation and Retrofit of Existing Buildings." *ASCE/SEI 41-17*, American Society of Civil Engineers, Reston, VA.

Astaneh-Asl, A., Goel, S. C., and Hanson, R. D. (1986). "Earthquake-Resistant Design of Double-Angle Bracings." *AISC Engineering Journal*, 133–147.

ATC (1992). "Guidelines for cyclic seismic testing of components of steel structures for buildings." *Report ATC-24*, Applied Technology Council, Redwood City, CA.

Baker, J. W. (2015). "Efficient Analytical Fragility Function Fitting Using Dynamic Structural Analysis." *Earthquake Spectra*, 31(1), 579–599.

Balazadeh-Minouei, Y., Koboevic, S., and Tremblay, R. (2017). "Seismic evaluation of a steel braced frame using NBCC and ASCE 41." *Journal of Constructional Steel Research*, 135, 110–124.

Balazadeh-Minouei, Y., Koboevic, S., and Tremblay, R. (2018a). "Seismic Assessment of Existing Steel Chevron Braced Frames." *Journal of Structural Engineering*, 144(6), 04018046.

Balazadeh-Minouei, Y., Tremblay, R., and Koboevic, S. (2018b). "Seismic Retrofit of an Existing 10-Story Chevron-Braced Steel-Frame." *Journal of Structural Engineering*, 144(10), 04018180.

Ballard, R. (2015). "Impact of connection type on performance of non-seismic concentrically braced frames." MS thesis, University of Washington, Seattle.

Black, R. G., Wenger, W. A. B., and Popov, E. P. (1980). "Inelastic buckling of steel struts under cyclic load reversals." *UCB/EERC-80/40*, Earthquake Engineering Reserach Center, Berkeley, CA.

Bradley, C. R., Fahnestock, L. A., Hines, E. M., and Sizemore, J. G. (2017). "Full-Scale Cyclic Testing of Low-Ductility Concentrically Braced Frames." *Journal of Structural Engineering*, 143(6), 04017029.

Carter, C. J., Muir, L. S., and Dowswell, B. (2016). "Establishing and Developing the Weak-Axis Strength of Plates Subjected to Applied Loads." *AISC Engineering Journal*, 147–157.

Chang, G. A. and Mander, J. B. (1994). "Seismic energy based fatigue damage analysis of bridge columns: Part I–Evaluation of seismic capacity." *Report NCEER-94-0006*, National Center for Earthquake Engineering Research, Buffalo, NY.

Clark, K. A. (2009). "Experimental performance of multi-story X-braced SCBF systems." MS thesis, University of Washington, Seattle.

Fell, B. V., Kanvinde, A. M., Deierlein, G. G., and Myers, A. T. (2009). "Experimental investigation of inelastic cyclic buckling and fracture of steel braces." *Journal of Structural Engineering*, 135(1), 19–32.

FEMA (2000). "State of the art report on systems performance of steel moment frames subject to earthquake ground shaking." *FEMA 355C*, Federal Emergency Management Agency, Washington, D.C.

FEMA (2009). "Quantification of Building Seismic Performance Factors." *FEMA P695*, Federal Emergency Management Agency, Washington, D.C.

Filippou, F. C., Popov, E. P., and Bertero, V. V. (1983). "Effects of Bond Deterioration on Hysteretic Behavior of Reinforced Concrete Joints." *Report no.*, Earthquake Engineering Research Center, Berkeley, CA.

Foutch, D. A., Goel, S. C., and Roeder, C. W. (1987). "Seismic Testing of FullScale Steel BuildingPart I." *Journal of Structural Engineering*, 113(11), 2111–2129.

Fukuta, T., Nishiyama, I., Yamanouchi, H., and Kato, B. (1989). "Seismic Performance of Steel Frames with Inverted V Braces." *Journal of Structural Engineering*, 115(8), 2016–2028.

Galambos, T. V. and Ravindra, M. K. (1978). "Properties of Steel for Use in LRFD." *Journal of the Structural Division*, 104(9), 1459–1468.

Goel, S. C. (1992). "Cyclic post buckling behavior of steel bracing members." *Stability and ductility of steel structures under cyclic loading*, CRC Press, Boca Raton, FL.

Gugerli, H. and Goel, S. C. (1982). "Inelastic cyclic behavior of steel bracing members." *Report UMCE 82R1*, University of Michigan, Ann Arbor, MI.

Han, S.-W., Kim, W. T., and Foutch, D. A. (2007). "Seismic behavior of hss bracing members according to width-thickness ratio under symmetric cyclic loading." *Journal of Structural Engineering*, 133(2), 264–273.

Herman, D. J. (2007). "Further improvements on an understanding of special concentrically braced frame systems." MS thesis, University of Washington, Seattle.

Hilber, H. M., Hughes, T. J. R., and Taylor, R. L. (1977). "Improved numerical dissipation for time integration algorithms in structural dynamics." *Earthquake Engineering & Structural Dynamics*, 5(3), 283–292.

Hsiao, P.-C. (2012). "Seismic performance evaluation of concentrically braced frames." Phd dissertation, University of Washington, Seattle.

Hsiao, P.-C., Lehman, D. E., Berman, J. W., Roeder, C. W., and Powell, J. (2014). "Seismic Vulnerability of Older Braced Frames." *Journal of Performance of Constructed Facilities*, 28(1), 108–120.

Hsiao, P.-C., Lehman, D. E., and Roeder, C. W. (2012). "Improved analytical model for special concentrically braced frames." *Journal of Constructional Steel Research*, 73, 80–94.

Hsiao, P.-C., Lehman, D. E., and Roeder, C. W. (2013a). "A model to simulate special concentrically braced frames beyond brace fracture." *Earthquake Engineering & Structural Dynamics*, 42(2), 183–200.

Hsiao, P.-C., Lehman, D. E., and Roeder, C. W. (2013b). "Evaluation of the response modification coefficient and collapse potential of special concentrically braced frames." *Earthquake Engineering & Structural Dynamics*, 42(10), 1547–1564.

ICBO (1979). *Uniform Building Code*. International Conference of Building Officials, Whittier, CA.

ICBO (1982). *Uniform Building Code*. International Conference of Building Officials, Whittier, CA.

ICBO (1988). *Uniform Building Code*. International Conference of Building Officials, Whittier, CA.

ICBO (1994). *Uniform Building Code*. International Conference of Building Officials, Whittier, CA.

Johnson, M. M. (2014). "Seismic evaluation of bolted connections in non-seismic concentrically braced frames." MS thesis, University of Washington, Seattle.

Johnson, S. M. (2005). "Improved seismic performance of special concentrically braced frames." MS thesis, University of Washington, Seattle.

Karamanci, E. and Lignos, D. G. (2014). "Computational Approach for Collapse Assessment of Concentrically Braced Frames in Seismic Regions." *Journal of Structural Engineering*, 140(8), A4014019.

Kelly, D. J., Bonneville, D. R., and Bartoletti, S. J. (2000). "1994 Northridge Earthquake: Damage to a four-story steel braced frame building and its subsequent upgrade." *Proceedings of the 12th World Conference on Earthquake Engineering*, Auckland, New Zealand.

Kotulka, B. A. (2007). "Analysis for a design guide on gusset plates used in special concentrically braced frames." MS thesis, University of Washington, Seattle.

Lai, J.-W. and Mahin, S. A. (2013). "Experimental and Analytical Studies on the Seismic Behavior of Conventional and Hybrid Braced Frames." *PEER 2013/20*, Pacific Earthquake Engineering Research Center, Berkeley, CA.

Lamarche, C.-P. and Tremblay, R. (2011). "Seismically induced cyclic buckling of steel columns including residual-stress and strain-rate effects." *Journal of Constructional Steel Research*, 67(9), 1401–1410.

Lee, S. (1988). "Seismic behavior of hollow and concrete-filled square tubular bracing members." *Report UMCE 87-11*, University of Michigan, Ann Arbor.

Lehman, D. E., Roeder, C. W., Herman, D., Johnson, S., and Kotulka, B. (2008). "Improved Seismic Performance of Gusset Plate Connections." *Journal of Structural Engineering*, 134(6), 890–901.

Lesik, D. F. and Kennedy, D. J. L. (1990). "Ultimate strength of fillet welded connections loaded in plane." *Canadian Journal of Civil Engineering*, 17(1), 55–67.

Lignos, D. G. and Krawinkler, H. (2011). "Deterioration Modeling of Steel Components in Support of Collapse Prediction of Steel Moment Frames under Earthquake Loading." *Journal of Structural Engineering*, 137(11), 1291–1302.

Liu, J. (2000). "Experimental and Analytical Studies of the Cyclic Behavior of Simple Connections in Steel Frame Buildings." Phd dissertation, University of California, Berkeley, University of California, Berkeley.

Liu, J. and Astaneh-Asl, A. (2000). "Cyclic Testing of Simple Connections Including Effects of Slab." *Journal of Structural Engineering*, 126(1), 32–39.

Liu, J. and Astaneh-Asl, A. (2004). "MomentRotation Parameters for Composite Shear Tab Connections." *Journal of Structural Engineering*, 130(9), 1371–1380.

Liu, Z. and Goel, S. C. (1987). "Investigation of Concrete-Filled Steel Tubes under Cyclic Bending and Buckling." *Report no.*, University of Michigan, Ann Arbor.

Liu, Z. and Goel, S. C. (1988). "Cyclic Load Behavior of Concrete?Filled Tubular Braces." *Journal of Structural Engineering*, 114(7), 1488–1506.

Lumpkin, E. J. (2009). "Enhanced seismic performance of multi-story special concentrically brace frames using a balanced design procedure." MS thesis, University of Washington, Seattle.

Lumpkin, E. J., Hsiao, P.-C., Roeder, C. W., Lehman, D. E., Tsai, C.-Y., Wu, A.-C., Wei, C.-Y., and Tsai, K.-C. (2012). "Investigation of the seismic response of three-story special concentrically braced frames." *Journal of Constructional Steel Research*, 77, 131–144.

Mahin, S. A. (1998). "Lessons from damage to steel buildings during the Northridge earthquake." *Engineering Structures*, 20(4-6), 261–270.

McKenna, F., Scott, M. H., and Fenves, G. L. (2010). "Nonlinear Finite-Element Analysis Software Architecture Using Object Composition." *Journal of Computing in Civil Engineering*, 24(1), 95–107.

Menegotto, M. and Pinto, P. E. (1973). "Method of Analysis for Cyclically Loaded R. C. Plane Frames Including Changes in Geometry and Non-Elastic Behavior of Elements under Combined Normal Force and Bending." *proceedings of IABSE Symposium on Resistance and Ultimate Deformability of Structures Acted on by Well Defined Loads*, Lisbon, 15–22.

Nakashima, M., Inoue, K., and Tada, M. (1998). "Classification of damage to steel buildings observed in the 1995 Hyogoken-Nanbu earthquake." *Engineering Structures*, 20(4-6), 271–281.

NRCC (1980). *National Building Code of Canada*. National Research Council Canada, Ottawa.

NRCC (2010). *National Building Code of Canada*. National Research Council Canada, Ottawa.

Okazaki, T., Lignos, D. G., Midorikawa, M., Ricles, J. M., and Love, J. (2013). "Damage to Steel Buildings Observed after the 2011 Tohoku-Oki Earthquake." *Earthquake Spectra*, 29(S1), S219–S243.

Palmer, K. D., Christopulos, A. S., Lehman, D. E., and Roeder, C. W. (2014). "Experimental evaluation of cyclically loaded, large-scale, planar and 3-d buckling-restrained braced frames." *Journal of Constructional Steel Research*, 101, 415–425.

Palmer, K. D., Roeder, C. W., and Lehman, D. E. (2016). "Connection design recommendations for improved BRBF performance." *AISC Engineering Journal*, 53(1), 29–46.

Powell, J. A. (2010). "Evaluation of special concentrically braced frames for improved seismic performance and constructability." MS thesis, University of Washington, Seattle.

Rai, D. and Goel, S. (2003). "Seismic evaluation and upgrading of chevron braced frames." *Journal of Constructional Steel Research*, 59(8), 971–994.

Rai, D., Goel, S., and Firmansjah, J. (1996). "A General Purpose Computer Program for Nonlinear Structural Analysis." *Report UMCEE 96-21*, University of Michigan, Ann Arbor, MI.

Rathje, E. M., Dawson, C., Padgett, J. E., Pinelli, J.-P., Stanzione, D., Adair, A., Arduino, P., Brandenberg, S. J., Cockerill, T., Dey, C., Esteva, M., Haan, F. L., Hanlon, M., Kareem, A., Lowes, L., Mock, S., and Mosqueda, G. (2017). "DesignSafe: New Cyberinfrastructure for Natural Hazards Engineering." *Natural Hazards Review*, 18(3), 06017001.

Richard, J. (2009). "Étude du Comportemenet Sismique de Bâtiments Industriels avec Systèmes de Contreventement en Acier de Faible Ductilitè." PhD dissertation, Ècole Polytechnique de Montrèal, Montreal, QC.

Roeder, C. W. (1989). "Seismic Behavior of Concentrically Braced Frame." *Journal of Structural Engineering*, 115(8), 1837–1856.

Roeder, C. W., Lehman, D. E., Clark, K., Powell, J., Yoo, J.-H., Tsai, K.-C., Lin, C.-H., and Wei, C.-Y. (2011a). "Influence of gusset plate connections and braces on the seismic performance of X-braced frames." *Earthquake Engineering & Structural Dynamics*, 40(4), 355–374.

Roeder, C. W., Lumpkin, E. J., and Lehman, D. E. (2011b). "A balanced design procedure for special concentrically braced frame connections." *Journal of Constructional Steel Research*, 67(11), 1760–1772.

Sen, A. D. (2014). "Seismic performance of chevron concentrically braced frames with weak beams." MS thesis, University of Washington, Seattle.

Sen, A. D., Roeder, C. W., Berman, J. W., Lehman, D. E., Li, C.-H., Wu, A.-C., and Tsai, K.-C. (2016a). "Experimental Investigation of Chevron Concentrically Braced Frames with Yielding Beams." *Journal of Structural Engineering*, 142(12), 04016123.

Sen, A. D., Roeder, C. W., Lehman, D. E., and Berman, J. W. (2018). "Nonlinear Modeling of Concentrically Braced Frames." *In preparation.*

Sen, A. D., Sloat, D., Ballard, R., Johnson, M. M., Roeder, C. W., Lehman, D. E., and Berman, J. W. (2016b). "Experimental Evaluation of the Seismic Vulnerability of Braces and Connections in Older Concentrically Braced Frames." *Journal of Structural Engineering*, 142(9), 04016052.

Sen, A. D., Swatosh, M. A., Ballard, R., Sloat, D., Johnson, M. M., Roeder, C. W., Lehman, D. E., and Berman, J. W. (2017). "Development and Evaluation of Seismic Retrofit Alternatives for Older Concentrically Braced Frames." *Journal of Structural Engineering*, 143(5), 04016232.

Shaback, B. and Brown, T. (2003). "Behaviour of square hollow structural steel braces with end connections under reversed cyclic axial loading." *Canadian Journal of Civil Engineering*, 30(4), 745–753.

Simpson, B. G. and Mahin, S. A. (2018). "Experimental and Numerical Evaluation of Older Chevron Concentrically Braced Frames with Hollow and Concrete-Filled Braces." *Journal of Structural Engineering*, 144(3), 04018007.

Sizemore, J. G., Fahnestock, L. A., Hines, E. M., and Bradley, C. R. (2017). "Parametric Study of Low-Ductility Concentrically Braced Frames under Cyclic Static Loading." *Journal of Structural Engineering*, 143(6), 04017032.

Sloat, D. A. (2014). "Evaluation and retrofit of non-capacity designed braced frames." MS thesis, University of Washington, Seattle.

Somerville, P., Smith, N., Punyamurthula, S., and Sun, J. (1997). "Development of ground motion time histories for phase 2of the FEMA/SAC steel project." *Rep. No. SAC/BD-97/04: SAC Background Document*, Federal Emergency Management Agency, Sacramento, CA.

Stephens, M. T., Lehman, D. E., and Roeder, C. W. (2018). "Seismic performance modeling of concrete-filled steel tube bridges: Tools and case study." *Engineering Structures*, 165, 88–105.

Swatosh, M. A. (2016). "Seismic evaluation and retrofit of concentrically braced frames." MS thesis, University of Washington, Seattle.

Tanaka, A., Morita, K., and Yamanouchi, H. (1980). "Damage of braced steel frames due to the 1978 Miyagiken-Oki Earthquake." *Proceedings of the 7th World Conference on Earthquake Engineering*, Istanbul, Turkey.

Tang, X. and Goel, S. (1987). "Seismic Analysis and Design Considerations of Braced Steel Structures." *Report UMCE 87-4*, University of Michigan, Ann Arbor, MI.

Terpstra, C. (2017). "Impact of beam strength on seismic performance of chevron concentrically braced frames." MS thesis, University of Washington, Seattle, <http://hdl.handle.net/1773/40001>.

Tirca, L. and Chen, L. (2014). "Numerical Simulation of Inelastic Cyclic Response of HSS Braces upon Fracture." *Advanced Steel Construction*, 10(4), 442–462.

Tremblay, R., Archambault, M.-H., and Filiatrault, A. (2003). "Seismic Response of Concentrically Braced Steel Frames Made with Rectangular Hollow Bracing Members." *Journal of Structural Engineering*, 129(12), 1626–1636.

Tremblay, R., Filiatrault, A., Bruneau, M., Nakashima, M., Prion, H. G. L., and DeVall, R. (1996). "Seismic design of steel buildings: lessons from the 1995 Hyogo-ken Nanbu earthquake." *Canadian Journal of Civil Engineering*, 23(3), 727–756.

Tremblay, R., Filiatrault, A., Timler, P., and Bruneau, M. (1995). "Performance of steel structures during the 1994 Northridge earthquake." *Canadian Journal of Civil Engineering*, 22(2), 338–360.

Tsai, C.-Y., Tsai, K.-C., Lin, P.-C., Ao, W.-H., Roeder, C. W., Mahin, S. A., Lin, C.-H., Yu, Y.-J., Wang, K.-J., Wu, A.-C., Chen, J.-C., and Lin, T.-H. (2013). "Seismic Design and Hybrid Tests of a Full-Scale Three-Story Concentrically Braced Frame Using In-Plane Buckling Braces." *Earthquake Spectra*, 29(3), 1043–1067.

Uriz, P. and Mahin, S. A. (2004). "Seismic Vulnerability Assessment of Concentrically Braced Steel Frames." *Steel Structures*, 4, 239–248.

Uriz, P. and Mahin, S. A. (2008). "Toward Earthquake-Resistant Design of Concentrically Braced Steel-Frame Structures." *PEER 2008/08*, Pacific Earthquake Engineering Research Center, Berkeley, CA.

USGS (2017). "National Seismic Hazard Mapping Project (NSHMP) Code, <https://github.com/usgs/nshmp-haz>.

Wakabayashi, M., Nakamura, T., and Yoshida, N. (1977). "Experimental studies on the elastic-plastic behavior of braced frames under repeated horizontal loading. Part 1: Experiments of braces with an h-shaped cross section in a frame." *Bulletin of the Disaster Prevention Research Institute*, 27(3).

Wakabayashi, M., Nakamura, T., and Yoshida, N. (1980). "Experimental studies on the elastic-plastic behavior of braced frames under repeated horizontal loading. Part 2: Experiments of braces composed of steel circular tubes, angle-shapes, flat bars or round bars." *Bulletin of the Disaster Prevention Research Institute*, 29(3).

Weigand, J. M. (2017). "Component-Based Model for Single-Plate Shear Connections with Pretension and Pinched Hysteresis." *Journal of Structural Engineering*, 143(2), 04016178.

Weigand, J. M., Liu, J., and Main, J. A. (2016). "Modeling of double-angle connections for robustness evaluation of steel gravity frames." *International Workshop on Connections in Steel Structures 2016*, Boston, MA.

Yang, F. and Mahin, S. A. (2005). *Limiting net section failure in slotted HSS braces.* Structural Steel Education Council, Moraga, CA.